



UNIVERSITÀ DEGLI STUDI DELL'AQUILA
DIPARTIMENTO DI INGEGNERIA INDUSTRIALE E DELL'INFORMAZIONE E DI
ECONOMIA

Dottorato di Ricerca in Ingegneria Industriale e
dell'Informazione e di Economia
Curriculum Ingegneria chimica
XXXIII ciclo

Titolo della tesi
**Catalytic hydrogenation/deoxygenation processes on vegetable oils
in order to obtain bio-products and green diesel**

SSD ING-IND/27 Chimica Industriale e Tecnologica

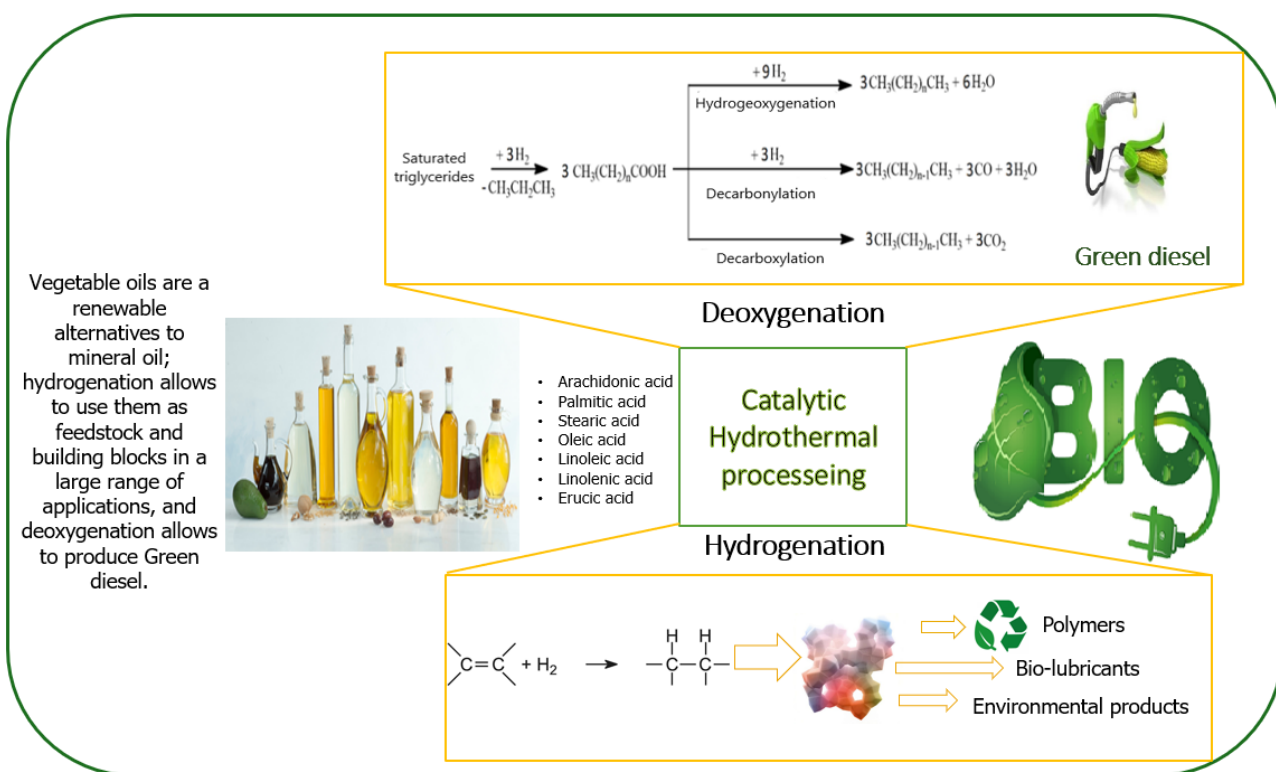
Dottorando
Rasha AlhajYoussef

Coordinatore del corso
Prof. Giuseppe Ferri

Tutor
Prof. Katia Gallucci

A.A. 2019/2020

GRAPHICAL ABSTRACT



ABSTRACT

This doctoral thesis is focused on Green Chemistry, particularly the study of catalytic hydrogenation/deoxygenation processes on vegetable oils to obtain biochemical products and green diesel.

Vegetable oils found widespread application in industry and transports as a sustainable alternative, clean automotive fuel, petrochemicals, and renewable building blocks in industrial applications.

Two hydrotreating processes on the vegetable oils (rapeseed and sunflower) have been concerned in this research:

- Selective catalytic hydrogenation in order to maximize the content of oleic acid, which is a monounsaturated carboxylic acid with eighteen carbon atoms. It has the suitable characteristics (stable in the presence of oxygen, and it remains liquid even at low temperatures) for use as a biodegradable lubricant and is a building block in the production of polymers and plastics from renewable resources.
- Selective catalytic deoxygenation to increase the green diesel range (C₁₅-C₁₈) hydrocarbons, it is a premium diesel-blending component, its boiling range is

comparable to the conventional diesel, and it has substantially higher cetane content and lower density than the conventional one. The development of green diesel could solve not only the problems of the continuous and inevitable fossil fuel exhaustion but also the gas emissions pollution from fossil fuels.

Our research activities in this doctoral thesis concerned the following arguments:

- State of the art exposed briefly, environmental pollution, green chemistry, fossil fuels shortage, renewable feeding stocks, catalytical hydrotreating reactions mechanisms, and their catalysis (homogeneous vs. heterogeneous).
- Studying the most updated techniques for both preparation and characterization of catalysts, five different synthesized heterogenous mono and bimetallic catalysts have been prepared by co-precipitation method (Pd/HT) and conventional wet impregnation one (Pd/FAC, CoMo/FAC, NiMo/FAC, and NiMo/zeolite X). The five synthesized catalysts and a commercial one (Pd Lindlar) were characterized by elemental analysis (ICP-AES), H₂-Chemisorption, Thermogravimetric analysis (TGA), X-ray diffraction (XRD), N₂ adsorption (BET), programmed temperature reduction (TPR), scanning electron microscopy with energy-dispersive X-ray spectroscopy (SEM-EDS), and NH₃-TPD acidity analysis.
- Carrying out the hydrogenation tests in a laboratory-scale plant reactor, this system's core is a Parr Instrument 4560 (600 mL) reactor unit operated in semi-batch mode, feeding the hydrogen continuously. The tests were performed with rapeseed and sunflower oils using different palladium supported catalysts (Pd Lindlar, Pd/HT, and Pd/FAC) under varying levels of conditions; temperature (60 ° C, 90 ° C, 120 ° C, 180 ° C, and 240 ° C), hydrogen pressure (4 bar, 8 bar, and 12 bar), and catalyst concentration (4 mg_{catalyst}/mL_{oil}, 2 mg_{catalyst}/mL_{oil}, 1 mg_{catalyst}/mL_{oil} ,and 0.5

mg_{catalyst}/mL_{oil}). The best results of monounsaturated C18:1 was obtained for Pd Lindlar catalyst at (180 ° C, 4 bar and 4 mg/ml) with 88.4 % of C18:1 after about 90 min of the reaction time, for Pd/HT at (180 ° C, 4 bar) but with half catalyst concentration of Pd Lindlar (2 mg/ml) obtaining 89.9 % of C18:1 after 180 min. In contrast, for Pd/FAC the best result was gotten at a higher temperature, higher pressure, and less catalyst concentration (a quarter of Pd Lindlar) (240 ° C, 8 bar and 1 mg/ml) with 82.7 % of C18:1 oleic acid after 210 min reaction time. The results highlight how it is possible to obtain the same conversion of polyunsaturated vegetable oils about 100 % and monoene acid C18:1 over 82 % with higher best reaction time using less concentration from the synthesized catalyst.

- Implementing the deoxygenation tests in a laboratory-scale plant reactor, this system's heart is a Parr microInstrument 4598 (100 mL) reactor unit operated in semi-batch mode, feeding the hydrogen continuously. The tests were performed with stearic acid and sunflower oils using different mono and bimetallic catalysts (Pd Lindlar, Pd/FAC, CoMo/FAC, NiMo/FAC, NiMo/zeolite X) under different levels of conditions; temperature (280 ° C, 300 ° C, 320 ° C), hydrogen pressure (20 bar, and 40 bar), and catalyst concentration (2.5 wt%, and 10 wt%). The main highlights on the best results obtained from the deoxygenation reactions over these catalysts; Pd Lindlar commercial catalyst as a reference point under (300 ° C, 40 bar, and 10 wt%) produced 23 % of green diesel yield and 55 % conversion in hydrocarbons after 8 h, with Pd/FAC 31% green diesel yield and 41 % conversion in hydrocarbons were obtained with selectivity towards DCO/DCO₂ pathway reaction under (320 ° C, 40 bar, and 10 wt%) after 6 h reaction time. For bimetallic CoMo/FAC, NiMo/FAC, and NiMo/zeolite X under (320 ° C, 40 bar, and 10 wt%) green diesel yield and conversion in hydrocarbons obtained (17 %, 25 %, and 35 %) and (20 %, 63 %, and 78 %) respectively after 6 h.

SOMMARIO

Questa tesi di dottorato è incentrata sulla chimica verde, in particolare lo studio del trattamento idrotermale catalitico su oli vegetali al fine di ottenere prodotti biochimici e diesel verde.

Gli oli vegetali hanno trovato ampia applicazione nell'industria e nei trasporti come combustibile pulito alternativo sostenibile per automobili, prodotti petrolchimici e elementi costitutivi rinnovabili nelle applicazioni industriali.

In questa ricerca sono stati coinvolti due processi idrotermali sugli oli vegetali (colza e girasole):

- Idrogenazione catalitica selettiva per massimizzare il contenuto di acido oleico, che è un acido carbossilico monoinsaturo con diciotto atomi di carbonio. Ha le caratteristiche adatte (stabile in presenza di ossigeno, e rimane un liquido anche a basse temperature) per essere utilizzato come lubrificante biodegradabile ed è un elemento costitutivo nella produzione di polimeri e plastiche da risorse rinnovabili.
- Deossigenazione catalitica selettiva per aumentare gli idrocarburi della gamma del diesel verde (C15-C18), è un componente di miscelazione diesel premium, il suo intervallo di ebollizione è paragonabile al diesel convenzionale e ha un contenuto di cetano sostanzialmente più elevato e una densità inferiore rispetto a quello

convenzionale. Lo sviluppo del green diesel potrebbe risolvere non solo i problemi del continuo e inevitabile esaurimento dei combustibili fossili, ma anche l'inquinamento delle emissioni gassose da combustibili fossili.

Le nostre attività di ricerca in questa tesi di dottorato hanno riguardato i seguenti argomenti:

- Lo stato dell'arte ha esposto brevemente l'inquinamento ambientale, la chimica verde, la carenza di combustibili fossili, le riserve di alimentazione rinnovabile, i meccanismi di reazioni idrotermali catalitiche e la catalisi idrotermale (omogenea vs. eterogenea).
- Studiando le tecniche più aggiornate sia per la preparazione che per la caratterizzazione dei catalizzatori, sono stati preparati 5 diversi catalizzatori eterogenei mono e bimetallici sintetizzati mediante il metodo di co-precipitazione (Pd / HT) e quello di impregnazione a umido convenzionale (Pd/FAC, CoMo/FAC, NiMo/FAC e NiMo/zeolite X). I 5 catalizzatori sintetizzati e uno commerciale (Pd Lindlar) sono stati caratterizzati da analisi elementare (ICP), H₂-Chemisorbimento, analisi gravimetrica termica (TGA), diffrazione di raggi X (XRD), adsorbimento di N₂ (BET), riduzione della temperatura programmata (TPR), microscopia elettronica a scansione con spettroscopia a raggi X a dispersione di energia (SEM-EDS) e analisi dell'acidità NH₃-TPD.
- Eseguendo i test di idrogenazione in un reattore di impianto su scala da laboratorio, il cuore di questo sistema è un'unità reattore Parr Instrument 4560 (600 mL) operata in modalità semi-batch, alimentando l'idrogeno in continuo. I test sono stati eseguiti con oli di colza e girasole utilizzando diversi catalizzatori supportati da palladio (Pd Lindlar, Pd/HT e Pd/FAC) in diversi livelli di condizioni; temperatura (60 ° C, 90 ° C, 120 ° C, 180 ° C e 240 ° C), pressione dell'idrogeno (4 bar, 8 bar e 12 bar) e concentrazione del catalizzatore (4 mg catalizzatore / mL olio, 2 mg catalizzatore / mL olio, 1 mg catalizzatore / mL_{oil}, 0,5 mg catalizzatore / mL_{oil}). I migliori risultati di C18: 1 monoinsaturo

sono stati ottenuti per catalizzatore Pd Lindlar a (180 ° C, 4 bar e 4 mg / ml) con 88,4 % di C18: 1 dopo circa 90 min del tempo di reazione, per Pd / HT a (180 ° C, 4 bar) ma con metà concentrazione di catalizzatore (2 mg / ml) ottenendo 89,9 % di C18: 1 dopo 180 min, mentre per Pd / FAC il miglior risultato si ottiene a temperatura più alta, pressione più alta e concentrazione di catalizzatore minore (un quarto di Pd Lindlar) (240 ° C, 8 bar e 1 mg / ml) con 82,7 % di acido oleico C18: 1 dopo 210 min di tempo di reazione. I risultati evidenziano come sia possibile ottenere la stessa conversione di oli vegetali polinsaturi al 100 % circa e acido monoenoico C18:1 oltre 82 % con tempi di reazione migliori utilizzando una concentrazione minore da catalizzatore sintetizzato.

- Implementando i test di deossigenazione in un reattore di impianto su scala di laboratorio, il cuore di questo sistema è un'unità reattore Parr micro Instrument 4598 (100 mL) operata in modalità semi-batch, alimentando l'idrogeno in modo continuo. Le prove sono state eseguite con acido stearico e oli di girasole utilizzando diversi catalizzatori mono e bimetallici (Pd Lindlar, Pd/FAC, CoMo/FAC, NiMo/FAC, NiMo/zeolite X) in diversi livelli di condizioni; temperatura (280 ° C, 300 ° C, 320 ° C), pressione dell'idrogeno (20 bar e 40 bar) e concentrazione del catalizzatore (2,5 wt% e 10 wt%). I principali punti salienti sui migliori risultati ottenuti dalle reazioni di deossigenazione su questi catalizzatori; Il catalizzatore commerciale Pd Lindlar come punto di riferimento sotto (300 ° C, 40 bar e 10 wt% in peso) ha prodotto il 23 % di resa di green diesel e il 55 % di conversione in idrocarburi dopo 8 h, con Pd/FAC 31 % di resa di green diesel e 41 % la conversione in idrocarburi è stata ottenuta con selettività verso DCO / DCO₂ sotto (320 ° C, 40 bar e 10 wt% in peso) dopo 6 ore di tempo di reazione. Per CoMo/FAC bimetallico, NiMo/FAC e NiMo/zeolite X sotto (320 ° C, 40 bar e 10 wt% in peso) resa e conversione in idrocarburi ottenute (17%, 25 % e 35 %) e (20 %, 63 % e 78 %) rispettivamente dopo 6 h.

CONTENTS

1	Literature review	21
1.1	Environmental pollution and climate change	21
1.2	Green Chemistry	22
1.3	Fossil fuel shortage and its alternatives.....	24
1.4	Renewable feeding stocks	25
1.5	Biofuels' generations	27
1.6	Vegetable oils.....	29
1.7	Catalytic hydrotreating reactions mechanisms on vegetable oils.....	33
1.7.1	Vegetable oils hydrogenation	33
1.7.2	Vegetable oils Deoxygenation.....	37
1.8	Hydrotreating catalysis (homogeneous vs. heterogeneous)	43
1.8.1	Homogeneous catalysis	44
1.8.2	Heterogeneous catalysis	45
2	Materials and methods	56
2.1	Catalysts and synthesis methods	56
2.1.1	Synthesis methods	56
2.1.2	Nomenclature and list of materials	58
2.1.3	Catalysts preparation	60
2.2	Characterization techniques	64
2.2.1	Thermal Gravimetric Analysis	65

2.2.2	Ion Coupled Plasma - Atomic Emission Spectroscopy	65
2.2.3	X-ray diffraction.....	66
2.2.4	Surface area and porosity analysis BET-BJH.....	69
2.2.5	Scanning Electron Microscopy	70
2.2.6	Temperature programmed reduction TPR.....	71
2.2.7	Temperature Programmed Desorption NH ₃ -TPD	73
2.2.8	H ₂ -Chemisorption.....	73
2.3	Gas Chromatographic Analysis techniques.....	74
2.3.1	Trace GC Ultra 7820	74
2.3.2	GC/3400cx Varian star coupled with MS/Varian Saturn 2000	75
2.3.3	GC/7820A Agilent	76
2.4	Experimental study of hydrogenation reactions.....	77
2.4.1	Vegetable oil selection for hydrogenation tests.....	77
2.4.2	Lab-scale experimental apparatus for hydrogenation test	78
2.4.3	Reactivity and Selectivity.....	81
2.5	Experimental study on the production of green diesel by hydroprocessing reactions.....	83
2.5.1	Vegetable oil selection for deoxygenation tests	83
2.5.2	Lab-scale experimental apparatus for hydrogenation test	84
2.5.3	Reactivity and Selectivity.....	86
3	Catalysts characterization	90
3.1	Lindlar catalyst characterization	90
3.1.1	Elemental analysis ICP-AES.....	90
3.1.2	Lindlar H ₂ -Chemisorption.....	91
3.1.3	BET-BJH analysis	91
3.1.4	Crystalline phases analysis XRD.....	92
3.2	Pd/HT catalyst characterization	93
3.2.1	Pd/HT Elemental analysis	93
3.2.2	Pd/HT, H ₂ -Chemisorption.....	94
3.2.3	Pd/HT, BET-BJH analysis	94
3.2.4	Pd/HT XRD analysis	95
3.2.5	Pd/HT SEM and EDS analysis	96

3.3	Pd/FAC catalyst characterization.....	98
3.3.1	Pd/FAC Elemental analysis.....	98
3.3.2	Pd/FAC TPR temperature programmed reduction analysis and H ₂ -Chemisorption.....	98
3.3.3	Pd/FAC TGA analysis.....	99
3.3.4	Pd/FAC, BET-BJH analysis.....	100
3.3.5	Pd/FAC XRD analysis.....	101
3.3.6	Pd/FAC SEM and EDS analysis	103
3.4	CoMo/FAC catalyst characterization.....	105
3.4.1	CoMo/FAC Elemental analysis.....	105
3.4.2	CoMo/FAC TPR temperature programmed reduction analysis and H ₂ -Chemisorption.....	105
3.4.3	CoMo/FAC TGA analysis.....	107
3.4.4	CoMo/FAC, BET-BJH analysis	108
3.4.5	CoMo/FAC XRD analysis.....	109
3.4.6	CoMo/FAC SEM and EDS analysis.....	111
3.5	NiMo/FAC catalyst characterization.....	113
3.5.1	NiMo/FAC Elemental analysis.....	113
3.5.2	NiMo/FAC TPR temperature programmed reduction analysis and H ₂ -Chemisorption	113
3.5.3	NiMo/FAC, BET-BJH analysis.....	115
3.5.4	NiMo/FAC XRD analysis	115
3.5.5	NiMo/FAC SEM and EDS analysis	117
3.6	NiMo/zeolite X catalyst characterization.....	119
3.6.1	NiMo/zeolite X Elemental analysis.....	119
3.6.2	NiMo/zeolite X TPR temperature programmed reduction analysis and H ₂ -chemisorption.....	120
3.6.3	NiMo/zeolite X, BET-BJH analysis.....	122
3.6.4	NiMo/zeolite XRD analysis	123
3.6.5	NiMo/zeolite X SEM and EDS analysis	124
3.6.6	NiMo/zeolite X NH ₃ -TPD temperature programmed desorption of ammonia analysis	126
3.7	Conclusions.....	127
4	Hydrogenation reactivity tests.....	131
4.1	Lindlar catalyst hydrogenation tests.....	131
4.2	Pd/HT catalyst hydrogenation reactivity tests.....	141

4.3	Pd/FAC catalyst hydrogenation reactivity tests	149
4.4	Conclusion	154
5	Deoxygenation reactivity tests	158
5.1	Lindlar catalyst deoxygenation reactivity tests	158
5.2	Pd/FAC catalyst Deoxygenation reactivity tests	164
5.2.1	Post-test 05 Pd/FAC	170
5.3	CoMo/FAC catalyst Deoxygenation reactivity tests	171
5.3.1	Post-test 06 CoMo/FAC	173
5.4	NiMo/FAC catalyst Deoxygenation reactivity tests	174
5.4.1	Post-test 08 NiMo/FAC	178
5.5	NiMo/zeolite X catalyst Deoxygenation reactivity tests	180
5.5.1	Post-test 11 NiMo/zeolite X	184
5.6	Conclusions	185
6	General conclusions	189
7	Addendum A: SEM results	194
7.1	A.1 Pd/HT	194
7.2	A.2 Pd/FAC	195
7.3	A.3 CoMo/FAC	196
7.4	A.4 NiMo/FAC	197
7.5	A.5 NiMo/zeolite x	198
8	Addendum b: hydrogenation tests results	199
8.1	B.1 Test 01- test 02	200
8.2	B.2 model fitting with Pd lindlar	200
8.3	B.3 model fitting with Pd/ht	201
8.4	B.4 model fitting with Pd/fac	202
9	Addendum c: characterization results for future activities	203
9.1	C.1 ICP-AES Elemental analysis	203
9.2	C.2 H ₂ -Chemisorption analysis	204
9.3	C.3 TPR temperature programmed	204
9.4	C.4 NH ₃ -TPD – acidity analysis	205
10	Addendum d: desalination technologies	207

10.1	Introduction.....	209
10.2	History of desalination.....	211
10.3	Overview of desalination technologies	212
10.3.1	Thermal desalination processes.....	214
10.3.2	Membrane process.....	217
10.3.3	Others Desalination Technologies.....	222
10.4	Parametric comparison of desalination technologies	226
10.4.1	Removal efficiency and performance ratio	226
10.4.2	Specific energy consumption SEC	227
10.4.3	Quality of feed water.....	228
10.4.4	Corrosion, scaling, and fouling	228
10.5	Operational desalination MSF&RO plants technologies	230
10.5.1	Methodology and design of Multi-Stage Flash distillation	230
10.5.2	Mythology and design of RO reverse osmosis desalination.....	235
10.6	Conclusions.....	241
11	Bibliography	243
12	Acknowledgments.....	276

LIST OF FIGURES

Figure 1.1 Biomass as a renewable feedstock. [21].....	26
Figure 1.2 Percentage composition of various vegetable oils in terms of saturated and unsaturated fatty acids[36].	29
Figure 1.3 Hydrogenation reaction mechanism as described by Dijkstra, where *= adsorbed intermediates, c= cis isomers, t=trans isomers, M=monoene, and D = diene, respectively.	35
Figure 1.4 Possible reaction pathways of triglycerides over a hydro-treating catalyst [64].	38
<i>Figure 1.5 Initial breakdown of triglycerides [73]</i>	<i>40</i>
Figure 1.6 Hydrodeoxygenation HDO pathway[74]	40
Figure 1.7 Decarboxylation DCO ₂ /Decarbonylation DCO pathway[74]	41
Figure 1.8 Possible gas-phase reactions[16].....	42
Figure 1.9 Energy diagram that can show the difference between catalyzed and uncatalyzed reaction, in terms of activation energy and reaction pathway[82].	43
Figure 1.10 trans-esterification of vegetable oil to produce Biodiesel	44
Figure 1.11 Diagram of common catalysts used for the DO [86].....	47
Figure 1.12 Hydrotalcite based Mg/Al [113].....	49
Figure 1.13 Morphological structure of the cenospheres.....	51
Figure 1.14 Bronsted acid sites present in zeolites.	53
Figure 1.15 Faujasite-type zeolites X structure. [131].....	53
Figure 2.1 Bragg's Low Reflection	67
Figure 2.2 XRD Bragg – Brentano geometry [156].	68
Figure 2.3 Schematic diagram [160]	72

Figure 2.4 Schematic diagram of the gas chromatographic analyzer.	75
Figure 2.5 Lab-scale plant reactor for hydrogenation of vegetable oils and their derivatives.	79
Figure 2.6 Photo of the laboratory scale setup.....	79
Figure 2.7 Lab-scale plant reactor for hydro processing of vegetable oils and their derivatives.....	85
Figure 2.8 Photo of the laboratory scale setup.....	85
Figure 3.1 BET Isotherms (left) BJH desorption pore size distribution (right) of Lindlar.	92
Figure 3.2 XRD spectra of Lindlar catalyst with CaCO ₃ principal rays reported.....	93
Figure 3.3 BET Isotherms (left) BJH desorption pore size distribution (right) of Pd/HT catalyst.	95
Figure 3.4 XRD spectra of Pd/HT catalyst with hydrotalcite phase.	96
Figure 3.5 Pd/HT SEM image analysis.	97
<i>Figure 3.6 Pd/HT analysis, SEM image (on the right), and relative EDS analysis (on the left).</i>	97
<i>Figure 3.7 Pd/FAC temperature programmed reduction</i>	99
Figure 3.8 Thermogravimetric analysis (TGA) of Pd/FAC.....	100
Figure 3.9 BET Isotherms (left) BJH desorption pore diameter size distribution (right) of Pd/FAC catalyst.....	101
Figure 3.10 X-ray diffraction spectrum of Pd/FAC (up) & FAC (down).....	102
Figure 3.11 Pd/FAC SEM image analysis.	103
Figure 3.12 Cenosphere and Pd/FAC analysis, SEM image (right) and relative EDS analysis (left).....	104
Figure 3.13 Map Scanning electron Microscope (SEM) of Pd/FAC	104
Figure 3.14 CoMo/FAC temperature programmed reduction	107
Figure 3.15 Thermogravimetric analysis (TGA) of CoMo/FAC.....	108
Figure 3.16 BET Isotherms (left) BJH desorption pore diameter size distribution (right) of CoMo/FAC catalyst.	109
Figure 3.17 X-ray diffraction spectrum of CoMo/FAC (up) & FAC (down)	110
Figure 3.18 CoMo/FAC SEM image analysis.	111
Figure 3.19 Cenosphere and CoMo/FAC analysis, SEM image (right) and relative EDS analysis (left).....	112
Figure 3.20 Map Scanning electron Microscope (SEM) of CoMo/FAC	112
Figure 3.21 NiMo/FAC temperature programmed reduction.	114
Figure 3.22 BET Isotherms (left) BJH desorption pore diameter size distribution (right) of NiMo/FAC catalyst	115
Figure 3.23 X-ray diffraction spectrum of NiMo/FAC (up) & FAC (down).....	116
Figure 3.24 NiMo/FAC SEM image analysis.....	118

Figure 3.25 Cenosphere and NiMo/FAC analysis, SEM image (right) and relative EDS analysis (left)	118
Figure 3.26 Map Scanning electron Microscope (SEM) of NiMo/FAC.....	119
Figure 3.27 NiMo/Zeolite X temperature programmed reduction.....	121
Figure 3.28 BET Isotherms (left) BJH desorption pore diameter size distribution (right) of NiMo/Zeolite X catalyst.....	122
Figure 3.29 X-ray diffraction spectrum of NiMo/zeolite X (up) & Zeolite X (down).	123
Figure 3.30 NiMo/zeolite X analysis, SEM image	125
Figure 3.31 Zeolite X and NiMo/zeolite X analysis, SEM image (Right) and relative EDS analysis (left)	125
Figure 3.32 Map Scanning electron Microscope (SEM) of NiMo/zeolite X.	126
Figure 3.33 NiMo/zeolite X temperature programed desorption with NH ₃	127
Figure 4.1 Test 03 (120 °C, 8 bar and 4 mg/ml) Hydrogenation with canola oil and Lindlar results, conversions of linolenic and linoleic acid and iodine value vs. time (right) relative percentage of C18 compounds vs. time (left)	133
Figure 4.2 Test 04 (180 °C, 4 bar and 4 mg/ml) Hydrogenation with canola oil and Lindlar results, conversions of linolenic and linoleic acid and iodine value vs. time (right) relative percentage of C18 compounds vs. time (left)	134
Figure 4.3 Test 05 (180 °C, 12 bar and 4 mg/ml) Hydrogenation with canola oil and Lindlar results, conversions of linolenic and linoleic acid and iodine value vs. time (right) relative percentage of C18 compounds vs. time (left)	134
Figure 4.4 Test 06 (180 °C, 4 bar and 2 mg/mL) Hydrogenation with canola oil and Lindlar results, conversions of linolenic and linoleic acid and iodine value vs time (right) relative percentage of C18 compounds vs time (left)	136
Figure 4.5 Test 07 (180 °C, 4 bar and 1 mg/mL) Hydrogenation with canola oil and Lindlar results, conversions of linolenic and linoleic acid and iodine value vs. time (right) relative percentage of C18 compounds vs. time (left)	136
Figure 4.6 Hydrogenated oil composition at 1h over five cyclic tests at 180°C, 4 bar and 4mg/mL with canola oil and Lindlar catalyst, (test 08-12)[8]	138
Figure 4.7 C18:1 and C18:2 conversions at 1h over five cyclic tests at 180°C, 4 bar and 4mg/mL with canola oil and Lindlar catalyst, (test 08-12)[8]	138
Figure 4.8 test 08 (180 °C, 4 bar and 4 mg/mL) Hydrogenation with sunflower oil and Lindlar results, conversions of linolenic and linoleic acid and iodine value vs. time (right) relative percentage of C18 compounds vs. time (left)	139
<i>Figure 4.9 Example of data with respective calculated compositions for test 04 (K1=0.0001, K2=0.0122, K3=0.02121) canola rapeseed oil (left) and test 13 (K1=0.0006, K2=0.009) sunflower oil (right).</i>	140
Figure 4.10 Tests 14(60 °C and 4 bar) and 15 (90 °C and 4 bar) of Pd-HT with sunflower oil	141
Figure 4.11 Hydrogenation results with Pd/HT catalyst at 120 °C and 4 bar with different catalyst concentrations (0.5, 1 and 2 mg _{catalyst} /mL _{oil}) tests 16, 20, 22	143
Figure 4.12 Test 20 (120 °C, 4 bar and 2 mg/mL) hydrogenation with sunflower oil and Pd/HT results, conversions of linoleic acid and iodine value vs. time (left) relative percentage of C18 compounds vs. time (right)	143

Figure 4.13 Test 18 (120 °C, 12 bar and 0.5 mg/ml) Hydrogenation with sunflower oil and Pd/HT results, conversions of linoleic acid and iodine value vs. time (left) relative percentage of C18 compounds vs. time (right)	144
Figure 4.14 Hydrogenation results with sunflower oil and Pd/HT at 120 °C and 0.5 mg _{catalyst} /mL _{oil} with different pure hydrogen pressure (4 and 12 bar), tests 16 and 18.....	145
Figure 4.15 Hydrogenation results with sunflower oil and Pd/HT 4 bar and 1 mg _{catalyst} /mL _{oil} with different temperature (120 and 180 °C), tests 22 and 25	146
<i>Figure 4.16 Test 25 (180 °C, 4 bar and 1 mg/mL) Hydrogenation with sunflower oil and Pd/HT results, conversions of linoleic acid and iodine value vs. time (left) relative percentage of C18 compounds vs. time (right)</i>	<i>146</i>
Figure 4.17 Test results for the cyclic test at (180 °C, 4 bar, and 1 mg _{catalyst} /mL _{oi}) with Pd/HT.....	147
<i>Figure 4.18 Figure 4.19 Three Examples of data with respective calculated compositions for test 20 (120 °C, 4 bar, 2 mg_{catalyst}/mL_{oil}) (up left) (K1=0.0007, K2=0.01232), test 18 (120 °C, 12 bar, 0.5 mg_{catalyst}/mL_{oil}) (up right) (K1=0.0006, 0.010124), and test 25 (180 °C, 4 bar, 1 mg_{catalyst}/mL_{oil}) (down) (K1=0.0002, K2=0.005642).</i>	<i>149</i>
Figure 4.19 Test 29 (180 °C, 4 bar and 1 mg/mL) Hydrogenation with sunflower oil and Pd/FAC results, conversions of linoleic acid and iodine value vs. time (left) relative percentage of C18 compounds vs. time (right)	151
Figure 4.20 Test 30 (120 °C, 8 bar and 1 mg/mL) Hydrogenation with sunflower oil and Pd/FAC results, conversions of linoleic acid and iodine value vs. time (left) relative percentage of C18 compounds vs. time (right)	151
Figure 4.21 Test 31 (240 °C, 8 bar and 1 mg/mL) Hydrogenation with sunflower oil with Pd/FAC results, conversions of linoleic acid and iodine value vs. time (left) relative percentage of C18 compounds vs. time (right)	152
Figure 4.22 Hydrogenation results with sunflower oil and Pd/FAC at 8 bar and 1 mg _{catalyst} /mL _{oil} with different temperatures (120 and 240 °C), tests 30 and 31	153
<i>Figure 4.23 Two examples of data with respective calculated compositions for test 31 (240 C, 8 bar, 1 mg_{catalyst}/mL_{oil}) (left) (K1=0.0004, K2=0.009), test 30 (120 C, 8 bar, 1 mg catalyst/mL_{oil}) (right) (K1=0.0006, K2=0.0083).</i>	<i>153</i>
Figure 5.1 Light (C9-C14), diesel (C15-C18), and oxygenates ranges distribution in a commercial diesel sample.	159
Figure 5.2 Cracking process during the deoxygenation reaction [216].	161
Figure 5.3 Test 01 (300 °C, 20 bar N ₂ and 10 wt% cat.) deoxygenation with stearic acid and Lindlar catalyst results, distribution of the light and diesel range hydrocarbons at the best conditions (right) relative percentage of product compounds vs. time (left)	161
Figure 5.4 Test 02 (300 °C, 40 bar H ₂ and 10 wt% cat.) deoxygenation with sunflower oil and Lindlar results, distribution of the light and diesel range hydrocarbons at the best conditions (right) relative percentage of product compounds vs. time (left)	162
Figure 5.5 Test 02 (300 °C, 40 bar H ₂ , and 10 wt% cat.) deoxygenation of sunflower oil with Lindlar: percentage results of green diesel hydrocarbons, oxygenates, and others	163
Figure 5.6 Test 03 (300 °C, 20 bar N ₂ and 10 wt% cat.) deoxygenation with stearic acid and Pd/FAC results, distribution of the light and diesel range hydrocarbons at the best conditions (right) relative percentage of product compounds vs. time (left)	166

Figure 5.7 Test 04 (320 °C, 20 bar H ₂ and 10% cat.) deoxygenation with sunflower oil and Pd/FAC results, distribution of the light and diesel range hydrocarbons at the best conditions (right) relative percentage of product compounds vs. time (left)	167
Figure 5.8 Test 05 (320 °C, 40 bar H ₂ and 10% cat.) deoxygenation with sunflower oil and Pd/FAC results, distribution of the light and diesel range hydrocarbons at the best conditions (right) relative percentage of product compounds vs. time (left)	168
<i>Figure 5.9 Test 04 and 05 (320 °C, 10 wt% cat.) deoxygenation with sunflower oil and Pd/FAC: percentage results green diesel hydrocarbons, oxygenates, and others. 20 bar H₂ (right) and 40 bar H₂ (left).</i>	<i>169</i>
Figure 5.10 Pd/FAC pre and post-test analysis, SEM image (on top), and relative EDS analysis (on bottom). ...	170
Figure 5.11 Test 06 (320 °C, 40 bar H ₂ and 10 wt% cat.) deoxygenation with sunflower oil and CoMo/FAC results, distribution of the light and diesel range hydrocarbons at the best conditions (right) relative percentage of product compounds vs. time (left)	172
Figure 5.12 Test 06 (320 °C, 40 bar H ₂ and 10 wt% cat.) deoxygenation with sunflower oil and CoMo/FAC results of green diesel hydrocarbons, oxygenates, and others.....	173
Figure 5.13 CoMo/FAC pre and post-test analysis, SEM image (on top), and relative EDS analysis (on bottom).	174
Figure 5.14 Test 07 (320 °C, 40 bar H ₂ and 2.5% cat.) deoxygenation with commercial sunflower oil and NiMo/FAC results, distribution of the light and diesel range hydrocarbons at the best conditions (right) relative percentage of product compounds vs. time (left)	176
Figure 5.15 Test 08 (320 °C, 40 bar H ₂ and 10 wt% cat.) deoxygenation with sunflower oil and NiMo/FAC results, distribution of the light and diesel range hydrocarbons at the best conditions (right) relative percentage of product compounds vs. time (left)	177
Figure 5.16 Test 08 (320 °C, 40 bar H ₂ and 10 wt% cat.) deoxygenation with commercial sunflower oil and NiMo/FAC percentage results of green diesel hydrocarbons, oxygenates, and others.....	178
Figure 5.17 NiMo/FAC pre and post-test analysis, SEM image (on top), and relative EDS analysis (on bottom).	179
Figure 5.18 Test 10 (320 °C, 40 bar H ₂ and 2.5 wt% cat.) deoxygenation with commercial sunflower oil and NiMo/zeolite X results% in green diesel hydrocarbons, oxygenates, and others.	182
Figure 5.19 Test 11 (320 °C, 40 bar H ₂ and 10 wt% cat.) deoxygenation with commercial sunflower oil and NiMo/zeoliteX results, distribution of the light and diesel range hydrocarbons at the best conditions (right) relative percentage of product compounds vs. time (left)	183
Figure 5.20 Test 11 (320 °C, 40 bar H ₂ t, and 10 wt% cat.) deoxygenation with commercial sunflower oil and NiMo/zeolite X: percentage results of green diesel hydrocarbons, oxygenates, and others.....	184
Figure 5.21 NiMo/zeolite X pre and post-test analysis, SEM image (on top), and relative EDS analysis (on bottom).	185
Figure 8.1 Test 01 (60 °C, 4 bar, 4 mg _{catalyst} /mL _{oil}) on the left, Test 02 (60 °C, 4 bar, 4 mg _{catalyst} /mL _{oil}) on the right.	200
Figure 8.2 Test 03 (120 °C, 8 bar, 4 mg _{catalyst} /mL _{oil}).....	200
Figure 8.3 Test 05 (180 °C, 12 bar, 4 mg _{catalyst} /mL _{oil}) (K1=0.0001, K2=0.040211, K3=0.051134).	200
Figure 8.4 Test 06 (180 °C, 4 bar, 1 mg _{catalyst} /mL _{oil}).....	201

Figure 8.5 Test 07 (180 °C, 4 bar, 0.5 mg _{catalyst} /mL _{oil}) (K1=0.0001, K2=0.009097, K3=0.019804).	201
Figure 8.6 Test 22 (120 °C, 4 bar, 1 mg _{catalyst} /mL _{oil}).....	201
Figure 8.7 Test 16 (120 °C, 4 bar, 0.5 mg _{catalyst} /mL _{oil}).....	201
Figure 8.8 Test 22 (180 °C, 4 bar, 2 mg _{catalyst} /mL _{oil}), (K1=0.0009, K2=0.0021).	202
Figure 9.1NH ₃ -TPD acidity analysis NiMo/Zeolite.....	205
Figure 9.2 NH ₃ -TPD acidity analysis NiMoCe/Zeolite	205
Figure 9.3 NH ₃ -TPD acidity analysis NiMoCa/Zeolite	206
Figure 10.1 Graphical abstract of global, conventional water resources, desalinated water production, and brine production [236].	208
Figure 10.2 Classification of the most applied desalination technologies.	210
Figure 10.3 Global desalination by number and capacity (a) of total and operational desalination facilities and (b) of desalination technology.....	212
Figure 10.4 Different Desalination Systems Capabilities Regarding Salinity of Feed and Produced Water measured in ppm.....	214
Figure 10.5 MSF desalination process with some adding [244].....	215
Figure 10.6 Multi-Effect desalination process scheme.....	216
Figure 10.7 Schematic diagram of a single mechanical vapor compression distillation process.....	217
Figure 10.8 Block diagram of reverse osmosis operations.	218
Figure 10.9 Pretreatment processes in the RO desalination technology.....	219
Figure 10.10 Major Types of RO membrane (a)Spiral wound, (b)Hollow fiber [242].	220
Figure 10.11 Reverse Osmosis Desalination process diagram	221
Figure 10.12 Forward osmosis process schematic.....	222
Figure 10.13 The basic design of a solar distillation desalination unit.....	223
Figure 10.14 Membrane Distillation Process	224
Figure 10.15 Schematic of the two-bed adsorption desalination system.....	226
Figure 10.16 Performance ratio of different desalination technologies.....	227
Figure 10.17 Heat and mass transfer in MSF brine circulation plant.	231
Figure 10.18 MSF Industrial plant design.	235
Figure 10.19 Heat and mass transfer in RO plant.....	237
Figure 10.20 RO industrial plant design.....	241

LIST OF TABLES

Table 1.1 Classification of biofuels based on the nature of feedstocks and their generation technologies [34].	28
Table 1.2 List of potential industrial applications of vegetable oils and derivatives[8].	30
Table 1.3 Ranking of the active phases[83].	44
Table 2.1 Lists of studied materials	59
Table 2.2 composition of sunflower and canola oils as-received sample.	78
Table 2.3 Reaction conditions of selective hydrogenation with Lindlar catalyst.	80
Table 2.4 Reaction conditions of selective hydrogenation with Pd-HT catalyst.	80
Table 2.5 Reaction conditions of selective hydrogenation with Pd/FAC catalyst.	81
Table 2.6 composition of sunflower oils as received sample	84
Table 2.7 Reaction conditions of catalytic Deoxygenation tests with Sunflower oil and Stearic acid.	86
Table 3.1 Elementary compositions of Lindlar catalyst.	91
Table 3.2 Metallic Pd surface area, dispersion, and particle size for Lindlar catalyst.	91
Table 3.3 ICP-AES analyses of Pd/HT catalyst	94
Table 3.4 Metallic Pd surface area, dispersion, and particle size for Pd/HT catalyst.	94
Table 3.5 ICP-AES analyses of FAC and Pd/FAC catalyst.	98
Table 3.6 Pd species reduction temperature, metallic active surface area, dispersion, and particle size for Pd/FAC catalyst.	99
Table 3.7 Crystal size of Cenopheres and Pd/FAC (NC, R).	102
Table 3.8 ICP-AES analyses of FAC and CoMo/FAC catalyst.	105
<i>Table 3.9 Co and Mo species reduction temperatures, Co metallic active surface area, dispersion, and particle size for CoMo/FAC catalyst.</i>	<i>106</i>

Table 3.10 Crystal size of CoMo/FAC (NC, R) and FAC.....	110
Table 3.11 ICP-AES analyses of FAC, and NiMo/FAC catalyst.....	113
Table 3.12 Ni and Mo species reduction temperature, metallic Ni surface area, dispersion, and particle size for NiMo/FAC catalyst.....	114
Table 3.13 Crystal size of NiMo/FAC and FAC.....	117
Table 3.14 ICP-AES analyses of the zeolite and NiMo/zeolite X catalyst.....	119
Table 3.15 Ni and Mo species reduction temperatures, metallic Ni surface area, dispersion, and particle size for NiMo/Zeolite X catalyst.....	120
Table 3.16 Crystal size of NiMo/zeolite X and zeolite X support.....	124
Table 4.1 Lindlar catalytic hydrogenation test results, isomer index SII index, and conversions.....	132
Table 4.2 Test results with canola oil and Lindlar catalyst for the cyclic test at 180 °C and 4 bar pressure calculated at 1 h.....	137
Table 4.3 Test results with Pd/HT, SII index, and conversions were calculated when the highest amount of oleic acid was observed.....	142
Table 4.4 Test results with Pd/FAC, SII index, and conversions calculated when the highest amount of oleic acid was observed.....	150
Table 4.5 A comparison of hydrogenation results obtained with various Pd-catalysts.....	154
Table 5.1 GC analysis results on a commercial diesel sample.....	159
Table 5.2 Lindlar catalytic hydrothermal deoxygenation test results with stearic acid and sunflower oil.....	160
Table 5.3 Lindlar catalytic hydrothermal deoxygenation test results, total conversion, Green diesel conversion, and HDO selectivity.....	163
Table 5.4 Pd/FAC catalytic hydrothermal deoxygenation test results with stearic acid and sunflower oil.....	165
Table 5.5 Pd/FAC catalytic hydrothermal deoxygenation test results, total conversion, GD conversion, and HDO selectivity.....	168
Table 5.6 CoMo/FAC catalytic hydrothermal deoxygenation test results with sunflower oil.....	171
Table 5.7 CoMo/FAC catalytic hydrothermal deoxygenation test results, total conversion, Green diesel conversion, and HDO selectivity.....	173
Table 5.8 NiMo/FAC catalytic hydrothermal deoxygenation test results with sunflower oil.....	175
Table 5.9 NiMo/FAC catalytic hydrothermal deoxygenation test results, total conversion, Green diesel conversion, and HDO selectivity.....	177
Table 5.10 NiMo/zeolite X catalytic hydrothermal deoxygenation test results with commercial sunflower oil...	181
Table 5.11 NiMO/zeolite X hydrothermal catalytic deoxygenation test results, total conversion, Green diesel conversion, and HDO selectivity.....	183
Table 5.12 comparison of deoxygenation results obtained with various mono and bimetallic catalysts.....	186
Table 9.1 ICP-AES analysis results.....	203

Table 9.2 Metallic surface area, dispersion, and particle size.....	204
Table 9.3 Metals reduction temperatures.....	204
Table 10.1 Top 10 countries employing desalination technologies	211
Table 10.2 The Energy consumption by different seawater Desalination technologies	228
Table 10.3 Comparison of all salient features of different desalination technologies	229
Table 10.4 Assumed parameters for designing MSF desalination plant.....	232
Table 10.5 Design parameters for MSF desalination plant.....	233
Table 10.6 Costing parameters for MSF plant designing	234
Table 10.7 Design parameters of RO plant	239
Table 10.8 Chemical doses treatment for RO plant desalination design	240
Table 10.9 Final costing and consumption parameters of RO plant designing.....	240

LIST OF ABBREVIATIONS AND NOMENCLATURE

ABBREVIATIONS

GHGs	Greenhouse gases
UN	United nations
COP24	Conference of Paris
UNFCCC	United nations framework convention on climate change
OECD	Organization for economic co-operation and development
VOCs	Volatile organic compounds
FAME	Fatty acids methyl ester
DO	Deoxygenation
DCO _x	Deoxygenation as carbon oxide, x (1,2)
HDO	Hydrodeoxygenation
GM	Genetically modified
GC-FID	Gas chromatography coupled with Flame Ionization Detector
GC-MS	Gas chromatography coupled with Mass spectrometry
LDH	Layered double hydroxides
LDHs	Layered double hydroxides
WI	Wet impregnation

DMF	Dimethylformamide
TGA	Thermo Gravimetric Analysis
ICP	Inductively Coupled Plasma
AES	Atomic Emission Spectroscopy
XRD	X-Ray Diffraction
BET	Brunauer-Emmett-Teller
BJH	Barrett-Joyner-Halenda
TPR	Temperature Programmed Reduction
TPD	Temperature Programmed Desorption
SEM	Scanning Electron Microscopy
EDS	Energy Dispersive X-ray Spectrometry
ICSD	Inorganic crystal structure database
<i>TCD</i>	Thermal Conductivity Detector
ASA	Active surface area
<i>GC</i>	Gas chromatograph
<i>MS</i>	Mass spectrometer
<i>GC-MS</i>	Gas chromatography coupled with mass spectrometry
CD	Ccommercial diesel

NOMENCLATURE

Latin

IV	Iodine value
D	Diene
M	Monoene
S	Saturated fatty acid
MH, DH	Semi hydrogenated intermediates
C15-C18	n-alkanes, diesel range
HT	Hydrotalcite
FAC	Cenosphere
C7-C40	Saturated alkanes standard
C20, C25	Saturated alkanes internal standard
TG	Triglycerides
/	Metallic supported
R	Catalyst reducibility
Dps	Metal particle size
n. c.	Non-acceptable
P	Pressure
T	Temperature
M ^{II}	Bimetallic
M ^{III}	Trimetallic
*	Adsorbed intermediate
C=C	Double bond
N	Stoichiometric rate of the chemisorption reaction
S _{at}	Surface occupied by one atom of metal
V _{ads}	Volume of gas adsorbed
V _m	Molar volume of gas adsorbed

M	Molar weight of metal
S	Surface of metallic particles with a spheric shape
V	Volume of metallic particles
K	Shape constant
B	Full width of half of the maximum (radian) at angle 2θ
L	Crystal size determined from Scherrer equation
d	Distance between rows of atoms in nm,
hkl	Miller indices
n	Integer
P / P_0	Adsorbed volume of nitrogen as a function of the adsorption pressure
v	Volume of gas absorbed
vm	Quantity of gas that constitutes the monolayer
c	BET constant
E_1	Heat adsorption of the monolayer
N	Mole number of gas
N_A	Avogadro number
V_l	Molar volume
r_k	Kelvin radius
$C18:0$	Stearic acid
$C18:1$	Monounsaturated C18 fatty acids
$c-C18:1$	Oleic acid
$t-C18:1$	Elaidic acid
$Iso-C18-2$	Isomers of linoleic acid
$C18:2$	Linoleic acid
$C18:3$	Linolenic acid
P	Pressure
t	Time
IV	Iodine value
$K1$	Kinetic constant for linolenic to linoleic acid
$K2$	Kinetic constant for linoleic to oleic acid

K_3	Kinetic constant for oleic to stearic acid
$XC_{18:3}$	Conversion of linolenic acid
$XC_{18:2}$	Conversion of linoleic acid
S_{Ln}	Selectivity of linolenic acid
S_{Ln}	Selectivity of linoleic acid
SII	Specific isomers index
tri	Retention time
z	Number of linear alkane carbon atoms
Y_{GD}	Green diesel yield
m_n	Mass of the final alkane product at the end of the reaction
m_{TG}	Mass of the initial triglycerides
C_n	Relative percentage of the alkane
m_{rt}	Final recovered mass at the end of the reaction
rt	Recovery time
X_{TG}	Conversion of triglycerides (TG)
X_n	Conversion in hydrocarbons
SI	Selectivity index
L	Crystal size determined from Scherrer equation

Greek

Δ	Heating
θ	Peak position
λ	Wavelength of incident light
σ_m	Molecular cross-sectional area
β	Chemical reaction in which atoms or groups are lost from the β position
γ	Transfer of hydrogen in γ position
Γ	Surface tension

CHAPTER 1

This chapter assembles theoretical and references information about the subject of this doctoral research.

- *Environmental pollution and climate change;*
- *Green chemistry;*
- *Fossil fuel shortage and its alternatives;*
- *Renewable feeding stocks;*
- *Biofuels' generations;*
- *Vegetable oils;*
- *Catalytic hydrothermal reactions mechanisms on vegetable oils;*
- *Hydrothermal catalysis (homogeneous vs. heterogeneous);*

1 LITERATURE REVIEW

1.1 ENVIRONMENTAL POLLUTION AND CLIMATE CHANGE

Earth's climate has changed due to the increasing pollutions from the products obtained by industrial activities, which often remain in the environment, transportation emissions, and agriculture. The air pollutants (including black carbon, nitrogen oxides, sulphur oxides, methane, and ozone) causing an essential impact on health and greenhouse gases (GHGs) [1]. Environmental pollution with climate change was the causing of many problems currently occurring on the Earth-like: global temperature rise which is previewed to increase up to 4.8 °C in 2100 in the worst scenario described by UN at the last COP24 (Conference of the Parties to the United Nations Framework Convention on Climate Change (UNFCCC)) [2]; sea-level rise because of the added water from the melting of ice sheets [3], ocean acidification due to the uptake of carbon dioxide CO₂ emission from the atmosphere, and many animal species may become extinct by 2100 and the spread of infectious diseases.

The problem of the petrochemicals production is not only their by-products air pollution such as CO₂ and N₂O, but their residues at the end of the chemicals life cycle, which may stay in the ecosystems longer than their life use, about 12% of solid wastes are composed by plastics

which are the first contaminants present in the oceans, and 44% of wastes are of organic origins [4].

Today, 183 countries have signed the Paris Climate Agreement, which signed at COP21 in 2015 and specifies that “Parties should when taking action to address climate change, respect, promote and consider their respective obligations on the right to health” and recognizes the central role of “mitigation actions and their co-benefits for adaptation, health and sustainable development” in enhanced action before 2020 [5].

The planet's issues are also strongly influenced by the ever-increasing population, and every action on climate or the environment must last and consider, as well as how this complex system is linked to the vastly growing numbers of people, by 2030 the wastes will arrive at 2.59 billion tones due to the growing population [5].

1.2 GREEN CHEMISTRY

Green chemistry was born to develop more sustainable, non-polluting, and non-dangerous chemical processes. In 1998, the book by P.T Anastas and J.C Werner was published, which is still considered the cornerstone of Green Chemistry, where the concept of Green Chemistry and the "twelve fundamentals of Green Chemistry" is defined [6]. Anastas described green chemistry, which today still refers to; "Green Chemistry based on the use of a set of principles that reduces or eliminates the use or formation of hazardous substances in the design, manufacture, and application of chemical products" [7]. Today, Green Chemistry should not be regarded as a separate branch of chemistry but must be a "philosophy" to be applied to chemistry perfectly integrated into the various branches of existing chemistry. It is hoped that over the years, Green Chemistry will simply be absorbed into every scientific discipline.

The most relevant (for this doctoral research purposes in particular) between twelve principles Green Chemistry are:

1- Waste prevention: of course, it is better to prevent the formation of waste than to treat or dispose of it after it has been formed.

2- Design of healthy chemical compounds: it is crucial that synthesized chemicals selectively express their function without being toxic, or at least not toxic, to humans and the environment.

3- Design for energy efficiency: energy requirements should be minimized whenever possible and reaction conditions lower than in standard processes (low P and low T); when possible, the ideal would be to work at room temperature and atmospheric pressure.

4- Use of renewable feedstocks: the ideal would be to work with substrates from renewable sources because they are always available and not subject to exhaustion. Of course, this is not always possible for practical and economic reasons (which is why we still prefer to use fossil fuels as their extraction and processing are less expensive). Still, the development of technologies innovative companies that would ensure the efficient use of renewable sources can also be cost-effective. A typical renewable source is a biomass that can be divided into lignin biomass, carbohydrate-based biomass, biomass-based on animal oils or fats, and waste biomass. These renewable materials can be used to synthesize many products with high added value; for example, vegetable oils can be used for the production of bio building blocks and biofuels (which is the main topic of this thesis work and which we will see later in detail).

5- Use of catalysts: in the catalytic reactions the catalysis is a very crucial point as they permit the reactions to take place in mild conditions by increasing the reaction rate.

6- Designed for degradation: synthesized products must be non-toxic and selectively carry out their activities, but they must also be designed in such a way that when their life ends, they easily degrade into substances non-toxic.

Using renewable feedstock as biomass to produce energy, bio-petrochemicals, and biomaterials is a key to producing sustainable issues. On the other hand, catalytic processes implemented on biomass feedstocks minimize by-products and achieve the Green Chemistry principles [8].

As mentioned before, since most vegetable oils and animal fats are edible, it brings about a potential food supply and the competition in land use with the bio-products and transportation biofuels for using crops as raw materials. Considering these issues, scientists tend to give preference to waste cooking oil [9][10], algae oils [11][12], agricultural wastes are processed, new crops are grown on marginal land (vegetable oils plants such as sunflower or rapeseed), and fast-growing vegetative biomass (grass, wood, stems, leaves, etc.) consisting of cellulose and lignocellulose (cereals and vegetable oils) [6].

In this doctoral research, catalytic hydrothermal processes on vegetable oils have been tested to evaluate their products representing a sustainable alternative to petrochemicals, such as biofuels and renewable building blocks in industrial applications.

1.3 FOSSIL FUEL SHORTAGE AND ITS ALTERNATIVES

The systematic exploitation of fossil fuels began towards the end of the eighteenth century with the advent of the industrial revolution and the growing need for energy sources. At that time, the primary energy source was derived from coal. It remained the primary energy source until the first half of the XX century when it was replaced by oil because it was considered less polluting and less expensive (in terms of extraction and processing). Fossil fuels are still the world's largest energy source and cover just over 80% of the world's energy needs, of which 34% is covered by oil, 26% by coal, and 22% by natural gas[13][14].

The need to develop alternative fuels such as biofuels from biomass is linked to the many problems that fossil fuels have entailed and still entails. The first problem is the inevitable depletion of fossil fuel reserves as they are not renewable sources. There is a gradual increase in global energy consumption due mainly to non-OECD regions (Organization for Economic Co-operation and Development). Developing countries (e.g., Asian regions) are part. The relentless increase in energy demand necessarily translates into a gradual decrease in fossil fuel

reserves, especially oil. Specifically, it is expected that among the main oil derivatives, diesel will see a significant increase in demand [15]. The second problem associated with fossil fuels is their environmental impact due to emissions generated by their combustion like CO, CO₂, sulphur oxides, nitrogen oxides, and volatile organic compounds (VOCs). The by-products of the petrochemical production industry and their life cycle residues, such as plastics, are considered the first contaminant present in the ocean.

So, it is clear that alternative fuels from renewable sources need to be developed, which must be as few pollutants as possible so that they can be used with the least possible environmental impact.

Currently, the scientific community has been intensely focused on developing alternative biofuels and bio-petrochemicals from biomass. Whereas all bio-products are considered environmentally friendly, biodegradable, non-toxic, and can be a sustainable alternative to conventional fossil fuels [16]. One of the main advantages of biofuels development is the dramatic decline in greenhouse gas emissions as a result of their combustion; the CO₂ emitted is part of a CO₂ cycle in which the CO₂ emitted is the same one that is used by plants during their life cycle to carry out photosynthesis [17]. Besides, especially in the case of biofuels from vegetable oils, there is a significant decrease in the emission of sulphur oxides as plants are very low in sulphur [18]. Biofuels can be produced biochemically (alcoholic fermentation of sugars or anaerobic digestion of biomass) or by thermo-chemical (catalytic deoxygenation, pyrolysis/gasification, thermal, and/or biomass catalytic cracking) [19].

1.4 RENEWABLE FEEDING STOCKS

Today, biomass and biogenetic residues are one of the cheapest, most sustainable renewable energy sources, alternative petrochemicals, and renewable building blocks in industrial applications. It is also readily available in large quantities [20]. By biomass, we mean any

material of biological origin derived, Figure 1.1, from woody materials, agricultural crops, animal husbandry, and marine waste, as well as human-made waste [21].

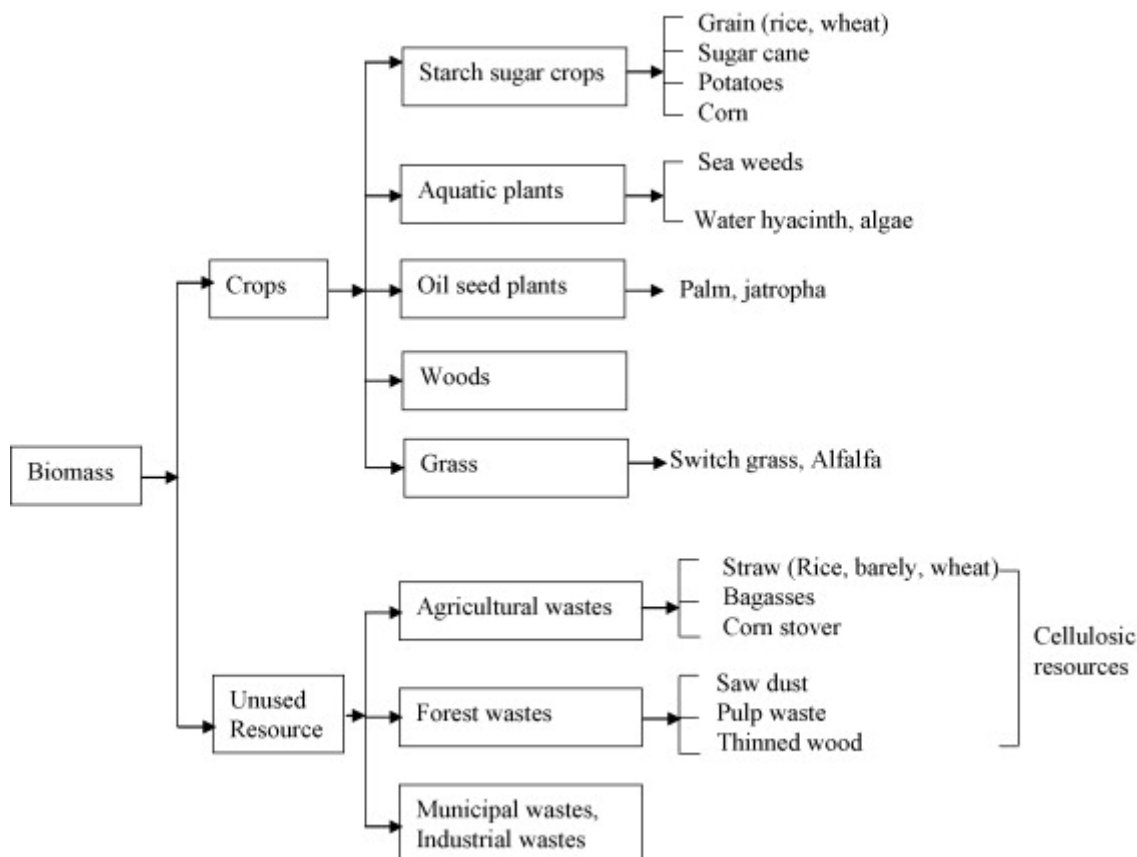


Figure 1.1 Biomass as a renewable feedstock. [21].

Vegetable oils and animal fats biomass consists mainly of triglycerides of fatty acids are made up have particularly long alkylic chains and are therefore rich in carbon content, making them suitable as a starting material for the production of hydrocarbon biofuels. One disadvantage in the use of vegetable oils is edible oils that would lead to competition between the food and fuel industries. As a result, it would be ideal to use non-edible vegetable oils and waste biomass as a waste of human, animal origin, and waste cooking oil, which would be not only ideal as it would not hinder the food industry but above all, it would allow added value to waste materials that would otherwise require disposal processes.

1.5 BIOFUELS' GENERATIONS

Biofuels can be divided into first, second, third, and fourth-generation according to the nature of the feedstock and corresponding production technology Table 1.1, the first-generation biofuel represented by fatty acid methyl esters (FAME) is developed via transesterification of triglycerides (vegetable oils and animal fats) over homogeneous basic catalysts under the optimal process conditions [22]. Despite the widespread commercial application of this kind of bio-diesel, it is contained a high content of oxygenated compounds, suffering from serious drawbacks such as low heating value, high viscosity, poor cold flow properties, low oxidation stability, and incompatibility with fossil fuel cause its high oxygen content and acidity [23]. They may also not be sustainable as their production involves the use of edible material (edible vegetable oils), and this results in competition between the food and biofuels industry that can lead to an increased basic cost of foodstuffs [24], therefore, more researches have been focused on the development of more stable and higher quality biofuel, second-generation hydrocarbon-based biodiesel via hydrodeoxygenation (HDO), decarboxylation (DCO₂), or decarbonylation (DCO) over specific heterogeneous catalysts [25][26]. The biodiesel derived from deoxygenation hydro processes contain high hydrocarbon content and low oxygen, sulphur, and nitrogen. It also has excellent physical and chemical properties with high cetane number, great cold flow, high heating value, and supper storage stability, making it fully compatible with fossil fuels [27].

The classification of second-generation fuels is unclear, depending on the type of treatment from biomass and the source material [28]; consequently, second-generation biofuels: all fuels that are technologically superior, sustainable, and with zero environmental impact are defined as second-generation biofuels. A primary goal in the development of second-generation biofuels is the use of lignocellulosic matrix, biomass from food waste, non-food waste to

increase their sustainability and, at the same time, avoid the production of unwanted products [29]. The second-generation biofuel production processes are the catalytic deoxygenation of vegetable oils and the process of training hydrocarbon biofuels via pyrolysis and/or biomass gasification to produce syngas (CO-H₂), which is then used in the Fisher-Tropsch process for the formation of hydrocarbon biofuels [30]. On the other hand, the most accepted definition for third-generation biofuels that would be produced from algal biomass, which has a very distinctive growth yield as compared with classical lignocellulosic biomass, where the production of biofuels from algae usually relies on the lipid content of the microorganisms. Lipids obtained from algae can be processed via transesterification by the previously described biodiesel process [31][32]. Regarding the fourth Generation Biofuels, they aim at not only producing sustainable energy but also a way of capturing and storing CO₂, whereas the genetically modified algae and biomass materials absorb CO₂ while growing and convert it into fuel using the same processes as second-generation biofuels, this carbon capture makes fourth generation biofuel production carbon-negative rather than simply carbon neutral, as it is 'locks' away more carbon than it produces. This system not only captures and stores carbon dioxide from the atmosphere but also reduces CO₂ emissions by replacing fossil fuels[33].

Table 1.1 Classification of biofuels based on the nature of feedstocks and their generation technologies [34].

Generation	Feedstocks	Examples
First-generation	Sugar, starch, vegetable oils, animal fats and, seeds for oil	ethanol, biodiesel, bio syngas, biogas.
Second generation	Non-food crops, wheat straw, corn, wood, solid waste, energy crop, lignocellulosic biomass	bio alcohols, bio-oil, biohydrogen, biodiesel.
Third generation	Algae	vegetable oil, biodiesel.
Fourth generation	genetically modified (GM) algae	bio gasoline.

1.6 VEGETABLE OILS

Vegetable oils consist of a mixture of triglycerides, which are composed of a glycerol backbone and three fatty acid chains, mostly unsaturated, with alkyl chains in the C_{12} - C_{20} range, and in smaller quantities also longer alkylic chain fatty acids up to 22 carbon atoms. Depending on the number of double bonds present in the chain, fatty acids will be classified into three groups: Saturated, monounsaturated, and polyunsaturated fatty acids [35]. The distribution of the type of fatty acids presents obviously depends on the kind of vegetable oil Figure 1.2. Furthermore, the chain length, configuration, and position of double bonds and their connectivity on glycerol backbone play significant roles in the chemical and physical properties of vegetable oils, consequently determining their applications [35].

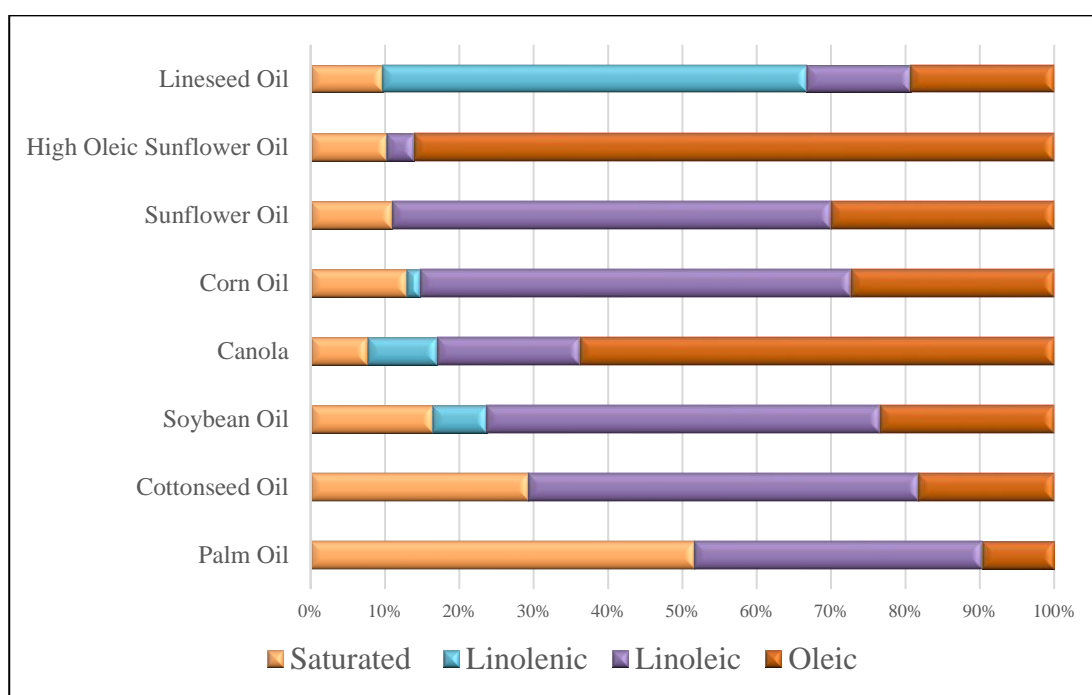


Figure 1.2 Percentage composition of various vegetable oils in terms of saturated and unsaturated fatty acids[36].

The major use of vegetable oils is food applications, although an important proportion is used for industrial applications (lubricants, plasticizers, coating, paints, cosmetics, pharmaceuticals, bioplastics, and biodiesel) Table 1.2 [8].

Table 1.2 List of potential industrial applications of vegetable oils and derivatives[8].

Food Application	Oleo-chemicals	Energy, Biomass & Others
Cooking oil	Surfactants	Biodiesel
Industrial frying fats	Personal care	Charcoal
Margarine	Cosmetics	Pulp and paper
Vegetable Ghee	Agrochemical	Animal feeds
Confectionary fats	Lubricant/grease	Bio-composite
Ice cream	Soap	Fertilizer
Non-dairy cream	Industrial cleaning	
Salad dressing	Printing ink	
Cheese analogues	Polyols	
Supplements/vitamins	Polyurethanes	
	Polyesters	
	Polyacids	

Since XIX century, vegetable oils found widespread application in industry and transports, but since the increase of oil drilling, their use decrease and only at the end of XX century, because of global crisis oil price and oil shortening due to political instability and consumption of reserves, a renewed interest in vegetable oils in diesel transport and as sustainable alternative petrochemicals and a renewable building blocks in industrial applications [37].

For industrial applications, in particular, for vegetable oils hydrogenation, there is a special interest for oleic acid due to its stability in the presence of oxygen and its lower melting point comparing with saturated fatty acids. Because of that, as starting materials, mixtures derived from natural vegetable oil which contains at least 72% by weight of oleic acid are found to be perfect for the synthesis of polyol esters which use in lubricating oils composition, besides for the casting and coating, it is better with high oleic and low stearic acids. However, the preferred vegetable oil range composition that guarantees low viscosity and high thermal instability for bio-lubricants and biofuels is 85–95% oleic acid, 2–8% linoleic, 0.5–2.5 stearic, and 2–5% palmitic [38].

Hydrogenation is the most important catalytic process performed on vegetable oils to reduce the poly-unsaturated fatty acids towards the monoene's production (partially hydrogenated fatty acids). The total number of double bonds in the oil is defined by the iodine value IV, which corresponds to the iodine weight (in grams) consumed by 100 g of oil or fat through the addition of I_2 to the carbon double bonds in the fatty acids of the oil. In turn, vegetable oils are partially and selectively hydrogenated for increasing the stability of the oil by selective partial hydrogenation of polyunsaturated fatty acids, which are highly prone to autooxidation, minimizing the full hydrogenation towards the saturation fatty acid and decreasing the isomerization across trans fatty acids as trans isomers have high melting points which may limit their applications in food or chemical industry [35].

Nowadays, the oleochemical industry is a significant producer of bio-based products, such as bio-lubricants, which low viscosity combined with high oxidative and thermal stability. As the developed countries (North America and Europe) governments' regulations promote bio-based compounds during manufacturing, the oleic acid market availability is not sufficient for all potential applications. Commercialized bifunctional building blocks for bio-based plastics include sebacic acid and 11-aminoundecanoic acid, both from castor oil, and azelaic and pelargonic acids derived from oleic acid [8].

Regarding the vegetable oils' properties like high energy, density, and chemical composition similar to that of oil derivatives, they were used as a substrate for biofuel production [39]. Currently, 95 % of biodiesel is produced from edible oils via transesterification on different homogeneous and heterogeneous catalysts [40], although the scientific researches intense towards non-edible oils [41] or other kinds of biofuels processes, such as deoxygenation process (hydrodeoxygenation, decarbonylation, and decarboxylation) of vegetable oils in order to produce biofuel with more oxidation stability and fewer air emissions pollution.

Rudolf Diesel used peanut oil directly to run his engine only, causing severe engine mechanics problems [42]. In May 2003, the European Union approved the 2003/30/EC Directive to promote the use of biofuels and other renewable fuels in the transport sector; in particular, the directive states that member countries in the European community must replace 5.75% of petroleum-derived fuels with biofuels by the end of 2010. In January 2007, the target for reducing fossil fuels increased to 10% by 2020 [43][44]. However, the hydro-processing treatment of triglycerides (vegetable oils) into hydrocarbons is a promising alternative technology to produce renewable diesel with high energy density, low nitrogen oxide emissions, good oxidation stability completely compatible with fossil fuels [45].

The choice of the type of vegetable oil used for the process depends on several factors, first of all, commercial availability; for example, in America, soybeans and peanut oil are particularly used as they are produced in large quantities while in Europe make great use of sunflower oil [46]. However, if possible, the use of as saturated vegetable oils as possible is preferred as they allow a significant reduction in hydrogen consumption and allow the reaction to less drastic conditions to take place. Also, IV is an important factor, recommended to be less than or equal to 130 [47].

So, the selective heterogeneous catalytic hydrothermal treatment of highly unsaturated oils is a key process addressed to a wide range of biocompatible products (green chemicals, bio-lubricants, poly-oils, biofuels, etc.) [48].

1.7 CATALYTIC HYDROTREATING REACTIONS

MECHANISMS ON VEGETABLE OILS

1.7.1 VEGETABLE OILS HYDROGENATION

The hydrogenation process was found by two French chemists, Sabatier and Senderens. The main focus of Sabatier was arriving at a new way to harden liquid oils for use in soaps and received the Nobel Prize for his work on catalysis in 1912 [49]. However, the first time the process was commercialized was in England and then in America by Procter & Gamble for the food industry. It radically changed the eating habits of at least three human generations [8].

Bio-based products (polymers, soaps, lubricants, polyalcohols, etc.) produced by oleochemical processes via partial catalytic hydrogenation of vegetable oils may be high potential development in many industrial fields.

Horiuti-Polanyi scheme based on nickel-catalyzed was adopted to understand the catalytic hydrogenation reaction's mechanism of vegetable oils and the addition of hydrogen [50][51],

As seen in Figure 1.3 where D = diene, M = monoene, S =saturate fatty acid, DH, MH = semi-hydrogenated intermediate, c = cis, t = trans, * = adsorbed intermediates, Molecular hydrogen is first absorbed on the catalytic surface and quickly separates in two hydrogen atoms, then and at the same time, fatty acids are adsorbed on the catalytic surface through their double bonds, one atom of hydrogen is added to the adsorbed C=C and form a semi-hydrogenated compound. Suppose the second atom of hydrogen is also attached to the double bond. In that case, the half-hydrogenated becomes saturated, and by releasing the reaction heat (105 kJ/mol), it is moved away from the active position. Even the half-hydrogenated intermediate can also dissociate from the active sites because the addition of the first hydrogen is a reversible step [49].

The concentration of the adsorbed hydrogen atoms on the catalyst surface depends on four factors:

- Hydrogen concentration: its increasing affect the 1 and 2 reaction balance towards H^* .
- Temperature: the constants' reaction balance of 1 and 2 dependent on temperature, increasing the hydrogenation temperature, the solubility of the hydrogen dissolved in the oil increases so its concentration on the catalyst will increase, also the activity of the catalyst will increase with the temperature then the reaction velocity will increase [52].
- Catalyst: An active catalyst (with high active sites) will have a relatively high H^* .
- Agitation rate: the importance of agitation rate is anticipated due to the fact that the main function of this parameter is to supply dissolved hydrogen to the catalyst surface. This reflects a considerable interdependence between the response variable and the mass transference phenomena of the gas and liquid to and from the solid catalyst surface [53]. The mixing can also affect the product distribution significantly and the trans isomers formation, which lessens with the agitation decreasing [54].

So, this mechanism can also explain how the reaction parameters affect the hydrogen concentration and then the isomerization index or trans selectivity as temperature, pressure, rate of agitation, the concentration of catalyst, and catalyst activity. It is worth noting that the proposed scheme does not consider the triglycerides, but the single-chain; for the raw oil, it was observed that unsaturated fatty acids attached to the same triglyceride affect each other's reactivity, so the reaction rate does not follow the exact same kinetics of single fatty acid chain.

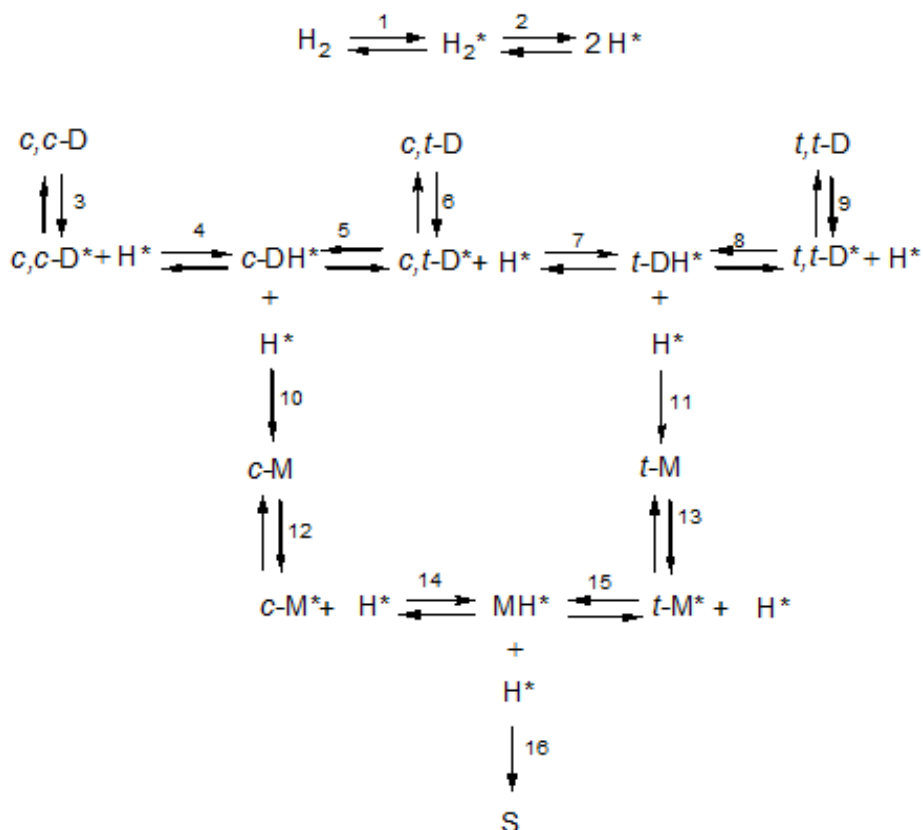


Figure 1.3 Hydrogenation reaction mechanism as described by Dijkstra, where * = adsorbed intermediates, c = cis isomers, t = trans isomers, M = monoene, and D = diene, respectively.

Activity and trans-selectivity were studied widely by scientists as Dijkstra, who has explained why cis-isomer moles are less than trans-isomers in equilibrium conditions (1 mole of cis-isomer for every 3 moles of trans-isomer): the activation energy of step 4 (hydrogen addition to c,c-diene) is lower than the activation energy of step 5 (hydrogen addition to c,t-diene), this would cause the cis-isomer to react about three times faster than the trans-isomer, arriving at the cis, trans-equilibrium. Dijkstra has also studied the activity and the formation of the saturated fatty acid S (step 16) and supposed that the extent of this reaction depends on the concentration of atomic hydrogen on the catalyst surface: when it is low, the isomerization prevails, and when it is high the saturation reaction prevails [55].

The major part of authors agrees with Horiuti-Polanyi scheme [56] and Dijkstra's mechanism proposed for Ni [57], accepting them also for Pd and other noble metals with additional integrations, because this mechanism does not consider the double bond migration reaction and

not all the catalysts follow exactly this mechanism. Regarding that, the double bond positions cannot be evaluated from the catalyst behavior; the composition of positional isomers may be estimated by GC-FID or GC-MS.

In industrial practice, the hydrogenation process is typically carried out using nickel-based catalysts, either in the form of nickels Raney, or supported on different materials [58]. Economical price, high activity, and easy availability of nickel make it superior over the other metals. This work aims to maximize the amount of oleic acid C18:1 in the final product, as well as to eliminate linolenic acid C18:3 and to reduce the content of linoleic acid C18:2 to a substantial extent, without going too far towards producing the fully saturated stearic acid (C18:0 - not easily digested as foodstuffs), therefore the nickel doesn't exhibit an adequate selectivity [59].

In the last two decades, there has been a growing interest in nanosized structures in the range of 1–20 nm in different research fields [60]. This is also the metal particles' size in the supported metal catalyst of the new generation of nickel and precious metal hydrogenation catalysts. In general, such nanoparticles of metals such as nickel, palladium, ruthenium, or platinum are used for hydrogenation, since the dissociative adsorbed hydrogen is easily accessible on these group VIII metals [61].

Many studies have considered the benefits of Pd catalysts for edible oil hydrogenation, especially for high conversion and moderate trans-fatty acids production. Modified Pd can achieve a compromise between the catalyst activity and trans-isomerization selectivity [62]. In this research, we have insisted on the use of supported palladium catalysts for the selective catalytic hydrogenation processes on the vegetable oils.

1.7.2 VEGETABLE OILS DEOXYGENATION

Deoxygenation of triglycerides and related feedstocks is one of the key processes to produce high-quality automotive fuels free of (sulphur, oxygen, nitrogen, and aromatics) [63]. Various routes for deoxygenation processes depending on the reaction conditions and type of used catalyst have been reported in the literature [64][65][66]. As suggested by Veriansyah [67] Figure 1.4 triglyceride conversions over hydro-treating catalysts in the presence of hydrogen have complex reaction pathways and consist of parallel and/or consecutive reaction steps, including fatty acids double bonds saturation, cracking to obtain free fatty acids, and finally, conversion of free fatty acids into hydrocarbons via three different reaction pathways;

- *Hydrodeoxygenation (HDO)* leads to the formation of an alkane with the same number of carbon atoms as the starting fatty acid and water,
- *Decarbonylation (DCO)* in which an alkane is formed with one less atom of carbon, CO and H₂O, and

Decarboxylation (DCO₂) converts fatty acid into the same alkane which is obtained from the DCO, but in this case, the oxygen is eliminated in the form of CO₂.

The liquid product generally contains straight chain n-alkanes with C₁₅-C₁₈ as major compounds. The content of iso-alkanes, cyclo-alkanes, and aromatics is usually not significant at a mild synthetic condition (200 °C, 20 bar of H₂, and 8 hours of the reaction time)[68]. This complex, known as **green diesel**, has better fuel properties than FAMEs produced via transesterification; furthermore, it is better than petroleum diesel fuel due to its higher cetane number (> 70), its boiling point range is comparable to typical petroleum, and it can be employed in the existing infrastructure of petroleum refineries [69][70][71].

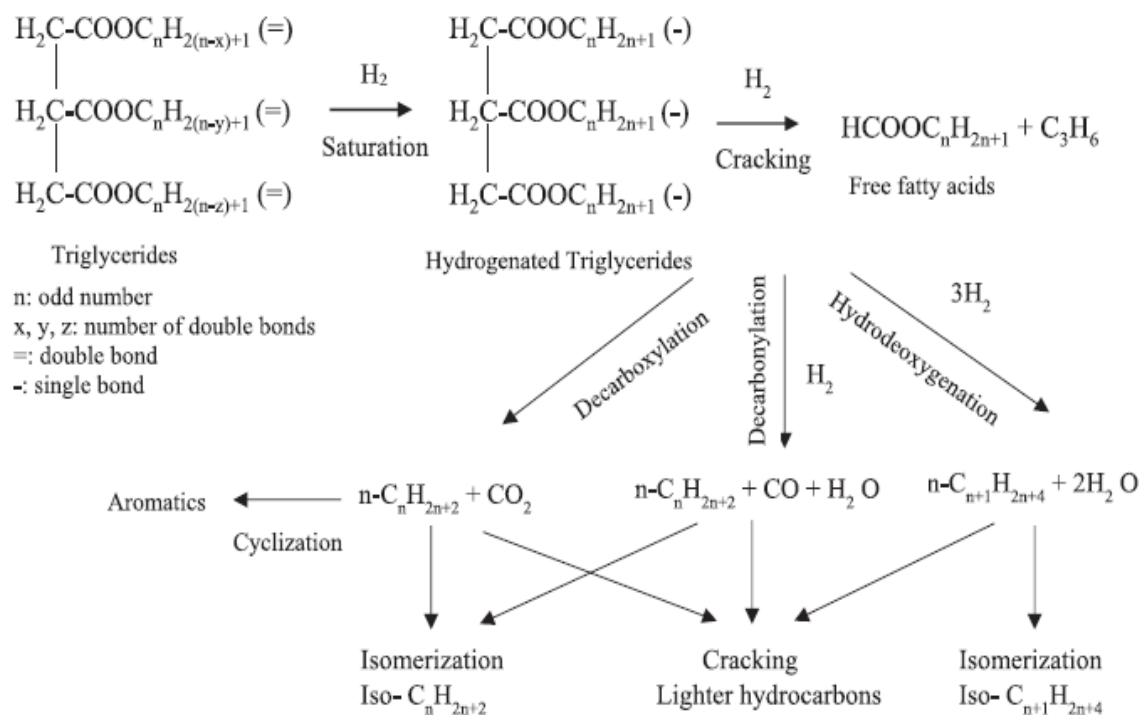


Figure 1.4 Possible reaction pathways of triglycerides over a hydro-treating catalyst [64].

In fact, the cracking step after the completed hydrogenation of triglycerides can take place through four different reaction mechanisms, β -elimination, hydrolysis, the transformation of hydrogen, and direct deoxygenation, as could be explained in Figure 1.5.

1. β -elimination: Triglyceride eliminates a fatty acid by converting into an unsaturated diglyceride, which must necessarily be hydrogenated to eliminate the second fatty acid. At the end of three elimination and hydrogenation cycles, three free fatty acids and a molecule of propane are obtained. Cleavage of triglyceride via β -elimination appears to be the main reaction mechanism for the formation of free fatty acids; therefore, the free fatty acid can follow the various reaction routes to transform into hydrocarbon [69].

2. Transfer of hydrogen in γ : In this case, the triglyceride is split in such a way as to directly form an alkane having two carbon atoms less than the starting fatty acid. This reaction does not involve the use of hydrogen, which represents an economic advantage, but, on the other hand, it seems to occur only through thermal decomposition at temperatures of at least 450 °C, in contrast with the typical temperatures in which catalytic deoxygenation is conducted [69].

3. Hydrolysis: triglyceride is hydrolyzed, leading to the formation of free fatty acids and glycerol. However, this reaction mechanism seems to occur only with the use of esters as model compounds. In contrast, it does not seem to occur at all in substrates such as triglycerides because it necessarily requires the presence of H₂O, and in a case like vegetable oil, the presence of water content is very low [66].

4. Direct deoxygenation: with direct deoxygenation, we mean the reaction that starts directly from the triglycerides, leads to the formation of hydrocarbons and glycerol without observing the presence of fatty acids as intermediates in the mixture. The direct deoxygenation has three pathways reaction, direct HDO, direct DCO₂, and direct DCO. The exact reaction mechanism of direct deoxygenation is not common, but Kubicka et al [72] has explained that the fact of not having the formation of acid intermediates is due to the high activity of the catalyst, where, as soon as the formation of the fatty acids takes place, these are still adsorbed on the catalyst surface and then rapidly converted before they could be desorbed.

The most favored reaction pathway is β -elimination as an indirect mechanism of the deoxygenation processes, and this is confirmed by the fact that in a lot of the literature where the propane and fatty acids are observed as intermediates [66].

As previously anticipated, once the fatty acids are formed, they can undergo three different reaction mechanisms to lead to the formation of hydrocarbons. So, HDO, DCO, DCO₂ are indirect competitive reactions, so they occur at the same time, and the selectivity towards one or the other reaction is governed by various parameters such as temperature, pressure, type of catalyst but also the type of support used for the catalyst synthesis [71].

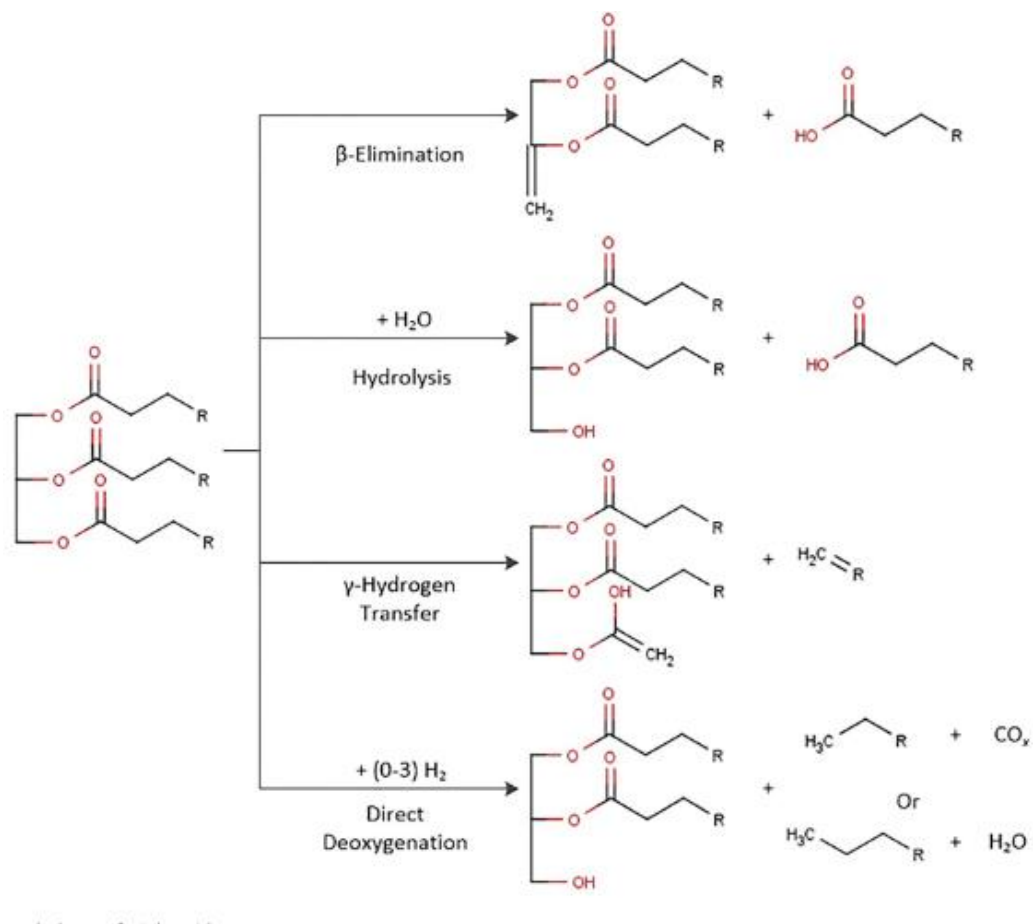


Figure 1.5 Initial breakdown of triglycerides [73]

- Indirect hydrodeoxygenation HDO pathway:

Once free fatty acids are formed, one of the possible mechanisms for the formation of alkanes is the HDO reaction pathway Figure 1.6.

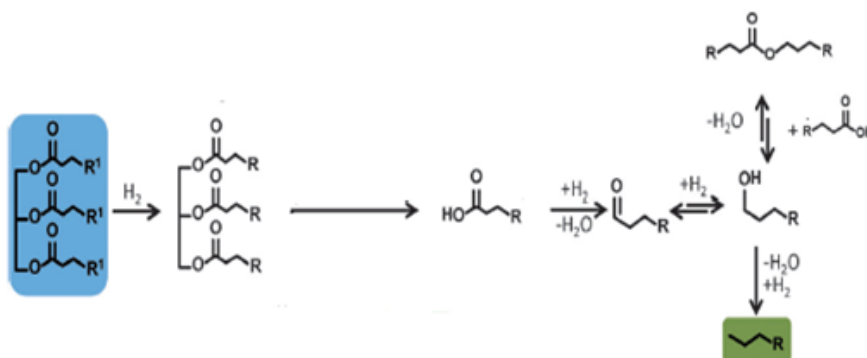


Figure 1.6 Hydrodeoxygenation HDO pathway[74]

The first step of the HDO involves a dehydration reaction followed by hydrogenation to form an aldehyde intermediate that is immediately reduced by the hydrogen which is already present to obtain alcohol, and this alcohol can then undergo another step of dehydration and hydrogenation, arriving at an alkane with the same number of carbon atoms as the starting fatty acid (C_n), it can also react with fatty acids and form an ester. This is a reversible reaction so, the consumption of alcohol to form an alkane may shift the esterification reaction equilibrium towards free alcohol, thus allowing a continuous consumption to form hydrocarbons [69][73].

- Indirect decarboxylation DCO_2 /decarbonylation DCO pathway:

After the first step, which involves triglycerides cleavage, Figure 1.7 the fatty acids can undergo the decarboxylation by eliminating oxygen such as carbon dioxide and forming an alkane with one less carbon atom than the starting fatty acid (C_{n-1}), or fatty acid can undergo the first step of dehydration and hydrogenation that leads to form an aldehyde which decomposes by leaving carbon monoxide and alkene that may give by hydrogenation reaction alkane (C_{n-1}), otherwise, it remains as alkene [69][73].

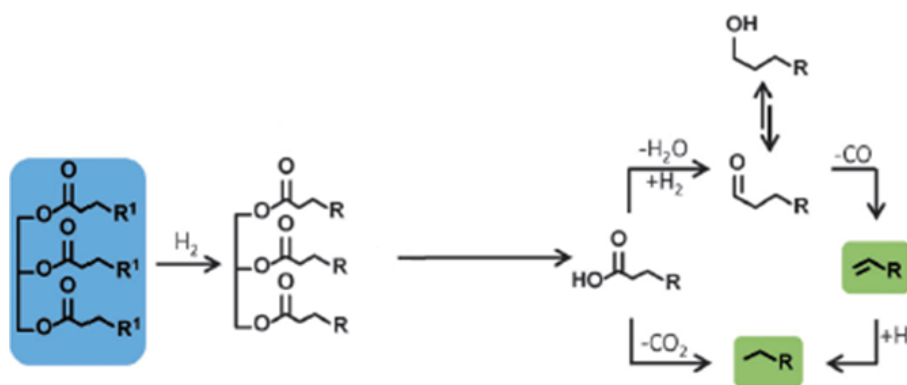


Figure 1.7 Decarboxylation DCO_2 /Decarbonylation DCO pathway[74]

So, hydrogen consumption decreases in the order:

Hydrodeoxygenation > Decarbonylation > Decarboxylation.

It seems that more economical decarboxylation (or decarbonylation) with relatively low reaction temperature would generate pollutants but shows lower hydrogen consumption [75],

while hydrodeoxygenation is environmentally friendly but consumes more hydrogen. However, it is interesting that CO_2/CO can be hydrogenated to produce methane over the hydrotreating catalysts, leading to even higher consumption of hydrogen than the case of hydrodeoxygenation [76][72][16]. So, it is true that hydrogen consumption is lower for DCO and DCO_2 than HDO, but the decarbonylation and decarboxylation routes seem to be more cost-and energy-efficient than the hydrodeoxygenation one [77].

The selectivity towards one of the deoxygenation reaction pathways can be observed comparing the alkanes concentration present in the liquid product; for example, if we observe the presence of C_{n-1} alkanes we can say that the reaction that has occurred is DCO/ DCO_2 but by this hypotheses, it is not possible to define which of the two reactions took place; this may be more accurate by the analysis of the gas phase but, even in this case, we cannot have absolute certainty due to the possibility to occur other reactions as water gas shift (WGS) and methanation in the gas phase of Figure 1.8 [78][16].

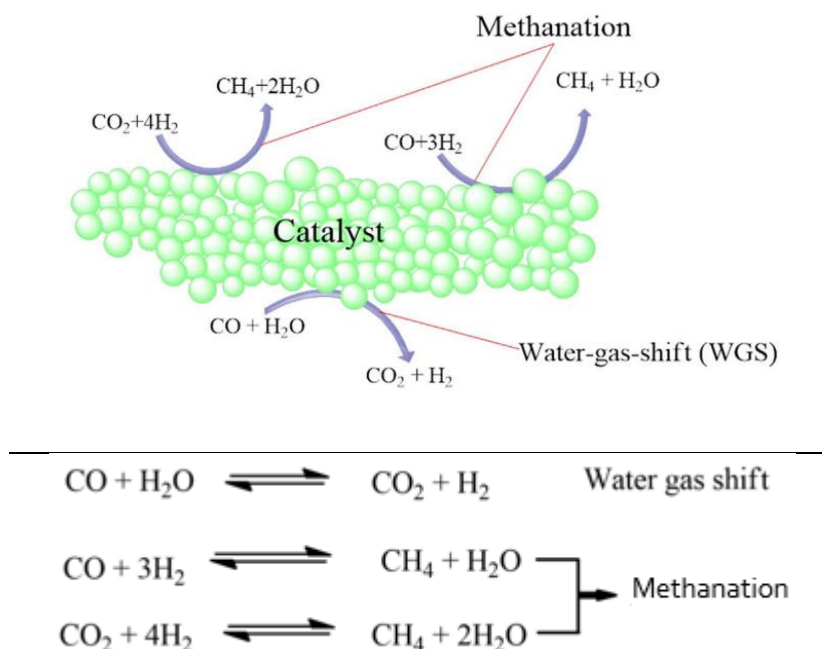


Figure 1.8 Possible gas-phase reactions[16]

1.8 HYDROTREATING CATALYSIS (HOMOGENEOUS VS. HETEROGENEOUS)

“Catalyst” is a chemical species that can increase the rate of the reaction without making any effect on the standard Gibbs free energy; in other words, it modifies the kinetics of a reaction without changing its thermodynamics, as shown in Figure 1.9. Nowadays, catalysis plays a very important role in most of the chemical industries, and it is present in the production of 90% of chemical-based products, including liquid fuels [79][80].

The transition metal catalysis is considered very important since, under this catalysis line, there are many interesting properties, i.e. selectivity, efficiency, and ability to be in a wide range of oxidation states, which give it the applicability of these elements in different reaction pathways, such as in the cases of our interest: catalytic hydrogenation of vegetable oils, catalytic deoxygenation, isomerization, oxidation, reduction, and C-H activation [81][82].

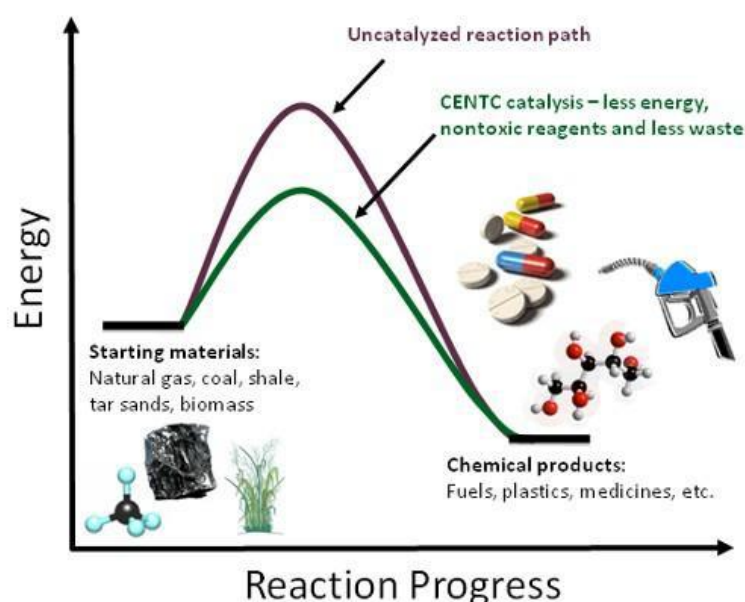


Figure 1.9 Energy diagram that can show the difference between catalyzed and uncatalyzed reaction, in terms of activation energy and reaction pathway[82].

It is worth mentioning that an absolute agreement was not achieved in the classification of the most active or selective transition metal active phase; Veldinsk et al. [83] proposed an attempt of classification of the principal catalytic active phase, reported in Table 1.3.

Table 1.3 Ranking of the active phases[83].

Characteristic	
Activity	Pd>Rh>Pt>>Ir>Ru=Ni>>Cu
Selectivity	Cu>Pd>Rh>Pt>>Ir>Ru=Ni

1.8.1 HOMOGENEOUS CATALYSIS

In this catalysis pathway, we have a homogeneous solution in which the catalyst and other reactants are in the same phase [84]. It is worth mentioning that the homogeneous catalysis pathways were studied overtime for the selective catalytic hydrogenation of vegetable oils like metal carbonyls, metal phosphine, and platinum-tin systems of Ziegler-type [85], and for the catalytic hydrothermal processes on vegetable oils using sodium hydroxide as a catalyst to produce Biodiesel, Figure 1.10[86].

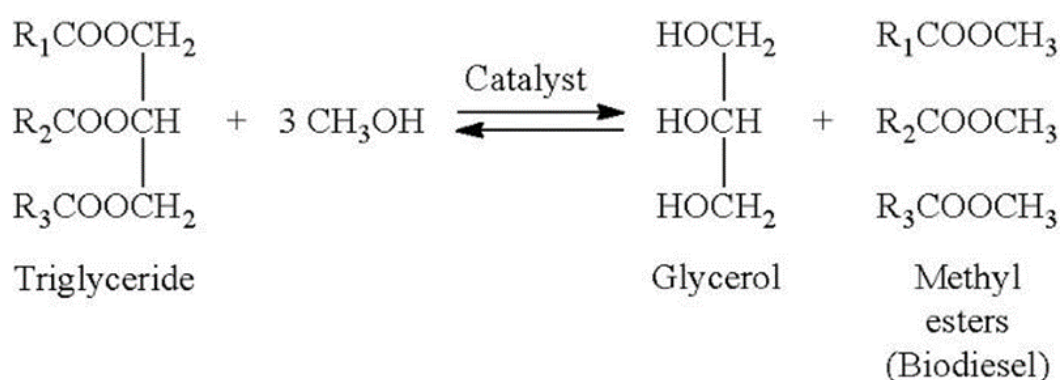


Figure 1.10 trans-esterification of vegetable oil to produce Biodiesel

These studies on homogeneous catalysis, although interesting from the research point of view, but have a significant disadvantage like the cost of the homogenous catalysts used and the inherent difficulty in the separation of the catalysts and the products.

1.8.2 HETEROGENEOUS CATALYSIS

Herein, the catalyst and the components of the reaction are present in separated phases, and in most cases, the actual reactivity occurs at the interface between two phases.

Nowadays, heterogeneous catalysis is widely more used than homogeneous one, and it is involved in 90% of the industrial processes [81][84] and there are several industrial catalyzed reactions based on heterogeneous catalysts use transition metals as supported active phase such as, the hydrogenation of vegetable oils with nickel on alumina [87], magnetite (Fe) catalyst in Haber-Bosch for the synthesis of ammonia (NH_3) [88], the conversion of coal to syngas and hydrocarbons in Fischer-Tropsch process which catalyzed by Co/Fe heterogeneous catalysts [89], and deoxygenation of triglycerides with cobalt-molybdenum on zeolite and carbide [%].

The ability to use heterogeneous catalysts more than homogeneous catalysts comes from the fact that these catalysts can be simply separated after their employment in a process, also they are stable, they can be recycled several times without loss of activity; all these properties make them more interesting for industrial applications from the economic and environmental point of view [84].

1.8.2.1 HETEROGENEOUS CATALYSIS IN HYDROGENATION PROCESSES

Several transition metals supported on silica, silicate, alumina, hydrotalcite, and zirconia were studied and used with vegetable oils' hydrogenation. Nickel catalysts, well known from the reactivity point of view, are used in many cases in the modeling of the process as standard template [57][90][91], its operating range conditions at 160–230 °C and 2– 5 bar H_2 [92]. By

the time and in order to reduce the by-products such as trans-isomers and stearic acid, researches on noble metal catalysts were carried out: platinum showed good activity and low formation of trans-isomers (selectivity) [93], palladium-based catalysts have often been proposed because of its activity at low temperature (120–140 °C), selectivity, recyclability, and stability [94]. Noble metals were also studied as bimetallic catalysts combined with nickel, and this innovative synthesis resulted in excellent activity and selectivity, such as Pt-Ni supported on mesoporous silica [95] and Pd-Ni [96][97].

The studies about hydrogenation reaction have shown that this process is also affected by the properties of the catalyst's support, porosity, pore diameter, and surface area. Numwong et al. [98], where they have studied the Effect of SiO₂ pore size diameter 3, 5, 30, and 50 nm, respectively, as a support of the palladium catalysts on partial hydrogenation of rapeseed oil-derived fatty acid methyl esters FAMEs and found that the pore size of SiO₂ support had a significant effect on the catalyst activity and selectivity toward trans-monounsaturated FAME. Whereas the smallest pore size (3 nm) and acidic catalyst properties presented the lowest trans-monounsaturated FAME selectivity.

1.8.2.2 HETEROGENEOUS CATALYSIS IN DEOXYGENATION PROCESSES

Sulphur catalysts were the first used in the catalytic deoxygenation reaction, containing mainly Mo and W sulphides with promoters such as Ni and Co supported on alumina, silica, and zirconia; this process is a thermal treatment of the catalyst in the presence of H₂S or CS₂ ensuring the formation of active sites on the surface of the catalyst [99][100][101]. These catalysts are very active with high selectivity towards HDO [86], but they suffer from rapid deactivation due to the low sulphur content in vegetable oils, leading sulphur to separate from the catalyst, thus causing an inevitable deactivation and contaminating hydrocarbon products that need sulphur removal treatments that result in higher costs and waste. This feature has

limited using sulphur catalysts and encourages researchers to develop non-sulphur catalysts, such as transition metal-based catalysts, as reported in Figure 1.11.

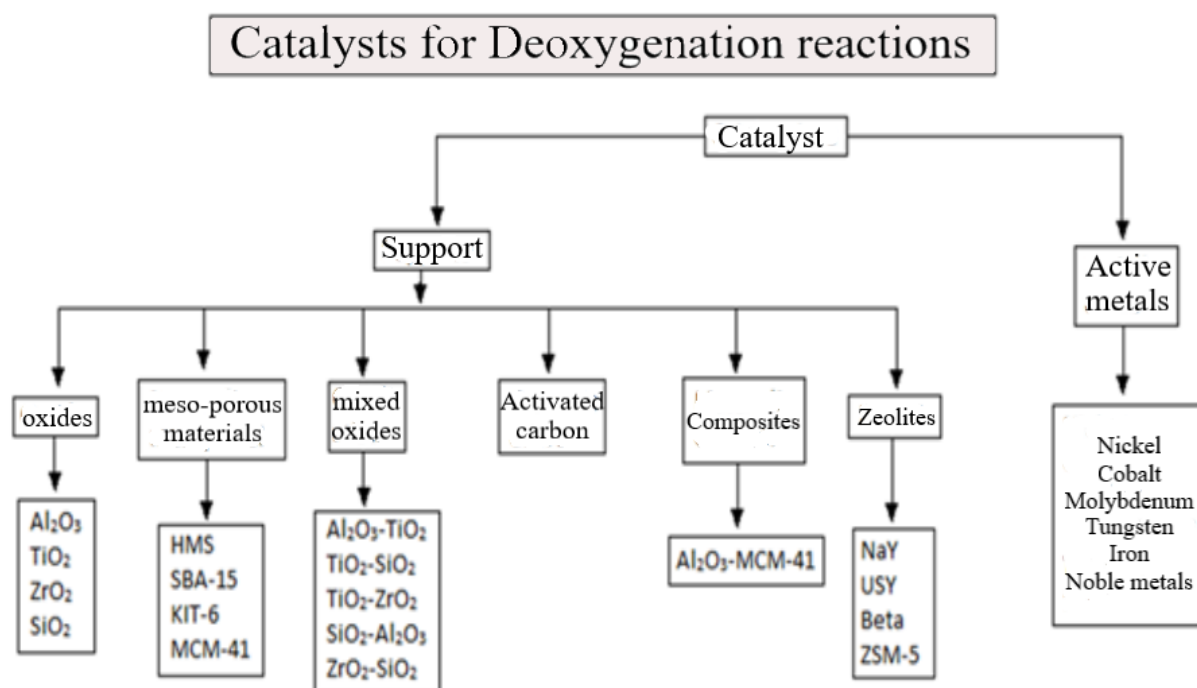


Figure 1.11 Diagram of common catalysts used for the DO [86]

Several transition metals supported on silica, silicate, alumina, zeolite, active carbon, mesoporous materials, zirconia, etc., were studied and used with the deoxygenation of triglycerides. Harnos et al. [102] studied the catalytic deoxygenation process on sunflower oil using Pd/C, Pd/Al₂O₃, Ni/Al₂O₃, and NiMo/Al₂O₃. Currently, noble metal-based catalysts are widely studied in the deoxygenation process due to their activities: palladium and platinum supported on coal are the most active catalysts [103]. As noble metal catalysts are expensive and this may limit their industrial uses, many studies were focused on nickel-based catalysts, in which Morgan et al. [104] have reported that a significant Ni content in the catalyst is more active than Pd and Pt. Catalytic deoxygenation reactions were also studied over bimetallic catalysts, where, Kubicka et al. [105] studied the comparison between monometallic Ni/Al₂O₃, Co/Al₂O₃, and bimetallic NiMo/Al₂O₃ catalysts and found that the bimetallic catalyst was more

active and stable than the mono-metallic one. Veriansyah et al. [106] obtained the same results with the deoxygenation of soybean oil over NiMo, CoMo, Pd, Pt, Ru supported on Al₂O₃.

1.8.2.3 HETEROGENEOUS CATALYSIS SUPPORT EFFECT

Furthermore, the metal percentage and its distribution on the support can significantly influence the catalytic activity and the product distribution, i.e., the pathway selectivity of the DCO, DCO₂, or HDO [74][107]. Catalytic deoxygenation reactions are affected not only by the metals but also by the properties of the catalyst's support, such as the surface area is an essential factor for its catalytic activity as it governs the adsorption capacity of the reactants on the material. Snare et al. [108], studying the DO reaction of stearic acid with different supports such as C, Al₂O₃, Cr₂O₃, and SiO₂, explained the best activity exhibited by the catalyst supported on carbon with its high surface area, which reduces its deactivation through sintering and coking. Another important parameter that affects the catalytic deoxygenation reaction is the acidity of the support and the type of acidic sites. Peng et al. [109] have examined the DO reaction of oil extracted from microalgae using two Ni-based catalysts supported on two different zeolites, H-ZSM5 and H-β, with the first one, which has a higher concentration of Bronsted acid sites, they have seen a complete conversion of the oil and a high cracking degree (43%), whereas with all the types of Ni / H-β used they obtained a high diesel range with negligible cracking. Besides, the size of the pores is also a very important factor for the DO reaction: in fact, support with very small pores to accommodate the reagents will not be able to carry out its activity [110]. Furthermore, the pore size could be important for the cracking phenomenon as a sufficient large pore structure could minimize the cracking and therefore lead to a higher diesel selectivity [111].

As it was used in this research Hydrotalcite (HT), Cenospheres (FAC), and Zeolite X as support materials, it is worth to expand the state of the art on them:

• Hydrotalcite HT

The use of hydrotalcite and their derivatives in catalysis received extensive attention in academic research and from industrial parties. Hydrotalcites are layered double hydroxides LDH that contain positively charged hydroxide layers and charge balancing anions in the interlayer region Figure 1.12. The layered structure of HTs provides a high surface area with the freedom to compensate various bimetallic (M^{II}) and trimetallic (M^{III}) ions on its surface [112].

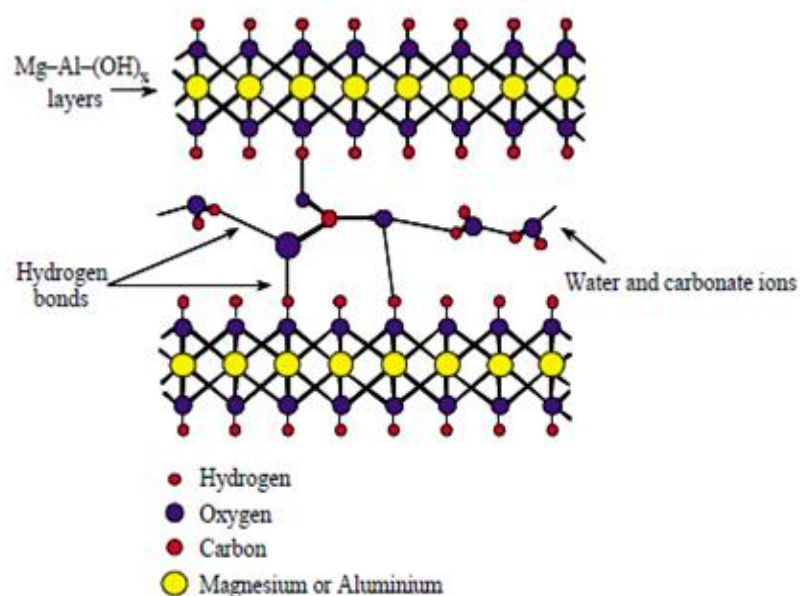


Figure 1.12 Hydrotalcite based Mg/Al [113].

The most interesting property of HT material as support is its surface basicity, which promotes the abstraction of protons from hydrocarbons even after the immobilization of active metal [114]. HT is generally used only after a heat treatment that induces dehydration, dihydroxylation, and losing of compensation anions, thus obtaining oxides that have interesting properties such as high surface area, basic properties on active sites, ability to form a mix of mixed oxides with very small crystal size and memory effect [115].

LDH can be synthesized with a wide range of compositions and a large number of materials, with a large variety of combinations of M (II) / M (III) cation pairs or as M (I) / M (III) with different anions in the interlayer. The interior of the octahedral sites of the hydroxide ions can

only be hosted by M (II) or M (III) ions, which have an ionic radius not too different from that of Mg^{2+} , well packed in the brucite-like layers, to form the LDHs compounds, while cations that are too small, such as Be^{2+} , or too large, such as Cd^{2+} lead to other compounds. So, inside the interlayers, there are anions, water molecules, and other neutral or charged particles, joined by weak bonds with the sheets [113]. A key feature of these materials is their ion exchange capacity, which makes them unique to the point of involving inorganic materials. A large variety of anionic species can be introduced into the interlayer region through one-step synthesis by co-precipitation or post-synthesis modifications, such as ion exchange. The incorporated anions can be simple such as carbonate, nitrate, or chloride. Considerable attention has been raised for the solid composed of alternating inorganic and organic sheets due to their applications, including their use as catalysts, functional materials, nanocomposite materials, and in separative processes [113]. They can also be used as a matrix to form supramolecular structures. Host layers can impose a restricted geometry on hosted layers, leading to increased stoichiometry control, reaction rate, and product distribution. Among the methods of synthesis of hydrotalcite, the most common is the co-precipitation method, which is used in this work also.

An enormous amount of research is dedicated to studying synthetic hydrotalcite and its suitability as an environmentally friendly material for applications including, but certainly not limited to, anti-corrosion[116], catalysis [115], encapsulation, controlled release, and CO_2 capture, and water technology [117].

- **Cenospheres FAC**

The cenospheres represents one of the fly ash components obtained from the combustion of coal [118]. They are characterized by a low density ($0.2-0.8 \text{ g / cm}^3$) and are easily separated from the other components of the ash by suitable gravitational methods [119][120]. The cenospheres formation occurs after the coal burning process in thermal power plants, which

produce fly ash containing ceramic particles made largely of alumina and silica. They are produced at temperatures of 1200 °C to 1700 °C through complex chemical and physical transformation. Their chemical composition and structure vary considerably depending on the composition of coal that generated them [121].

The ceramic particles in fly ash have three types of structures. The first type of particles is solid and are called precipitators. The second type of particles are hollow and are called cenospheres. The third type of particles is called plerospheres, which are hollow particles of large diameter filled with smaller size precipitator and cenospheres [122].

The granulometry and chemical composition essentially depend on the composition of the coal from which they come and the type of treatment that the coal undergoes. From a morphological point of view, they are characterized by spherical particles ranging in size from 5 to 500 μm [119] Figure 1.13., and mainly composed of aluminum silicates, SiO₂ (50-67wt%), Al₂O₃ (20-36wt%), and other oxides of various metals such as Fe, Ca, Mg, Na, Ti and K [119][123][124][121].

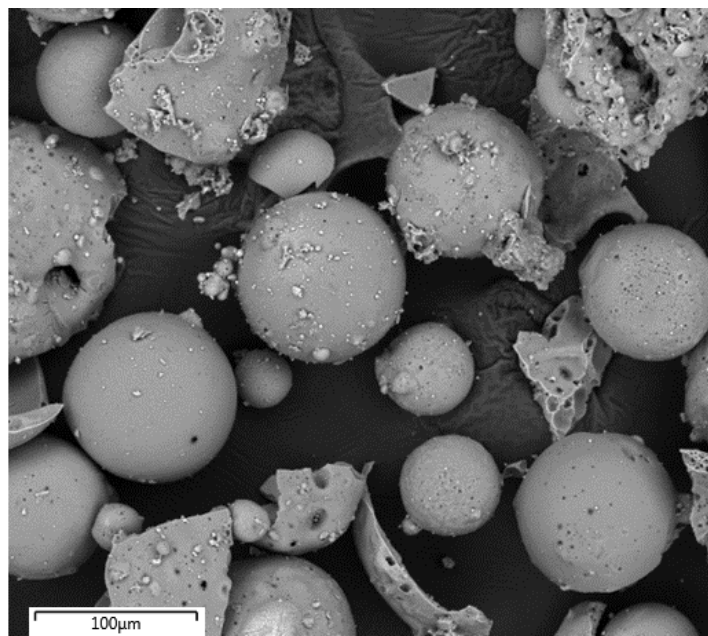


Figure 1.13 Morphological structure of the cenospheres.

Cenospheres is a material that is finding numerous applications thanks to peculiar properties such as high thermal resistance, high compressive strength, chemical inertia, and low H₂O absorption [125]. Some of these characteristics, like thermal resistance, make the suitable cenospheres support for the catalytic deoxygenation reaction. The ash from which the cenospheres used in this work was obtained derives from a coal-fired power system located in the city of Kolkanta in India. The use of this type of material as support allows to give an added value to a product deriving from waste; it is also inexpensive and is obtained in large quantities from coal-fired power systems that are still particularly active especially in the countries via of development.

- **Zeolite X**

Zeolites belong to the hydrated aluminosilicate minerals family—the crystalline porous structure composed of aluminum, silicon, and oxygen, plus counteractions. Zeolites are widely used in the oil industry as molecules can undergo cracking and isomerization reactions inside cavities, which lead to the production of hydrocarbon mixtures suitable for use as fuels [126]. Having numerous negative charges, there must also be cations for the balance of the charges, and these cations are generally Ca²⁺ and Na⁺. Zeolites are a material characterized by surface areas ranging from 300 to 700 m² / g and pore size 4-10 Å. The porous structure's regularity often allows zeolites to have a high selectivity both in terms of catalysis and adsorption processes [127]. The Si / Al ratio can vary depending on the synthetic conditions and the post-synthetic treatments, but in general, it is always greater than 1. As the Si / Al ratio increases, the content of the cations decreases; subsequently, there is a lower density of acid sites. Zeolite is also rich in Bronsted acid sites Figure 1.14, which are favorable for the hydrogenation and dehydration reactions that occur during the catalytic deoxygenation processes [128].

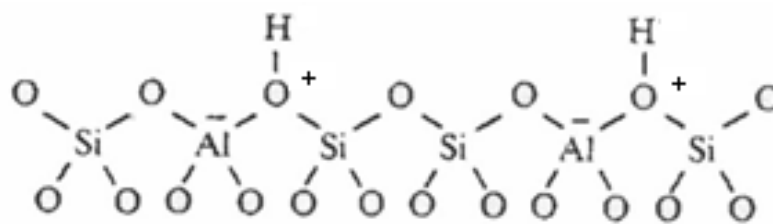


Figure 1.14 Bronsted acid sites present in zeolites.

There are nearly 50 different naturally occurring and synthetic types of zeolites (clinoptilolite, chabazite, phillipsite, mordenite, etc.) with varying physical and chemical properties, each with a unique structure. The pore sizes commercially available range from approximately 3 Å to approximately 8 Å. Some of the commercial materials are A, beta, mordenite, Y, ZSM-5, 13X [129][130].

The zeolite X is a type of zeolite characterized by a ratio Si / Al = 1-1.5 and having Na⁺ as a counter ion and an average pore diameter of about 8 Å. The monocrystalline unit of a typical zeolite X consists of a faujasite-like structure Figure 1.15 which consists of 10 cages of sodalite (sodium and aluminum silicate) connected by hexagonal prisms [131] [127].

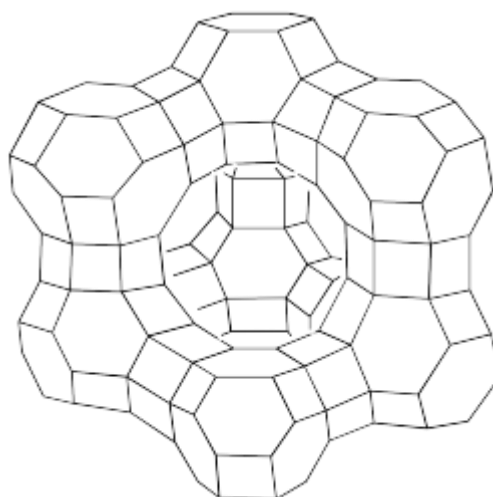


Figure 1.15 Faujasite-type zeolites X structure. [131]

This type of zeolite has a high ion exchange capacity, a high affinity with polar molecules, good capabilities as a catalyst, and also seems to adsorb gases such as H₂ well [132].

Which are the first contaminants present in the oceans, and 44% of wastes are of organic origins [4].

CHAPTER 2

This chapter illustrates the techniques employed to produce information and data collected in this thesis.

Four main subject areas are developed:

- *Catalysts and synthesis methods;*
- *Catalysts characterization methods;*
- *Procedures of an experimental study in hydrogenation reactions;*
- *Procedures of an experimental study on the production of green diesel by hydroprocessing reactions;*

2 MATERIALS AND METHODS

2.1 CATALYSTS AND SYNTHESIS METHODS

Several catalysts and synthesis methods were studied, developed, and tested during this Ph.D. thesis on the catalytic hydrothermal processes of vegetable oils:

- Palladium Lindlar commercial catalysts (Pd-based), used as reference catalyst.
- Palladium supported on Mg-Al hydrotalcite catalyst.
- Palladium supported on cenospheres.
- Bi-metallic nickel molybdenum catalyst supported on zeolite X.
- Bi-metallic nickel molybdenum catalyst supported on cenospheres.
- Bi-metallic cobalt molybdenum catalyst supported on cenospheres.

2.1.1 SYNTHESIS METHODS

The synthesis methods are illustrated in scientific literature, including coprecipitation under low supersaturation conditions [133][134], conventional impregnation methods [135], calcination, and reduction [136].

2.1.1.1 LOW SUPERSATURATION CO-PRECIPIATION METHOD

The mechanism of coprecipitation is based on the condensation of complexes in solution in equal quantities to have a uniform distribution of cations and anions. It has been widely used for the direct synthesis of layered double hydroxides (LDHs) containing a variety of cations and anions. In order to ensure the simultaneous precipitation of two or more cations, it is necessary to carry out the synthesis under supersaturation conditions, obtained by maintaining the pH of the solution higher or equal to that in which the more soluble hydroxide precipitates.

In general, the low supersaturation precipitation is performed by slowly adding a mixed solution of salts of divalent or trivalent metals, in a chosen ratio, inside a reactor containing an aqueous solution of the desired anion. The second solution of a base is added to the reactor simultaneously at a rate such as to maintain the pH, favoring the co-precipitation of the two metal salts. The addition can be controlled by manually monitoring the pH; however, the best results are obtained with an automatic titration tool. The anion that must be introduced should have a high affinity with the LDHs layers and be present in excess; the counter-anions of the metal salts, on the other hand, can be incorporated by means of competitive reactions. As a result, the metal nitrate and chloride salts are commonly used for the low selectivity of LDHs for these anions. Moreover, the LDHs have a great affinity for carbonate anions, and therefore, unless it is the anion chosen, the reactions are generally carried out in the presence of nitrogen in order to avoid the absorption of atmospheric CO₂ that would generate carbonate ions. LDHs, containing variable quantities (0.04-5% in atomic ratio) of noble metals such as Rh³⁺, Ir³⁺, Ru³⁺, Pd²⁺ and Pt²⁺, were prepared by coprecipitation at pH = 10.0 in aqueous solution. The presence of noble metal ions inside an inert matrix leads to materials characterized by good thermal stability and relatively high surface areas that facilitate a good dispersion of the noble metal particles [137].

2.1.1.2 CONVENTIONAL WET IMPREGNATION METHOD WI

Adsorption of a precursor of an active component by impregnating technique onto the support surface can determine the final distribution of the active component through the support bodies after the drying process. Adsorption of the active precursor is often employed with noble metals.

Wet impregnation is a commonly used technique for the synthesis of heterogeneous catalysts. Typically, the active metal precursor is dissolved in an aqueous or organic solution. Then the metal-containing solution is added to catalyst support containing the same pore volume as the volume of the added solution [138].

The impregnation method involves three steps: (1) contacting the support with the impregnating solution for a certain period of time, (2) drying the support to remove the imbibed liquid, and (3) activating the catalyst by calcination, reduction, or other appropriate treatment [139].

2.1.1.3 CALCINATION AND REDUCTION

In wet impregnation, a salt precursor of a catalytic element (nitrate, carbonate...) is used, so to remove all these nitrates or carbonates (and water) from the catalyst; we need to calcine it by a thermal treatment in stagnant air. Also, during the calcination, the metal is oxidized, so during the reduction step, the metal oxides will be reduced and activated. It is important to know that, calcination and reduction process depends on the support that is used because sometimes the calcination (depending on the temperature) might destroy it [140].

2.1.2 NOMENCLATURE AND LIST OF MATERIALS

All reactants are purchased from Sigma -Aldrich® and used as received.

(NH₄)₆Mo₇O₂₄·4H₂O 99%, Ni (CH₃COO)₂·4H₂O abbreviated Ni (OAC)₂·4H₂O 99%, Mg (NO₃)₂·6 H₂O 99%, Al (NO₃)₂·9H₂O, Na₂CO₃ 99.5%, NaOH 97%, Pd (NO₃)₂·2H₂O 40%, N, N-Dimethylformamide (DMF) 99.8%, Co (NO₃)₂·6H₂O 98%, HNO₃ 98%, deionized water (Millipore), NaOH 97%, CH₃OH 99.8%, Boron trifluoride methanol BF₃ 10%, NaCl 99.7%, cenospheres (FAC) [138] (FAC produced by an electric generation plant fed by coal and located in the city of Kolkanta in India), sunflower oil (*H. Annus*) as standard oil, hexane as a solvent ≥99, C₇-C₄₀ saturated alkanes standard, C₂₀, and C₂₅ saturated alkanes as an internal standard during the deoxygenation tests; commercial rapeseed (canola) and sunflower oils which were purchased from the food market. Canola rapeseed oil was chosen because it is more exploitable at the industrial level. On the other hand, sunflower oil allows obtaining a higher C18:1 increment during the hydrogenation reaction, starting from a relatively low initial percentage of C18:1.

Table 2.1 lists all materials synthesized or used (Lindlar), with their nominal composition. Herein, the nomenclature applies for their identification, where all the catalysts have maintained their names in the following discussion.

Table 2.1 Lists of studied materials

Name	Nominal phase	Nominal Pd loading [%w/w]	Nominal NiO loading [%w/w]	Nominal CoO loading [%w/w]	Nominal MoO loading [%w/w]
Lindlar	Pd-calcium carbonate	5	0	0	0
Pd/HT	Pd-hydrotalcite	1	0	0	0
Pd/FAC	Pd-cenosphere	2	0	0	0
NiMo/zeolite X	NiMo-zeolite X	0	3	0	12

NiMo/FAC	NiMo-cenosphere	0	3	0	12
CoMo/FAC	CoMo-cenosphere	0	0	3	15

2.1.3 CATALYSTS PREPARATION

2.1.3.1 LINDLAR CATALYST

Lindlar is a palladium-based catalyst supported on calcium carbonate, poisoned with lead oxide in order to increase the catalyst selectivity. It could also be further poisoned with quinoline or sulphur to reduce the formation of alkanes in the alkynes hydrogenation reaction. However, the manufacturer does not give any clues about this step neither in the security sheet of the sample nor in the technical data. sulphur or quinoline Lindlar catalysts bought from Sigma Aldrich® have a nominal Pd content around 5%w/w. Lindlar is a common commercial heterogeneous catalyst, mostly employed in selective hydrogenation reactions[141][142] besides other reactions [143][144]. The common synthesis starts from a slurry of PdCl₂ and calcium carbonate (CaCO₃), and by the addition of lead acetate (Pb (OCOCH₃)₂) or lead oxide (PbO₂).

This catalyst was used as a reference catalyst for our catalytic hydrothermal processes in a preliminary series of tests carried out in a laboratory-scale apparatus.

2.1.3.2 PALLADIUM SUPPORTED ON HYDROTALCITE[133][134][145]

Palladium noble metal has a perfect property like selectivity and activity at low temperature. This last point is very important from the view of saving energy, which is one of the main principles of green chemistry. Hydrotalcite was chosen as support because:

- During the synthesis by impregnation method and after reduction, palladium dispersed very well on the surface.

- High mean pore size minimizes the limitation of large oleic acid and triglycerides molecules in to the pore of the catalyst [146].
- Active acid sites improve the catalytic activity of palladium.

The Pd/HT catalyst was prepared by the coprecipitation method at constant pH under low supersaturation conditions, the most commonly used method since it ensures the formation of precipitates with a high degree of crystallinity [147][133]. Firstly, the hydrotalcite Mg /Al 2: 1 was synthesized by using two solutions containing Mg (NO₃)₂·6H₂O (38.4 g) and Al (NO₃)₂·9H₂O (28.14 g), both of them were inserted, drop by drop, inside a beaker containing a solution of Na₂CO₃ (1.34 g in 250ml) in deionized water under stirring and 60 °C. The pH value of the solution was kept around 10 with additions of NaOH (20 g). The solid obtained (16.7g of HT) is placed in a solution of Na₂CO₃ (5.76g) with water (V = 835ml) (1g of HT for 0.345g of Na₂CO₃ in 50ml of H₂O) put in an oven at 100 °C for 2h, then it is washed, filtered with water and added Na₂CO₃ with subsequent evaporation and new filtration/washing to let it finally dry. The solid obtained is made into powder and weighed (16.08g).

The hydrotalcite obtained (5 g) reacts with Pd (NO₃)₂·2H₂O (0.125 g) in the presence of N, N-dimethylformamide (50ml) at room temperature and stirring for 24 hours. The solvent (DMF) is evaporated, and the solid residue is dried in an oven. The solid produced is defined as HT/Pd (II). The Pd (II) present in it is reduced to Pd (0) by using cyclohexene as a hydrogen donor at 83 °C for 1 hour and magnetic stirring.

2.1.3.3 MONOMETALLIC PALLADIUM SUPPORTED ON CENOSPHERES

The raw cenospheres were treated with an acid solution at 10% by weight of nitric acid (HNO₃) to wash the impurities present inside them. The procedure follows what is reported in the literature [148][139][140]. The acid solution is prepared by diluting concentrated nitric acid 98% with distilled water. The cenospheres are then placed inside a flask containing the acid

solution; approximately 20 ml of the acid solution is used for every 10g of cenospheres. Leaching was carried out for 1 hour at room temperature and under magnetic stirring, and then the obtained slurry is filtered with distilled water until a neutral pH is reached. After this step, the slurry is dried in an oven at 120 ° C for 12h.

The catalyst was prepared by wet impregnation method with magnetic stirrers. The synthesis procedure is 9.8 g of cenospheres (FAC) as support with Pd (NO₃)₂ · 2H₂O (0.5g) solved in deionized water (Millipore) as promoter under stirring for 3h at room temperature. At the end of the reaction, the solution obtained was evaporated at (T = 35 °C, P = 2.7 KPa), dried at 110°C in an oven for one day, calcinated at 600 °C with a ramp program of 5 °C/min for 2h under static air, and then reduced by using a measured amount of catalysts (4.342 g), the sample was placed in fixed bed reactor and heated until 600 °C at the rate of 5 °C/min then for three hours in 600 °C in the presence of H₂ (10vol % H₂ in N₂).

2.1.3.4 BI-METALLIC (NICKLE-MOLYBDENUM) SUPPORTED ON ZEOLITE X

Monometallic transition-metal Ni and the noble metals Pt and Pd catalysts are very common for the deoxygenation of fatty acid/triglycerides due to their selectivity towards DCO_x reactions. The development of monometallic as bimetallic catalysts was to improve their activity towards DO reaction pathways and to increase catalyst stability [149].

The process leading to the transformation of cenospheres into zeolite X follows the protocol reported in the literature [139][140]. A solid mixture of cenospheres and NaOH was then prepared in a 1: 1.2 ratio by grinding the two components in a mortar until homogeneity was achieved. The resulting paste was heated at 560 ° C for 1 hour. At this point, the molten sample is cooled to room temperature, mixed with distilled water until a slurry is obtained (solid/liquid ratio about 0.2), and stirred (600 rpm) in a beaker at room temperature for 8h. At the end of 8h, the whole is kept at a temperature of 80 ° C under stirring for 24h. Finally, the sample is

filtered, washed with distilled water to remove excess NaOH, and then dried in an oven at 120 °C.

The catalyst was prepared by wet impregnation method with magnetic stirrers, and the synthesis procedure is 4.25g of zeolite X as support with 10ml of H₂O, to dissolve Ni (OAC) 4H₂O (0.5 g) as a promoter and (NH₄)₆Mo₇O₂₄·4H₂O (0.735 g) as a precursor in bimetallic catalysts, were impregnated onto support under stirring for 3h. At the end of the impregnation, the solution obtained was evaporated at (T = 40 °C, P = 9.6KPa), dried at 120 °C in an oven for 2/3 days, calcinated at 500 °C for 4 h under static air, with a heating rate 5 °C/min and then reduced by using a measured amount of catalysts (3.71 mg): the samples were placed in fixed bed reactor and heated until 500 °C at the rate of 5 °C/min then for three hours in 500 °C in the presence of H₂ (10 vol % H₂ in N₂).

2.1.3.5 BI-METALLIC (NICKLE-MOLYBDENUM) SUPPORTED ON CENOSPHERES

The catalyst was also prepared by the wet impregnation method with magnetic stirrers. The synthesis procedure is 4.25g of cenospheres (FAC) [138] as support and 10 ml of deionized water to dissolve, with Ni (OAC) 4H₂O (0.5g) as a promoter and (NH₄)₆Mo₇O₂₄·4H₂O (0.735g) as a precursor in bimetallic catalysts under stirring for 3h. At the end of the impregnation, the solution obtained was evaporated at (T = 40 °C, P = 9.6 KPa, dried at 120°C in an oven for 2/3 days, calcinated at 500 °C with ramp program of 5 °C/min for 4 h under static air. The reduction step was performed by using a measured amount of catalysts (3.80 mg); the samples were placed in a fixed bed reactor and heated until 500 °C at the rate of 5 °C/min, then for three hours at 500 °C in the presence of H₂ (10vol % H₂ in N₂).

2.1.3.6 BI-METALLIC (COBALT-MOLYBDENUM) SUPPORTED ON CENOSPHERES

The catalyst was also prepared by the wet impregnation method with magnetic stirrers. The synthesis procedure is 4.142g of cenospheres (FAC) [138] as support and deionized water to dissolve, with $\text{Co}(\text{NO}_3)_2 \cdot 6\text{H}_2\text{O}$ (0.580g) as a promoter and $(\text{NH}_4)_6\text{Mo}_7\text{O}_{24} \cdot 4\text{H}_2\text{O}$ (0.917g) as a precursor in bimetallic catalysts under stirring for 24hr. At the end of the impregnation, the solution obtained was evaporated at ($T = 35\text{ }^\circ\text{C}$, $P = 2.7\text{ KPa}$), dried at 110°C in an oven for one day, calcinated at $600\text{ }^\circ\text{C}$ with a ramp program of $5\text{ }^\circ\text{C}/\text{min}$ for 2h under static air and then reduced by using a measured amount of catalysts (3.878 g), the sample was placed in fixed bed reactor and heated until $600\text{ }^\circ\text{C}$ at the rate of $5\text{ }^\circ\text{C}/\text{min}$ then for three hours in $600\text{ }^\circ\text{C}$ in the presence of H_2 (10 vol % H_2 in N_2).

2.2 CHARACTERIZATION TECHNIQUES

Characterization of synthesized materials consists of the application of:

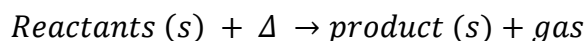
- 1- TGA (Thermal Gravimetric Analysis) for thermal decomposition analysis.
- 2- ICP-AES (Inductively Coupled Plasma – Atomic Emission Spectroscopy) for the quantification of:
 - Pd, Ca, and Pb in Lindlar catalysts.
 - Pd, Al, and Mg in Pd/HT.
 - Ni and Mo in bi-metallic systems supported on Zeolite X.
 - Pd, Ni, Co, and Mo in mono-metallic and bi-metallic systems supported on cenospheres.
- 3- XRD (X-Ray Diffraction) for crystalline phase investigation.
- 4- BET (Brunauer-Emmett-Teller) multipoint method for surface area quantification [150].

- 5- BJH (Barrett-Joyner-Halenda) method for mesopores assessment [151].
- 6- TPR (Temperature Programmed Reduction) to study sample reducibility.
- 7- TPD (Temperature Programmed Desorption) for the acidity of catalysts (with NH₃);
- 8- SEM (Scanning Electron Microscopy) combined with EDS (Energy Dispersive X-ray Spectrometry) for morphological, textural, and chemical surface analysis;
- 10- H₂-Pulse Chemisorption for metal surface and dispersion analysis;

2.2.1 THERMAL GRAVIMETRIC ANALYSIS

The thermal gravimetric analysis of the samples was investigated by Linseis Thermo Gravimetric Analyser (TGA) STA TP1000, where the change in the sample weight is recorded as a function of temperature or time.

The following changes are possible in the TGA:



In this manuscript and in order to study at which temperature the calcination process could be done, the first one was used under 800 °C with program ramp 10 °C /min, which involves losing in the sample weight that may occur due to the gas obtained from the decomposition of reactants by heating or may due to the existing H₂O with the reactants.

2.2.2 ION COUPLED PLASMA - ATOMIC EMISSION SPECTROSCOPY

Samples elemental mass percentages are detected by a VARIAN 720-ES ICP-AES. Solid samples are decomposed in a concentrated strong acid H₂SO₄, then diluted in deionized water

to be ready for nebulization operated by the device and introduced inside the plasma flame. Collisions with plasma electrons and charged ions break molecules into the atoms involved. Atoms repeatedly lose electrons and re-combine, giving off radiation in the specific wavelength of the elements involved. These wavelengths are then collected by the atomic emission spectrometer. The instrument is equipped with a custom-designed Charge Coupled Device (CCD) detector, which is a highly sensitive photon detector. An estimation of detection limits for the quantified metals is Mo 0.018 mg/kg, Ni 0.004 mg/kg, Pd 0.025 mg/kg, Ca 0.035 mg/kg, Mg 0.036 mg/kg, Al 0.020 mg/kg, Ce 0.010 mg/kg, Si 0.066mg/kg [152][153].

2.2.3 X-RAY DIFFRACTION

X-ray diffraction is a very useful technique in order to determine information about the crystalline structure of powder and solid samples. The method is based on the interaction between the X-ray wave and the atoms of a crystalline structure because there is an interference between the signal that the instrument sends to the sample and the signal that comes from it [154].

The interferential structure produced is called the diffraction pattern. It is possible to identify such interference from the diffraction patterns in which diffraction peaks contain information about crystalline phases present. The condition of constructive interference is Bragg's law.

Bragg's equation is one of the keystones in understanding X-ray

diffraction whose mathematical equation is Equation 2.1

Equation 2.1

$$[138][155]: 2d \sin \theta = n\lambda$$

where:

θ is the incidence angle of the X radiation, λ is the wavelength in nm, d is the interplanar distance between rows of atoms in nm, hkl are the Miller indices, n is an integer.

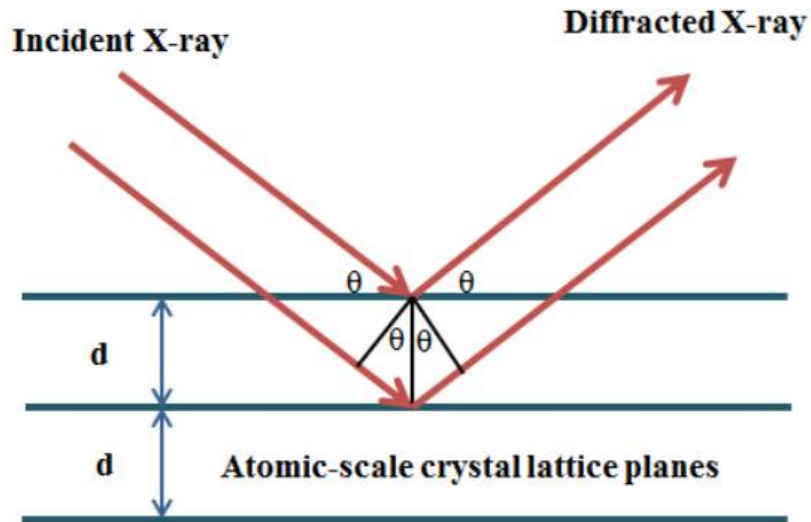


Figure 2.1 Bragg's Law Reflection

To have a diffraction effect for any value of hkl , it is necessary that the difference of optical route between the various reflected waves is an integer multiple of the wavelength λ .

The sample is transformed to fine powder whose particles are as much as possible randomly oriented so as not to have preferential directions along which the crystalline grains are oriented, and this allows the identification of all the crystalline planes.

The X-ray diffraction instrument that has been used is PANalytical X'Pert PRO diffractometer it has the typical characteristic of Bragg-Brentano geometry. The X-ray wave is emitted in the source tube, using a Cu target ($K_{\alpha 1}=1,540598 \text{ \AA}$; $K_{\alpha 2}=1,544426 \text{ \AA}$; $K_{\beta}=1,39225 \text{ \AA}$), and after that is collimated by the soller slit and divergence slit before reach the sample. Then the scatted wave goes through the second series of soller slits, and a monochromator is necessary to select the desired wavelength to the detector Figure 2.2

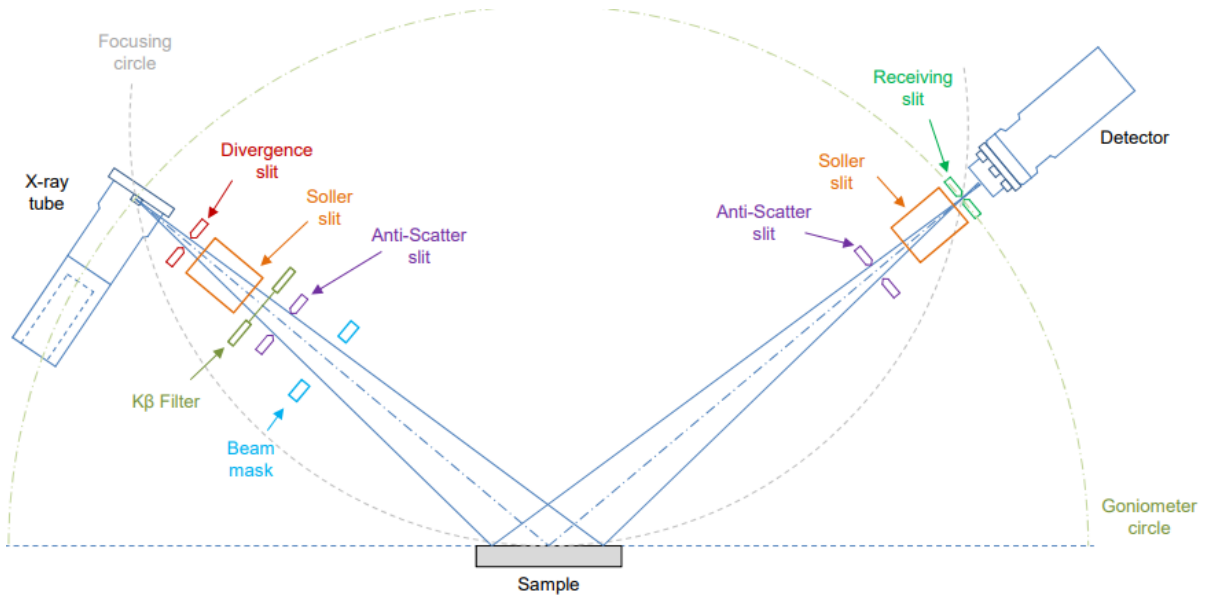


Figure 2.2 XRD Bragg – Brentano geometry [156].

In this geometry, the sample is fixed, and the detector rotates at a velocity 2θ with an angle between 5° and 90° in order to detect signals from all planes. It is managed by X'Pert HighScore Plus collector software, which collects data from the sample, and then the phase identification is made by matching the spectrum with an international reference database, i.e., the inorganic crystal structure database (ICSD).

The starting powder is first ground in an agate mortar and then sieved with standard sieves UNI 2331 and ISO R565 up to dimensions less than $150\ \mu\text{m}$. Then the powder is adhered on a zero-background sample holder based on single-crystal silicon for use in reflection geometry. Only, in the case of Pd/HT, ethanol is used as a "glue" ($\geq 98\%$) to make the powders adhere. The characteristics that can be identified in a diffraction pattern are the phases present (peak positions), the concentration of the various phases (peak height), amorphous content (background trend), and the size or presence of stress in the crystallites (width and shape of the peaks) by Debye-Scherrer equation, Equation 2.2:

$$L = K\lambda / \beta \cos\theta$$

Equation 2.2

Where β is the full width of half of the maximum (radian) at angle 2θ , K is the shape constant, λ is the wavelength of incident light (nm), L is the crystallite size in (nm), θ is peak position (degree).

2.2.4 SURFACE AREA AND POROSITY ANALYSIS BET-BJH

"NOVA 1200e Surface Area & Pore Size Analyzer" from Quanta-chrome Instruments is used. The BET analysis (Brunauer-Emmet-Teller) and porosity analysis (Barret-Joiner-Halenda) are two methods to determine the superficial area and pore diameters of solid samples. Recording N_2 adsorption and desorption isotherms at -196.15°C . It can be determined when the "statistical monolayer" of atoms has been reached. So, knowing the number of molecules that necessary to cover a single layer with already knowing the area occupied by a single molecule ($\approx 16.2 \text{ \AA}^2$) then, it is possible to calculate the area.

The adsorption isotherm of nitrogen can be obtained by Cartesian plane, where the adsorbed volume of nitrogen as a function of the adsorption pressure, expressed as relative pressure P / P_0 where P_0 is the nitrogen saturation pressure at work temperature[6]:

$$1/v [(P/P_0) - 1] = (c - 1)/vm^c * ((P/P_0) + 1)/vm^c \quad \text{Equation 2.3}$$

where v is the volume of gas absorbed, vm is the quantity of gas that constitutes the monolayer, and c is the BET constant defined as:

$$c = \exp ((E_1 - E_L) / RT) \quad \text{Equation 2.4}$$

Where E_1 is the heat adsorption of the monolayer, E_L is for the following layers, R is the gas constant, and T is the temperature in Kelvin. Given the adsorbed nitrogen volume vm is possible to calculate the moles' number of gas (n):

$$m + n_m = 1/vm \quad \text{Equation 2.5}$$

BET surface is then obtained from the monolayer quantity adsorbed:

$$S_{BET} = \frac{n_m N_A \sigma_m}{m} \quad \text{Equation 2.6}$$

Where σ_m is the molecular cross-sectional area (0.162 nm² for N₂), N_A is the Avogadro number, and m is the mass of the sample.

BJH mesoporosity assessment (V_{BJH} and $D_{av,BJH}$) method is an iterative method; it is possible to obtain pore diameter distribution starting from the Kelvin equation, which is based on two assumptions: (i) all the pores have a cylindrical shape, (ii) there are no interconnected pores:

$$\ln \frac{P}{P_0} = - \frac{2\gamma V_l}{r_k RT} \quad \text{Equation 2.7}$$

Where γ is the surface tension, V_l is the molar volume, R is the universal gas constant, T is the temperature of the adsorption/desorption measure, r_k is the Kelvin radius.

N₂ desorption data are recommended for BJH because they are a reversible liquid-vapor transition in the case of capillary condensed molecules typical of mesopores (2-50 nm) [157][158]. In this manuscript, the pore size diameter was determined by Equation 2.8:

$$D = 4V/S \quad \text{Equation 2.8}$$

Where V is the V_{BJH} (N₂ desorption), S is the BET surface area.

2.2.5 SCANNING ELECTRON MICROSCOPY

SEM micrographs are recoded by a ZEISS GEMINI SEM 500 microscope device. A scanning electron microscope (SEM) uses a focused beam of high energy electrons to generate a variety of signals at the surface of solid specimens. The signals that derive from electron-sample interactions reveal information about the sample, including external morphology, chemical composition, and crystalline structure. In most applications, data are collected over a selected area of the surface of the sample, and a 2-dimensional image is generated. In a typical SEM, an

electron beam is thermionically emitted from an electron gun fitted with a tungsten or lanthanum hexaboride cathode. The electron beam, which has an energy ranging from 0.2 keV to 40 keV, is focused by one or two condenser lenses to a spot about 0.4 nm to 5 nm in diameter. The electrons pass into the scanning system, where they are deflected by a special deflection coil, which allows scanning of the surface.

The signals include secondary electrons, which are valuable for showing morphology and photography on samples, backscattered electrons, which are most useful for illustrating contrasts in composition in multiphase samples, diffracted backscattered electrons used to determine crystal structures and orientation of materials, photos (characteristic X-rays that are used for elemental analysis and continuum X-rays).

To control the sample, it is necessary to generate the vacuum inside the microscope ($P = 10^{-4}$ - 10^{-5} mbar) in order to reduce the interactions between electrons and gas molecules. The current intensity is in the order of 10^{-12} - 10^{-17} A° with associated energy between 5-50 keV.

Elemental analyses are performed by in-situ EDS; the ZEISS GEMINI SEM 500 is equipped with an OXFORD ENERGY 250 INCAx-act detector. EDS spectra are acquired both on spots or zones of external surfaces. Also, some topography analysis is made with the instrument on the surfaces of the samples; these kinds of maps give qualitative information about the distribution of metals.

2.2.6 TEMPERATURE PROGRAMMED REDUCTION TPR

Temperature Programmed Reduction (TPR) is carried out on a MICROMERITICS AUTOCHEM II 2920 chemisorption analyzer. The sample of 50 mg catalyst, was loaded in a Flow-Thru “U” shaped fused quartz tube (9 mm ID), which is placed as a bed between two quartz wool flocks and fixed inside a furnace controlled by an internal thermocouple.

Before TPR, only for the catalyst supported over zeolite X, a TPD (Temperature Programmed Desorption) is operated to eliminate all the possible absorbed gases on the catalyst surface, with a ramp of $15\text{ }^{\circ}\text{C min}^{-1}$ up to $450\text{ }^{\circ}\text{C}$, 30 minutes as a holding time, and cooling down to room temperature, all under Ar stream of $50\text{ cm}^3\text{ min}^{-1}$. After this, actual TPR starts with a $15\text{ }^{\circ}\text{C min}^{-1}$ ramp heating up to $900\text{ }^{\circ}\text{C}$, 30 minutes as a holding time, under $50\text{ cm}^3\text{ min}^{-1}$ flow of reducing gas ($10\%_{\text{vol}}\text{ H}_2$ in Ar).

Downstream the reaction cell, a cold trap retains the produced steam then a TCD (Thermal Conductivity Detector) measures H_2 consumption, and then recorded together versus temperature and time. The data are saved by AUTOCHEM II software v4.02.

In order to examine the reducibility of the single metal phase in which present in the catalyst, the reduction degree R was calculated by Equation 2.9[159].

$$R = \frac{H_2 \text{ consumption from TPR}}{\text{theoretical } H_2 \text{ consumption}} \cdot 100 \quad \text{Equation 2.9}$$

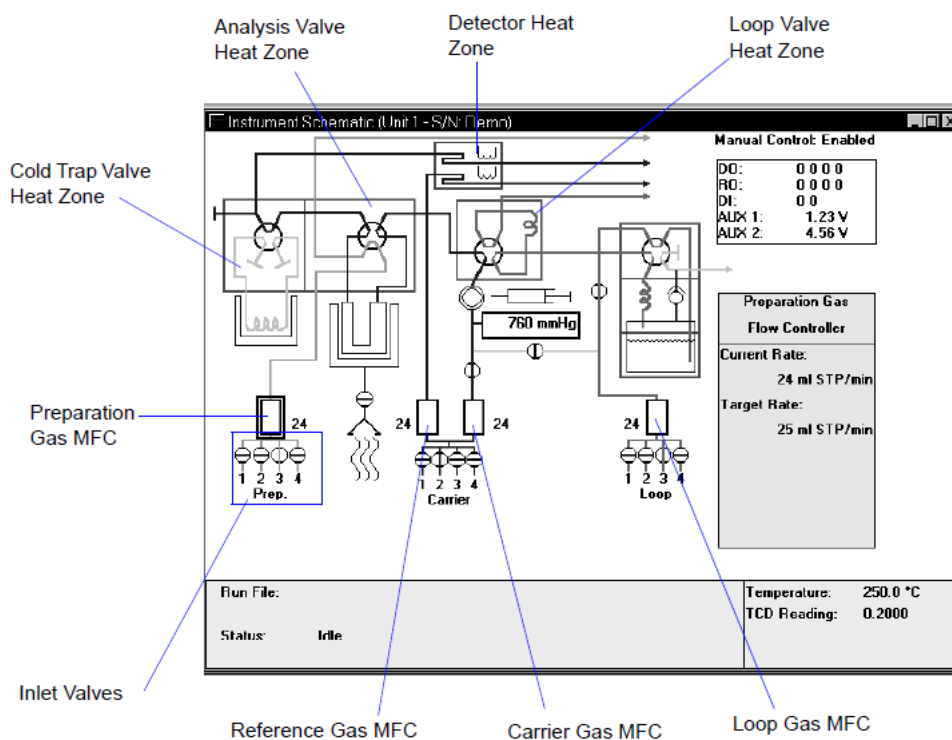


Figure 2.3 Schematic diagram [160]

2.2.7 TEMPERATURE PROGRAMMED DESORPTION NH₃-TPD

Surface concentrations of acidic centers were determined by temperature-programmed desorption of ammonia (NH₃-TPD). Experiments were carried out in the temperature range of 70 – 650 °C in a Flow-Thru “U” shaped fused quartz tube (9 mm ID), which is placed as a bed between two quartz wool flocks and fixed inside a furnace controlled by an internal thermocouple. The molecules desorbing was monitored by a mass spectrometer (ThermoStarTM GSD 301 T (Pfeiffer Vacuum)) coupled to a Q500 thermogravimetric analyzer. Before TPD experiments, the calcined catalyst (50 mg) was pre-treated at 450 °C and then cooled down to 50 °C. Subsequently, the sample was saturated in the flow of a gas mixture containing 10 vol.% of NH₃ in helium until no adsorption of probe molecules was observed. Then the sample was purged in the helium flow until a constant baseline level was attained. Desorption was carried out at 450 °C with a linear heating rate (10°C/min).

2.2.8 H₂-CHEMISORPTION

Active surface area (ASA), metal dispersion, and particle size were estimated from the chemisorption of H₂. Chemisorption was carried out in the same apparatus as for TPR experiments, using a pulsed flow system.

H₂ chemisorption was carried out as follows: fresh calcined sample (50 mg) was loaded in the sample tube and reduced in a flow of 10%H₂ in Ar (50 cm³min⁻¹), the temperature was increased up to 500 °C with a heating rate of 15 °C min⁻¹, and the final temperature was held for 30 minutes. The sample was cooled in Ar down to 50 °C. Pulses of 10%H₂ in Ar were injected at certain time intervals until saturation was reached. The amount of H₂ chemisorbed was determined from cumulative integrated areas. A dissociative adsorption hypothesis was applied, and metal: H₂ stoichiometry was chosen as (1 for calculations for Ni and Pd) and (1-3

for Co depending on its oxidation state $\text{Co}_3\text{O}_4 \rightarrow \text{CoO} \rightarrow \text{Co}$ [161]). The spherical geometry of the metal crystallites was assumed for calculating average particle diameters.

From the H_2 -Chemisorption analysis, we can obtain:

- Active surface area

$$ASA = n \cdot N_A \cdot S_{at} \cdot \frac{V_{ads}}{V_m} \quad \text{Equation 2.10}$$

where, n stoichiometric rate of the chemisorption reaction, N_A Avogadro's number, S_{at} surface occupied by one atom of metal, V_{ads} volume of gas adsorbed, V_m molar volume of gas adsorbed.

- Metal dispersion %

$$metal\% = n \cdot \frac{V_{ads}}{V_m} \cdot \frac{M}{m} \cdot 100 \quad \text{Equation 2.11}$$

Where, M molar weight of the metal, m mass of metal in the catalyst.

- Particle size

$$D_{ps} = 6 \cdot \frac{V}{A} \quad \text{Equation 2.12}$$

Where, A surface of metallic particles with spheric shape, V volume of metallic particles.

2.3 GAS CHROMATOGRAPHIC ANALYSIS TECHNIQUES

2.3.1 TRACE GC ULTRA 7820

The concentrations of the different fatty acids were evaluated after transesterification (all the reactants are purchased from Sigma -Aldrich® and used as received) by means of a IUPAC AOAC standardized method [162]. In the transesterification process, 350 mg of hydrogenated oil were reacted with 6 mL of 2N NaOH methanolic solution and heated under reflux

conditions until the droplets of fat disappear (5-10 min). Then, 7 mL of 10 % BF_3 methanolic solution was added, and then the solution was boiled for 1 min. A brine of NaCl was added, and the resulting solution was extracted with n-hexane (5 mL); in the end, the organic phase was dried with Na_2SO_4 .

The trans-esterified samples from the hydro-processing tests were analyzed with a Trace GC Ultra 7820 equipped with a Flame-Ionization detector (FID) and with a Supelco® SP-2380 GC column (30 m x0.25mmx 25 μm). Gas chromatography runs were conducted in isothermal conditions (N_2 carrier; injector 250 °C; column 180 °C for 25 min; FID 250°C; split 25ml/min). Identification of FAME was achieved by comparison with commercially available standards.

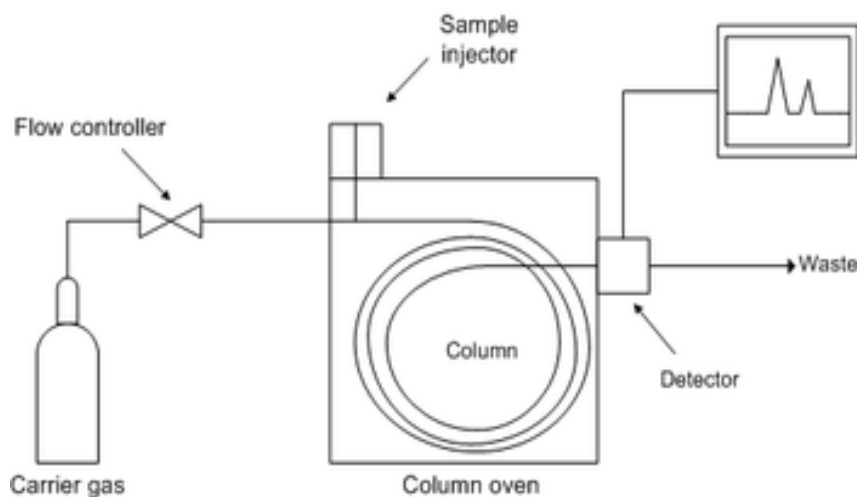


Figure 2.4 Schematic diagram of the gas chromatographic analyzer.

2.3.2 GC/3400CX VARIAN STAR COUPLED WITH MS/VARIAN SATURN 2000

The samples analyzed with GC-MS, which are taken from the hydro-processing deoxygenation tests, were dissolved in the hexane. For the $\text{C}_7\text{-C}_{40}$ standard and the $\text{C}_{11}\text{-C}_{13}\text{-C}_{14}\text{-C}_{17}\text{-C}_{19}$ standard, they were taken from a 100 μl certified solution (1 mg/ml). The Gas Chromatograph

used is the Varian Star 3400 cx model, and the mass spectrometer is the Varian Saturn 2000 model. The GC column is HP-5 (30m × 0.25µm × 0.25 nm). Gas chromatography runs were conducted in conditions the duration of the chromatographic run is 35 minutes, split 50 ml/min, the detector temperature is 50°C; a temperature ramp was used for heating the column, which provides an initial temperature of 50°C for 5 minutes and a temperature increase of 5°C up to 280 degrees and subsequently fixed temperature at 280°C for 5 minutes. Identification of n-alkanes was achieved by comparison with the standards [163].

The presence of hydrocarbons was confirmed by the comparison with the retention times of a standard of saturated linear alkanes; C₇-C₄₀, while the identification of unknown peaks is carried out with the analysis at GC-MS and by comparing it with a reference library. In addition, the identification of unknown peaks was also made by calculating the Kovatz(I) retention index of each peak, as indicates in Equation 2.13[164].

$$I = 100 \times \left[\frac{tr_i - tr_z}{tr_z - tr_{z+1}} + z \right] \quad \text{Equation 2.13}$$

Where: tr_i the retention time of the compound, tr_z linear alkane retention time that comes before the i peak of the compound, tr_{z+1} linear alkane retention time that comes after the compounds' peak, z number of linear alkane carbon atoms that come before the compound's peak.

2.3.3 GC/7820A AGILENT

The samples analyzed with GC-7820A Agilent, which are taken from the hydro-processing tests, were dissolved in the hexane. For the C₇-C₄₀ standard and the C₁₁-C₁₃-C₁₄-C₁₇-C₁₉ standard, they were analyzed by this GC. The Gas Chromatograph used is the GC/7820A Agilent model. The GC column is HP-5 30 m × 0.32 mm × 0.25 µm (19091J-413). Solvents for washing (A: Acetone, B: Hexane), injection volume 1µL. Gas chromatography runs were

conducted in conditions the duration of the chromatographic run is 35 minutes, split 50 ml/min, the detector temperature is 50°C; a temperature ramp was used for heating the column, which provides an initial temperature of 50°C for 5 minutes and a temperature increase of 10°C/min up to 280 degrees and subsequently fixed temperature at 280°C for 5 minutes. Identification of n-alkanes was achieved by comparison with the standards.

2.4 EXPERIMENTAL STUDY OF HYDROGENATION

REACTIONS

2.4.1 VEGETABLE OIL SELECTION FOR HYDROGENATION TESTS

Nowadays, the oleochemical industry is a major producer of bio-based products, such as important products of unsaturated oils (soybean, sunflower, and linseed oil). To respond to industrial needs, it should give at least 80% oleic acid [165].

The most common vegetable oils in which used for selective catalytic hydrogenation process: corn oil, with 60% linoleic acid and about 25% oleic acid, the oil of soybeans, with 50% linoleic acid and 25% oleic acid, and cottonseed oil, with about 50% of linoleic acid and 15% of oleic acid [166].

Our choice of sunflower and rapeseed (canola) vegetable oils for selective catalytic hydrogenation tests because they are particularly rich in polyunsaturated fatty acids. Gas chromatographic composition analysis of sunflower and canola oils is observed in Table 2.2.

Table 2.2 composition of sunflower and canola oils as-received sample.

Vegetable oil	C18:0%	C18:1c%	C18:0t %	C18:2%	C18:2 iso%	C18:3%
Sunflower	2.9	32.5	0.0	64.5	0.0	0.2
Canola	1.3	67.8	0.0	20.5	0.1	10.3

2.4.2 LAB-SCALE EXPERIMENTAL APPARATUS FOR HYDROGENATION TEST

Figure 2.5 and Figure 2.6 illustrate the lab-scale plant.

The batch slurry reactor was a Parr Instruments 4560 model unit of 600 mL equipped with a mechanical mixing shovel (E-1). Tests were carried out in semi-batch conditions, flowing H₂ continuously in the reactor. The gas flow rate is regulated with mass flow control (MFC-1, MFC-2 Bronkhorst®), and the pressure system is controlled by a back-pressure regulator (Bronkhorst®) at the exit of the reactor. The reactor was charged with 200 ml of oil and the selected percentage of catalyst; then, the whole system is purged from the air with N₂ and heated and pressurized at the required conditions. The reactor was filled with hydrogen and maintained under quite isothermal conditions during the test run. Samples (1 ml) were periodically (15 or 30 min) collected from the sampling valve (V-4) after the purge of residues, then centrifuged to remove the catalyst and collected in a vial in order to perform the subsequent analysis steps.

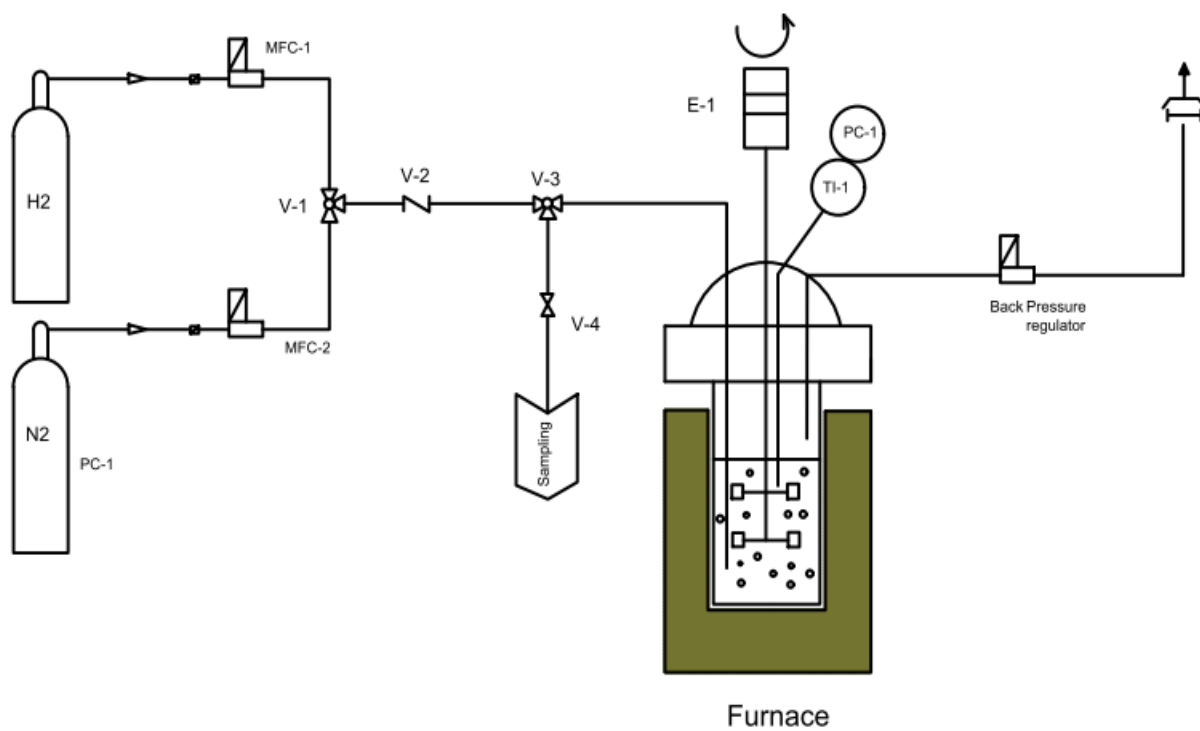


Figure 2.5 Lab-scale plant reactor for hydrogenation of vegetable oils and their derivatives.



Figure 2.6 Photo of the laboratory scale setup.

The catalytic partial hydrogenation tests were carried out with Lindlar as reference catalyst, Pd/HT, and Pd/FAC catalysts under different operative conditions reported in Table 2.3, Table 2.4, and Table 2.5, respectively.

Table 2.3 Reaction conditions of selective hydrogenation with Lindlar catalyst.

Entry	Oil	Catalyst [mg/mL _{oil}]	T [°C]	P [bar]	t [h]	Sampling [min]
Test 01	canola	4	60	4	6	30
Test 02		4	60	12	6	30
Test 03		4	120	8	6	30
Test 04		4	180	4	6	30
Test 05		4	180	12	6	30
Test 06		2	180	4	2	15
Test 07		1	180	4	2	15
Test 08		4	180	4	1	15
Test 09		4	180	4	1	15
Test 10		4	180	4	1	15
Test 11		4	180	4	1	15
Test 12		4	180	4	1	15
Test 13	sunflower	4	180	4	6	30

Table 2.4 Reaction conditions of selective hydrogenation with Pd-HT catalyst.

Entry	oil	Catalyst [mg/mL _{oil}]	T [°C]	P [bar]	t [h]	Sampling [min]	Cyclic number
Test 14	sunflower	0.5	60	4	4	15	I
Test 15		0.5	90	8	4	15	I
Test 16		0.5	120	4	6	30	I
Test 17		0.5	120	4	2	15	II
Test 18		0.5	120	12	6	30	I

Test 19		0.5	120	12	2	15	II
Test 20		2	120	4	6	30	I
Test 21		2	120	4	2	15	II
Test 22		1	120	4	6	30	I
Test 23		1	120	4	2	30	II
Test 24		1	120	4	2	15	III
Test 25		1	180	4	6	30	I
Test 26		1	180	4	2	15	II
Test 27		1	180	4	2	15	III
Test 28		1	180	4	2	15	IV

Table 2.5 Reaction conditions of selective hydrogenation with Pd/FAC catalyst.

Entry	oil	Catalyst [mg/mLoil]	T [°C]	P [bar]	t [h]	Sampling [min]
Test 29	sunflower	1	180	4	6	30
Test 30		1	120	8	6	30
Test 31		1	240	8	6	30

2.4.3 REACTIVITY AND SELECTIVITY

Iodine Value (IV) was calculated in accordance with ISO 3961:2018 [165] from GC results; it is used to determine the amount of unsaturation in fatty acids.

$$IV = (x_{C16:1} \cdot 0.950) + (x_{C18:1} \cdot 0.860) + (x_{C18:2} \cdot 1.732) + (x_{C18:3} \cdot 2.616) + (x_{C20:1} \cdot 0.785) + (x_{C22:1} \cdot 0.723) \quad \text{Equation 2.14}$$

Reactivity performances were evaluated in terms of linolenic conversion Equation 2.15 and linoleic conversion Equation 2.16.

$$\cdot\chi_{C18:3} = \frac{(C18:3)_0 - (C18:3)_t}{(C18:3)_0} * 100 \quad \text{Equation 2.15}$$

where $(C18:3)_0$ and $(C18:3)_t$ are the relative percentage of linolenic acid at the initial time ($t = 0$) and at given time t .

$$\chi_{C18:2} = \frac{\sum_j(C18:2)_0 - \sum_j(C18:2)_t}{\sum_j(C18:2)_0} * 100 \quad \text{Equation 2.16}$$

where $\sum_j(C18:2)_0$ and $\sum_j(C18:2)_t$ are the relative percentage of linoleic acid and his isomers at the initial time ($t = 0$) and at given time t .

The selectivity is the total amount of desired product formed per total amount of limiting reactant consumed, and the saturation hydrogenation reaction, in the presence of excess hydrogen, from linolenic acid to stearic acid, which is consequential, can be described as irreversible and in order to evaluate the selectivity towards various acids a simple pseudo-first-order scheme of series reactions, omitting isomerization of double bonds and the diffusivity limitation (the maximum rpm set point of the mixer is adopted in each test), was taken into account Equation 2.17, [167][168]:



The scheme reported can be used because tests were conducted under mild pressure and temperature conditions as found in the previous work [169]. When higher pressures were imposed, direct hydrogenation of C18:2 to C18:0 and C18:3 to C18:1 should be taken into account as reported in the literature [170][171].

This system can be described by a series of first-order differential equations:

$$\frac{d(C18:3)}{dt} = -k_3 \cdot (C18:3) \quad \text{Equation 2.18}$$

$$\frac{d(C18:2)}{dt} = k_3 \cdot (C18:3) - k_2 \cdot (C18:2) \quad \text{Equation 2.19}$$

$$\frac{d(C18:1)}{dt} = k_2 \cdot (C18:2) - k_1 \cdot (C18:1) \quad \text{Equation 2.20}$$

According to the literature [170][171][172], the selectivity of linolenic acid (S_{Ln}) Equation 2.21 and of linoleic acid (S_{Le}) Equation 2.22 and selectivity towards geometric isomers of C18:1 expressed by the specific isomers index (SII) Equation 2.23 were defined as:

$$S_{Ln} = k_3/k_2 \quad \text{Equation 2.21}$$

$$S_{Le} = k_2/k_1 \quad \text{Equation 2.22}$$

$$SII = \frac{(trans)_t - (trans)_0}{IV_0 - IV_t} \quad \text{Equation 2.23}$$

Where IV_0 and IV_t are the iodine value at the initial time ($t = 0$) and at the given time t . In this doctoral thesis, we employed Maple2019 software for the integration of the differential equation system, and the set of differential equations was analytically solved by software Excel Microsoft Office (see Addendum B).

2.5 EXPERIMENTAL STUDY ON THE PRODUCTION OF GREEN DIESEL BY HYDROPROCESSING REACTIONS

2.5.1 VEGETABLE OIL SELECTION FOR DEOXYGENATION TESTS

Recently, the biofuel industry, like biodiesel and green diesel, is very important not only for human utilities but also for the environment and climate protection[173]. Biomass like vegetable oils, wood, grasses, and algae is a widely available resource that can be characterized by its high production potential enabling the production of different types of biofuels. Besides, there is extensive knowledge of the biofuel production process, and technologies enabling the production of biofuels with high caloric value and better physicochemical properties are developed [174].

Our choice of sunflower vegetable oil for catalytic hydrothermal deoxygenation tests because particularly rich in polyunsaturated oleic fatty acids, and it is available commercially economically. Gas chromatographic composition analysis of sunflower oil used in this work is observed in Table 2.6.

Table 2.6 composition of sunflower oils as received sample

Vegetable oil	C18:0%	C18:1%	C18:2%	C18:3%
Sunflower	3.39	41.27	55.11	0.22

2.5.2 LAB-SCALE EXPERIMENTAL APPARATUS FOR HYDROGENATION TEST

The lab-scale plant is illustrated in Figure 2.7 and Figure 2.8. The catalytic hydro-processing (hydro-deoxygenation, decarbonylation, decarboxylation) tests were carried out, and stearic acid is a standard point of the reaction because it is no need for the hydrogenation step because it is already free fatty acids.

The batch slurry reactor used was a Parr microreactor 4598 model unit of 100 with Parr magnetic drives and a 4848-reactor controller; the pressure and temperature operability limit values are 138 bars and 350 °C, respectively. Tests were carried out in semi-batch conditions, under H₂ pressurized atmosphere, controlled by (pc-1) pressure controller, and measured by a digital manometer installed at the existence of the reactor. The reactor was charged with reactants (triglycerides (stearic acid or sunflower oil), solvent, internal standard (C25 or C20), and catalyst) placed in a liner; then, the system is purged from the air with N₂, heated and pressurized at the required conditions. The reactor was filled with hydrogen and maintained under quite isothermal conditions during the test run. Liquid samples (1 ml) were collected every two or three hours of the reaction from the sampling valve (V-2) after the purge of residues, filtered from the catalyst, diluted in hexane solvent, and then analyzed with gas chromatographic techniques once the reaction mixture is recovered at the end of every test, a vacuum filtration was carried out to recover the catalyst, while the rest mixture was also evaporated by rotary evaporator, trans-esterified, and then analyzed with GC-MS and GC-FID.

The catalyst also is recovered and washed with hexane and chloroform solvents and filtered under vacuum backed system.

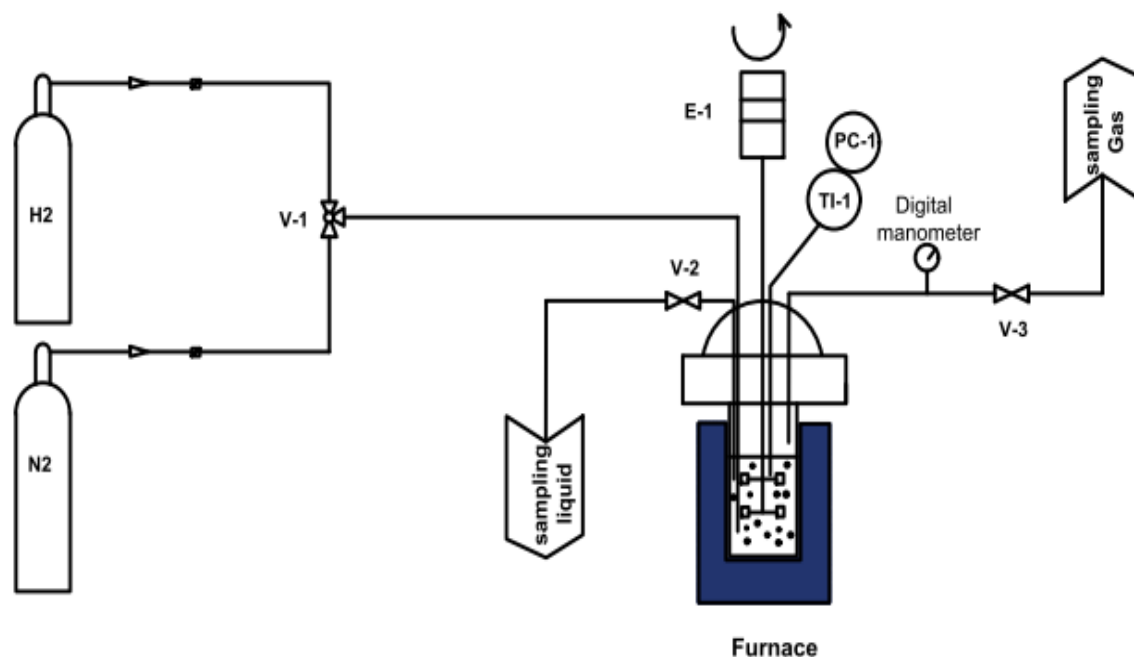


Figure 2.7 Lab-scale plant reactor for hydro processing of vegetable oils and their derivatives.



Figure 2.8 Photo of the laboratory scale setup.

The sunflower oil is used with Lindlar as a commercial catalyst, NiMo/FAC, NiMo/zeolite X, Pd/FAC, and CoMo/FAC catalysts under different operative conditions Table 2.7.

Table 2.7 Reaction conditions of catalytic Deoxygenation tests with Sunflower oil and Stearic acid.

Entry	catalyst	(Cat/TG) wt %	T [°C]	P [bar]	t [h]	Three Glyceride TG	solvent	Internal standard
Test 01	Lindlar	10	300	20N ₂	6	Stearic acid	20	C20
Test 02	Lindlar	10	300	40H ₂	8	Sunflower oil	20	C25
Test 03	Pd/FAC	10	300	20N ₂	7	Stearic acid	20	C25
Test 04	Pd/FAC	10	320	20H ₂	7	Sunflower oil	20	C20
Test 05	Pd/FAC	10	320	40H ₂	7	Sunflower oil	20	C20
Test 06	CoMo/FAC	10	320	40H ₂	8	Sunflower oil	20	C25
Test 07	NiMo/FAC	2.5	320	40H ₂	6	Sunflower oil	0	C25
Test 08	NiMo/FAC	10	320	40H ₂	6	Sunflower oil	20	C25
Test 09	NiMo/zeolite X	10	280	40H ₂	6	Sunflower oil	20	C25
Test 10	NiMo/zeolite X	2.5	320	40H ₂	7	Sunflower oil	12	C25
Test 11	NiMo/zeolite X	10	320	40H ₂	6	Sunflower oil	20	C25

2.5.3 REACTIVITY AND SELECTIVITY

In order to have qualitative information on the conversion of the reaction, the reaction mixture, recovered at the end of the process, is trans-esterified and analyzed with GC-FID or GC-MS. The trans-esterification reaction is necessary to assess the presence of triglycerides and/or residual fatty acids at the end of the reaction and, therefore, verify if all the oil used has been converted into alkanes and/or other compounds (reaction intermediates, unsaturated compounds, aromatics, compounds resulting from unwanted reactions).

To estimate the green diesel yield in the product, it could be calculated by Equation 2.24.

$$Y_{GD} = \sum_{n=15}^{n=18} \frac{(m_n)_{rt}}{(m_{TG})_0} \quad \text{Equation 2.24}$$

$$(m_n) = \frac{c_n}{100} \times (m)_{rt} \quad \text{Equation 2.25}$$

Where: Y_{GD} is the green diesel range, (m_n) the mass of the final alkane product at the end of the reaction (recovery time, rt), $(m_{TG})_0$ the mass of the initial triglycerides ($t=0$), C_n the relative percentage of the alkane, $(m)_{rt}$: the final recovered mass at the end of the reaction (recovery time, t).

On the other hand, it is very worthy of knowing the conversion of initial tri glycerides (sunflower oil and stearic acid) to other products (hydrocarbons and esters) by Equation 2.26 :

$$X_{TG} = \frac{(m)_t}{(m_{TG})_0} \times 100 \quad \text{Equation 2.26}$$

Where X_{TG} is the conversion of triglycerides (TG), $(m)_t$ is the mass of the final product at the end of the reaction (rt), $(m_{TG})_0$ is the initial mass of TG at ($t=0$).

Also, it is very important to calculate the conversion of triglycerides in hydrocarbons, Equation 2.27 [175][176]:

$$X_n = \left(1 - \frac{(m_{TG})_t}{(m_{TG})_0}\right) \quad \text{Equation 2.27}$$

Where X_n is the conversion in hydrocarbons, $(m_{TG})_t$ is the final mass of TG (FAME e Oxygenates) at the end of the reaction (t), $(m_{TG})_0$ is the initial mass of TG at ($t=0$).

To evaluate the selectivity towards hydrodeoxygenation HDO or decarboxylation DCO_2 /decarbonylation DCO pathway, it can be done by the gas phase analysis (CH_4 , CO_2 , CO) or by the selectivity index, if both $SI > 1$ Equation 2.28 and Equation 2.29 the selectivity is towards DCO/CO_2 and if both $SI < 1$ then it is towards HDO [177].

$$SI_{17/18} = \frac{C_{17}}{C_{18}} \quad \text{Equation 2.28}$$

$$SI_{15/16} = \frac{C_{15}}{C_{16}} \quad \text{Equation 2.29}$$

Where SI is the selectivity index, C18 and C16 are the relative percentage of the alkanes with 18 and 16 carbon's atom numbers respectively, in which come from the HDO reaction pathway, C17 and C15 are the relative percentage of the alkanes with 17 and 15 carbon's atom numbers respectively, in which come from the DCO₂/DCO reaction pathway.

CHAPTER 3

This chapter reports the characterization results for each catalyst used and synthesized during the thesis.

- *Lindlar catalyst characterization;*
- *Pd/HT characterization;*
- *NiMo/zeolite X characterization;*
- *Cenospheres supported catalysts' characterization;*

3 CATALYSTS CHARACTERIZATION

The catalysts were characterized according to the methods described above (chapter 2) to evaluate the elementary composition (ICP-AES), the reducibility of metal oxides (TPR), the metal dispersion (H₂-chemisorption), the thermal properties (TGA), the external properties (BET-BJH), the presence of crystalline phases and their crystallites size (XRD), the morphology (SEM-EDS), and the acidic properties (TPD-NH₃), whereas the main information obtained from the characterization is illustrated in the following chapter:

3.1 LINDLAR CATALYST CHARACTERIZATION

Lindlar is a commercial catalyst, so just some essential characterizations, ICP-AES, H₂-Chemisorption, BET-BJH, and XRD were performed:

3.1.1 ELEMENTAL ANALYSIS ICP-AES

Lindlar catalyst ICP-AES elementary results have shown that the actual Pd load is less than the nominal Pd content (Pd ≤ 5%), while the content of calcium and lead is confirmed, Table 3.1.

Table 3.1 Elementary compositions of Lindlar catalyst.

Sample	Pd (%)	Ca (%)	Pb (mg/kg)
Lindlar	2.03±0.07	40±1	0.37±0.03

3.1.2 LINDLAR H₂-CHEMISORPTION

The palladium – hydrogen interaction has been studied by hydrogen chemisorption and TPD of the hydrogen from the Pd surface, Table 3.2 illustrates the active surface area, dispersion, and particle size for the palladium in the commercial Lindlar sample, whereas the Palladium active phase has a high dispersion percentage of 95 % with low particle size 1.17 nm and this is in accordance with the dispersion properties of Palladium, where the amount of hydrogen strongly adsorbed on the Pd surface increase with the metal dispersion[178] [179].

Table 3.2 Metallic Pd surface area, dispersion, and particle size for Lindlar catalyst.

Pd ASA (m ² /g)	Pd dispersion (%)	Pd particle size (nm)
9	95	1.17

3.1.3 BET-BJH ANALYSIS

BET-BJH characterizations and N₂ adsorption curves Figure 3.1 shows mesoporous material (isotherm type IV with hysteresis loop type H3) and low surface area in accordance with the literature [180], pore-volume, and pore size (S_{BET} 4.12±0.09 m²/g, V_{BJH} 7.81±0.05 mm³/g and average pore size 7.21±0.87 nm). Perhaps the specific surface is equal to the surface area of the low porosity calcium carbonate substrate.

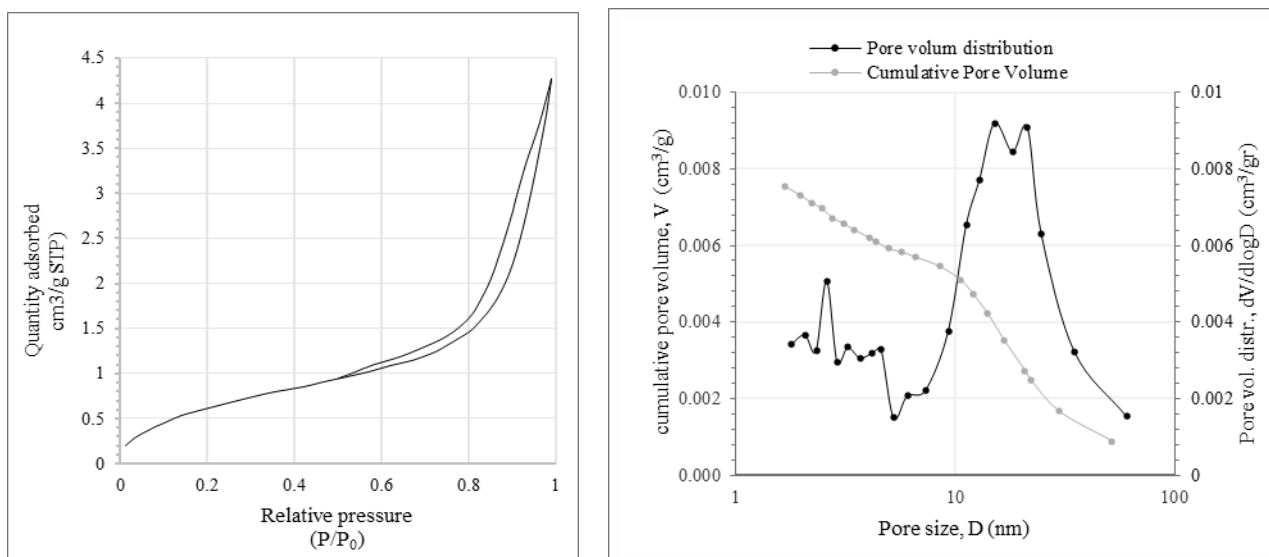


Figure 3.1 BET Isotherms (left) BJH desorption pore size distribution (right) of Lindlar.

It is worth to note from the cumulative pores volume and the pores volume distribution Figure 1.1, that the presence of micro (below 2 nm) and macro-porosities (up to 50 nm) is very low, while the majority of the pores are in the mesopores range (2 – 50 nm).

3.1.4 CRYSTALLINE PHASES ANALYSIS XRD

XRD analysis of Lindlar catalyst Figure 3.2 shows only one phase of calcium carbonate in crystalline form (crystallite size around 9 nm calculated from the more intense ray at 29.4°) associated with metallic palladium. In particular, the first ray of Pd at 39.8° may have been covered with the deformation of the CaCO₃ ray at 40°. The secondary rays of Pd at 46° and 79° are partially covered or are not found. Moreover, XRD spectra did not permit to detect of any trace of PdO since the principal rays of this phase (at 34°, 54.9°, and 71.2°) are not present.

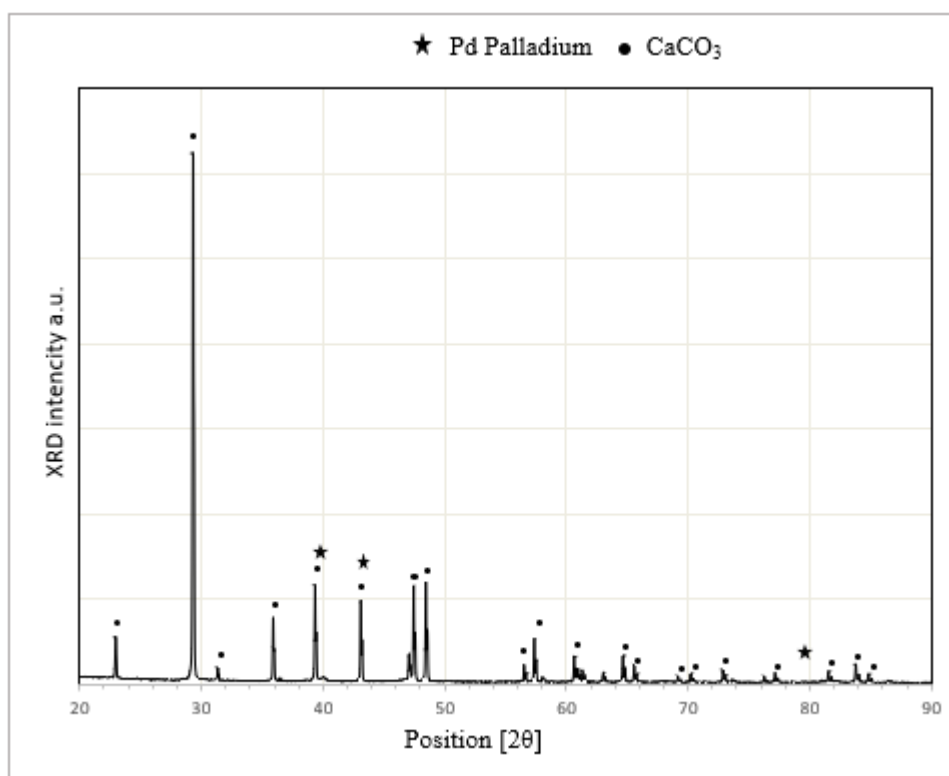


Figure 3.2 XRD spectra of Lindlar catalyst with CaCO_3 principal rays reported.

3.2 Pd/HT CATALYST CHARACTERIZATION

Here all the information acquired about the synthesized Pd/HT catalyst, elementary composition, metal dispersion, surface area, crystalline phase, and morphology is reported:

3.2.1 Pd/HT ELEMENTAL ANALYSIS

The first overview of synthesis comes from the elemental quantification of catalyst from ICP-AES. The experimental ICP-AES values are agreed with the nominal compositions, although Pd load has a slightly higher value than the expected one, which may explain by experimental variability in the synthesis as seen in Table 3.3.

Table 3.3 ICP-AES analyses of Pd/HT catalyst

Sample	Pd (%)	Al (%)	Mg (%)
Pd/HT	1.18 ± 0.06	14.4 ± 0.4	24.7 ± 0.6

3.2.2 Pd/HT, H₂-CHEMISORPTION

Also, with the Pd/HT the H₂-chemisorption results illustrate a good dispersion percentage of 79%, less than the Pd Lindlar case due to the lower palladium load in the Pd/HT (1 %), 1.41nm palladium particle size, and 4 m²/g Palladium active surface area Table 3.4.

Table 3.4 Metallic Pd surface area, dispersion, and particle size for Pd/HT catalyst.

Pd ASA (m ² /g)	Pd dispersion (%)	Pd particle size (nm)
4	79	1.41

3.2.3 Pd/HT, BET-BJH ANALYSIS

N₂ adsorption curves, followed by capillary condensation, which indicates the formation of aggregates of plate like-particles forming slit-like[181] shows in Figure 3.3, permit the investigation of mesoporous material (isotherm type IV with hysteresis loop type H3). These curves allow evaluating a S_{BET} 50.7±0.5 m²/g, which is in line with the average surface area obtained for other 2:1 Mg-hydrotalcite [182][183], V_{BJH} 0.25±0.01 cm³/g, and an average pore diameter 20.02±0.33 nm., this about the high specific surface area can be attributed to the relatively large pore volume of the mesopores in this sample [184].

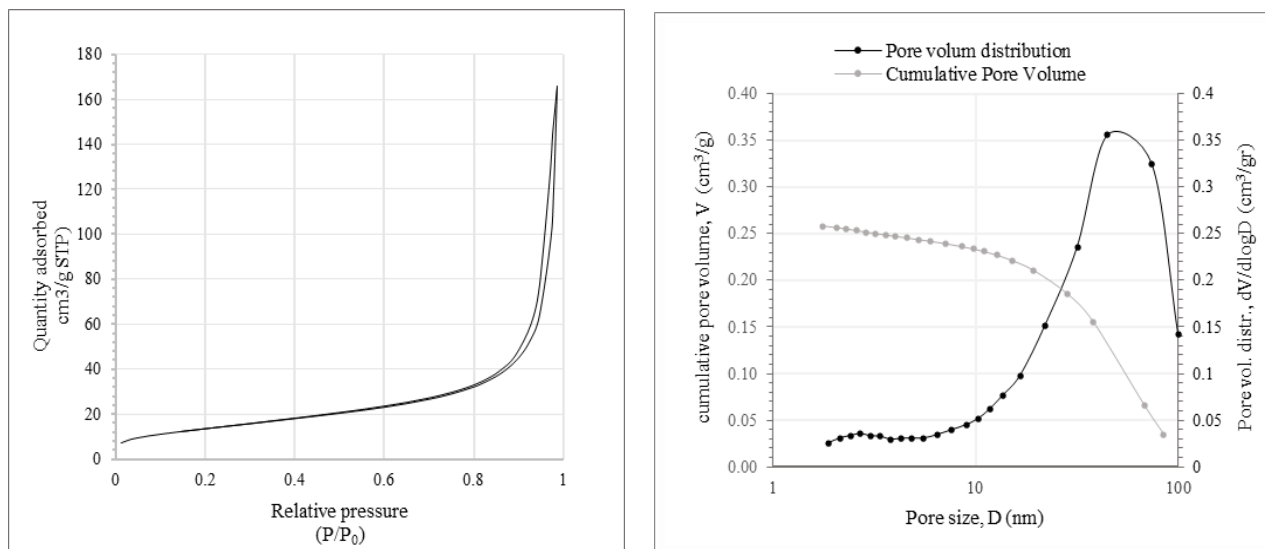


Figure 3.3 BET Isotherms (left) BJH desorption pore size distribution (right) of Pd/HT catalyst.

From the cumulative pores volume and the pores volume distribution Figure 3.3, it is possible to infer the presence of micropores range (below 2 nm) is very low, while the majority of the pores are in the mesopores (2-50 nm) and macro (up to 50 nm) porosity range.

3.2.4 Pd/HT XRD ANALYSIS

X-ray diffraction analysis has been performed in order to determine the presence of palladium and hydrotalcite in which characterized by both Al/Mg in a molar ration 2:1 with some carbonate's groups present inside the structure, besides, to evaluate a quantitative composition of crystalline phases. XRD analysis on Pd/HT Figure 3.4 exhibits that the sample is completely crystallized, and the only phase is hydrotalcite. The presence of metallic palladium could not be determined due to its low percentage of 1.18 %, and they may overlap with the much more intense rays of hydrotalcite support, but it could be glimpsed by the enlargement and shift of the two rays of the hydrotalcite at 40° and 46°. Furthermore, the calculation of the Scherrer equation (indicated in chapter 2), for all the isolated hydrotalcite crystals size (11.6°, 23.4°, 60.7°, and 62.1°), gives an average value of crystallite size between 18 nm and 25 nm.

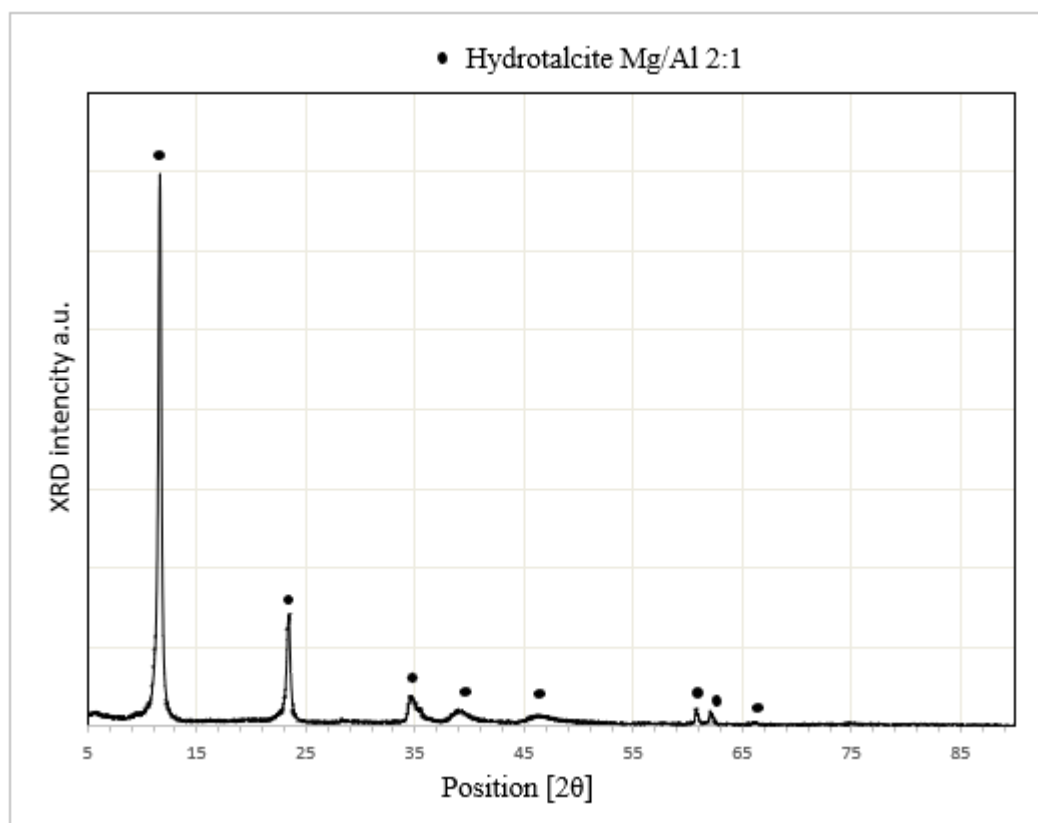


Figure 3.4 XRD spectra of Pd/HT catalyst with hydrotalcite phase.

3.2.5 Pd/HT SEM AND EDS ANALYSIS

SEM micrographs, coupled with EDS elemental analyses, allow getting a deeper insight into the morphology and elemental topography of synthesized catalysts materials.

Figure 3.5 demonstrates that; the structure of the Pd/HT catalyst is heterogeneous and is made from some particles linked with other bigger, smoother, and homogenous particles.

Moreover, since the image was produced with BSE electron, some points are brighter than others highlighting a higher amount of heavier elements. However, both surfaces contain the same elements (Mg and Al), in similar relative amounts, and Pd.

EDS analysis on two different points from the same sample Figure 3.6 detects the similar relative amounts of the Mg and Al elements; the Pd seems well dispersed on the

surface because the same amount of Pd is detected in different points on the surface of the catalyst (point 1 and 2, for example), which in accordance with the H₂-Chemisorption results (79 % metal dispersion).

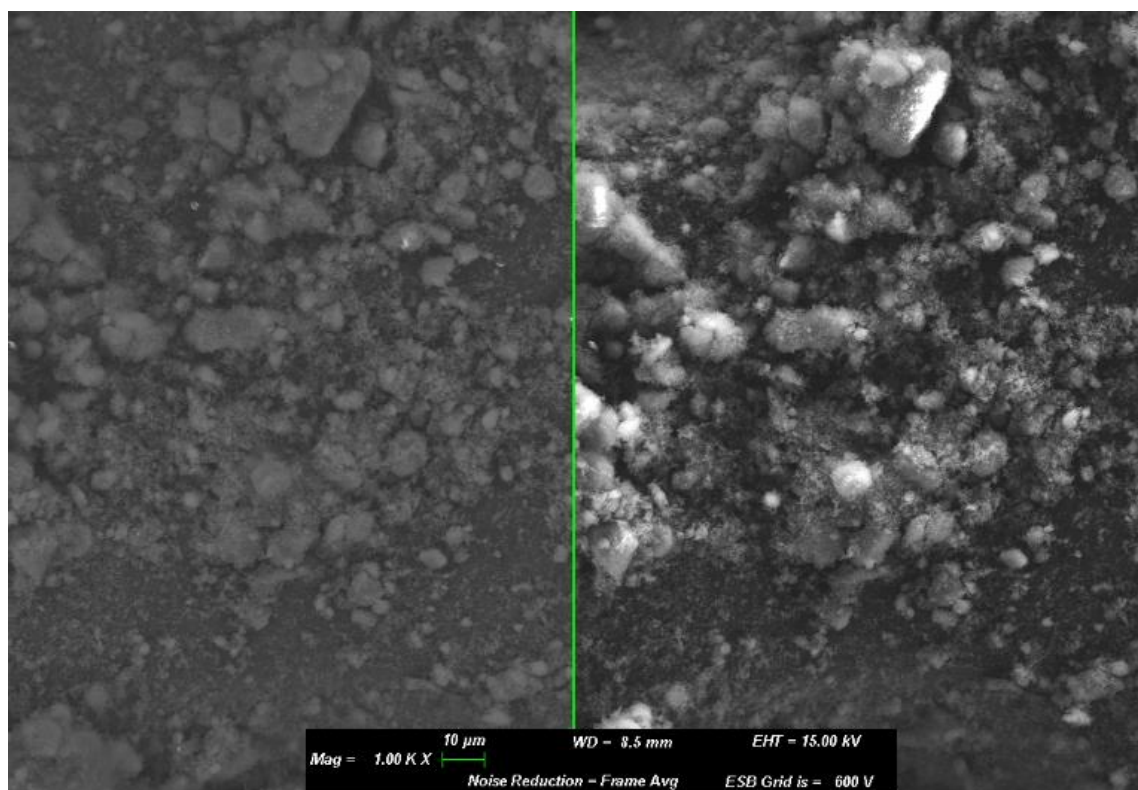


Figure 3.5 Pd/HT SEM image analysis.

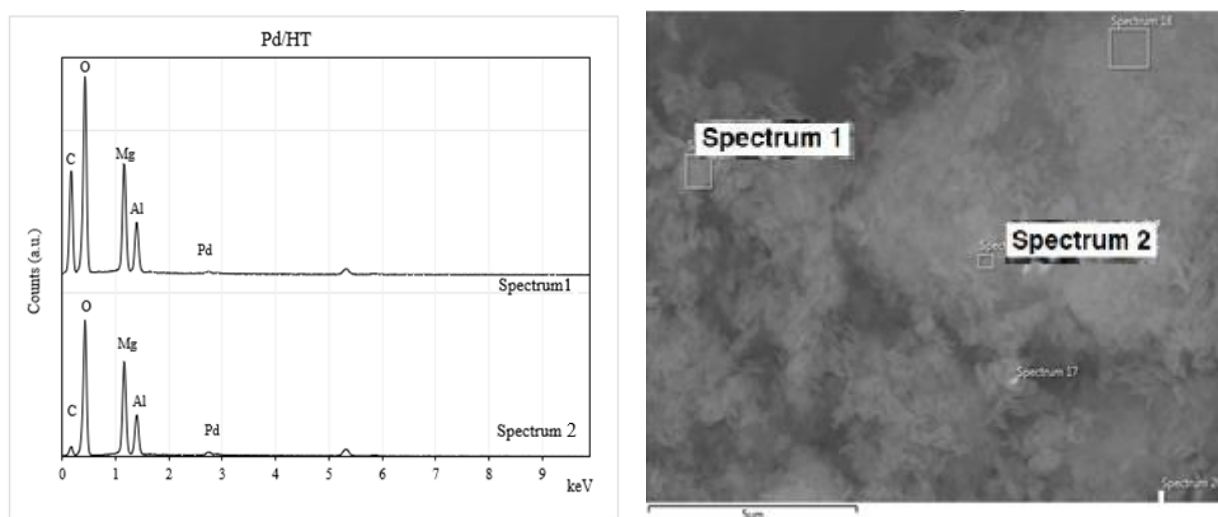


Figure 3.6 Pd/HT analysis, SEM image (on the right), and relative EDS analysis (on the left).

3.3 Pd/FAC CATALYST CHARACTERIZATION

In this part, Pd/FAC catalyst characterization information; elementary composition ICP-AES, reducibility TPR, metal dispersion measurement H₂-Chemisorption, thermogravimetric analysis TGA, surface area BET measurement, crystalline phase analysis XRD, and morphology SEM-EDS analysis is reported.

3.3.1 Pd/FAC ELEMENTAL ANALYSIS

The catalyst firstly has been characterized by ICP-AES. Table 3.5 demonstrates that the overview about syntheses experimental ICP-AES values agreed with the nominal compositions for palladium (2 %), The Al and Si are comparable with previous research [185][186] and in accordance with the ICP – AES analysis results of the FAC support ($13.4 \pm 0.3\%$) and ($22 \pm 1\%$) respectively.

Table 3.5 ICP-AES analyses of FAC and Pd/FAC catalyst.

Catalyst	Pd (%)	Si (%)	Al (%)
Pd/FAC	1.89 ± 0.07	20.7 ± 0.8	12.8 ± 0.4
FAC	0	22 ± 1	13.7 ± 0.3

3.3.2 Pd/FAC TPR TEMPERATURE PROGRAMMED REDUCTION

ANALYSIS AND H₂-CHEMISORPTION

Using the same support FAC with the palladium as an active metal, the H₂-TPR curves profile Figure 3.7 shows only one principal peak. Indeed, two distinct peaks, i.e., consumption of hydrogen for PdO reduction and subsequent desorption of hydrogen from bulk palladium hydride, can be observed. The first peak is at 92 °C, and the second one is at about 600 °C; these results are in accordance with the literature [179][187]. In fact, reduced Pd is highly

sensitive to atmospheric oxygen, and during handling and storing of the samples, a superficial Pd oxide layer can be formed.

Table 3.6 Pd species reduction temperature, metallic active surface area, dispersion, and particle size for Pd/FAC catalyst.

Pd T _{red} (°C)	Pd surface (m ² /g)	Pd dispersion (%)	Pd particle size (nm)
92.03	7	88	1.26

On the other hand, Table 3.6 illustrates that palladium has very good characterization properties, dispersion percentage 88%, active surface area 7 m²/g, and particle size 1.33 nm, which is in line with results obtained by W. Zhao et.al. with his Pd/C catalyst [179].

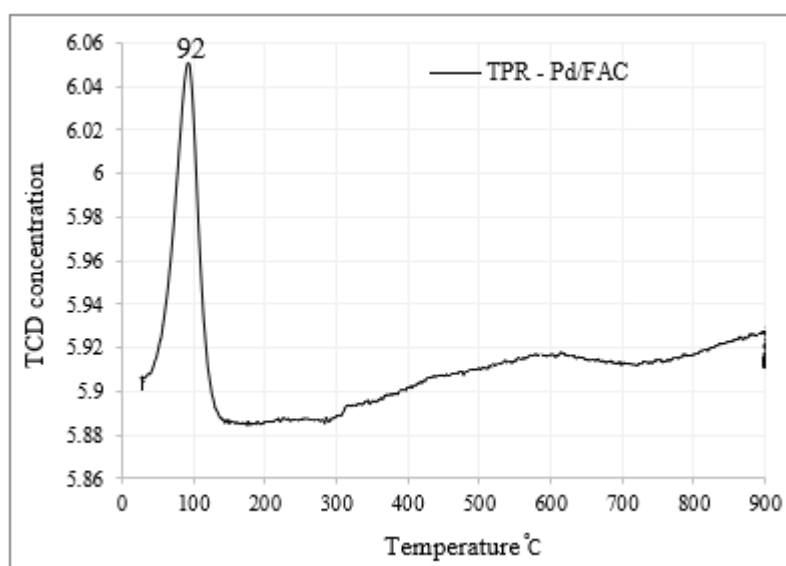


Figure 3.7 Pd/FAC temperature programmed reduction

3.3.3 Pd/FAC TGA ANALYSIS

The thermogravimetric analysis TGA of non-calcined Pd/FAC catalyst, 10 °C/min till 800 °C, has been done in order to understand the thermal properties of the material and to know at which temperature it can be oxidized and /or decomposed. Figure 3.8 illustrates that the catalyst at about 130 °C lost 0.3% as H₂O where the sample powder may possibly contain some

unbound humidity, while, at about 630 °C it is decomposed and lost about 5% of the weight, and this is in line with the TPR results where the second peak was at 600 °C, so the calcination and reduction processes could be done at 600 °C.

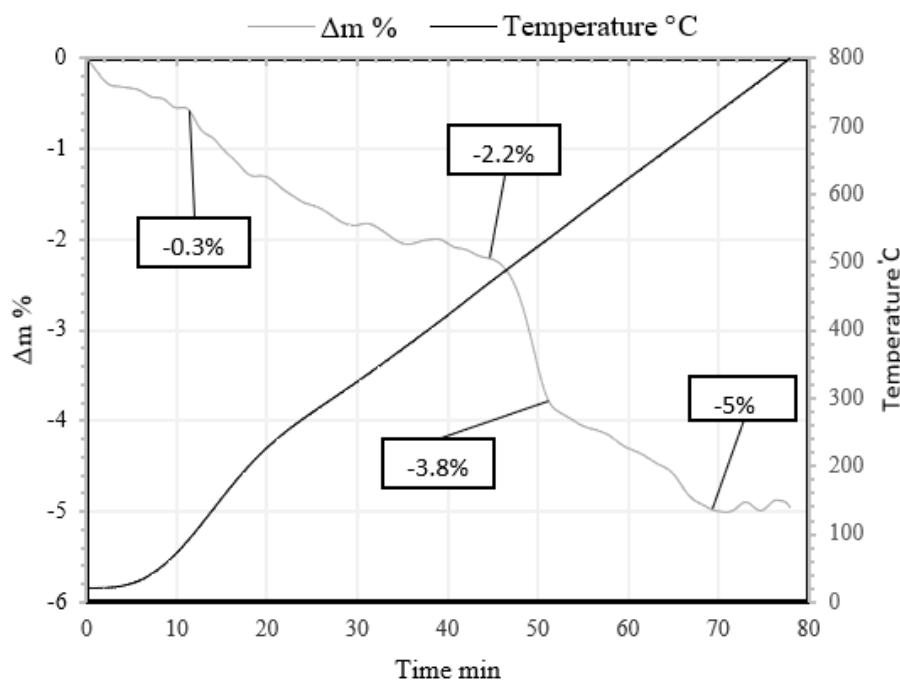


Figure 3.8 Thermogravimetric analysis (TGA) of Pd/FAC.

3.3.4 Pd/FAC, BET-BJH ANALYSIS

BET-BJH characterization in which has done for the FAC support, non-calcined and reduced (up to 600 °C) Pd/FAC catalyst respectively, ($S_{\text{BET}} 0.58 \pm 0.1 \text{ m}^2/\text{g}$, $V_{\text{BJH}} 0.002 \pm 0.001 \text{ cm}^3/\text{g}$, and an average pore diameter $6.87 \pm 0.02 \text{ nm}$), ($S_{\text{BET}} 0.26 \pm 0.03 \text{ m}^2/\text{g}$, $V_{\text{BJH}} 0.002 \pm 0.001 \text{ cm}^3/\text{g}$, and an average pore diameter $14.49 \pm 0.01 \text{ nm}$), and ($S_{\text{BET}} 5.521 \pm 0.01 \text{ m}^2/\text{g}$, $V_{\text{BJH}} 0.02 \pm 0.01 \text{ cm}^3/\text{g}$, and an average pore diameter $7.96 \pm 0.02 \text{ nm}$), which illustrates an increase in surface area, pore-volume, and pore size after the impregnation of palladium oxide respect to the FAC support, and this is due to the effective high temperature (600 °C) of the calcination and reduction processes.

Figure 3.9 observes that Pd/FAC is a mesoporous material (isotherm type IV with hysteresis loop type H3), cumulative pores volume, and the pores volume distribution profile illustrates the presence of the mesopores range (2 – 50 nm) with a majority.

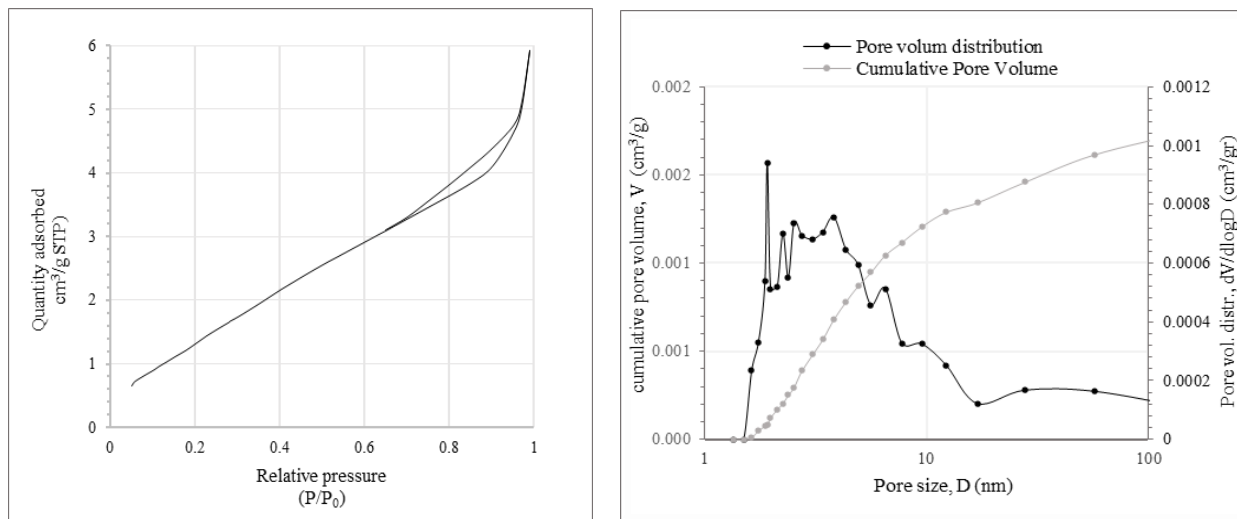


Figure 3.9 BET Isotherms (left) BJH desorption pore diameter size distribution (right) of Pd/FAC catalyst

3.3.5 Pd/FAC XRD ANALYSIS

The X-ray diffraction analysis on FAC support, non-calcined, and reduced Pd/FAC catalysts, respectively Figure 3.10 confirms the occurrence of PdO reduction to metallic Pd, which could be determined in a little amount at 42° and 48° , after the impregnation, formation of a new phase (sodium palladium silicate NaPd_3Si_2) was noticed at and then disappeared after the reduction process. The phases here are almost those of FAC, and the structure of the support is not changed after the impregnation process.

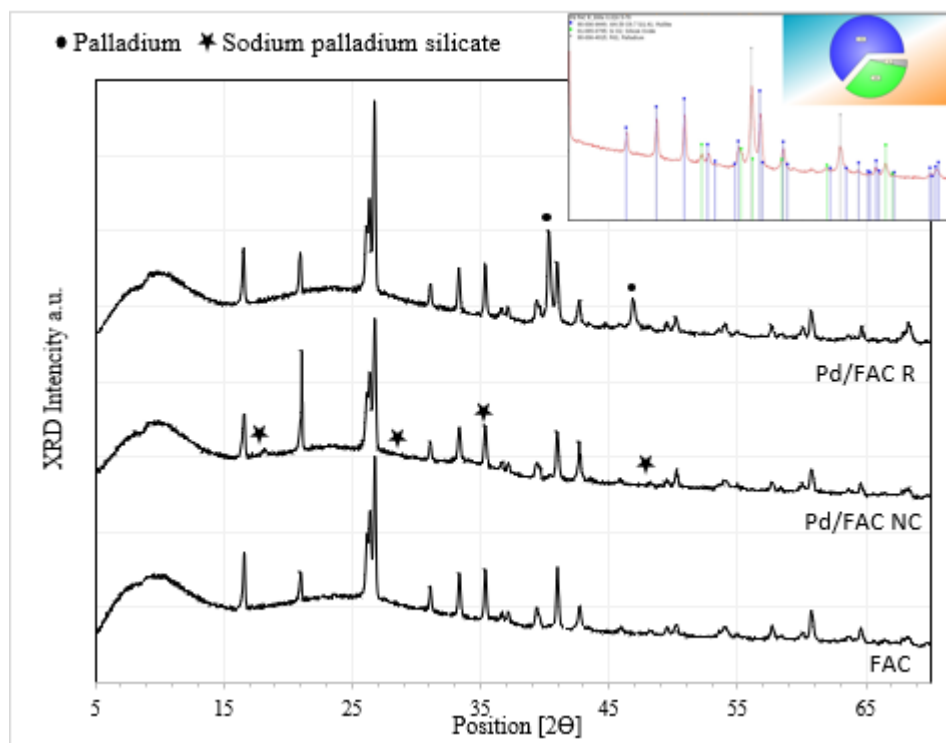


Figure 3.10 X-ray diffraction spectrum of Pd/FAC (up) & FAC (down)

Table 3.7 illustrates the crystallite sizes calculated by Debye-Scherrer formula equation with error ± 5 nm, and there is about no change in crystallite sizes before and after the impregnation process.

Table 3.7 Crystal size of Cenospheres and Pd/FAC (NC, R).

Sample	Phases	Formula	crystallite size (nm)
Cenospheres	Mullite	$Al_{4.59}O_{9.7}Si_{1.41}$	44
	silicon oxide	SiO_2	49
Pd/FAC Non-calcined	Mullite	$Al_{4.59}O_{9.7}Si_{1.41}$	42
	silicon oxide	SiO_2	51
	sodium palladium silicate	$NaPd_3Si_2$	22
Pd/FAC Reduced	Mullite	$Al_{4.59}O_{9.7}Si_{1.41}$	43
	silicon oxide	SiO_2	46
	Palladium	Pd	44

The difference of palladium particle size results obtained by the H₂-chemisorption (1.26 nm) and the Scherrer formula (44 nm) may refer to the divergence of the techniques.

3.3.6 Pd/FAC SEM AND EDS ANALYSIS

In order to get more information about the structure, morphology, and elemental topography of raw and synthesized materials, SEM micrographs, coupled with EDS elemental analyses were done; Figure 3.11 clarifies that the support FAC spheres structure is about totally destroyed comparing with the impregnated Pd/FAC. EDS analysis on the same samples (FAC and Pd/FAC) Figure 3.12 detects elemental Pd, Si, Al, Na, O, K, and Fe with different peak intensity ratios in different spots. From

Figure 3.13, it can be noticed a good dispersion of the Pd on the FAC support, which in accordance with the H₂-Chemisorption results with 88% Pd dispersion.

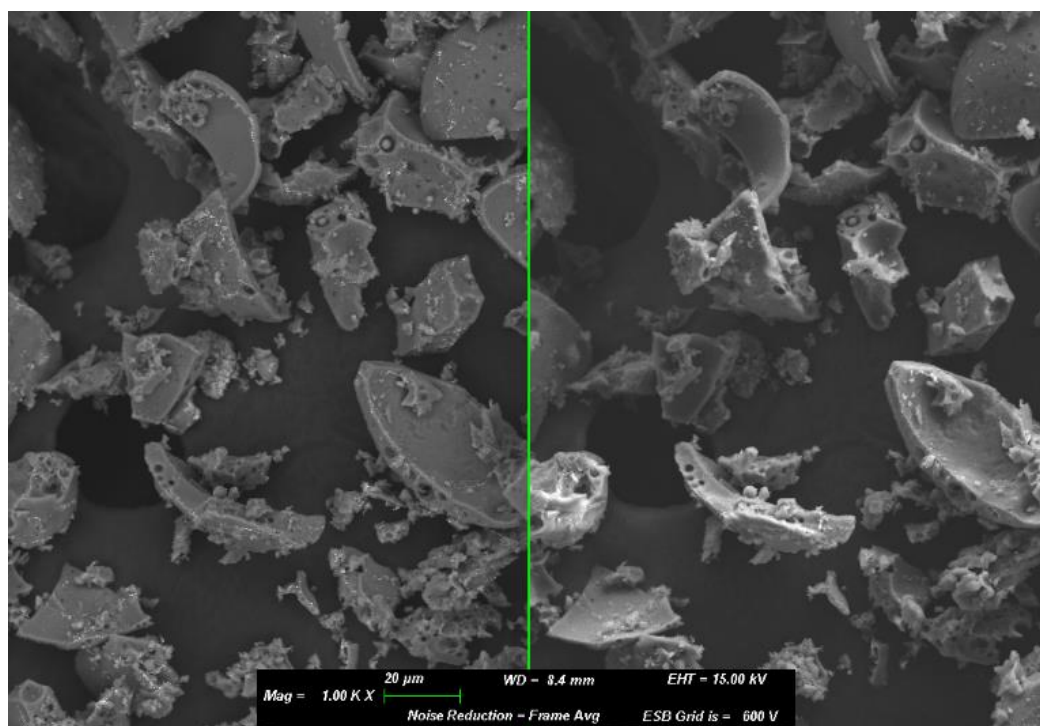


Figure 3.11 Pd/FAC SEM image analysis.

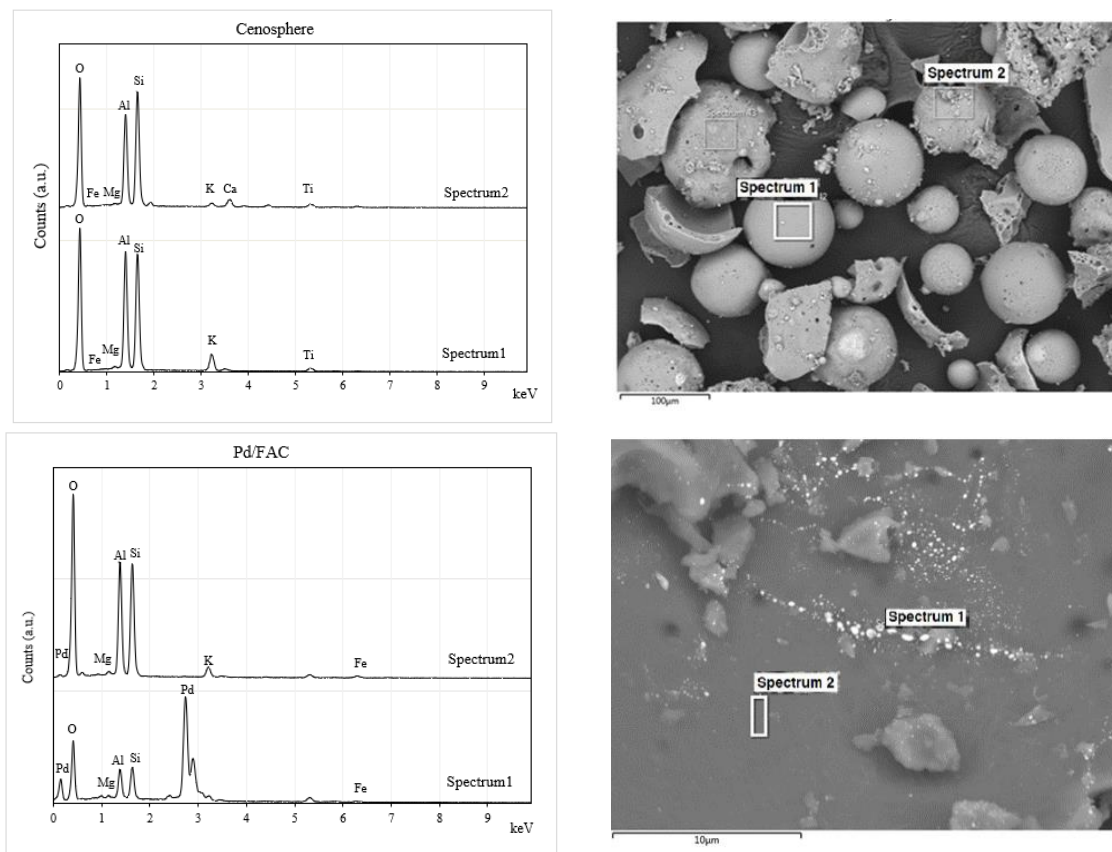


Figure 3.12 Cenosphere and Pd/FAC analysis, SEM image (right) and relative EDS analysis (left)

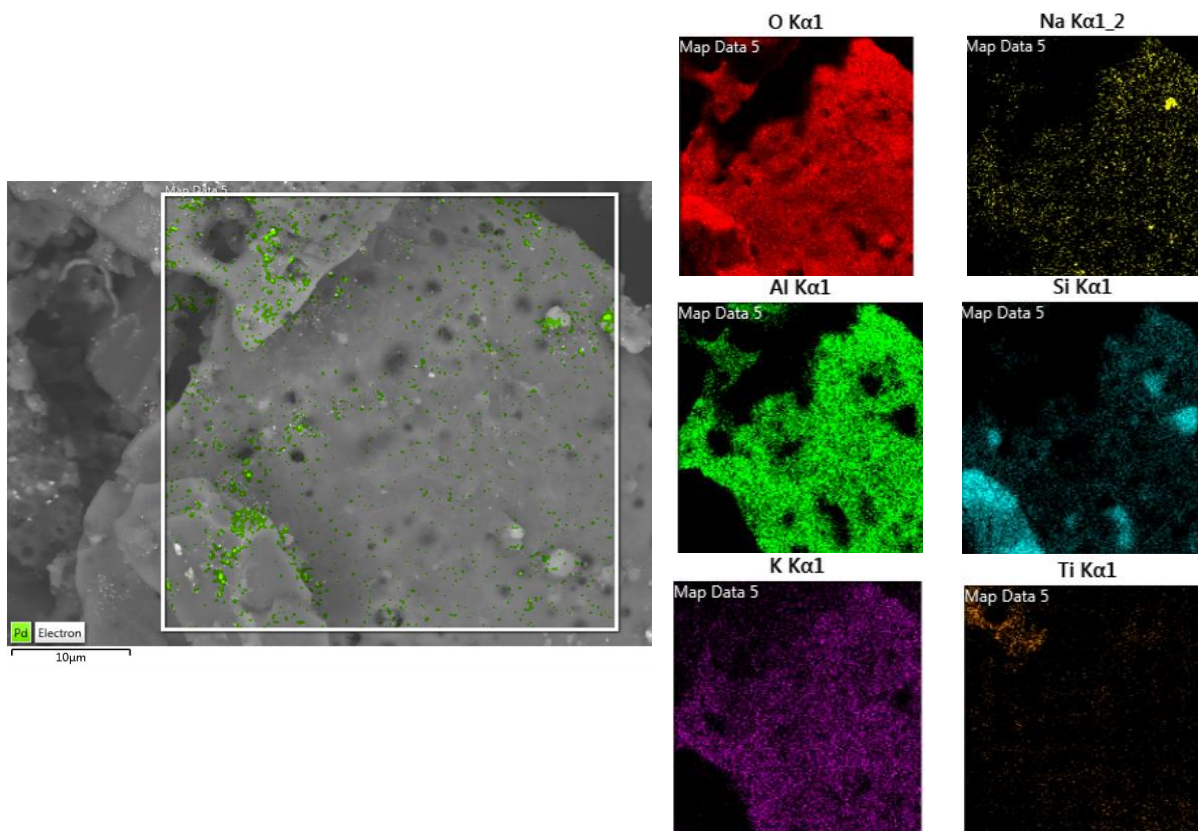


Figure 3.13 Map Scanning electron Microscope (SEM) of Pd/FAC

3.4 CoMo/FAC CATALYST CHARACTERIZATION

Here the information acquired about the CoMo/FAC catalyst, elementary composition ICP/AES, reducibility TPR, metal dispersion H₂-Chemisorption, Thermo- Gravimetric Analysis TGA, surface area BET, crystalline phase XRD, and morphology SEM-EDS is reported.

3.4.1 CoMo/FAC ELEMENTAL ANALYSIS

The catalyst firstly has been characterized by ICP-AES. The overview about syntheses experimental ICP-AES values is more or less agreed with the nominal compositions for cobalt but for molybdenum is less than the nominal one, which may be explained by the preparation procedure analysis of the sample or the synthesis process. The Al and Si are about comparable with the previous research [185][186] and in line with the ICP – AES analysis of the FAC support ($13.4 \pm 0.3\%$) and ($22 \pm 1\%$) respectively, whereas their decreasing can be attributed by the impregnation of new elements to the structure (Co and Mo) as seen in Table 3.8.

Table 3.8 ICP-AES analyses of FAC and CoMo/FAC catalyst.

Catalyst	Co (%)	Mo (%)	Al (%)	Si (%)
CoMo/FAC	3.1 ± 0.1	$12,7 \pm 0.5$	10.6 ± 0.3	15.9 ± 0.5
FAC	0	0	13.7 ± 0.3	22 ± 1

3.4.2 CoMo/FAC TPR TEMPERATURE PROGRAMMED REDUCTION

ANALYSIS AND H₂-CHEMISORPTION

The FAC support interaction effect with other active metal phases, from the profile of the H₂-TPR curve of Figure 3.14, can be dissociated into two peaks; the first peak is assigned to the reduction of CoO into metallic cobalt (It is well-known that the reduction of cobalt oxide takes

place in just one step ($\text{Co}^{2+} \rightarrow \text{Co}^0$) with the consumption of 1 mol of H_2 per mol of Co^{2+} , while at lower temperature 200-400 °C Co_3O_4 can be reduced to CoO [161][188]), and the second one to the first step reduction of Mo^{6+} species and the complete reduction of the CoO , whereas the reduction of MoO_3 is a complex process that needs in total 3 moles of H_2 and it consists of two consecutive steps ($\text{Mo}^{6+} \rightarrow \text{Mo}^{4+}$ and $\text{Mo}^{4+} \rightarrow \text{Mo}^0$) with about 700 °C for the first step and (over 1000 °C) for the second one [189]. TPR with H_2 indicates that the active cobalt phase is strongly bonded to the FAC support because an increase in its reduction temperature (678.2 °C) is observed comparing with CoO reduction temperature 600 °C reported by different authors [190][191], whereas the molybdenum exhibits a reduction peak at about 800 °C and this could be explained by the interaction not only with the FAC support but also with the cobalt metal.

Table 3.9 Co and Mo species reduction temperatures, Co metallic active surface area, dispersion, and particle size for CoMo/FAC catalyst.

Co T_{red} (°C)	Mo T_{red} °C)	Co surface (m^2/g)	Co dispersion (%)	Co particle size (nm)
678.2	796.4	1	5	19.9

The cobalt particle size results obtained by the H_2 -chemisorption (19.9 nm) and the Scherrer formula (28 nm) Table 3.10 are about closed although the divergence of the techniques, which may due to its order of magnitude.

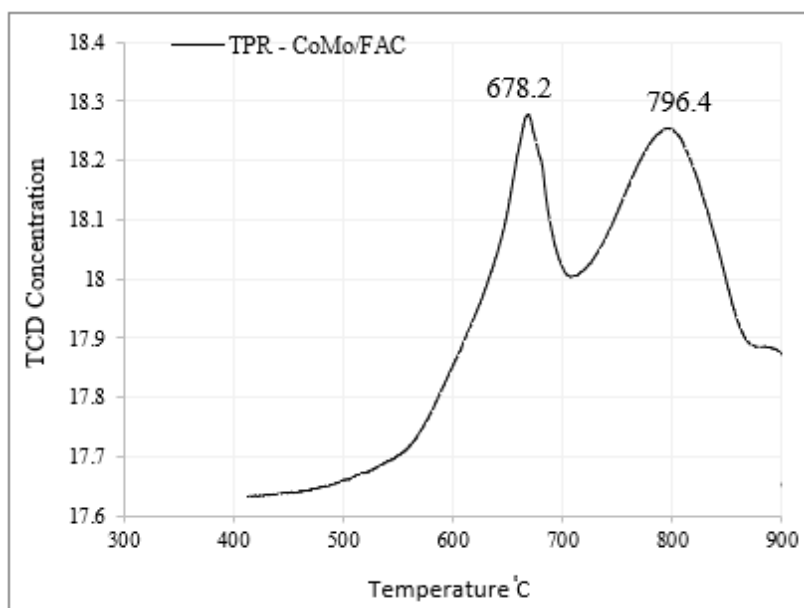


Figure 3.14 CoMo/FAC temperature programmed reduction

3.4.3 CoMo/FAC TGA ANALYSIS

In order to get a deep insight into the thermal properties of the material and having an idea at which temperature it can be oxidized and/or decompose, a thermogravimetric analysis of the non-calcined CoMo/FAC catalyst at 10 °C/min till 800 °C has been done. Figure 3.15 shows that the catalyst at about 150 °C lost 1.8% as H₂O where the sample powder may possibly contain some unbound humidity, while, approximately at about 790 °C the weight loss undergone by the sample is about 10%, and this is in accordance with the TPR results where the second peak was at 796.4 °C, so the calcination and reduction processes could be done at 600 °C as we were interested in the Co active phase.

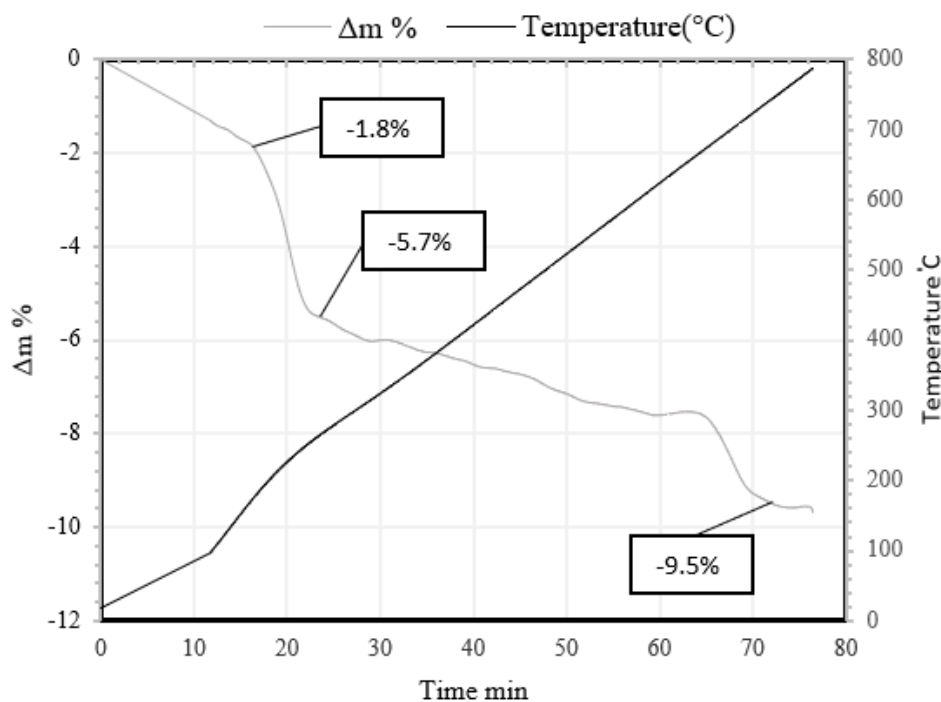


Figure 3.15 Thermogravimetric analysis (TGA) of CoMo/FAC.

3.4.4 CoMo/FAC, BET-BJH ANALYSIS

BET-BJH characterization has been done for the cenospheres support ($S_{\text{BET}} 0.58 \pm 0.1 \text{ m}^2/\text{g}$, $V_{\text{BJH}} 0.002 \pm 0.001 \text{ cm}^3/\text{g}$, and an average pore diameter $6.87 \pm 0.02 \text{ nm}$), non-calcined ($S_{\text{BET}} 2.84 \pm 0.01 \text{ m}^2/\text{g}$, $V_{\text{BJH}} 0.006 \pm 0.01 \text{ cm}^3/\text{g}$, and an average pore diameter $8.34 \pm 0.02 \text{ nm}$) and reduced CoMo/FAC catalyst ($S_{\text{BET}} 6.94 \pm 0.01 \text{ m}^2/\text{g}$, $V_{\text{BJH}} 0.03 \pm 0.01 \text{ cm}^3/\text{g}$, and an average pore diameter $18.44 \pm 0.01 \text{ nm}$); these results illustrate increasing results in surface area, pore volume and pore size after the impregnation of Co and Mo respect to the FAC support: this can be attributed by the doping effect, the dispersion state of the catalyst, and creating new pores due to an effective diffusion of the CoO and MoO₃ species in the support after the calcination (600 °C) and the reduction (600 °C) processes[192].

N₂ adsorption curves of reduced CoMo/FAC catalyst Figure 3.16 shows a mesoporous material (isotherm type IV with hysteresis loop type H3), whereas the adsorption of N₂ followed by

capillary condensation, the cumulative pores volume, and the pores volume distribution illustrates the presence of all porosity ranges, micro (below 2 nm), meso (2 – 50 nm), and macro (up to 50 nm) range.

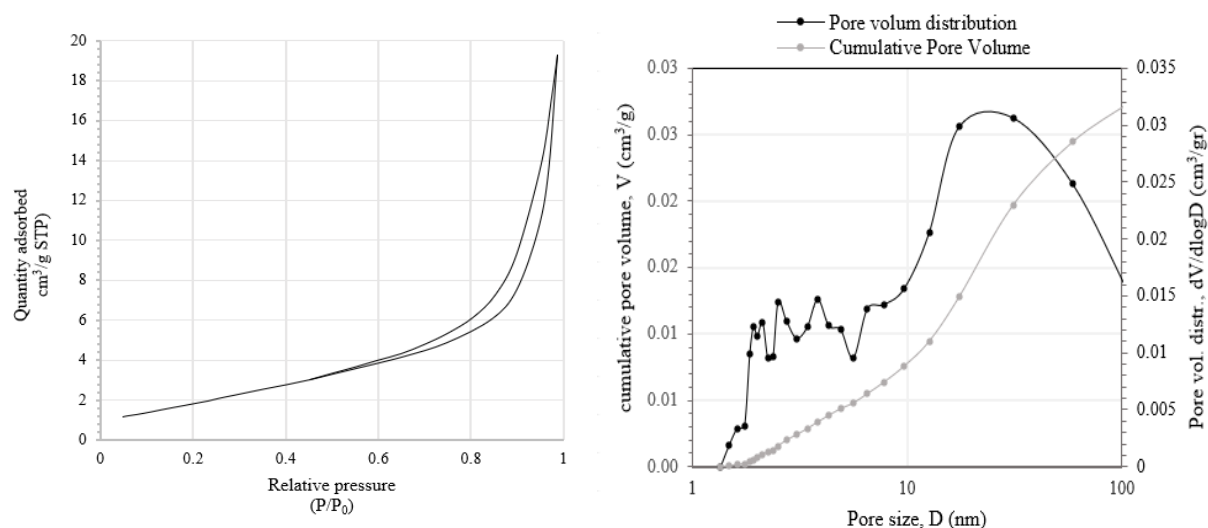


Figure 3.16 BET Isotherms (left) BJH desorption pore diameter size distribution (right) of CoMo/FAC catalyst.

3.4.5 CoMo/FAC XRD ANALYSIS

X-ray diffraction analyses on FAC support, non-calcined CoMo/FAC, and reduced CoMo/FAC catalysts, respectively, are compared. Figure 3.17 confirms the occurrence of a partially CoO reduction at 600 °C to metallic Co, but not totally because some part has reacted with the MoO₃ as Co₂Mo₃O₈ [193], which is also in line with the TPR results. So, the phases of the reduced CoMo/FAC catalyst are almost, mullite, silicon oxide, and dicobalt octaoxotrimolybdate.

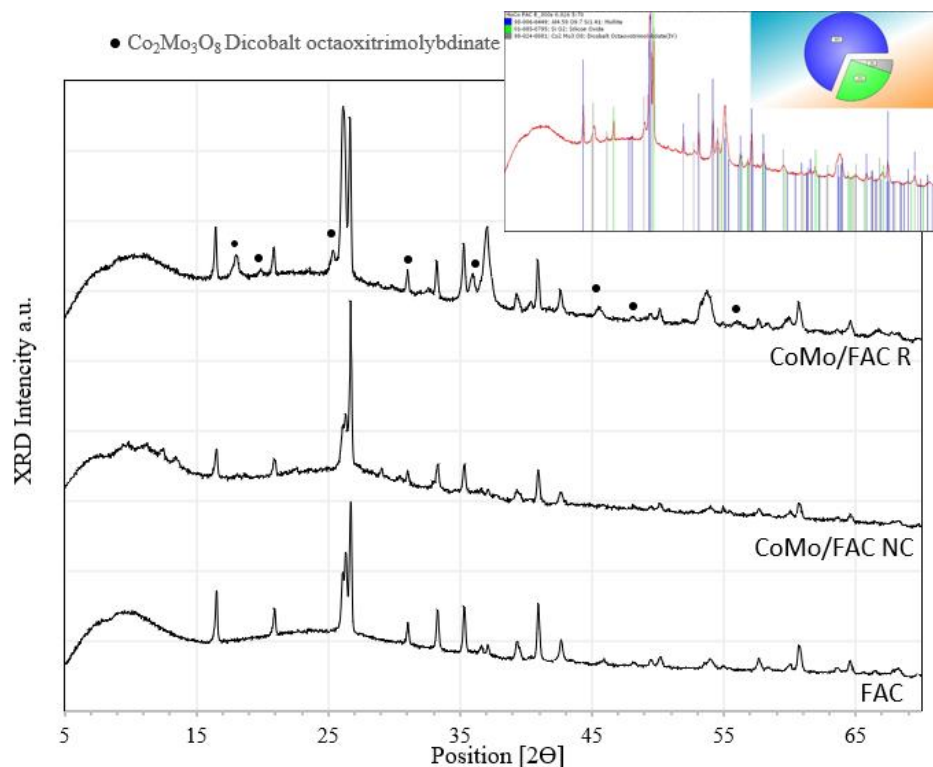


Figure 3.17 X-ray diffraction spectrum of CoMo/FAC (up) & FAC (down)

Crystallite sizes calculated from the average values of the principal peaks from the well-known Debye-Scherrer formula equation with error ± 5 nm is reported in Table 3.10, which shows about very slight decrease of the mullite crystal phase after the impregnation process.

Table 3.10 Crystal size of CoMo/FAC (NC, R) and FAC.

Sample	Phases	Formula	crystallite size [nm]
cenosphere	mullite	$Al_{4.59}O_{9.7}Si_{1.41}$	44
	silicon oxide	SiO_2	49
CoMo/FAC Non-calcined	mullite	$Al_{4.59}O_{9.7}Si_{1.41}$	40
	silicon oxide	SiO_2	49
	cobalt molybdenum oxide	$CoMoO_4$	28
CoMo/FAC Reduced	mullite	$Al_{4.59}O_{9.7}Si_{1.41}$	46
	silicon oxide	SiO_2	50
	dicobalt octaoxotrimolybdate(IV)	$Co_2Mo_3O_8$	32
	cobalt	Co	28

3.4.6 CoMo/FAC SEM AND EDS ANALYSIS

SEM and EDS analyses of the CoMo supported on FAC before and after the impregnation process are reported in Figure 3.18 and

Figure 3.19; show that the support spheres after the impregnation are almost destroyed, and the structure of the particle of the catalyst spread, due to the mixing during synthesis phases. EDS analysis on the same sample before and after the impregnation detects elemental Mo, Co, Si, Al, Na, O, K, Fe. with different peak intensity ratios in different spots.

Figure 3.20 demonstrates the dispersion of the different impregnated sample elements, molybdenum and cobalt are positioned almost together, and Mo is more concentrated, so it covers it. This technique explains the previous results, X-ray diffraction, and H₂-Chemisorption dispersion results about the presence of Co₂Mo₃O₈ phase.

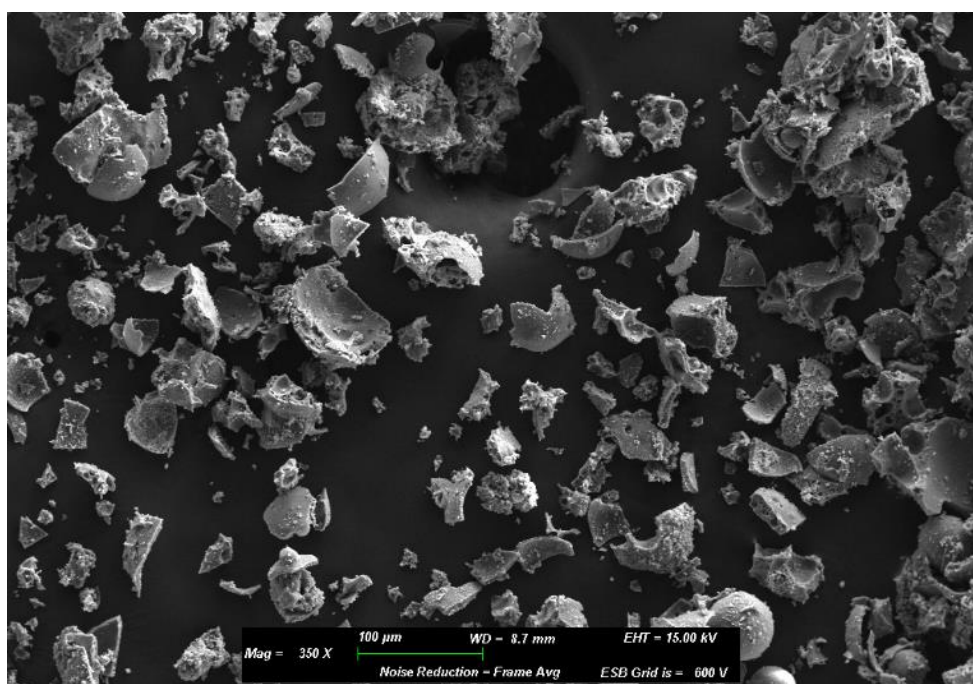


Figure 3.18 CoMo/FAC SEM image analysis.

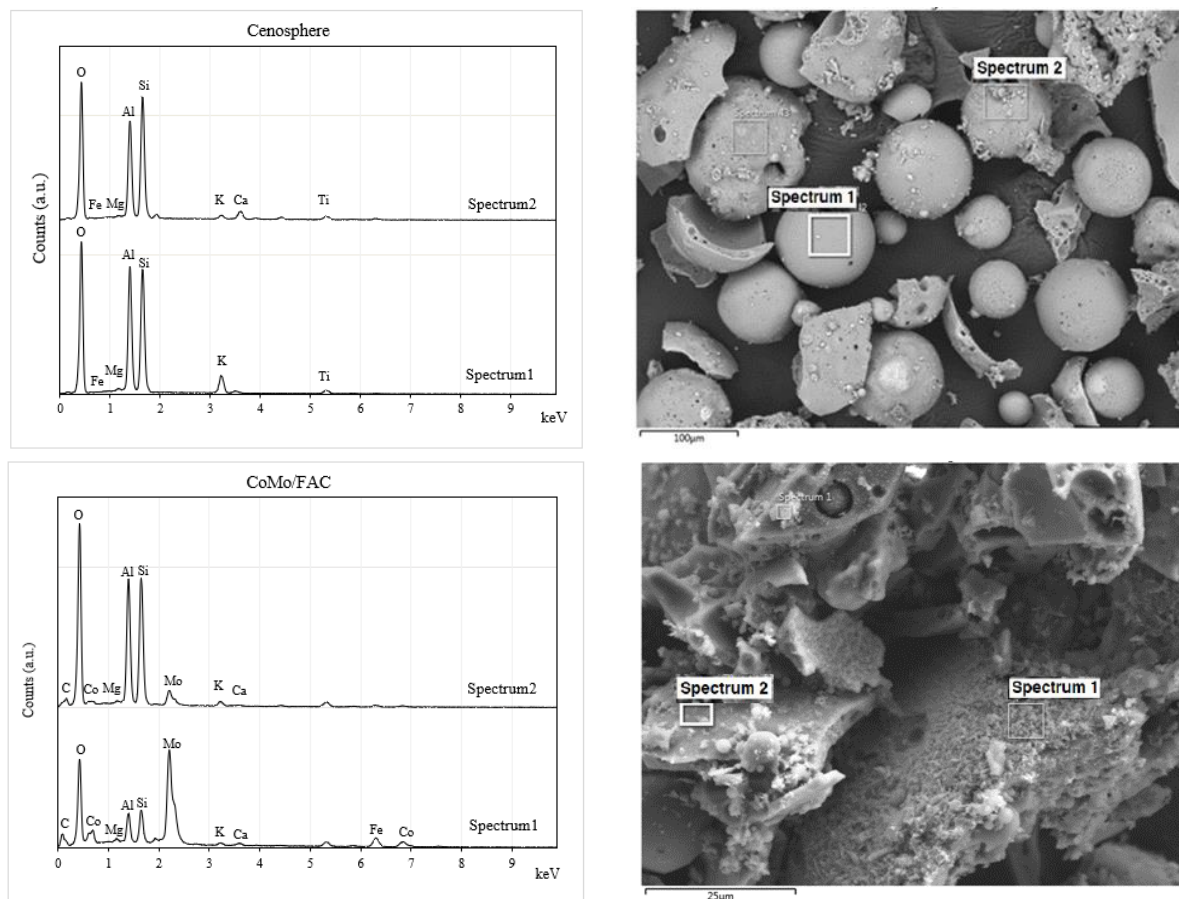


Figure 3.19 Cenosphere and CoMo/FAC analysis, SEM image (right) and relative EDS analysis (left).

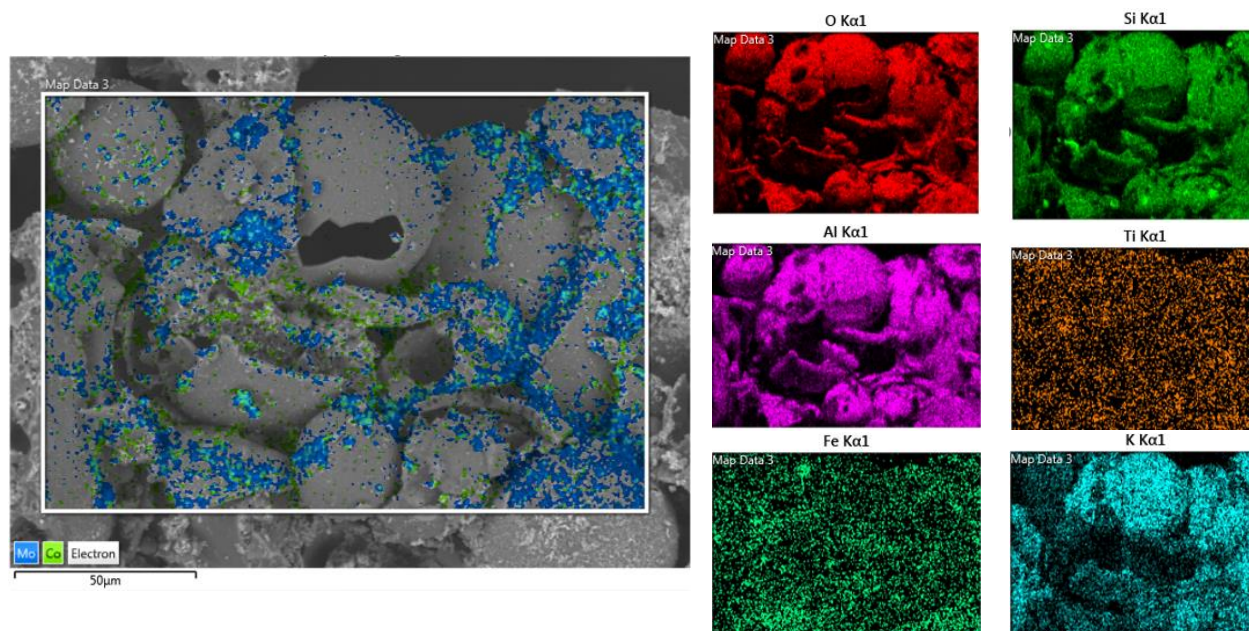


Figure 3.20 Map Scanning electron Microscope (SEM) of CoMo/FAC

3.5 NiMo/FAC CATALYST CHARACTERIZATION

All the data acquired about the NiMo/FAC catalyst like its elementary composition, metal dispersion, reducibility, surface area, crystalline phase, and morphology is reported here:

3.5.1 NiMo/FAC ELEMENTAL ANALYSIS

The catalyst firstly has been characterized by ICP-AES. Table 3.11. exhibits that the experimental ICP-AES values are about agreed with the nominal compositions for nickel, but for molybdenum, is slightly less than the expected one, which can be attributed by the preparation procedure of the sample for the ICP-AES, where, after the attack with the H₂SO₄ it has been filtered, The Al is less than previous research [185][186] and the ICP – AES analysis of the cenospheres support (13.7 ± 0.3 %), due to the addition of other elements after the impregnation process, the Si analysis has been out of the range (not acceptable), which may occur due to some problems with the apparatus

Table 3.11 ICP-AES analyses of FAC, and NiMo/FAC catalyst

Catalyst	Ni (%)	Mo (%)	Al (%)	Si (%)
NiMo/FAC	2.46 ± 0.07	6.7 ± 0.3	5.9 ± 0.2	n. c.
FAC	0	0	13.7 ± 0.3	22 ± 1

3.5.2 NiMo/FAC TPR TEMPERATURE PROGRAMMED REDUCTION

ANALYSIS AND H₂-CHEMISORPTION

The H₂-TPR curves profile, Figure 3.21, can be deconvoluted in to two peaks, he first peak (610 °C) is related to the reduction of NiO into metallic nickel (It is well-known that the reduction of nickel oxide takes place in just one step (Ni²⁺→Ni⁰) with the consumption of 1

mole of H₂ per mole of Ni²⁺) and the second one (737 °C) to the first step reduction of Mo⁶⁺ species and the complete reduction of the NiO.

Comparing with the previous catalyst CoMo/FAC, the molybdenum exhibits a reduction peak at about 737 °C, which means that it has less interaction with the support.

Table 3.12 Ni and Mo species reduction temperature, metallic Ni surface area, dispersion, and particle size for NiMo/FAC catalyst.

Ni T _{red} (C)	Mo T _{red} (C)	Ni surface (m ² /g)	Ni dispersion (%)	Ni particle size (nm)
610.3	737	1	4	22.8

For the active phase characterizations, from Table 3.12, we can conclude that the nickel has a very low surface area, large particle size, and low dispersion percentage; this result proves the fact that the nature of the support, its affinity with the species, and the synthesis methods have a remarkable effect on the reducibility of samples.

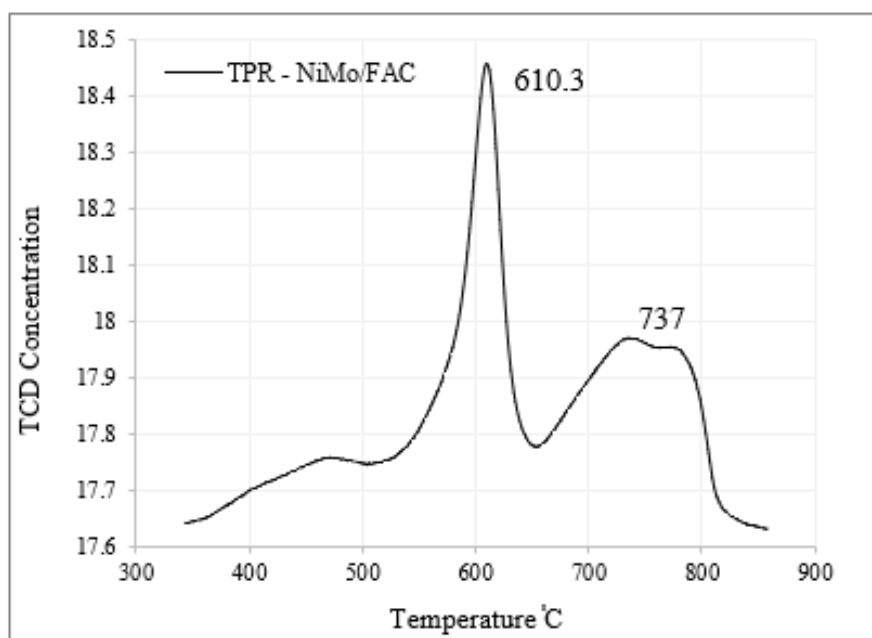


Figure 3.21 NiMo/FAC temperature programmed reduction.

3.5.3 NiMo/FAC, BET-BJH ANALYSIS

The results obtained from the textural characterization of the cenospheres support and the reduced NiMo catalyst shows an increase in surface area, pore volume, and pore size after the impregnation of Ni and Mo ($S_{\text{BET}} 4.55 \pm 0.01 \text{ m}^2/\text{g}$, $V_{\text{BJH}} 0.02 \pm 0.01 \text{ cm}^3/\text{g}$, and an average pore diameter $14.06 \pm 0.03 \text{ nm}$) respect to the FAC support ($S_{\text{BET}} 0.58 \pm 0.1 \text{ m}^2/\text{g}$, $V_{\text{BJH}} 0.002 \pm 0.001 \text{ cm}^3/\text{g}$, and an average pore diameter $6.87 \pm 0.02 \text{ nm}$) which is in line with the typical surface area obtained for cenospheres [194]. Figure 3.22 illustrates that NiMo/FAC catalyst is a mesoporous material (isotherm type IV with hysteresis loop type H3), and cumulative pores volume and the pores volume distribution shows that the presence of micro-porosity (below 2 nm) is low, while the majority of the pores are in the mesopores range (2-50 nm) and macro range (up to 50 nm).

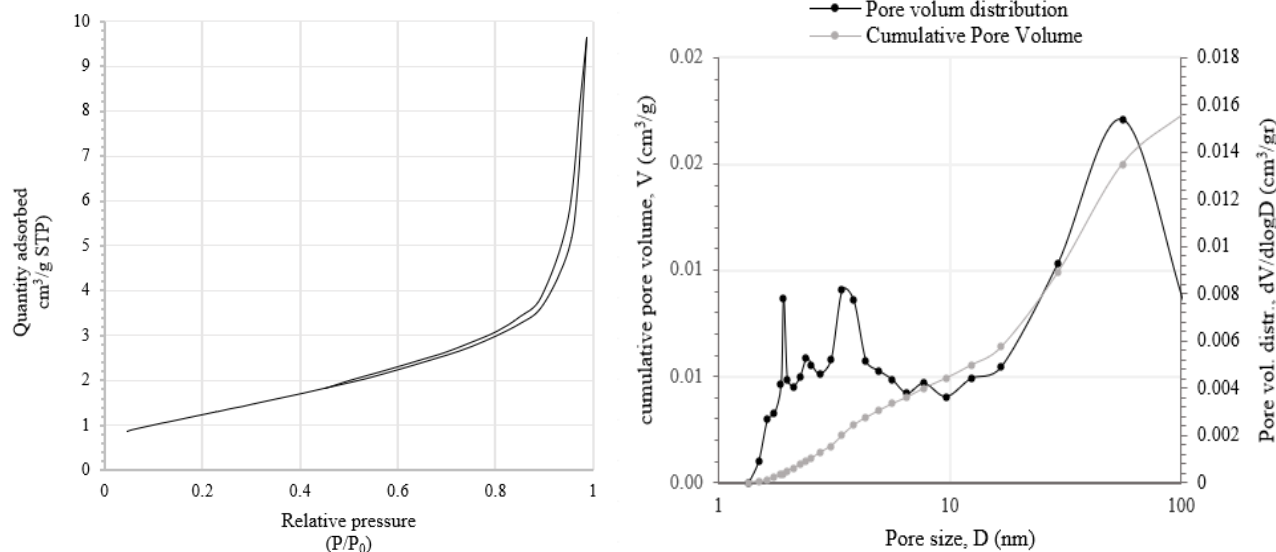


Figure 3.22 BET Isotherms (left) BJH desorption pore diameter size distribution (right) of NiMo/FAC catalyst

3.5.4 NiMo/FAC XRD ANALYSIS

The X-ray diffraction analysis of the cenospheres supports FAC and reduced NiMo/FAC catalyst (up to $500 \text{ }^\circ\text{C}$) in Figure 3.23 confirms the occurrence of NiO reduction to metallic Ni

which could be determined in a little amount at 45° and 52.4° , while the MoO_3 is not reduced by the reduction process at 500°C and posted over the FAC crystals. The sample after the impregnation process is less again crystallized, showing a higher amorphous content, and the main detectable phases of the NiMo/FAC catalyst are those already recognized of support (mullite and silicon oxide) and molybdenum oxide.

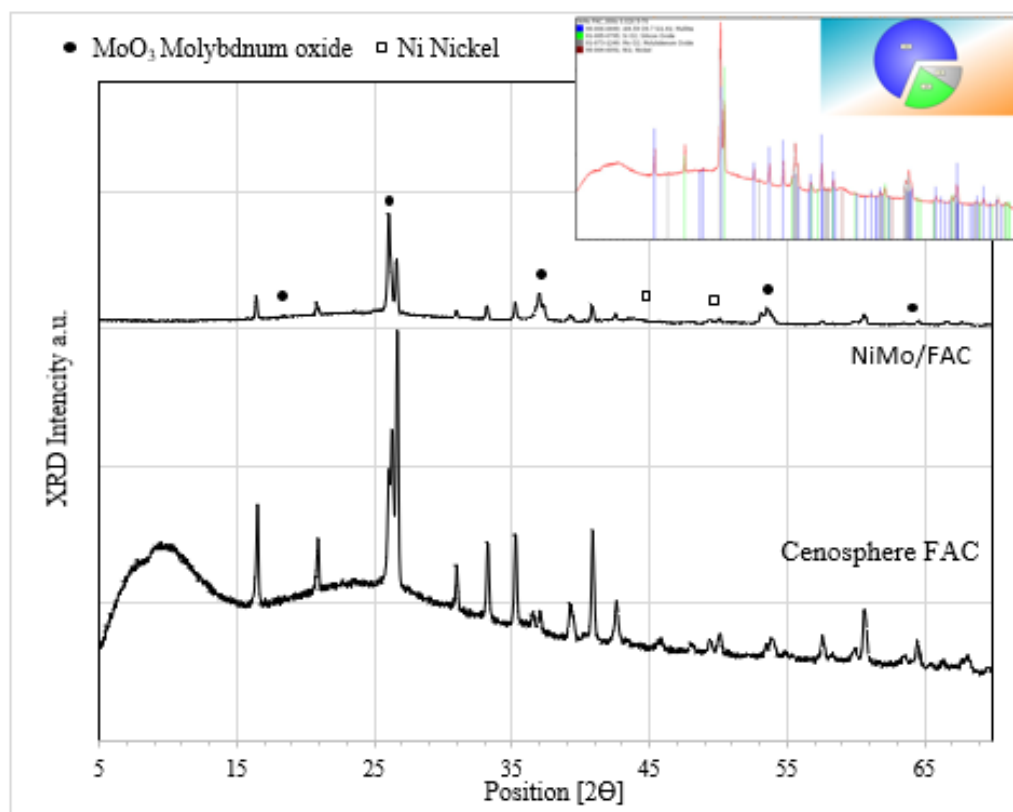


Figure 3.23 X-ray diffraction spectrum of NiMo/FAC (up) & FAC (down)

Crystallite size calculated from the average values of the principal peaks in Table 3.13 illustrates a low decrease of the FAC crystal size after the impregnation process which may result due to the metal dispersion and the interaction with the support [195].

Table 3.13 Crystal size of NiMo/FAC and FAC.

Sample	Phases	Formula	crystallite size (nm)
Cenospheres	Mullite	$Al_{4.59}O_{9.7}Si_{1.41}$	44
	silicon oxide	SiO_2	49
NiMo/FAC	Mullite	$Al_{4.59}O_{9.7}Si_{1.41}$	40
	silicon oxide	SiO_2	46
	Molybdenum Oxide	MoO_3	43
	Nickel	Ni	16

3.5.5 NiMo/FAC SEM AND EDS ANALYSIS

SEM micrographs Figure 3.24 of reduced NiMo/FAC catalyst illustrates that the spheres of the FAC are almost destroyed after the impregnation process comparing with the cenospheres support, which may occur due to the synthesis procedure. EDS analysis on the FAC and reduced impregnated samples Figure 3.25 detects elemental Mo, Ni, Si, Al, Ti, O, K, Fe with different peak intensity ratios in different spots; these compositions are distributing clearly together. Molybdenum and nickel are positioned almost together on the shells, and Mo is more concentrated, so it is covering the Ni,

Figure 3.26.

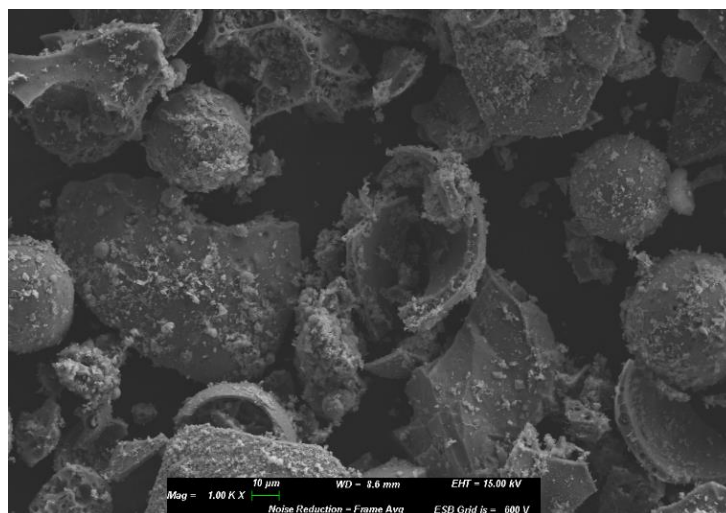


Figure 3.24 NiMo/FAC SEM image analysis.

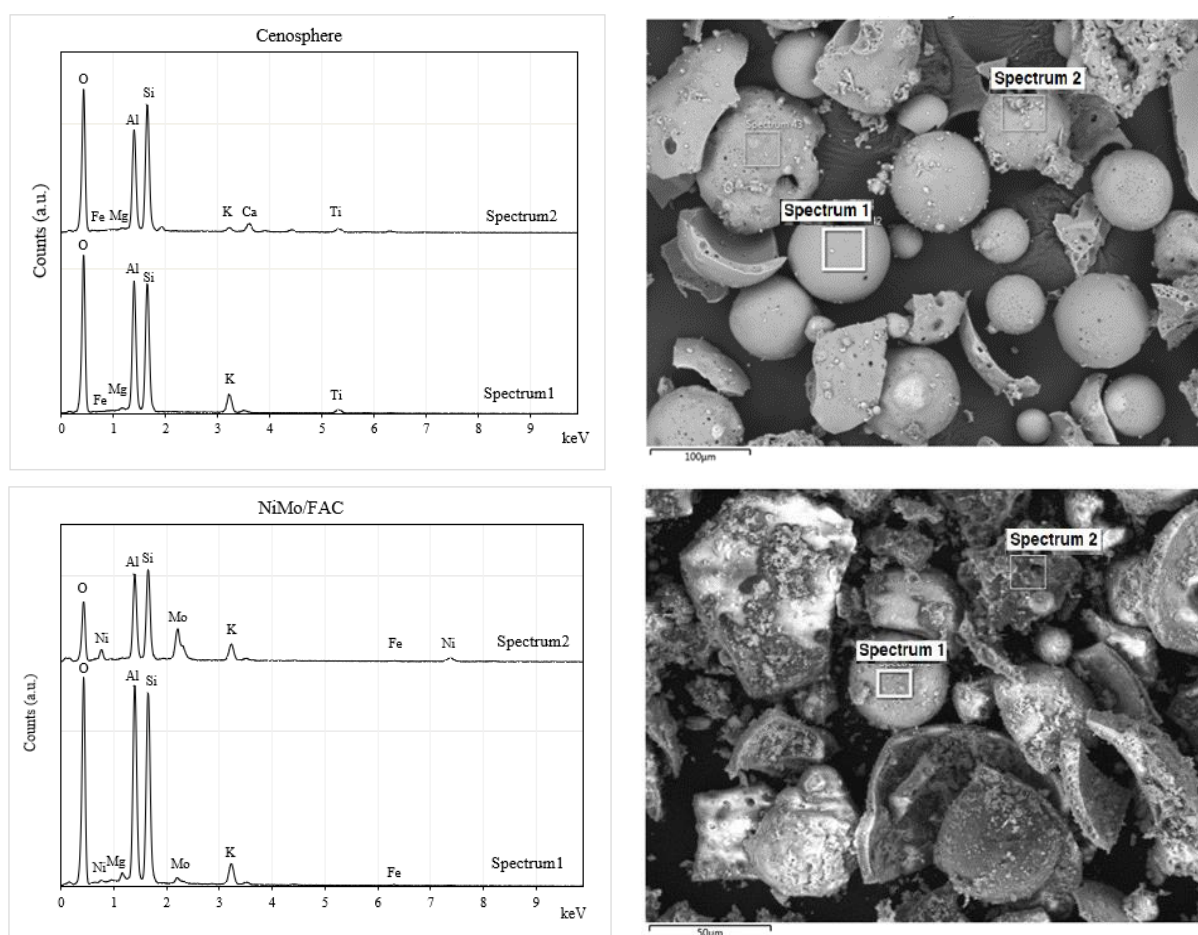
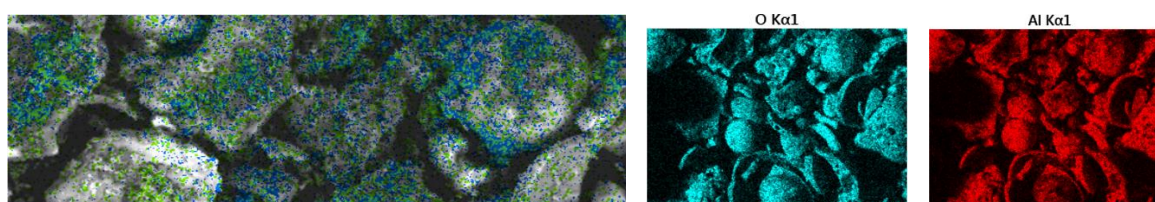


Figure 3.25 Cenosphere and NiMo/FAC analysis, SEM image (right) and relative EDS analysis (left)



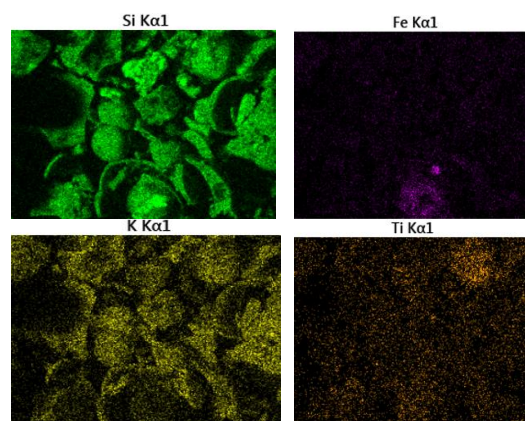


Figure 3.26 Map Scanning electron Microscope (SEM) of NiMo/FAC.

3.6 NiMo/ZEOLITE X CATALYST CHARACTERIZATION

In this paragraph, information acquired about the NiMo/zeolite X catalyst, elementary composition, reducibility, metal dispersion, acidic sites, surface area, crystalline phases, and morphology is reported.

3.6.1 NiMo/ZEOLITE X ELEMENTAL ANALYSIS

The catalyst firstly has been characterized by ICP-AES, whereas the experimental ICP-AES values are approximately in agreement with the nominal compositions for nickel, although molybdenum is somewhat less than the expected one, perhaps due to the preparation procedure of the sample for the ICP-AES, where, after the attack with the H_2SO_4 it has been filtered, The Al is comparable with previous research [185][186] and in line with the ICP – AES analysis of the zeolite X support ($12.4 \pm 0.4 \%$), while the Si analysis has been out of the range (not acceptable) due to some problems with the apparatus as seen in Table 3.14

Table 3.14 ICP-AES analyses of the zeolite and NiMo/zeolite X catalyst.

Catalyst	Ni (%)	Mo (%)	Al (%)	Si (%)

NiMo/zeolite X	2.33±0.05	5.8 ± 0.3	12.5±0.3	n. a.
Zeolite X	0	0	12.4 ± 0.4	35± 1

3.6.2 NiMo/ZEOLITE X TPR TEMPERATURE PROGRAMMED

REDUCTION ANALYSIS AND H₂-CHEMISORPTION

In order to study the reducibility and the active phases characterizations of our as synthesized catalysts, a temperature programmed reduction, and hydrogen chemisorption was applied. TPR data interpretation follows the principle that peaks of hydrogen consumption depict a chart of the interaction's energies between the active phase and the support; thus, the stronger interactions mean higher reduction temperatures measured. In Table 3.15 is gathered the TPR reduction temperature and the active surface area ASA, metal dispersion, and particle size for the as-synthesized NiMo/zeolite X sample. The temperatures in the table are two reduction temperature peaks of the bimetallic catalyst.

Table 3.15 Ni and Mo species reduction temperatures, metallic Ni surface area, dispersion, and particle size for NiMo/Zeolite X catalyst.

Ni T _{red} (°C)	Mo T _{red} (°C)	Ni ASA (m ² /g)	Ni dispersion (%)	Ni particle size (nm)
528.3	707.3	3	22	4.67

In fact, the TPR with H₂ indicates that the active nickel phase is strongly bonded to the zeolite support because an increase in the reduction temperature (528.3 °C) as seen in Figure 3.27, is observed comparing with NiO reduction temperature (around 400°C) reported by different authors [196][197], while the higher temperature signal can be ascribed to both: the complete reduction of the NiO and the first step of reduction of Mo⁶⁺ species [198], while the second Mo step could be reduced at a higher temperature (over 1000 °C) [189].

Comparing with previous NiMo/FAC TPR and keeping in mind that zeolite X materials were synthesized from the cenospheres FAC, it is possible to conclude that the nickel has more interaction with the support in the case of NiMo/FAC as its peak reduction is shifted at a higher temperature (610.3 °C), while for the molybdenum peak was detected about the same temperature (737 °C), but slightly higher anyway.

The difference of Nickel (NiMo/Zeolite X) particle size results obtained by the H₂-chemisorption (4.67 nm) and the Scherrer formula (14 nm) Table 3.16 is about the same of the previous case of the cobalt which refers to the divergence of the techniques.

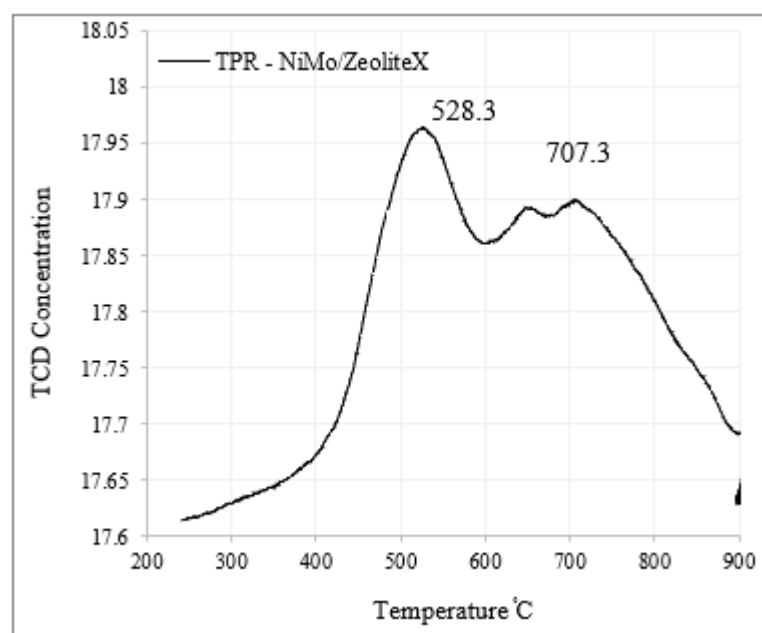


Figure 3.27 NiMo/Zeolite X temperature programmed reduction

Regarding the active phase characterizations, from Table 3.15, we can conclude that the nickel has a low active surface area, large particle size, and not bad dispersion percentage, these results were expected due to the nickel sintering phenomenon which may happen during the calcination process (500 °C) or the TPR step before the H₂ chemisorption (800 °C).

3.6.3 NiMo/ZEOLITE X, BET-BJH ANALYSIS

BET-BJH characterization, done for the support and the catalyst, showed decreasing in surface area and pore volume and increasing in the pore size after the impregnation of Ni and Mo (S_{BET} $67.01 \pm 0.1 \text{ m}^2/\text{g}$, V_{BJH} $0.09 \pm 0.01 \text{ cm}^3/\text{g}$, and an average pore diameter $5.37 \pm 0.03 \text{ nm}$) with respect to the zeolite (S_{BET} $238.01 \pm 0.1 \text{ m}^2/\text{g}$, V_{BJH} $0.1 \pm 0.01 \text{ cm}^3/\text{g}$, and an average pore diameter $1.66 \pm 0.02 \text{ nm}$), this, drop in surface area, pore size, and pore volume with impregnation metal loading possibly due to the coverage of support surface or blockage of zeolite channels by the high atomic weight of Mo or/and Ni metal/ metal oxides. These observations agree with the reduction of surface area for impregnated Ni/HY zeolite catalysts in the literature [199][200].

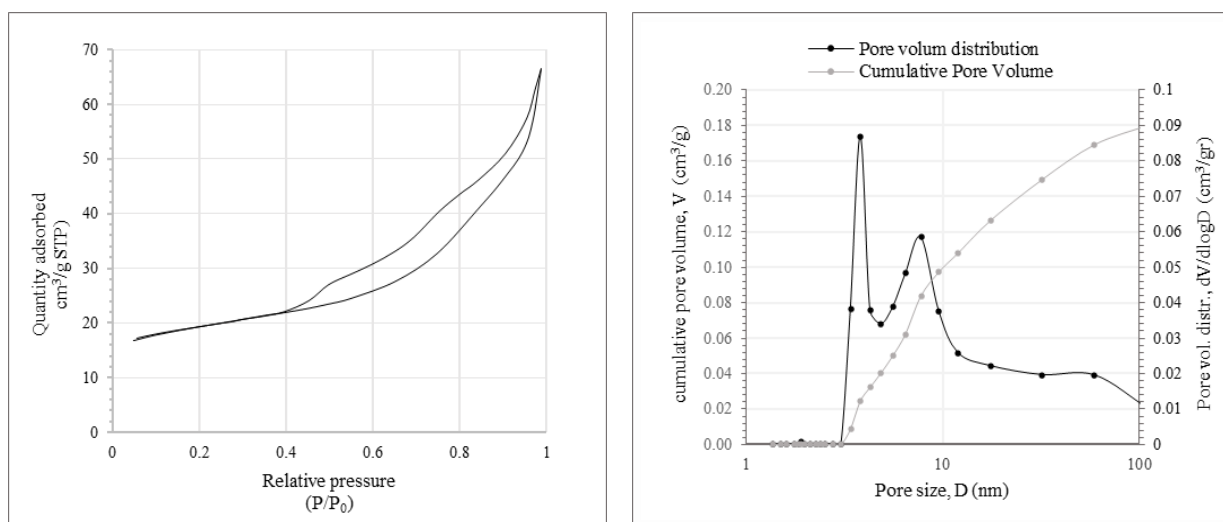


Figure 3.28 BET Isotherms (left) BJH desorption pore diameter size distribution (right) of NiMo/Zeolite X catalyst.

Figure 3.28 permit the investigation of mesoporous material (isotherm type IV with hysteresis loop type H3), the appearance of the loops at low p/p_0 values indicates a preference for quite small mesopores in this sample. It is important to note from the cumulative pores volume and the pores volume distribution that the presence of macro-properties (up to 50 nm) is very low, and there is no micro range (below 2nm), while the majority of the pores are in the mesopores range.

3.6.4 NiMo/ZEOLITE XRD ANALYSIS

The X-ray diffraction analysis of the reduced NiMo/zeolite X sample Figure 3.29 confirms that nickel oxide is reduced to nickel, while molybdenum oxide cannot be reduced by reduction process (up to 500 °C) which is confirmed with the TPR results where Mo could be reduced partially up to 700 °C. The main recognizable phases are zeolite X (sodium aluminium silicate hydrate and sodium aluminium silicate nitrate) and molybdenum oxide, whereas the presence of metallic nickel in a little amount could appear at 44.5° and 51.8° but due to the overlapping with the much more intense rays of zeolite x support, it can't be determined definitely. The sample after the impregnation process was less crystallized with more amorphous content;

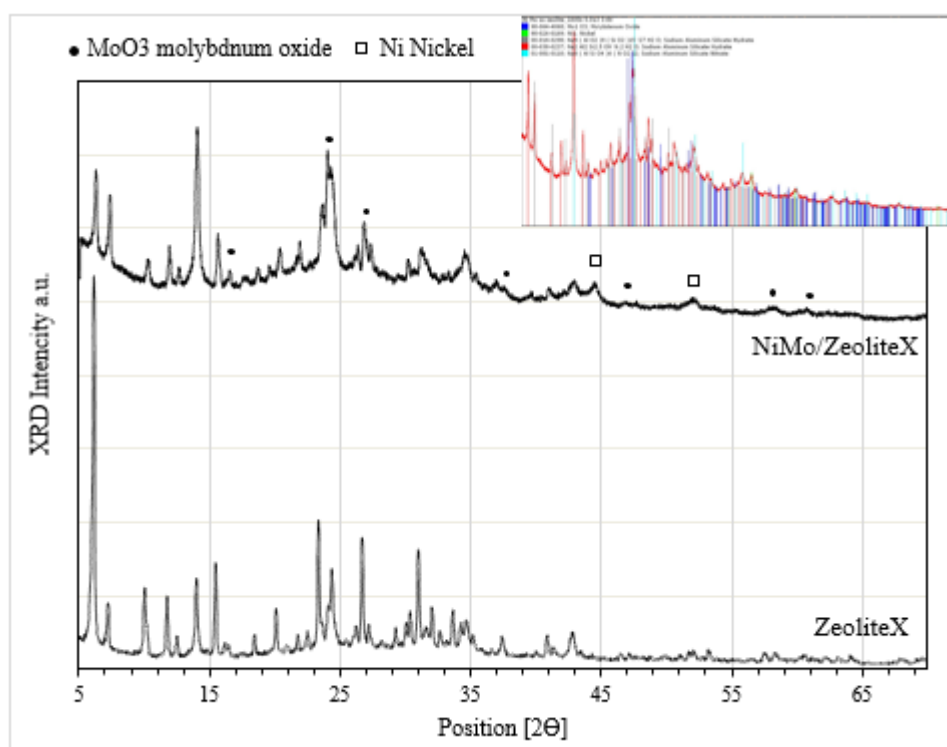


Figure 3.29 X-ray diffraction spectrum of NiMo/zeolite X (up) & Zeolite X (down).

As seen in Table 3.16, the crystallite size of the zeolite x support after the impregnation is more or less the same, whereas the crystallite size was determined from the average values of the principal peaks from the well-known Debye-Scherrer formula equation with error ± 5 nm.

Table 3.16 Crystal size of NiMo/zeolite X and zeolite X support.

Sample	Phases	Formula	crystallite size (nm)
Zeolite X	sodium aluminum silicate hydrate	$\text{Na}_2\text{Al}_2\text{Si}_{2.5}\text{O}_9 \cdot 6.2\text{H}_2\text{O}$	55
	sodium aluminum silicate nitrate	$\text{Na}_8(\text{AlSiO}_4)_6(\text{NO}_2)_2$	54
NiMo/Zeolite X	sodium aluminum silicate hydrate	$\text{Na}_2\text{Al}_2\text{Si}_{2.5}\text{O}_9 \cdot 6.2\text{H}_2\text{O}$	58
	sodium aluminum silicate nitrate	$\text{Na}_8(\text{AlSiO}_4)_6(\text{NO}_2)_2$	50
	molybdenum oxide	MoO_3	28
	nickel	Ni	14

3.6.5 NiMo/ZEOLITE X SEM AND EDS ANALYSIS

Samples analysis employing the SEM micrographs, coupled with EDS elemental analyses, allow getting more insight into the morphology and elemental topography of synthesized materials. It is also worthy to compare the structure of the catalyst before and after the impregnation. From Figure 3.30, the SEM images, it is possible to notice that zeolite crystals have a cubic shape before and after the impregnation; also, the dispersion of the metals, molybdenum, and nickel is about homogeneous. EDS analysis on the same sample, Figure 3.31 detects elemental Mo, Ni, Si, Al, Na, O, K, Fe. with different peak intensity ratios in different spots. Molybdenum stands clearly comparing with Nickel, i.e., less widespread; also, Al, Si, and O are strongly present in

Figure 3.32; this morphology may lead to an increase in the external surface area [201]. And this hypothesis is supported by BET surface area results.

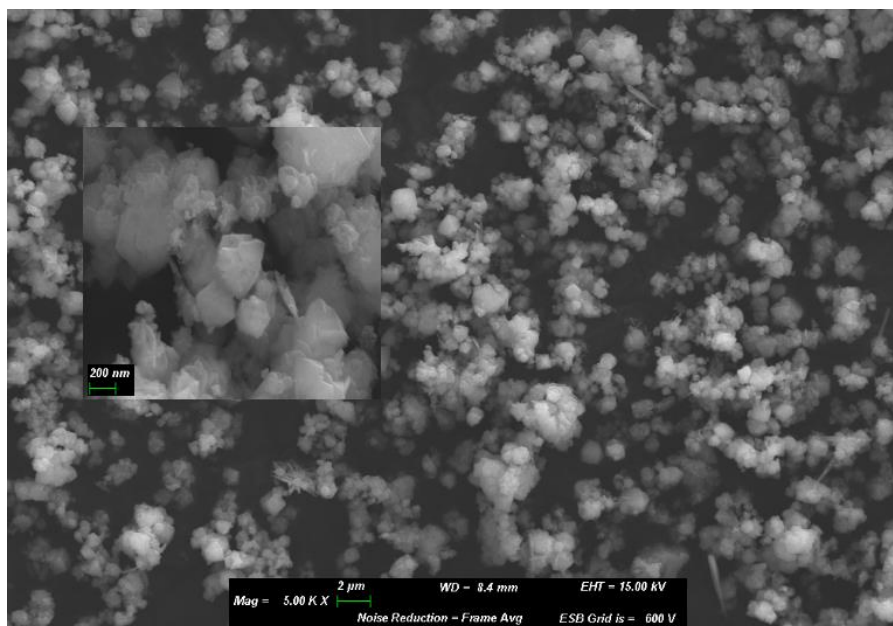


Figure 3.30 NiMo/zeolite X analysis, SEM image

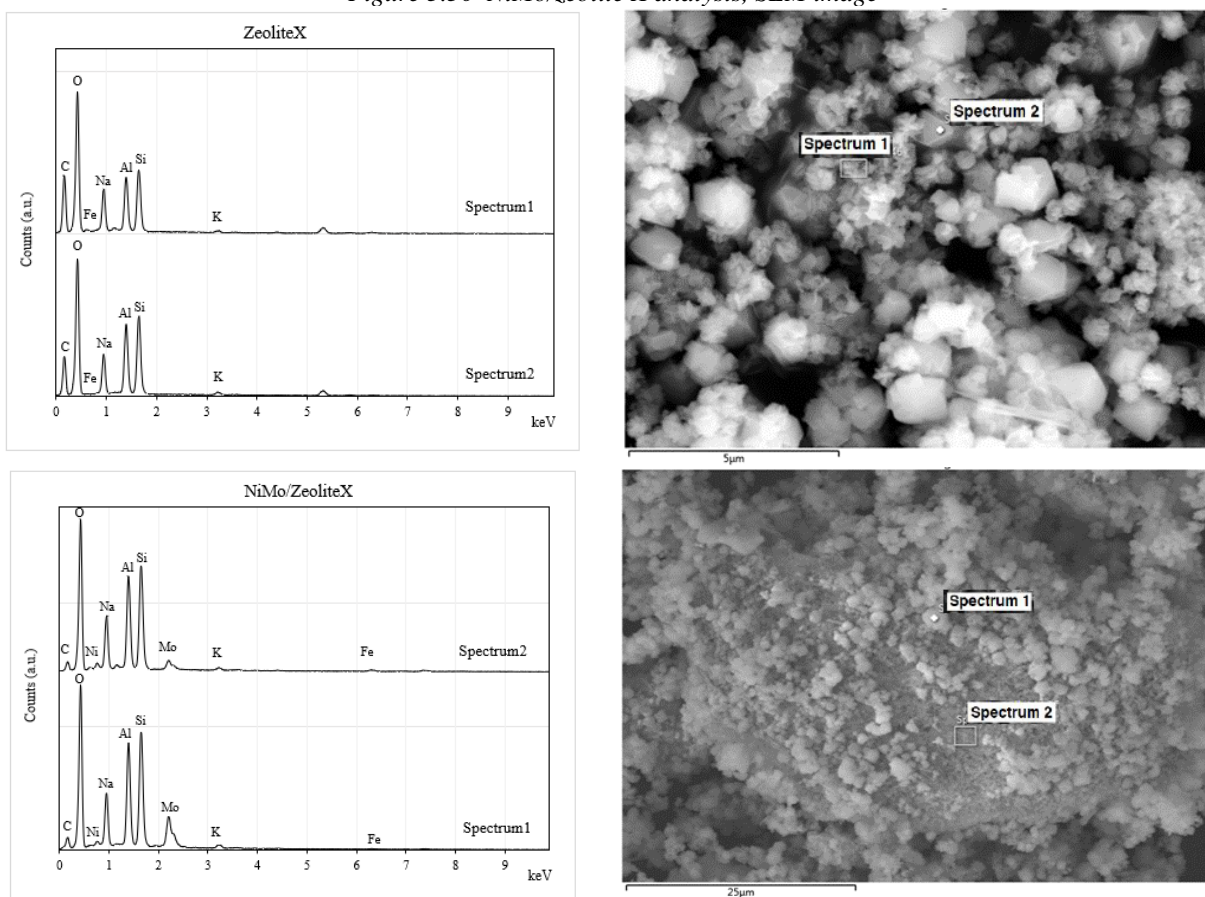


Figure 3.31 Zeolite X and NiMo/zeolite X analysis, SEM image (Right) and relative EDS analysis (left)

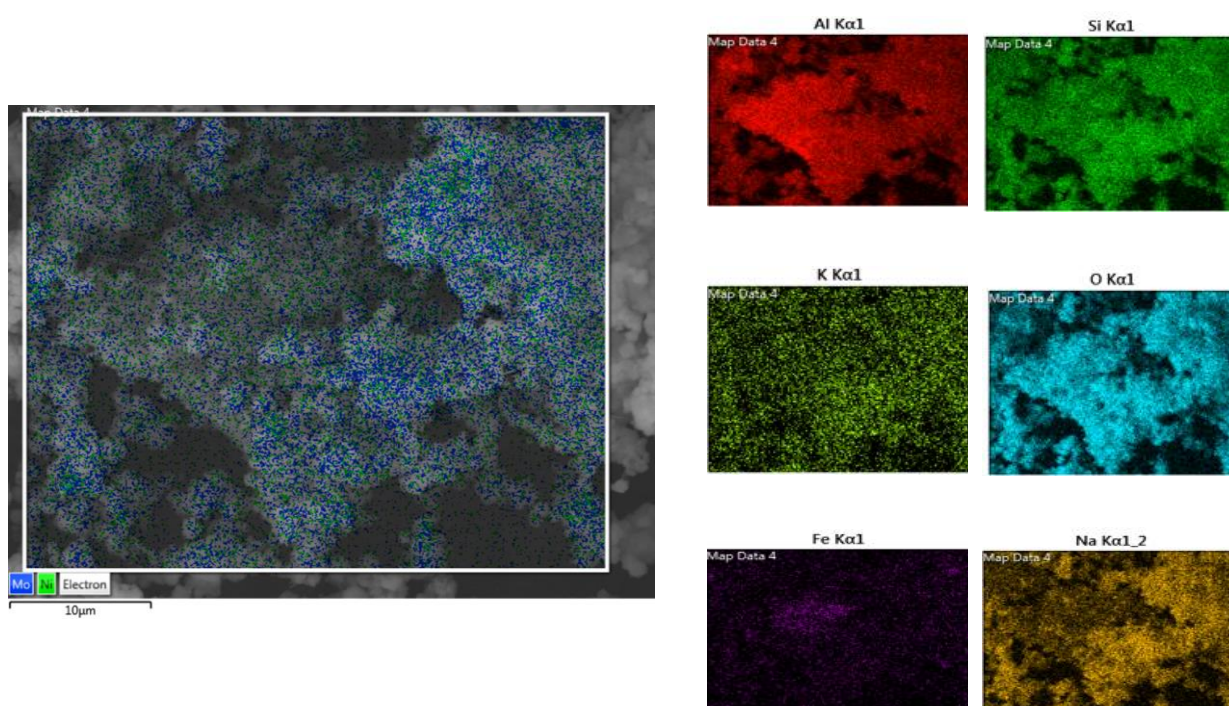


Figure 3.32 Map Scanning electron Microscope (SEM) of NiMo/zeolite X.

3.6.6 NiMo/ZEOLITE X NH₃-TPD TEMPERATURE PROGRAMMED

DESORPTION OF AMMONIA ANALYSIS

The aim of studying the acid properties for this catalyst is to find out the acid sites which could be responsible for the deoxygenation pathway selectivity towards the hydrodeoxygenation or decarboxylation/decarbonylation reactions [202]. Therefore, it is important to determine the number of acidic sites on the catalyst's surface and to study whether they are strong (Bronsted), medium (Bronsted and Lewis), or weak (Lewis) acidic sites.

Figure 3.33 presents ammonia TPD for NiMo metal oxides supported on zeolite X. It is possible to distinguish two high peaks. The first one is detected at a temperature of 130.2 °C, which means weak acidic sites, and the maximum of the second one is centered at 321.2 °C: this temperature significantly matches with medium acidic sites. In conclusion, this catalyst doesn't exhibit strong acid sites which should be at about 400 °C for the zeolite X [203].

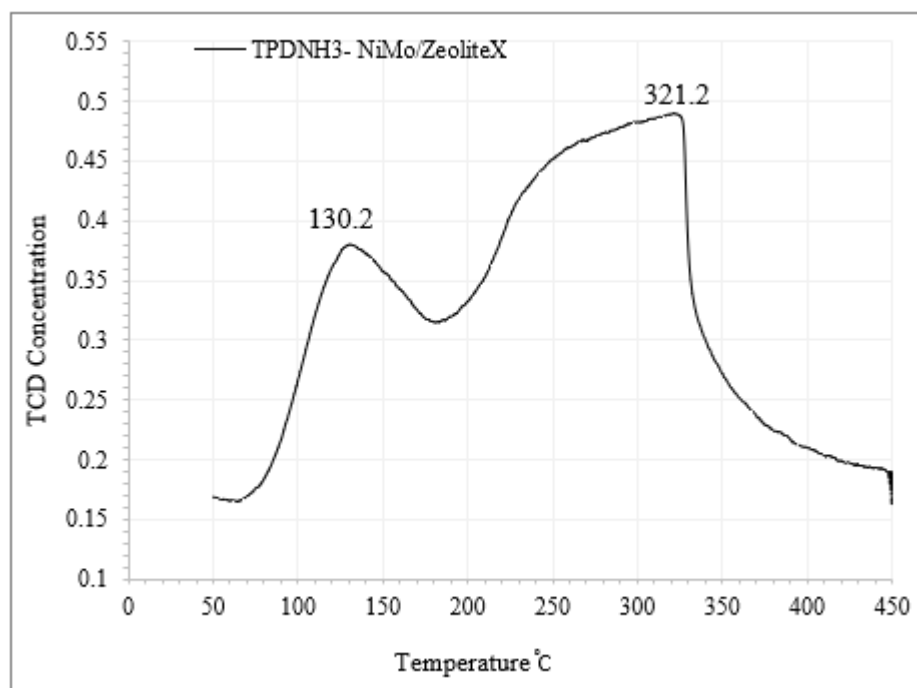


Figure 3.33 NiMo/zeolite X temperature programed desorption with NH₃.

3.7 CONCLUSIONS

Different materials were characterized before the reactivity tests, as shown in this chapter using different techniques:

I. For Lindlar catalysts, a small surface area, related to the low pore area of the support calcium carbonate is observed. Calcium carbonate by XRD is the only phase that it is possible to establish the presence. High dispersion percent of the palladium on the support by H₂-Chemisorption.

II. The Pd/HT catalyst method proves to be reliable in the synthesis of palladium supported hydrotalcites with the wanted content of Pd (ICP-AES); the material is in accordance with the characteristic of this kind of materials, with comparable the BET surface area and the shape of isotherms. As in the case of Lindlar, for Pd/HT it is not possible to identify the Pd phases by

XRD, due to the low Pd content. Although the low Pd content, the dispersion percentage on the hydrotalcite support is very significant.

III. For the bimetallic NiMo/zeolite X catalyst, TPR results show that the materials present two H₂ consumption peaks; these peaks are over the range reported in the literature for the reduction of the bimetallic nickel and molybdenum oxides. The Ni area was studied by chemisorption of H₂ and highlighted low area, and so low dispersion, due to the nickel sintering attitude.

From a morphological point of view, the NiMo/zeolite X catalyst has a structure with a cubic crystal-shaped before and after the impregnation process; also, the dispersion of the metals, molybdenum, and nickel is homogeneous.

From the TPD by NH₃, was observed two types of acidic sites, low one at low temperature, which may refer to the Lewis acidic sites, and the other is medium at a mild temperature, which could include the two types of Lewis and Bronsted acidic centers.

IV. For the mono and bimetallic catalysts supported on the FAC material:

- In the case of the bimetallic NiMo/FAC catalyst, the TPR results show that the materials present two H₂ consumption peak; these peaks are over the range reported in the literature for the reduction of the bimetallic nickel and molybdenum oxides which could be due to the strong interaction between the metals and the support. By the chemisorption of H₂, the Ni active surface area and the dispersion percentage were lower than the NiMo/zeolite X, which shows the support type effect. The BET surface area was very low, too, cause its low in the raw cenospheres materials. Regarding the morphological crystalline point of view, the NiMo/FAC catalyst has a structure with the

destruction of the spheres after the impregnation process. Ni and Mo posted almost together on the shells of the spheres.

- For the bimetallic CoMo/FAC catalyst, the TPR results have shown a strong interaction not only with the support but also between the metals each other's where the two peaks are over the range reported in the literature for the reduction of the bimetallic cobalt and molybdenum oxides. The XRD results have illustrated that the CoMo/FAC catalyst has kept its structure of crystallinity and morphology after the impregnation process with two phases (FAC and $\text{Co}_2\text{Mo}_3\text{O}_8$). SEM analysis has demonstrated that the support spheres are almost destroyed after the impregnation process; Co is about covered with Mo.
- Finally, for the monometallic Pd/FAC catalyst, the TPR results were very in accordance with the literature, with only one central peak for the palladium. The BET results have illustrated increasing in surface area and pore volume, and pore size after the impregnation of palladium oxide with respect to the FAC support. Also, in the Pd impregnation, the crystallinity was kept after the process. From the morphological point of view, the support spheres structure is about totally destroyed, and Pd spread very well after the impregnation, which may occur due to the mixing during the synthesis phase, and this is confirmed with the H_2 -Chemisorption results of high Pd dispersion 88%.

CHAPTER 4

This chapter reports the activity test results of the catalytic hydrogenation reactions on canola and Sunflower vegetable oils using:

- *Lindlar catalyst test activities;*
- *Pd/HT catalyst test activities;*
- *Pd/FAC catalyst test activities;*

4 HYDROGENATION REACTIVITY TESTS

4.1 LINDLAR CATALYST HYDROGENATION TESTS

The catalytic hydrogenation activity tests using Lindlar catalyst (indicated in Table 2.3) results, performed with canola rapeseed and sunflower vegetable oils, are illustrated in this section as selectivity, conversions, and fatty acids composition during the reaction time, where the most meaningful tests' results are reported in Table 4.1 [168][204]. In order to evaluate the possibility of homogeneous phase reactions, two blank tests without catalyst were carried out under the corresponding conditions for six hours, and no homogenous phase reactions were noted.

Table 4.1 Lindlar catalytic hydrogenation test results, isomer index SII index, and conversions

Entry	Oil	T (°C)	P (bar)	t ^a (min)	S _{Ln} (%)	S _{Le} (%)	SII	IV	χ _{C18:3} (%)	χ _{C18:2} (%)	(C18:1) ^b (%)
Test 03	Canola	120	8	120	1.3	23.9	0.7	89.2	84.6	60.8	82.6
Test 04		180	4	90	1.4	33.6	1.4	89.3	90.1	84.6	88.4
Test 05		180	12	60	1.3	20.2	1.2	79.4	92.7	84.3	86.0
Test 06		180	4	120	1.7	35.8	1.5	91	92.1	51.4	83.2
Test 07		180	4	120	2.2	37.3	1.8	93	90.6	51.0	84.4
Test 13	Sunflower	180	4	240	-	13.9	2.3	80	-	98.7	83.0

a: Time corresponding to the maximum relative percentage of the monoene C18:1

b: Maximum C18:1 relative percentage obtained during the test

The tests 01 and 02 (conducted at 60 °C under 4 bar and 12 bar) in Table 2.3 are not reported in Table 4.1 cause the conversion of both linoleic (3.5% and 6% respectively) and linolenic acids (15.9% and 21% respectively) even after 6 hours of the reaction was so small to be considered (Addendum B).

The study of the selectivity of linolenic S_{Ln} and linoleic S_{Le} acids reported in Table 4.1 allows to infer that the S_{Ln} results are in accordance with the literature values [205][206], while for the S_{Le} results are higher: the linoleic selectivity values imply that the reaction rate of linoleic fatty acids is higher than the formation rate of stearic acid. For this reason, the reaction must be stopped before the complete saturation of double bonds.

Increasing the temperature higher than 60 °C, the conversion of linolenic and linoleic acids is increased: Test 03 (120 °C and under 8 bar) Figure 4.1 illustrates that after about four hours of the hydrogenation reaction, almost all the polyunsaturated fatty acids are transformed in C18:1,

and C18:0 compounds with iodine value 69.1, which decrease from 121 and this give a significant parameter to illustrate the efficiency of the hydrogenation process. The maximum concentration of C18:1 (82.6 %) was achieved at 120 minutes, with a corresponding stearic acid C18:0 7.8 % and 8.1% of linoleic acid C18:2 compositions.

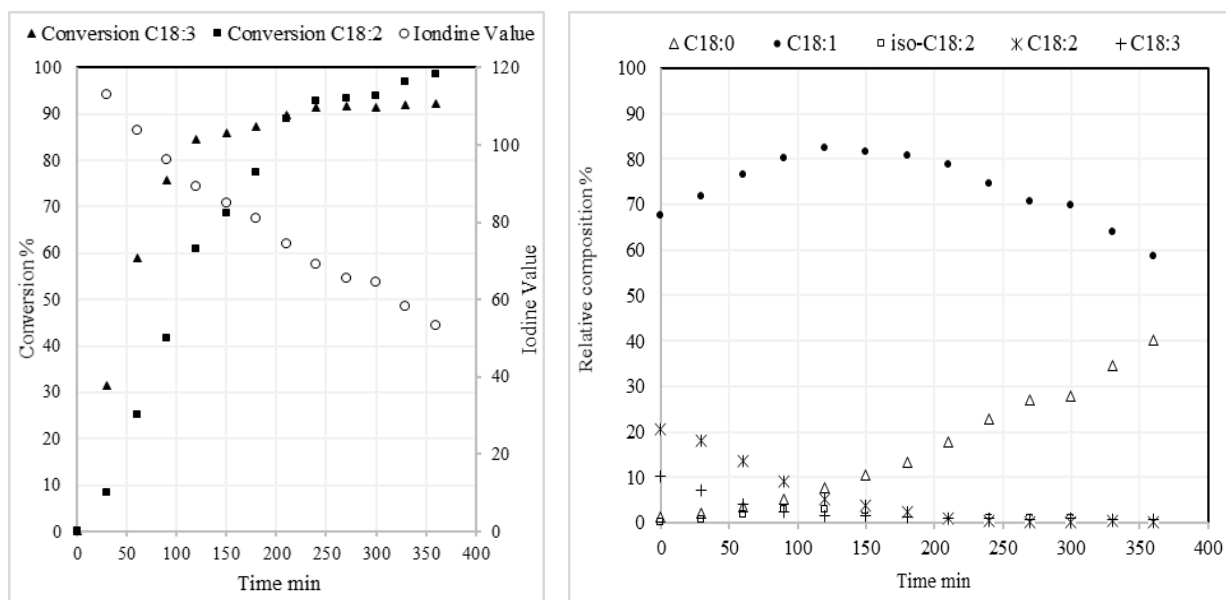


Figure 4.1 Test 03 (120 °C, 8 bar and 4 mg/ml) Hydrogenation with canola oil and Lindlar results, conversions of linolenic and linoleic acid and iodine value vs. time (right) relative percentage of C18 compounds vs. time (left)

Test 04 at 180 °C and 4 bar show similar attitudes, but a higher activity than Test 03, as can be observed in Figure 4.2 whereas, after 120 min, the maximum conversion of polyunsaturated compounds of about 95% and the iodine value equal to 82.2 is reached. At 90 minutes, the highest composition of monoene C18:1 (88.4% compared to 82.6% of test 03) and 4.5 % of stearic acid C18:0 is obtained.

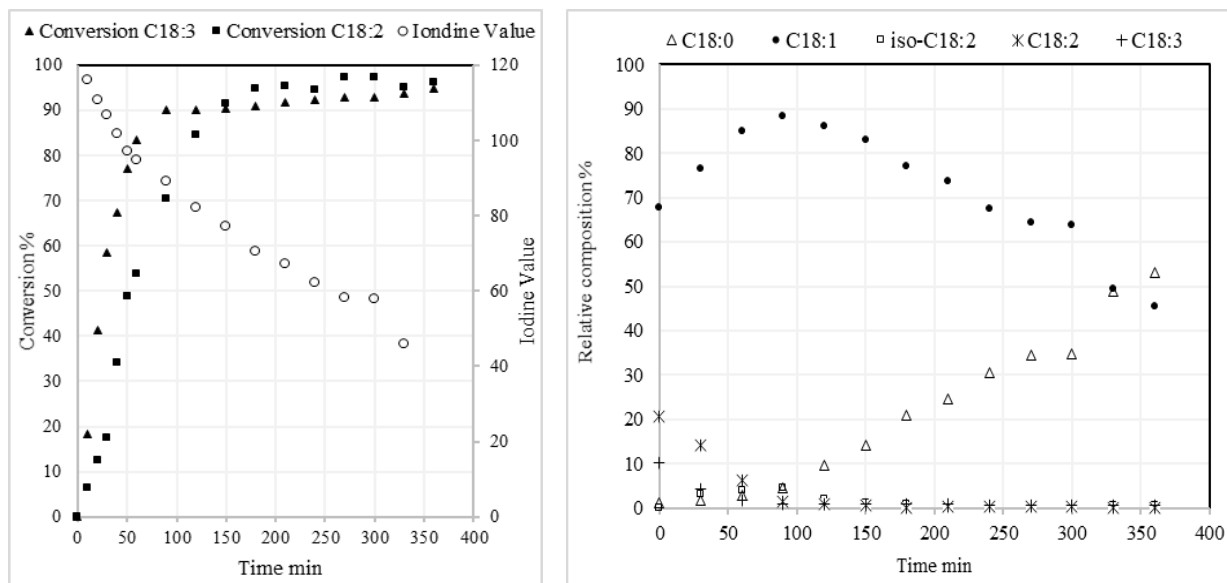


Figure 4.2 Test 04 (180 °C, 4 bar and 4 mg/ml) Hydrogenation with canola oil and Lindlar results, conversions of linolenic and linoleic acid and iodine value vs. time (right) relative percentage of C18 compounds vs. time (left)

Increasing the pressure of H_2 at 180 °C (Test 05 in Figure 4.1), the reaction rate increase and the complete conversion of C18:3 and C18:2 is observed after about 90 minutes, meaning that a higher concentration of molecular H_2 solubilized in the oil leads to higher activity, so as increasing the solubilized H_2 means increasing the reaction activity, it also means that increasing the mixing velocity will lead then to higher activity and higher conversion.

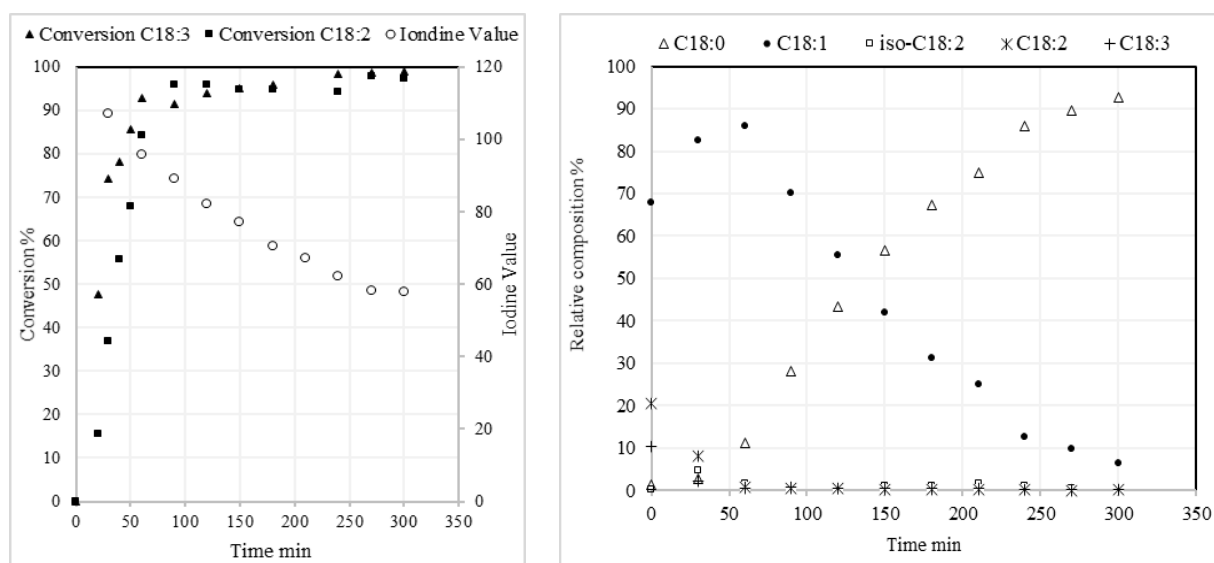


Figure 4.3 Test 05 (180 °C, 12 bar and 4 mg/ml) Hydrogenation with canola oil and Lindlar results, conversions of linolenic and linoleic acid and iodine value vs. time (right) relative percentage of C18 compounds vs. time (left)

Since the main desired goal of the hydrogenation process is achieving a great conversion of polyunsaturated fatty acids, a high concentration of monoene's, keeping a low concentration of stearic acid, it is necessary to identify the best reactions conditions and stop the reaction before the complete conversion of the polyenes. After evaluating the previous hydrogenation results, the higher temperature 180 °C (Test 04 and Test 05) is better than 120°C (Test 03) since the higher reaction rate (same degree of conversion at shorter reaction times) and higher amounts of C18:1 is obtained. It was worth doing other tests under the same operating conditions and lower catalyst concentration (Test 06 and Test 07).

In Figure 4.4 (test 06) and Figure 4.5 (test 07), the tests with lower catalyst concentrations half and quarter respect to test 04, shows only a slight decrease in the hydrogenation rate and about complete conversion of linolenic acid C18:3 (92%), whereas the conversion of linoleic acid C18:2 is about 52% for both tests. Although SII achieves almost the same results, less stearic acid is formed (about 6%), comparing with the previous one test 04 (about 15%). However, we conclude that it is possible to obtain comparable results using a quarter of the amount of the initial catalyst ($1 \text{ mg}_{\text{catalyst}}/\text{mL}_{\text{oil}}$ vs. $4 \text{ mg}_{\text{catalyst}}/\text{mL}_{\text{oil}}$), but with a longer reaction time (double) to obtain 90% linolenic conversion.

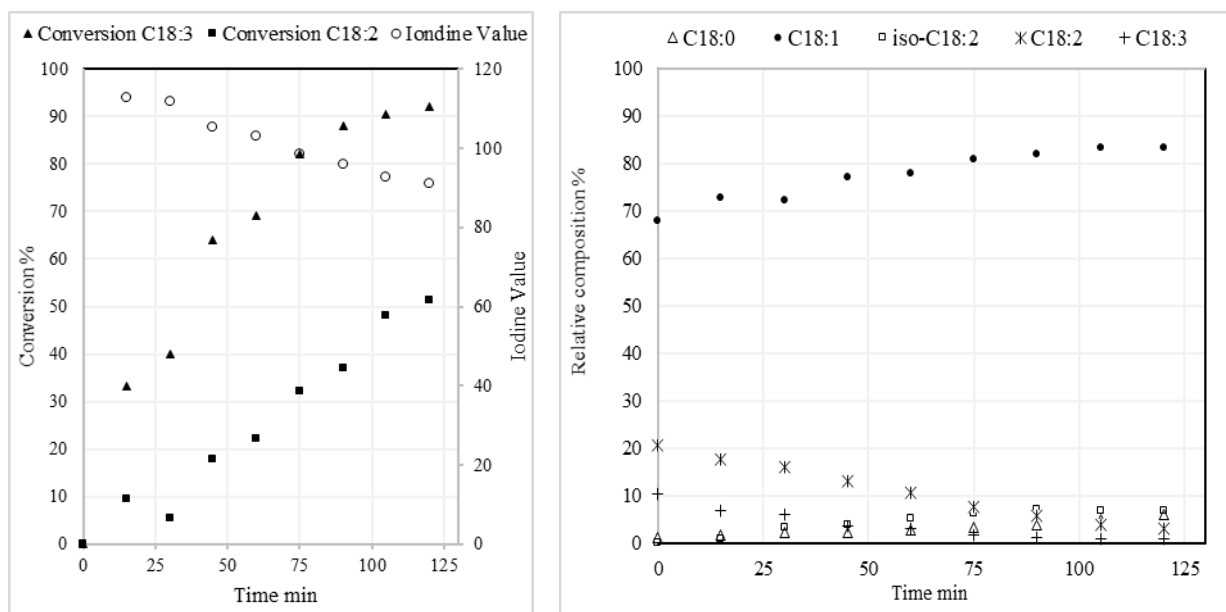


Figure 4.4 Test 06 (180 °C, 4 bar and 2 mg/mL) Hydrogenation with canola oil and Lindlar results, conversions of linolenic and linoleic acid and iodine value vs time (right) relative percentage of C18 compounds vs time (left)

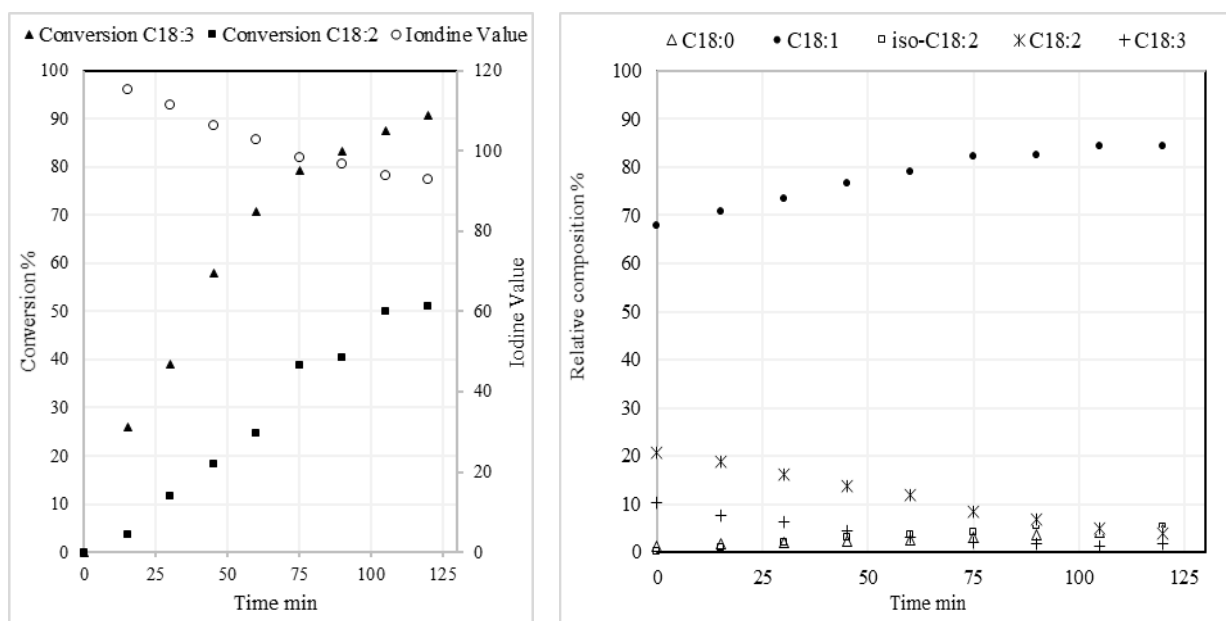


Figure 4.5 Test 07 (180 °C, 4 bar and 1 mg/mL) Hydrogenation with canola oil and Lindlar results, conversions of linolenic and linoleic acid and iodine value vs. time (right) relative percentage of C18 compounds vs. time (left)

In order to study the recyclability and the sustainable efficiency of the Lindlar catalyst, five cyclic tests with canola rapeseed oil were investigated at the best operative conditions of 180 °C and 4 bar of hydrogen, 1 hour for every cycle. The conversions, selectivity, iodine value, and relative compositions of fatty acids over 5 cyclic tests are reported in Table 4.2.

Table 4.2 Test results with canola oil and Lindlar catalyst for the cyclic test at 180 °C and 4 bar pressure calculated at 1 h.

Entry	S _{Ln}	S _{Le}	S _{II}	IV	χ _{C18:2} (%)	χ _{C18:3} (%)	(C18:1) (%) ^c
Test 08	1.21	47.8	0.40	94	42.8	65.8	86.6
Test 09	1.24	40.8	0.76	95.3	55.2	80.8	86.2
Test 10	1.05	39.3	0.93	95.2	54.2	75.1	83.8
Test 11	1.01	26.0	0.94	96.8	49.2	67.7	81.4
Test 12	1.11	20.5	0.75	99	42.8	65.8	80.7

c : Maximum C18:1 relative percentage obtained at 60 minutes

Cyclic tests result for the relative composition of fatty acids and the polyunsaturated fatty acids conversion, are reported in Figure 4.6 and Figure 4.7 respectively, illustrate a small loss of catalytic activity over hydrogenation runs which could be explained with:

- incomplete recovery of the catalyst after each cycle.
- deactivation of the catalyst and blocking the pores cause the formation of coke or carbon monoxide [207]. Pd leaching may happen, which was confirmed by doing post-test ICP-AES analysis on the recovered catalyst washed with acetone, and n-hexane shows a loss of Pd less than 10 %_{w/w} [208].
- poisoning elements in the oil (sulfur and phosphorous compounds or heavy metals traces) could affect the catalyst activity and selectivity [209][210].
- the presence of some complex molecules in vegetable oils, such as chlorophyll, which may block the pores of the catalyst and prevent the access for reactants [211].

The catalyst deactivation could be solved by making-up the appropriate amount of fresh catalyst.

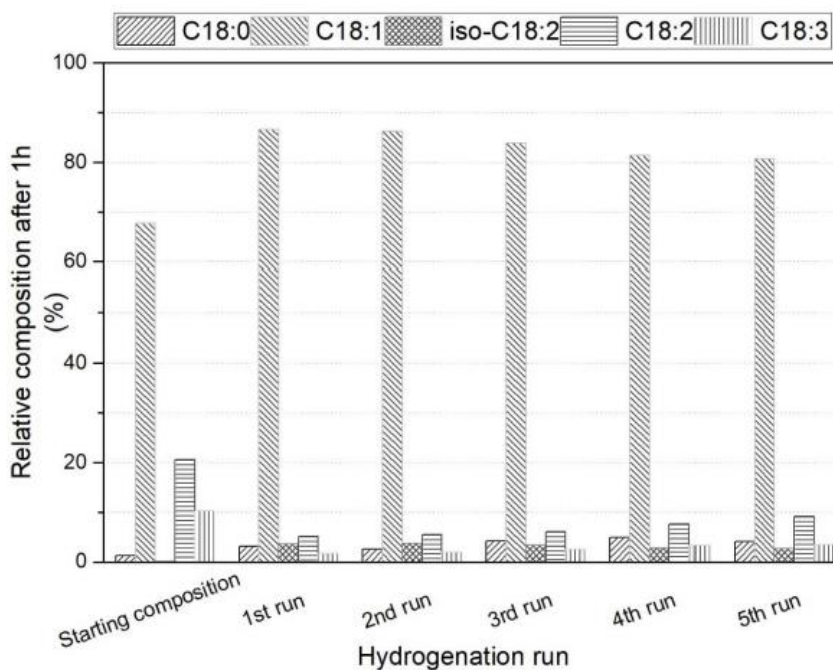


Figure 4.6 Hydrogenated oil composition at 1h over five cyclic tests at 180°C, 4 bar and 4mg/mL with canola oil and Lindlar catalyst, (test 08-12)[8]

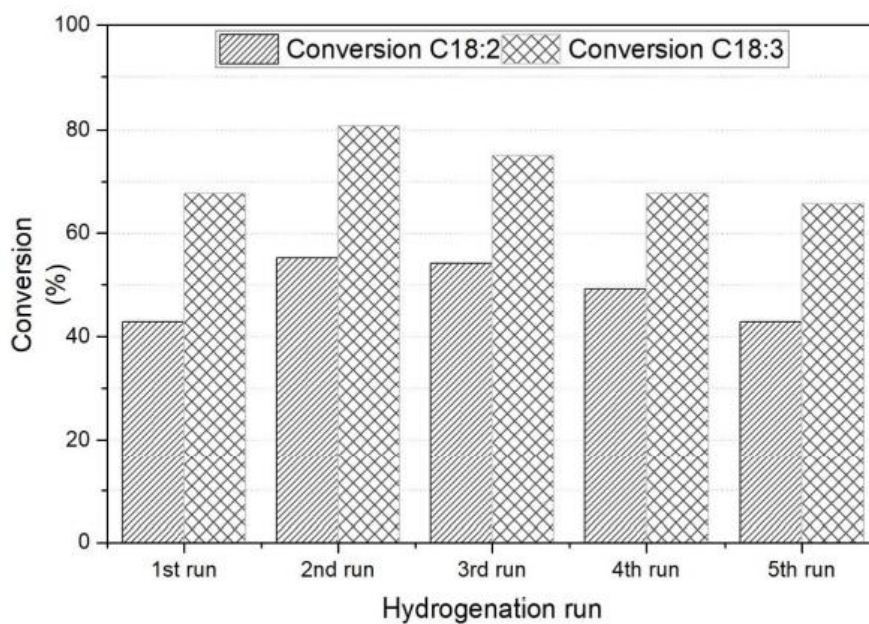


Figure 4.7 C18:1 and C18:2 conversions at 1h over five cyclic tests at 180°C, 4 bar and 4mg/mL with canola oil and Lindlar catalyst, (test 08-12)[8]

As the choice of the type of vegetable oil used for the hydrogenation process depends on commercial availability and taking into consideration all the tests carried out; the best reaction conditions are 180 °C, 4 bar of hydrogen and 4 mg of Lindlar catalyst of 1 mL_{oil}, another

hydrogenation test with commercial sunflower oil was carried out because in Europe great use of sunflower is made and it is produced in large quantities [212].

Hydrogenation results for Test 13 at 180 °C and 4 bar using sunflower oil, with lower initial contents of C18:3 and C18:1, and higher content of C18:2 than canola rapeseed oil, shows in Figure 4.8 where, the conversion of linoleic acid C18:2 is almost complete after about 4 hours with iodine value about 80, maximum C18:1 relative composition about 83%, and low amount of C18:0, about 12% at the same time. So, comparing the hydrogenation of canola rapeseed and sunflower oil under the same conditions (Test 04 and Test 13), it could be observed that the polyenes react more easily, and the hydrogenation is favored over the formation of monoene in oil having a significant of linolenic fatty acids C18:3.

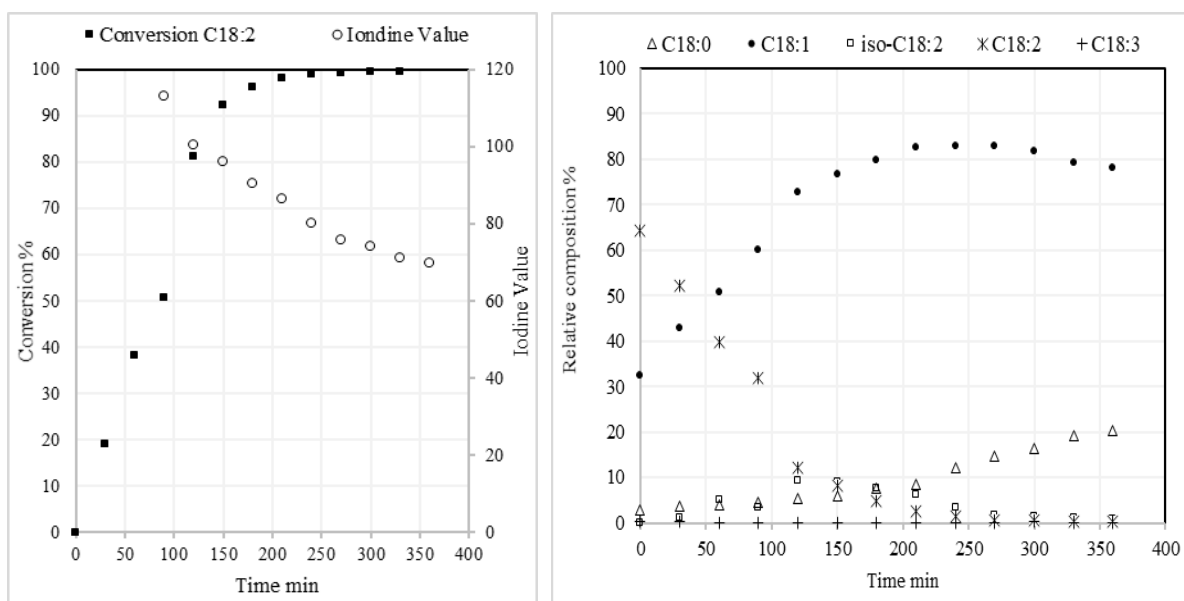


Figure 4.8 test 08 (180 °C, 4 bar and 4 mg/mL) Hydrogenation with sunflower oil and Lindlar results, conversions of linolenic and linoleic acid and iodine value vs. time (right) relative percentage of C18 compounds vs. time (left)

In order to study the suitability of the experimental data with the theoretical one, the proposed model is used for the data analysis (Equation 2.18, Equation 2.19, and Equation 2.20) implemented in Maple 2019 as reported in Addendum B. As seen in Figure 4.9, in the case of

canola rapeseed oil, the model fits well, test 4, the composition data for C18:2 and C18:3, for C18:1, the proposed model is only adapted (with an error of around 10 %) to the start of the reaction until the maximum of C18:1 was reached. For sunflower oil hydrogenation, the first reaction (from C18:3 to C18:2) was neglected because the initial concentration of linolenic acid (0.2 % percentage of C18:3) and so the relative variation is low; the model predicts the compositions of C18:1 and C18:2 with low errors (less than 3 %). It is possible to improve the model, for example, changing the reaction order, introducing the cis-trans equilibrium reaction, and also considering the mass transfer resistances.

Two examples of the fitted data, for the best conditions' tests with Lindlar catalyst, are shown in Figure 4.9, one for canola rapeseed oil (stopped at 120 min reaction) and the other for sunflower oil (360 min). The discrepancies between the experimental data and the model's calculated results are correlated to both a possibly different order of reaction and a more complex reaction mechanism [37]. Although the model does not consider the cis-trans equilibrium reaction and the mass transfer resistances, it predicts the relative percentages in a rather acceptable way.

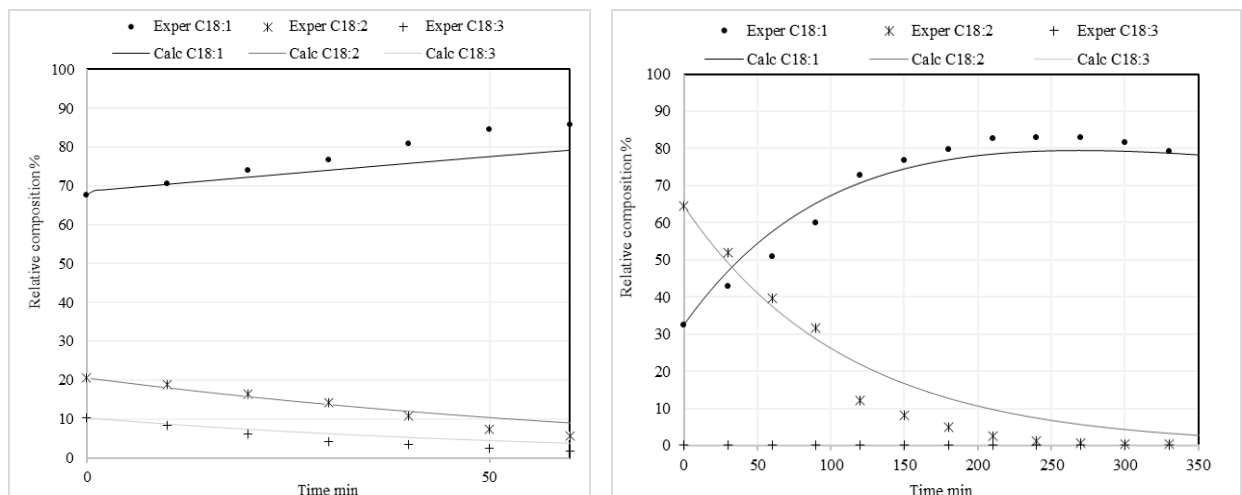


Figure 4.9 Example of data with respective calculated compositions for test 04 ($K1=0.0001$, $K2=0.0122$,

$K3=0.02121$) canola rapeseed oil (left) and test 13 ($K1=0.0006$, $K2=0.009$) sunflower oil (right).

4.2 Pd/HT CATALYST HYDROGENATION REACTIVITY

TESTS

As a start point of the study, two preliminary tests were carried out: Test 14 at 60 °C, 4 bar of hydrogen and 0.5 mg_{catalyst}/mL_{oil}, and Test 15 at 90 °C, 4 bar of hydrogen and 0.5 mg_{catalyst}/mL_{oil} (Table 2.4). These operating conditions of low temperature and pressure were chosen from the literature, as suggested by Fernández et al.[67]. Although the conversion of linoleic C18:2 acid is low (about 31 % and 15% for Test 14 and Test 15, respectively - Figure 4.10), these tests at very low temperature exhibit a promising activity of the original synthesized catalyst compared to the commercial one.

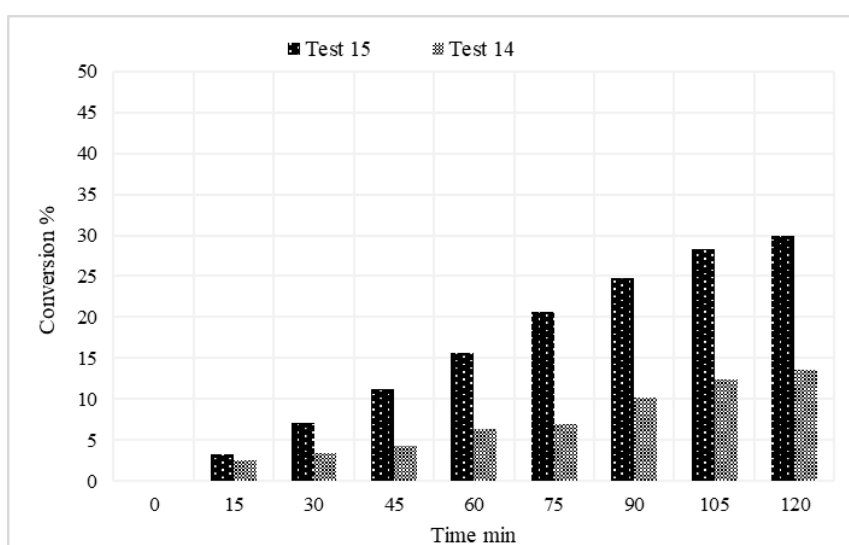


Figure 4.10 Tests 14(60 °C and 4 bar) and 15 (90 °C and 4 bar) of Pd-HT with sunflower oil

Because of few data about the attitude of hydrotalcite as support of catalyst in the hydrogenation processes found in the literature[162], the main parameters such as catalyst concentration, pressure, and the temperature was studied widely, taking into consideration the previous results with Lindlar in order to achieve the best conditions of hydrogenation process with Pd/HT catalyst. By using sunflower oil, five tests were carried out, changing pressure, temperature, and concentration of Pd/HT catalyst in order to compare the performance of the

catalysts under the same operating conditions. All the results from catalytic activity tests are performed with commercial sunflower vegetable oil, reaching maximum linoleic conversion, the high relative percentage of C18:1, and minimum C18:0 content, Table 4.3

Table 4.3 Test results with Pd/HT, SII index, and conversions were calculated when the highest amount of oleic acid was observed.

Entry	t ^a (min)	T (°C)	Cat. (mg/ml)	P (bar)	S _{Le}	SII	χ _{C18:2} (%)	(C18:1) ^b (%)	IV
Test 16	210	120	0.5	4	36.75	0.23	22.39	46.94	127.3
Test 18	240	120	0.5	12	17.8	0.99	95.2	88.2	81.5
Test 20	180	120	2	4	18.4	0.98	96.3	89.9	81.8
Test 22	360	120	1	4	27.5	0.45	29	51.2	123.7
Test 25	270	180	1	4	37.2	0.44	89.1	85.8	85.9

a Time corresponding to the maximum relative percentage of C18:1
b Maximum C18:1 relative percentage obtained during the test

Table 4.3 shows that only at the highest temperature (Test 25), concentration (Test 20), and hydrogen pressure (Test 18), the relative percentage of C18:1 reached a value higher than 85% and C18:2 conversions higher than 89%. From the selectivity point of view, the S_{Le} values increased with temperature, and they are higher than the data found in the literature at 160 °C for alumina supported catalysts 7 and ZSM-5, catalysts 15 [213].

In order to study the effect of the catalyst concentration on the reaction rate of the hydrogenation of sunflower oil, three tests 16, 20, and 22 were compared. Figure 4.11 illustrates a slight increase of the linoleic acid isomers content iso C18:2, 1.5 %, 2.5 %, and 5 %, and a significant increase of the monoene relative percentage C18:1 48 %, 54 %, and 90 % for tests 20, 18, 22 respectively.

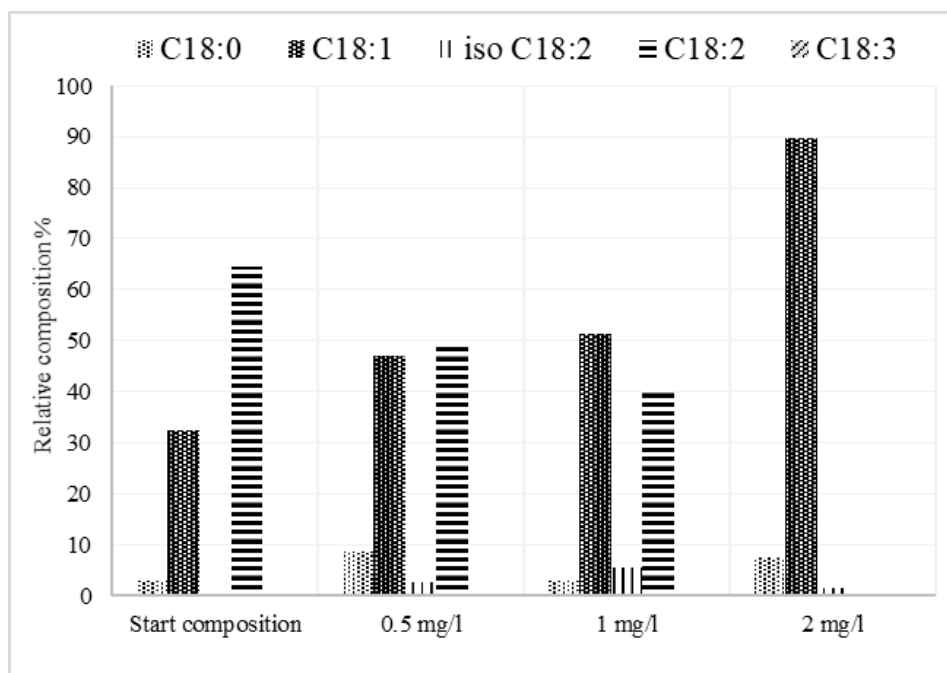


Figure 4.11 Hydrogenation results with Pd/HT catalyst at 120 °C and 4 bar with different catalyst concentrations (0.5, 1 and 2 mg_{catalyst}/mL_{oil}) tests 16, 20, 22

Test 20, in Figure 4.12, shows almost complete conversion of linoleic acid and about 90 % relative composition of monoene after 3 hours of reaction and 81.8 of iodine value, which illustrates a significant efficiency of the hydrogenation process as it decreased from 140 value.

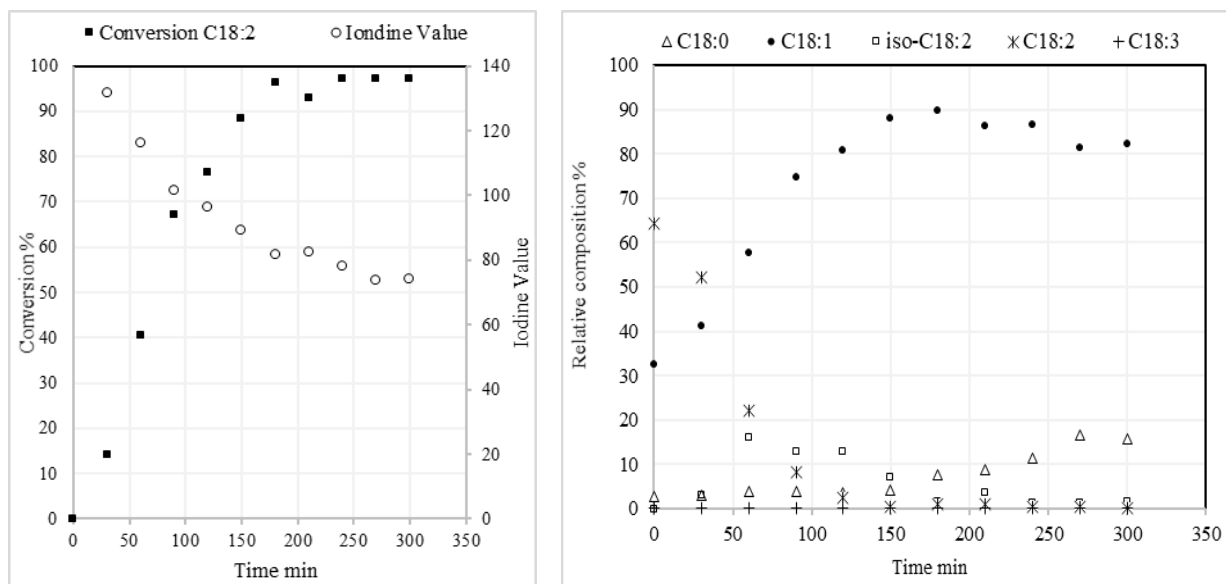


Figure 4.12 Test 20 (120 °C, 4 bar and 2 mg/mL) hydrogenation with sunflower oil and Pd/HT results, conversions of linoleic acid and iodine value vs. time (left) relative percentage of C18 compounds vs. time (right)

As the Pd/HT catalyst has shown very high activity at the conditions of Test 20 (120 °C, 4 bar, and 2 mg_{catalyst}/mL_{oil}), another cycle of 120 minutes (Test 21) has been carried out in order to study the reusability of the catalyst, where the catalyst still has a high activity after the second cycle with about 84.3% conversion of C18:2 vs. 88.30 % after 120 minutes for the first cycle.

Figure 4.13 shows the increasing pressure effect with 120 °C, 12 bar, and 0.5 mg_{catalyst}/mL_{oil} (Test 18), where about all the linoleic acid C18:2 is converted and about 90% of monoene C18:1 after 4 hours of reaction is performed.

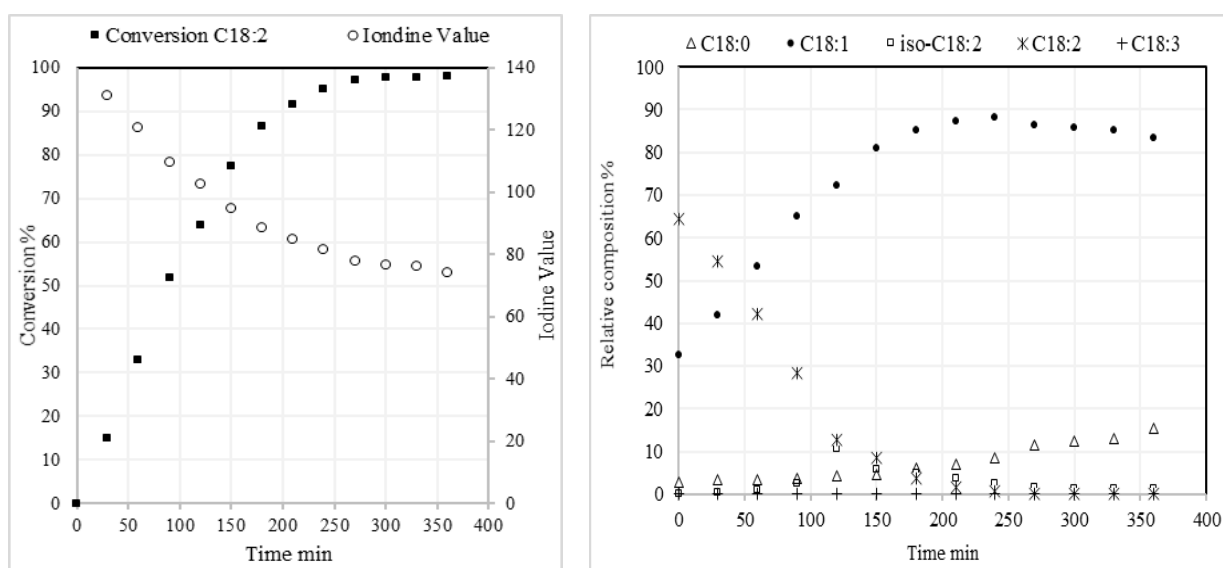


Figure 4.13 Test 18 (120 °C, 12 bar and 0.5 mg/ml) Hydrogenation with sunflower oil and Pd/HT results, conversions of linoleic acid and iodine value vs. time (left) relative percentage of C18 compounds vs. time (right)

Figure 4.14 illustrates pressure effect comparison between test 16 (120 °C, 4 bar, and 0.5 mg_{catalyst}/mL_{oil}) and test 18 (120 °C, 12 bar, and 0.5 mg_{catalyst}/mL_{oil}), the linoleic acid C18:2 conversion is significantly increased simultaneously with the increasing of the relative composition of monoene C18:1, reaching about 89%, which can be explained by increasing the solubility of pure hydrogen in the oil.

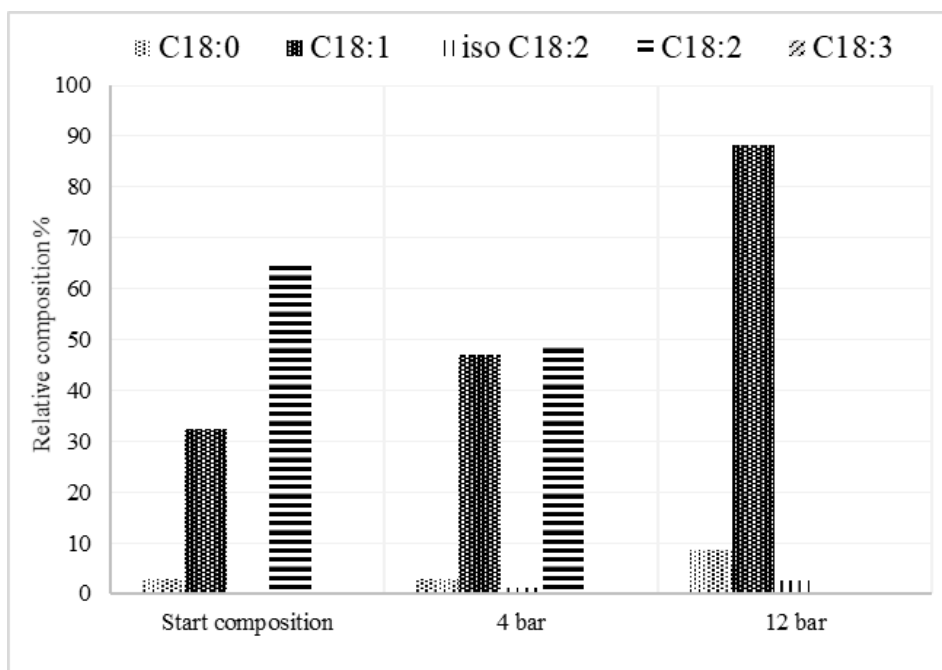


Figure 4.14 Hydrogenation results with sunflower oil and Pd/HT at 120 °C and 0.5 $\text{mg}_{\text{catalyst}}/\text{mL}_{\text{oil}}$ with different pure hydrogen pressure (4 and 12 bar), tests 16 and 18

Also, with these conditions (120 °C, 12 bar, and 0.5 $\text{mg}_{\text{catalyst}}/\text{mL}_{\text{oil}}$) of test 18, it is worth to study the recyclability of Pd/HT synthesized catalyst, a second cycle of 120 minutes (Test 19) has been carried out, and the results illustrate that the catalyst still has a high activity with about 78% conversion of C18:2 vs., 80 % after 120 minutes for the first cycle.

Regarding the study of temperature effects, Test 25 were investigated at 180 °C, 4 bar, and 1 $\text{mg}_{\text{catalyst}}/\text{mL}_{\text{oil}}$ comparing with the Test 22 (120 °C, 4 bar, and 1 $\text{mg}_{\text{catalyst}}/\text{mL}_{\text{oil}}$), which was reported previously, and the results are in line with those expected: high catalytic activity and conversion of linoleic acid C18:2 are achieved Figure 4.15 and this is also in line with results obtained with Lindlar catalyst and in accordance with the literature [214] from the point of view of the conversion value (>85%) using palladium (1%_{w/w}) supported on Al₂O₃ under similar temperature condition (170 °C and 3 bar of H₂).

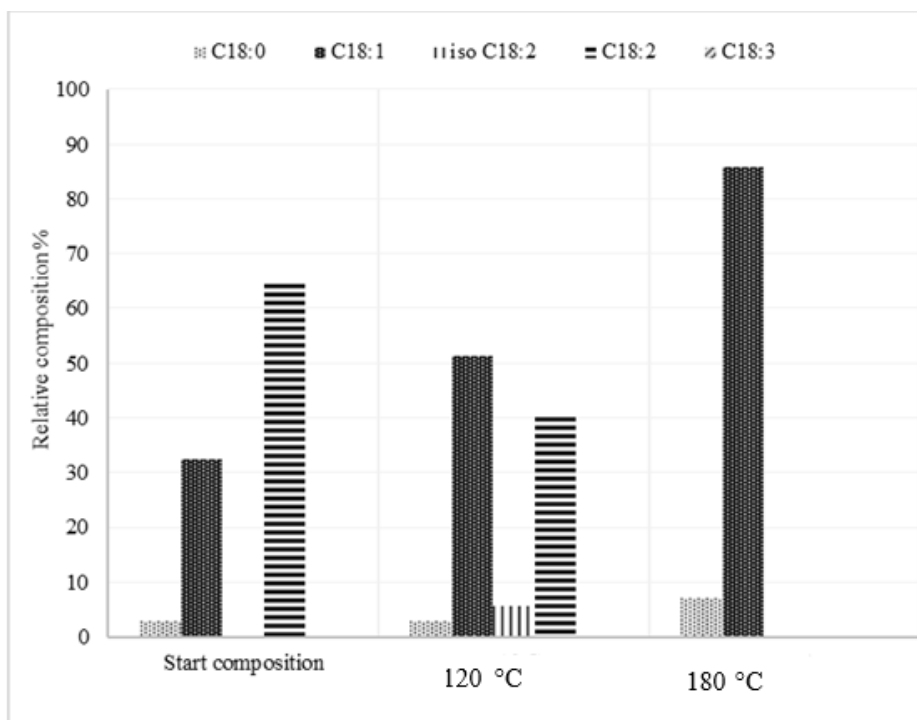


Figure 4.15 Hydrogenation results with sunflower oil and Pd/HT 4 bar and 1 mg_{catalyst}/mL_{oil} with different temperature (120 and 180 °C), tests 22 and 25

Figure 4.16 illustrates the hydrogenation reaction results of Test 25 and shows that almost complete conversion of linoleic acid was achieved after about 6 hours and high relative composition of monoene C18:1 of about 86% after 4 hours and 7.2% of stearic acid C18:0.

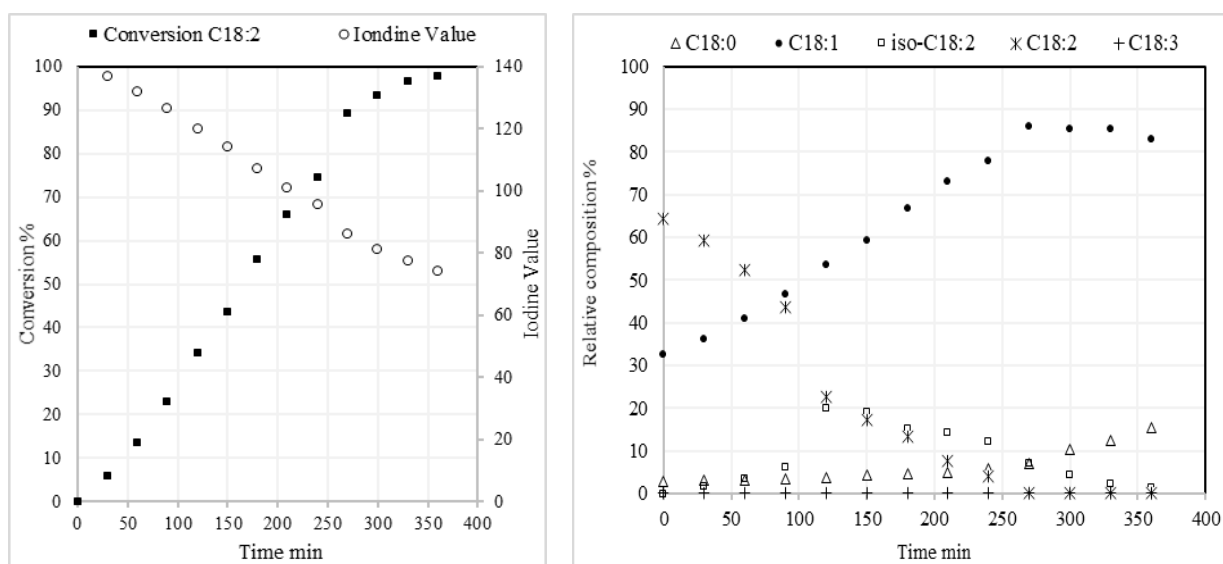


Figure 4.16 Test 25 (180 °C, 4 bar and 1 mg/mL) Hydrogenation with sunflower oil and Pd/HT results, conversions of linoleic acid and iodine value vs. time (left) relative percentage of C18 compounds vs. time (right)

The catalyst recycling effect was conducted to evaluate the catalyst's efficiency and stability after several cycles. So, four cycles have been applied with the Test 25 conditions (180 °C, 4 bar, and 1 mg_{catalyst}/mL_{oil}). Figure 4.17 shows the results of four cycles and illustrates that although the catalyst still active after the second cycle with about 82.7 % conversion of C18:2 vs. 90 % for the first cycle, there is a degradable decrease of the activity towards the 4th cycle.

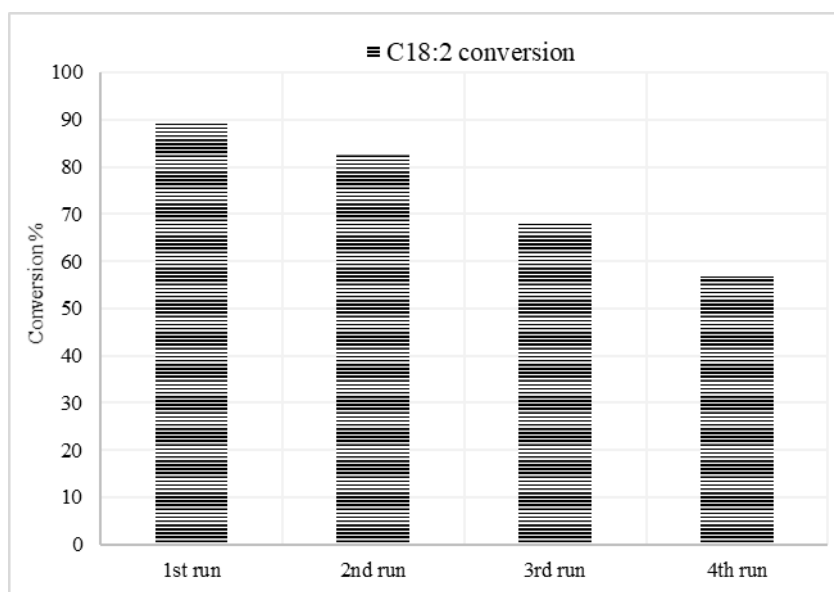


Figure 4.17 Test results for the cyclic test at (180 °C, 4 bar, and 1 mg_{catalyst}/mL_{oi}) with Pd/HT.

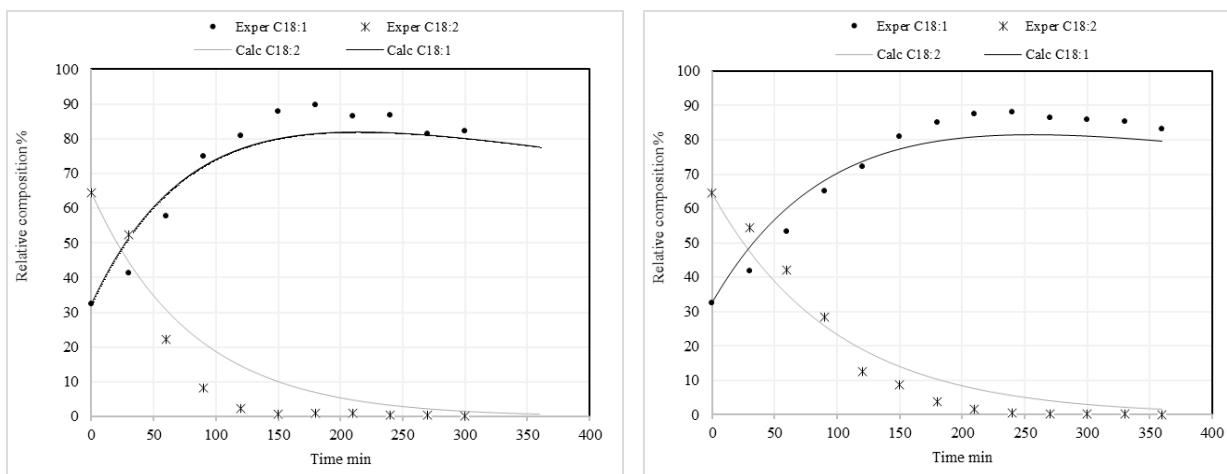
In order to illuminate some information on the cyclic tests and explain the loss of activity and efficiency of the catalyst over cycles, the catalyst was recovered from the reaction medium and reutilized in consecutive runs (simulation with industry procedure). As mentioned, and discussed in the case of Lindar, the reasons behind the deactivation and the gradient decrease of the activity over the cycles are:

- Poisoning with components of the oil.
- Formation of coke on the palladium catalyst.
- Recovery does not complete between cycles and loss in catalyst mass.

The samples' post characterization was not possible since the reacted hydrogenated oil remains inside the catalyst also after a washing protocol with different solvents (toluene, hexane, acetone, and chloroform) for three times.

In the end, it is worth noting that the Pd/HT catalyst has shown better performance than the Lindlar catalyst since comparable results are obtained with less amount of catalyst and longer life cycle (120 min for Pd/HT vs. 60 min for Lindlar) was investigated.

Regarding the fitted data, for the best conditions' tests with Pd/HT catalyst and sunflower oil, where the first reaction (from C18:3 to C18:2) was neglected because the initial concentration of linolenic acid (0.2 % percentage of C18:3) and so the relative variation is low, three examples are shown in Figure 4.18, for the test 20 (120 °C, 4 bar, 2 mg_{catalyst}/mL_{oil}), the model about fits well with an error around 10%, also for the tests 25 (180 °C, 4 bar, 1 mg_{catalyst}/mL_{oil}) and test 18 (120 °C, 12 bar, 0.5 mg_{catalyst}/mL_{oil}) there is a fitting with the model, error about 10%.



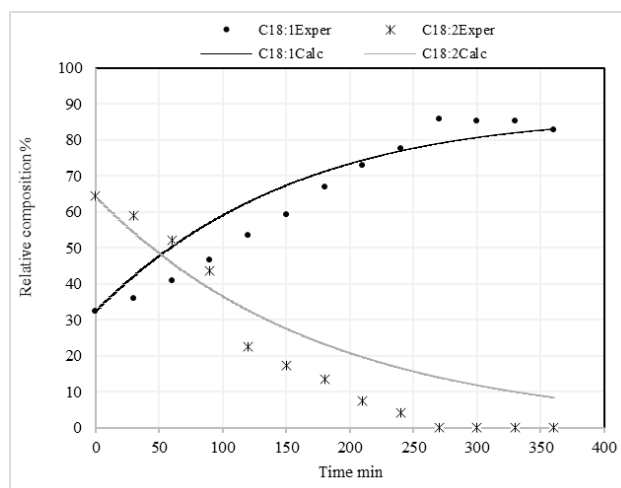


Figure 4.18 Figure 4.19 Three Examples of data with respective calculated compositions for test 20 (120 °C, 4 bar, 2 mg_{catalyst}/mL_{oil}) (up left) ($K1=0.0007$, $K2=0.01232$), test 18 (120 °C, 12 bar, 0.5 mg_{catalyst}/mL_{oil}) (up right) ($K1=0.0006$, 0.010124), and test 25 (180 °C, 4 bar, 1 mg_{catalyst}/mL_{oil}) (down) ($K1=0.0002$, $K2=0.005642$).

4.3 Pd/FAC CATALYST HYDROGENATION REACTIVITY

TESTS

The cenospheres material (FAC) is original support; in this thesis, it has been used for the first time as a supported catalyst in the hydrogenation processes, as it is waste material, obtaining good results will very positive and exciting from the environmental and economic points of view. Taking into account the previous results with Lindlar and Pd/HT in order to understand the attitude of cenospheres and to achieve the best conditions of the hydrogenation process using Pd/FAC and sunflower oil, three tests were carried out under different pressure conditions, temperature, and concentration of catalyst (Table 2.5). All the catalytic activity tests results, showing the maximum linoleic conversion, high relative percentage of C18:1, and minimum C18:0 content, are reported in Table 4.4.

Table 4.4 Test results with Pd/FAC, SII index, and conversions calculated when the highest amount of oleic acid was observed.

Entry	T ^a (min)	T (°C)	P (bar)	Cat. (mg/ml)	S _{Le}	SII	χ _{C18:2} (%)	(C18:1) ^b (%)	IV
Test 29	360	180	4	1	2.5	0.9	57.8	64.73	100.7
Test 30	360	120	8	1	15.1	0.39	99.6	84.04	72.9
Test 31	210	240	8	1	23.7	1.21	97.9	82.74	86.3
<p>a Time corresponding to the maximum relative percentage of C18:1</p> <p>b Maximum C18:1 relative percentage obtained during the test</p>									

The selectivity of linoleic S_{Le} acids in Table 4.4 allows concluding that the S_{Le} results are higher (test 31) with increasing the pressure and the temperature; thus, the reaction rate of linoleic fatty acids is higher than the formation rate of stearic acid due to the selectivity of the reaction towards the monoene C18:1.

As in the previous two studies, the starting point of operating conditions is 180 °C, 4 bar of hydrogen, and 200 mg of Pd/FAC catalyst for 200 mL_{oil} with commercial sunflower oil.

Figure 4.19 illustrates the hydrogenation reaction results of Test 29 and shows that the maximum achieved the conversion of linoleic acid under these conditions (180 °C, 4 bar, and 1 mg/mL) was about 60% after 6 hours and relative composition of monoene C18:1 about 65%, but the conversion percentage still tends to increase with the time which means that increasing the reaction time we should get better results of monoene C18:1.

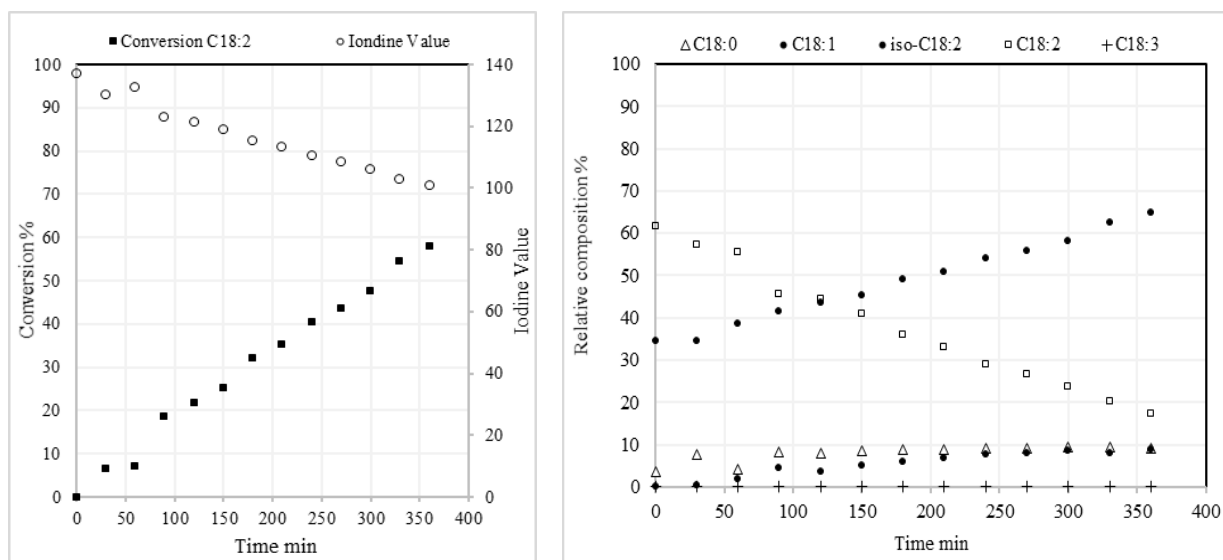


Figure 4.19 Test 29 (180 °C, 4 bar and 1 mg/mL) Hydrogenation with sunflower oil and Pd/FAC results, conversions of linoleic acid and iodine value vs. time (left) relative percentage of C18 compounds vs. time (right)

It could also be worth to increase the pressure of H₂ and decrease the temperature to 120 °C in order to achieve better results of monoene: Test 30 Figure 4.20, demonstrates that the reaction rate increase and the complete conversion of C18:2 are observed after about 6 hours, which means that higher concentration of the H₂ in the oil leads to higher activity. However, a relative percentage of monoene c18:1 about 84% and stearic acid about 18% are achieved after 6 hours of the reaction.

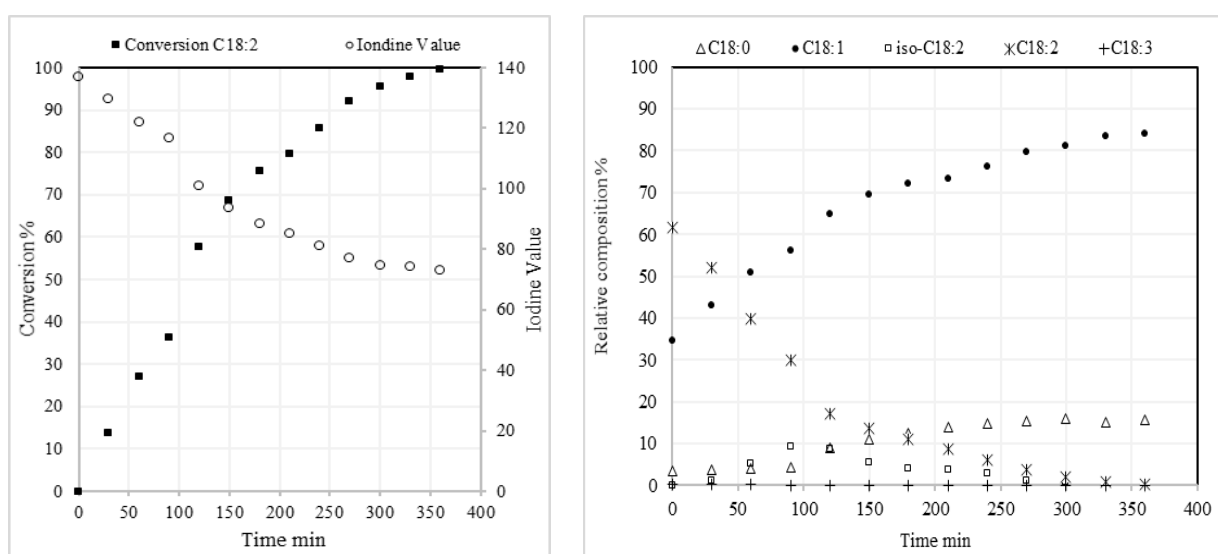


Figure 4.20 Test 30 (120 °C, 8 bar and 1 mg/mL) Hydrogenation with sunflower oil and Pd/FAC results, conversions of linoleic acid and iodine value vs. time (left) relative percentage of C18 compounds vs. time (right)

Increasing the temperature higher till 240 °C with the same pressure of hydrogen 8 bar, the conversion of linoleic acids is increased to arrive about 100%: Test 31 (240 °C, 8 bar, and 1 mg/mL) in Figure 4.21, illustrates that after about four hours of hydrogenation reaction almost all the polyunsaturated fatty acids are transformed in C18:1 and C18:0 compounds with iodine value 86.3. with a maximum concentration of C18:1 (82.7 %) and stearic acid C18:0 8 %.

The comparison between the two tests 30 (120 °C, 8 bar, and 1 mg/mL) and 31 and (240 °C, 8 bar, and 1 mg/mL) allows concluding that the increase of the hydrogen concentration in the oil plays a very important point to achieve a high relative percentage of monoene C18:1 of about 85%, whereas increasing the temperature plays on the selectivity towards the monoene C18:1 S_{Le} which has increased to 23.7 in test 31.

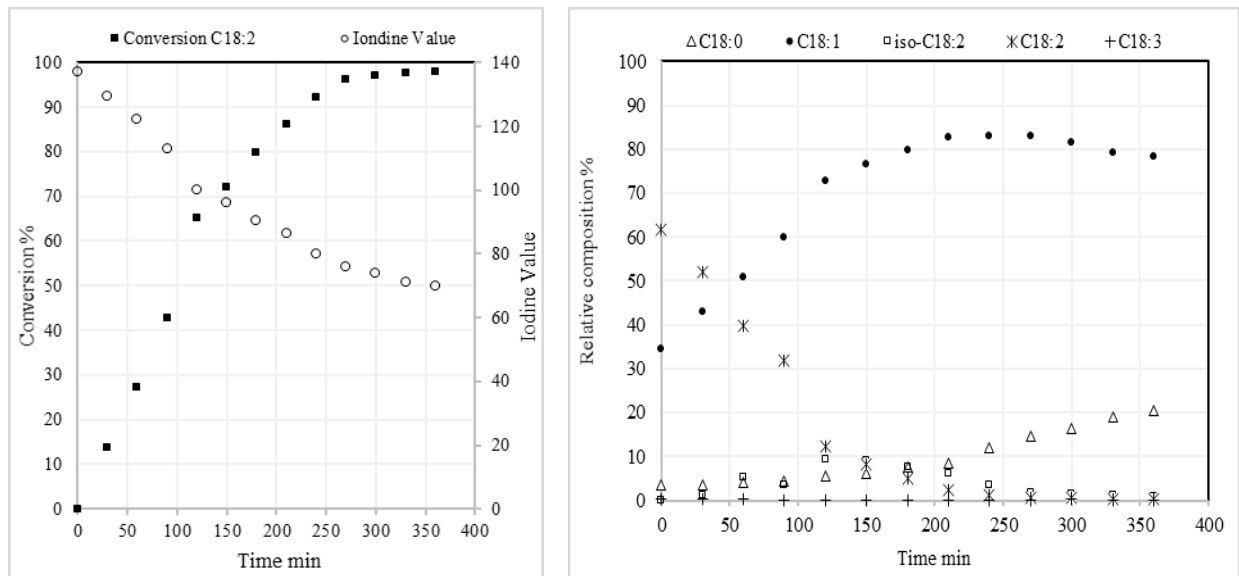


Figure 4.21 Test 31 (240 °C, 8 bar and 1 mg/mL) Hydrogenation with sunflower oil with Pd/FAC results, conversions of linoleic acid and iodine value vs. time (left) relative percentage of C18 compounds vs. time (right)

Figure 4.22 illustrates the temperature effect on the activity and selectivity where under a pressure of 8 bar, the lower temperature is better for selectivity, while for the activity, the same result of about 83% of monoene C18:1 is obtained.

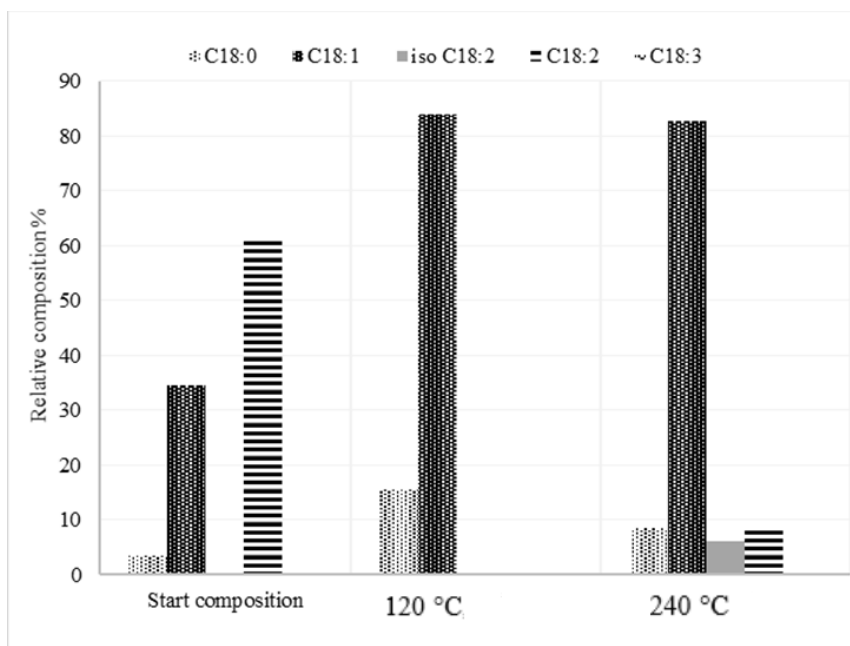


Figure 4.22 Hydrogenation results with sunflower oil and Pd/FAC at 8 bar and $1 \text{ mg}_{\text{catalyst}}/\text{mL}_{\text{oil}}$ with different temperatures (120 and 240 °C), tests 30 and 31

Fitting data, for the best conditions with Pd/FAC catalyst and sunflower oil, Figure 4.23 clarifies that for the test 30 (120 °C, 8 bar, $1 \text{ mg}_{\text{catalyst}}/\text{mL}_{\text{oil}}$), the model about fits well with an error around 5 % before the minutes 100 of the reaction time, where for the tests 31 (240 °C, 8 bar, $1 \text{ mg}_{\text{catalyst}}/\text{mL}_{\text{oil}}$) is a fitting with the model, error about 7%.

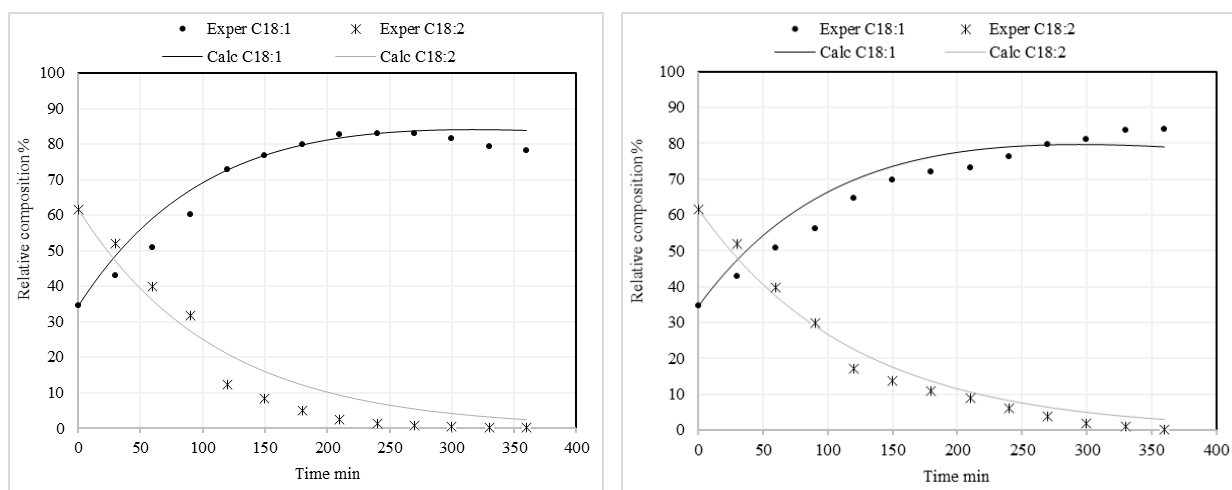


Figure 4.23 Two examples of data with respective calculated compositions for test 31 (240 C, 8 bar, $1 \text{ mg}_{\text{catalyst}}/\text{mL}_{\text{oil}}$) (left) ($K1=0.0004$, $K2=0.009$), test 30 (120 C, 8 bar, $1 \text{ mg}_{\text{catalyst}}/\text{mL}_{\text{oil}}$) (right) ($K1=0.0006$, $K2=0.0083$).

4.4 CONCLUSION

Mono-metallic catalysts (Lindlar, 1 %wt Pd/HT, and 2 %wt Pd/FAC) in the hydrogenation of vegetable oils (canola and sunflower oil) was proved in this work.

Table 4.5 A comparison of hydrogenation results obtained with various Pd-catalysts.

Cat.	Oil	T (C)	P (bar)	(mg/ml)	T ^{max} (min)	S _{Ln} (%)	S _{Le} (%)	SII	IV	χ _{C18:3} (%)	χ _{C18:2} (%)	C18:1 (%)
Pd-Lindlar	Canola	120	8	4	120	1.3	23.9	0.7	89.2	84.6	60.8	82.6
		180	4	4	90	1.4	33.6	1.4	89.3	90.1	84.6	88.4
		180	12	4	60	1.3	20.2	1.2	79.4	92.7	84.3	86.0
		180	4	2	120	1.7	35.8	1.5	91	92.1	51.4	83.2
		180	4	1	120	2.2	37.3	1.8	93	90.6	51.0	84.4
Pd-HT	Sunflower	180	4	4	240	-	13.9	2.3	80	-	98.7	83.0
		120	4	0.5	210	-	36.7	0.23	127.3	-	22.39	46.94
		120	12	0.5	240	-	17.8	0.99	81.5	-	95.2	88.2
		120	4	2	180	-	18.4	0.98	81.8	-	96.3	89.9
		120	4	1	360	-	27.5	0.45	123.7	-	29	51.2
Pd-FAC	Sunflower	180	4	1	360	-	2.5	0.9	100.7	-	57.8	64.73
		120	8	1	360	-	15.1	0.39	72.9	-	99.6	84.04
		240	8	1	210	-	23.7	1.21	86.3	-	97.9	82.74

The theoretical optimal value of IV is 83.6 corresponding to completed conversion of C18:3 and C18:2 in C18:1.

Vice versa, the optimum values of S_{Ln} , S_{le} can't be determined because these ratios are related to kinetic equilibrium constants and the classical definition of selectivity (ratio of moles of product divided on moles of reference reagent) is not applied. Anyway, it is possible to observe that small values of selectivities correspond to higher conversions.

For the commercial Lindlar catalyst, the main highlights are:

I The best hydrogenation conditions are at 180 °C and 4 bar with the high formation of C18:1 (both elaidic and oleic) and low formation of stearic acid (less than 10%);

II In order to study the recyclability of the catalyst, it was tested in cyclic tests, which was illustrated that the activity decreases by every cycle, which could be solved with a catalyst make-up, and then it could be probably reusable over multiple cycles. This deactivation phenomenon of the catalyst must be referred to as a poisoning linked to the natural poisons found in vegetable oils or due to a loss of catalyst between one cycle and the successive one;

III Using sunflower oil, the Lindlar catalyst has shown good activity in 6 hours of the tests, with less selectivity, which could be referred to as the different reaction velocities of linolenic and linoleic acid reaction rates.

For synthesized Pd/HT catalyst, the most important highlights are:

I Pd/HT had shown more selectivity and lower activity compared with Lindlar catalyst; therefore, it had taken longer reaction times to obtain the same degree of hydrogenation (conversion of C18:2) at 180 °C;

II Although at a lower temperature (120 °C), the Pd/HT catalyst has illustrated a good activity and selectivity;

III The cyclic tests on Pd/HT had shown that the catalyst could be recovered and reused in successive tests, directly without complicated washing of the catalyst. The activity and selectivity losses during one run could be easily overcome by means of a catalyst's make-up, so reducing its cost.

In the case of studying the synthesized Pd/FAC catalyst, the main results are:

I Pd/FAC had illustrated lower activity 60 % of linoleic acid conversion under the best conditions of the previous two catalysts Lindlar and Pd/HT (about 100 % of linoleic acid conversion) (180°C and 4bar), which could be due to the small specific surface area ($S_{\text{BET}} 0.26 \pm 0.03 \text{ m}^2/\text{g}$), Cause the active sites, are formed typically in the surface of the catalyst, so, if the material has more porosity, so it has more surface area to form the sites and this usually lead to more activity;

II Increasing the concentration of the hydrogen which dissolved in the oil to the double had shown much better activity and more selectivity towards the monoene over 85%;

III With high temperature 240 °C and hydrogen pressure 8 bar, the Pd/FAC catalyst had also illustrated more activity (100% linoleic acid conversion) and selectivity towards C18:1 (about 90%)

These results at the hydrogenation level encouraged us to continue our work to remove the oxygen from the vegetable oils with hydrodeoxygenation, decarboxylation, and decarbonization levels of hydro-processing reactions to the green diesel (chapter 5).

CHAPTER 5

This chapter reports the activity test results of the catalytic deoxygenation reactions on the sunflower oils using:

- *Lindlar catalyst test activities;*
- *Pd/FAC catalyst test activities;*
- *CoMo/FAC catalyst test activities;*
- *NiMo/FAC catalyst test activities;*
- *NiMo/zeoliteX catalyst test activities;*

5 DEOXYGENATION REACTIVITY TESTS

5.1 LINDLAR CATALYST DEOXYGENATION REACTIVITY TESTS

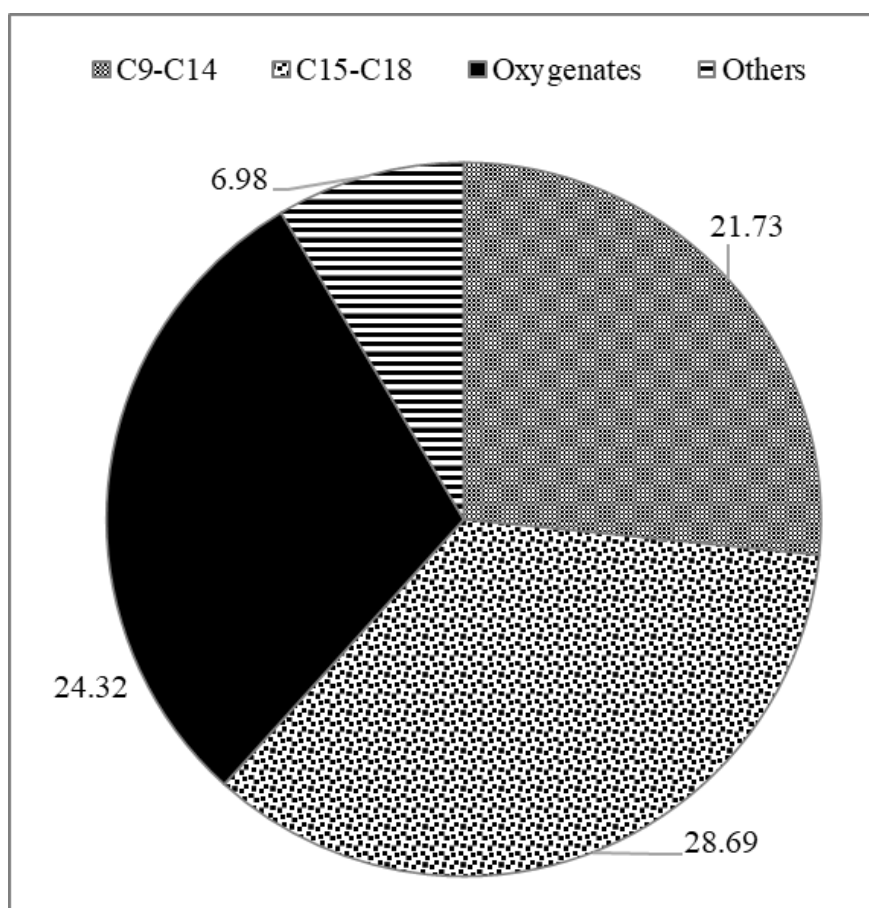
Before starting the catalytic deoxygenation reactions on the triglyceride's TG feedstocks, it was worth to examine the GC analysis on a commercial diesel C.D., Table 5.1 and Figure 5.1 demonstrates the alkanes relative percentage (C10-C24), the oxygenates (methyl palmitate, methyl octadecenoate, and methyl stearate), and others unidentified compositions, Nowadays, from a sustainable point of view, the commercial diesel is blended with the synthesized biodiesel with maximum percentage 30%, And this could explain the oxygenates existing in this commercial sample.

The diesel's oxygenated content could decrease its heating value and stability, so the main challenge of this section is represented by the performing of catalytic deoxygenation reactions with vegetable oil (sunflower) and getting the green diesel with the properties of the pure mineral diesel.

Table 5.1 GC analysis results on a commercial diesel sample.

Entry	C ₁₀	C ₁₁	C ₁₂	C ₁₃	C ₁₄	C ₁₅	C ₁₆	C ₁₇	C ₁₈	C ₁₉	C ₂₀	C ₂₁	C ₂₂	C ₂₃	C ₂₄	Oxygenates	Others
C.D.	2.13	3.56	4.38	5.09	6.57	8.14	6.97	7.91	5.67	4.61	3.56	3.33	2.67	2.13	1.87	24.32	6.89

The oxygenates are methyl palmitate, methyl octadecenoate, and methyl stearate.
Others are unidentified GC peaks.

Figure 5.1 Light (C₉-C₁₄), diesel (C₁₅-C₁₈), and oxygenates ranges distribution in a commercial diesel sample.

As the palladium is one of the most powerful catalysts for the deoxygenations reactions [215], and the commercial Lindlar catalyst, palladium poisoned with Pb and supported on calcium carbonate, had exhibited in this research (chapter4) excellent results on the vegetable oils

hydrogenation processes, its activity on more advanced stages of the catalytic hydrothermal processing, completed hydrogenation, hydrodeoxygenation, decarboxylation, and decarbonylation was investigated. The catalytic deoxygenation activity tests using Lindlar catalyst, as a reference point, (Table 2.7) results performed with stearic acid and a commercial sunflower vegetable oils, as triglycerides feedstocks TG, are illustrated in this section as hydrocarbons C_n , light hydrocarbons (C_9 , C_{10} , C_{11} , C_{12} , C_{13} , C_{14}) and Diesel range hydrocarbons (C_{15} , C_{16} , C_{17} , C_{18}), selectivity, conversions, and yield of the product compositions after transesterification. The most meaningful tests results are reported in Table 5.2 and Table 5.3.

Table 5.2 Lindlar catalytic hydrothermal deoxygenation test results with stearic acid and sunflower oil.

Entry	Cat/TG (wt%)	T (°C)	P (bar)	C_9	C_{10}	C_{11}	C_{12}	C_{13}	C_{14}	C_{15}	C_{16}	C_{17}	C_{18}	Oxygenates	Others
Test 01	10	300	20 N_2	12.7	7.4	3.1	3.4	4.7	6.8	24.8	5.8	20.5	1.0	3.1	6.7
Test 02	10	300	40 H_2	0.57	0.43	0.67	0.6	0.67	0.96	7.7	4.9	24.6	7.7	39.1	12.1

These results correspond to the maximum relative percentage of the range of alkanes C_{15} - C_{18} obtained during the tests.

Oxygenates are methyl stearate, methyl myristate, methyl palmitate, and nonadecane

Others are the non-identified GC peaks.

The deoxygenation reactivity test on the stearic acid over Lindlar catalyst, test 01 (300 °C, 20 bar N_2 , 10 wt % cat., and 20g hexane as solvent) demonstrates an exciting diesel range (C_{15} - C_{18}) after 6 hours 52.1%, and a very low percentage of the oxygenates 3.1%, it is clear also the high percentage of the light hydrocarbons range (C_9 - C_{14}) 38.1% which means that the cracking

process has happened during the reaction (Figure 5.2). Figure 5.3 shows the estimating of the relative percentage of the liquid compositions after 3hr and 6hr of the reaction time, where the best diesel range was obtained after 6 h of reaction 52%, it also shows selectivity of the catalyst towards DCO/DCO₂ reaction pathways.

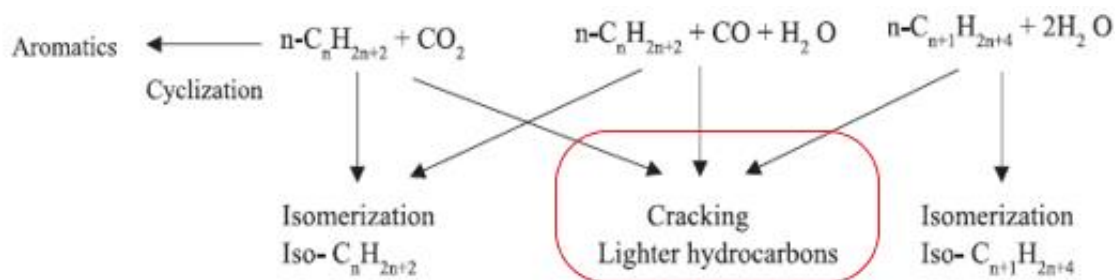


Figure 5.2 Cracking process during the deoxygenation reaction [216].

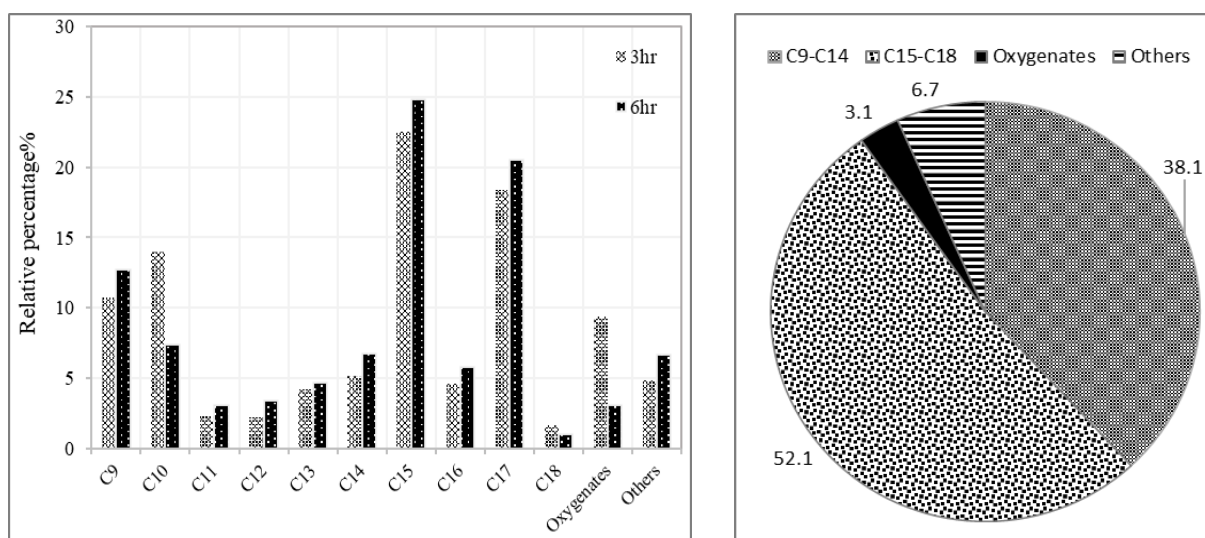


Figure 5.3 Test 01 (300 °C, 20 bar N₂ and 10 wt% cat.) deoxygenation with stearic acid and Lindlar catalyst results, distribution of the light and diesel range hydrocarbons at the best conditions (right) relative percentage of product compounds vs. time (left)

The same catalyst, Lindlar, for carrying out the same catalytic deoxygenation test with sunflower oil as a feedstock, test 02 (300 °C, 40 bar H₂, 10% cat., and 20g hexane as solvent) shows about no cracking process with a good diesel range after 3 and 8 hr of the reaction time, 43.6 % and 44.9 % respectively. Figure 5.4 (test 02) has illustrated a high percentage of the oxygenates comparing with the previous (test 01), which is logical consequence of the complex

of fatty acids in the sunflower oil comparing with stearic acid (test 01), which didn't need the hydrogenation step and the nitrogen gas has been used for pressurizing the reactor, on the other hand, with the oil all the stages of the catalytic hydrothermal deoxygenation process (hydrogenation, deoxygenation, isomerization) the pressure of the pure hydrogen 40 bar is necessary.

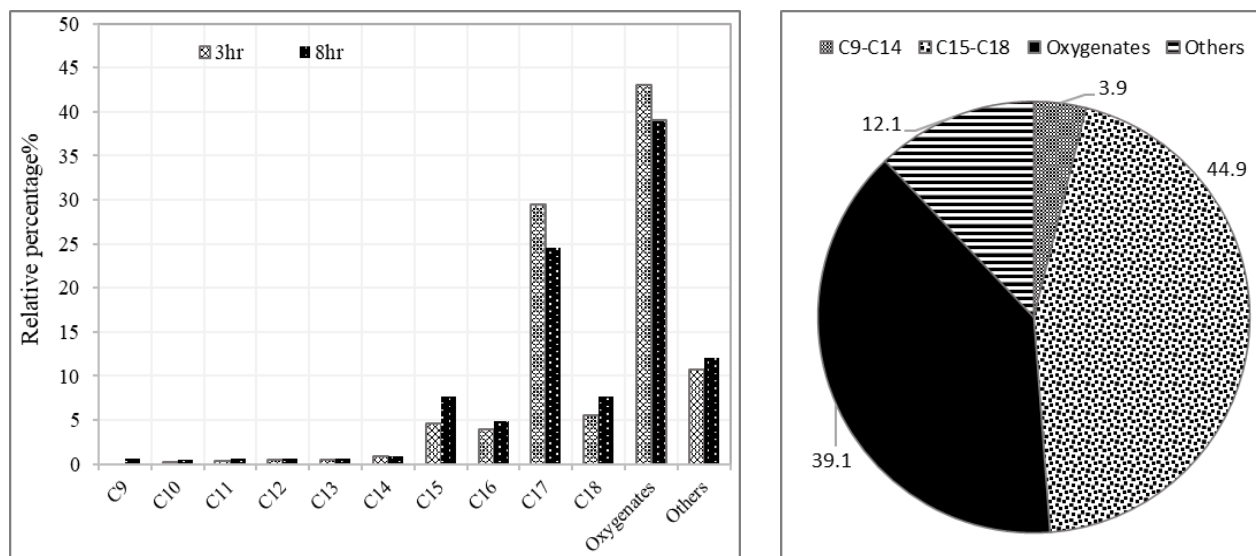


Figure 5.4 Test 02 (300 °C, 40 bar H_2 and 10 wt% cat.) deoxygenation with sunflower oil and Lindlar results, distribution of the light and diesel range hydrocarbons at the best conditions (right) relative percentage of product compounds vs. time (left)

In order to complete the studying and knowing of the conversion and the selectivity, Table 5.3 illustrates the total conversion of the raw material X_{TG} for stearic acid and sunflower oil, the conversion in hydrocarbons X_n , Green Diesel yield Y_{GD} , and the pathway selectivity hydrodeoxygenation HDO or the decarboxylation/decarbonylation DCO_2/DCO , $SI_{15/16}$ and $SI_{17/18}$.

From Table 5.3, we can presume that the selectivity of the commercial Lindlar catalyst is more towards C₁₇ and C₁₅ in test 01 and test 02 cases where both $SI_{17/18}$ and $SI_{15/16} > 1$, which means that the deoxygenation reaction is more selective to the decarboxylation/decarbonylation pathway DCO_2/DCO than hydrodeoxygenation one HDO.

Table 5.3 Lindlar catalytic hydrothermal deoxygenation test results, total conversion, Green diesel conversion, and HDO selectivity.

Entry	X _{TG} (%)	X _n (%)	Y _{GD} (%)	SI _{15/16}	SI _{17/18}
Test 01	85.8	22.1	4.0	4.3	20.5
Test 02	69.4	56.4	22.9	1.6	3.2

These values are calculated for the product after the transesterification reaction.

Figure 5.5 illustrates the Y_{GD} % of the final product after the transesterification analysis, where the yield of the GD hydrocarbons C₁₅-C₁₈ is about 23%, and the yield of the oxygenated compositions (methyl stearate, methyl myristate, methyl palmitate, and nonadecane) is about 39% and TG conversion about 70%. So, practically we can estimate that using Pd Lindlar in the deoxygenation process of 1 liter sunflower oil produces 229 g green diesel range (C₁₅-C₁₈).

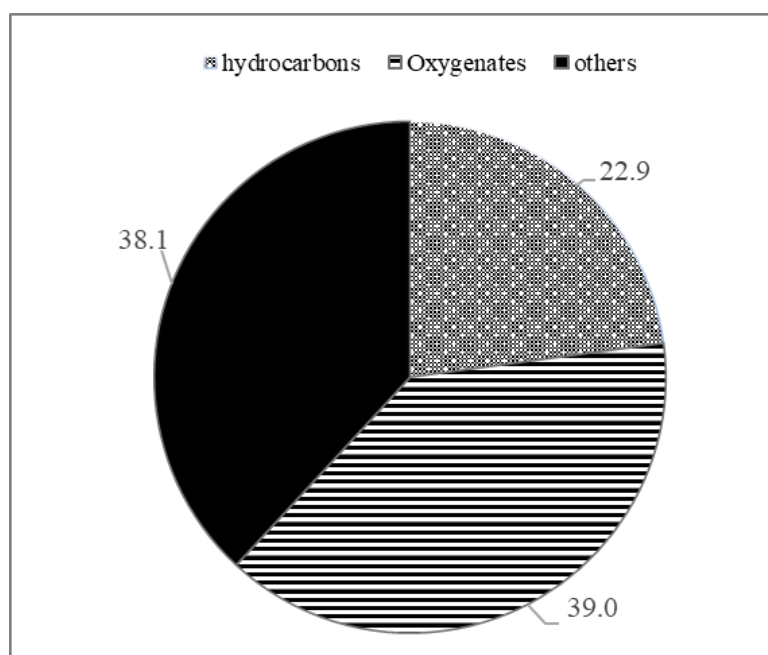


Figure 5.5 Test 02 (300 °C, 40 bar H₂, and 10 wt% cat.) deoxygenation of sunflower oil with Lindlar: percentage results of green diesel hydrocarbons, oxygenates, and others

5.2 Pd/FAC CATALYST DEOXYGENATION REACTIVITY

TESTS

As we mentioned before, that the palladium-based catalysts are the most effective for hydrogenation and deoxygenation[217], it has been synthesized the 2% palladium catalyst supported over FAC materials. Since there is almost no data about the attitude of FAC as a supported catalyst in the deoxygenation processes in the literature, starting with the stearic acid as the triglycerides feedstock test 03 under (300 °C, 20 bar N₂, 10 wt% cat., and 20g hexane as solvent) conditions and then studying the effect of the hydrogen pressure on the reaction with vegetable oil (sunflower) has been followed, taking in consideration the previous results with Lindlar in order to achieve the best conditions of deoxygenation process catalyst.

Using sunflower oil, two tests were carried out, test 04 and test 05 (320 °C, 10 wt% cat., and 20g hexane as solvent) under 20 bar and 40 bar of H₂, respectively. All the results from catalytic hydrothermal activity tests performed with stearic acid and sunflower vegetable oils as triglycerides feedstock (TG) are reported in this section, such as light hydrocarbons content C₉-C₁₀, Diesel range hydrocarbons C₁₅ - C₁₈, selectivity, conversions, and yield of the product compositions after transesterification. The most interesting tests results are reported in Table 5.4 and Table 5.5.

Table 5.4 Pd/FAC catalytic hydrothermal deoxygenation test results with stearic acid and sunflower oil.

Entry	Cat/TG (wt%)	T (C)	P (bar)	C ₉	C ₁₀	C ₁₁	C ₁₂	C ₁₃	C ₁₄	C ₁₅	C ₁₆	C ₁₇	C ₁₈	Oxygenates	Others
Test 03	10	300	20 N ₂	5	3.39	2.36	1.99	1.94	3.06	23.8	4.04	18.5	2.1	33.9	0
Test 04	10	320	20 H ₂	3.7	3.3	2.2	2.3	2.5	3.3	6.5	7.4	28.6	24	13	3.2
Test 05	10	320	40 H ₂	0	0.3	0.3	0	1	1.5	3.3	5.2	23.5	45.8	18.3	0.8

These results correspond to the maximum relative percentage of the range of alkanes C₁₅-C₁₈ obtained during the tests.

Oxygenates are methyl stearate, methyl myristate, methyl palmitate, and nonadecane

Others are the non-identified GC peaks.

The deoxygenation reactivity test on the stearic acid as TG with Pd/FAC catalyst (test 0 3) shows a very interesting diesel range (C₁₅-C₁₈) after 3 h 48.3 %, 17.7 % of the light hydrocarbons (C₉-C₁₄), and 33.9 % oxygenates (methyl stearate, methyl myristate, methyl palmitate, and nonadecane). Figure 5.6 shows the relative percentage of the liquid compositions after 3hr and 6hr, where the best diesel range was after 3 h of reaction, while after 6 h we have got more oxygenates 56.3% and less hydrocarbon diesel range (35.32%). These results are in line, although our catalyst with 2% Pd/FAC with the results obtained by I.Edeh et. al. using palmitic acid and 5% Pd/C catalyst in order to get 35.4% diesel range [218].

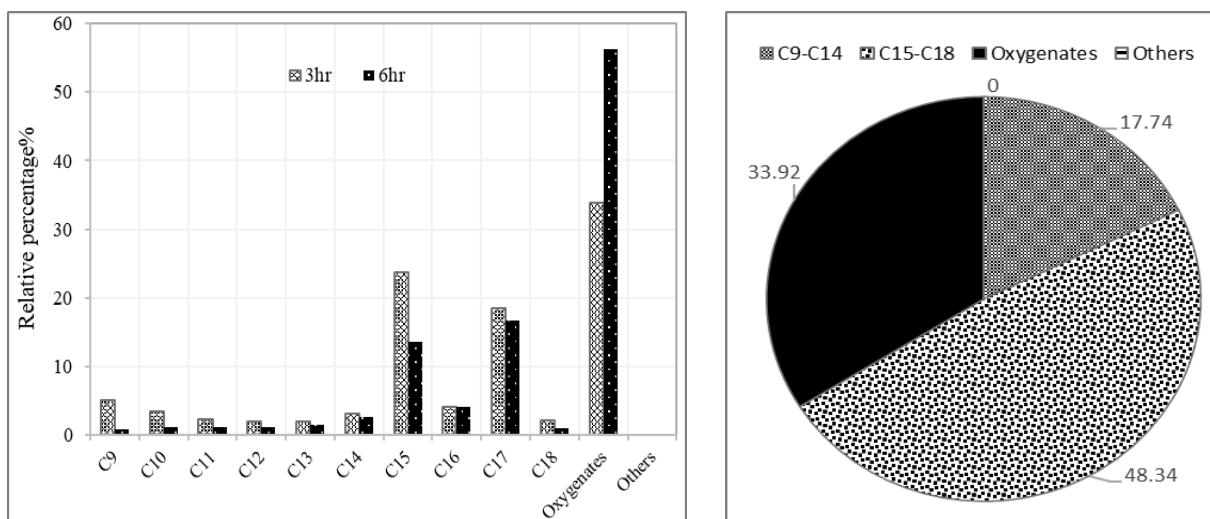


Figure 5.6 Test 03 (300 °C, 20 bar N_2 and 10 wt% cat.) deoxygenation with stearic acid and Pd/FAC results, distribution of the light and diesel range hydrocarbons at the best conditions (right) relative percentage of product compounds vs. time (left)

Pd/FAC for carrying out the catalytic deoxygenation tests with sunflower oil confirms the high activity of the palladium even under low pressure of hydrogen 20 bar (test 04) with about 70% of the hydrocarbon diesel range, which is in line with the results that performed by Veriansyah et al. where they use (400 °C, 20 bar H_2 , Pd/ Al_2O_3 , and soybean oil) [219]. Figure 5.7 illustrates the results of test 04 at 4 and 7 h of the reaction time, where at the first 4 h of the reaction, we have got about 61% of the green diesel range (C_{15} - C_{18}), 29% of light hydrocarbons (C_9 - C_{14}), and about 8% oxygenates, whereas after 7 h of the reaction time we have obtained better conditions of about 67% of green diesel range (C_{15} - C_{18}), 17% of light hydrocarbons (C_9 - C_{14}), and about 13% oxygenates (methyl stearate, methyl palmitate, and nonadecane).

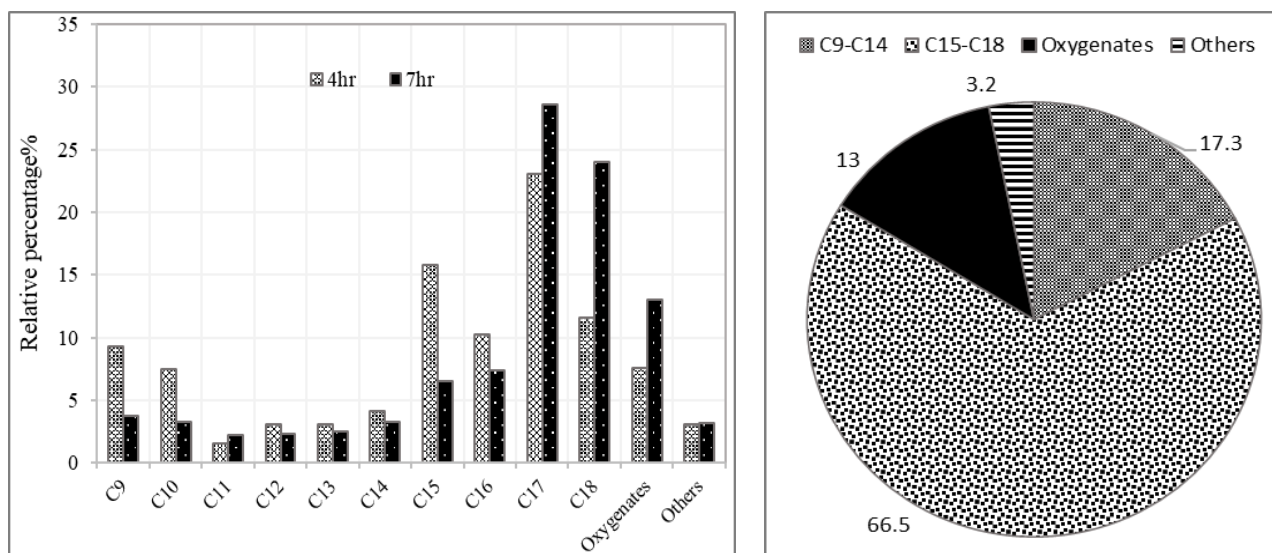


Figure 5.7 Test 04 (320 °C, 20 bar H₂ and 10% cat.) deoxygenation with sunflower oil and Pd/FAC results, distribution of the light and diesel range hydrocarbons at the best conditions (right) relative percentage of product compounds vs. time (left)

In order to evaluate the pressure effect on the deoxygenation reaction, in test 05, all the operating conditions remain unchanged (320 °C, sunflower oil, and 10 wt% cat), where the pressure increases up to 40bar, which lead obtaining 80% hydrocarbon green diesel range after 7 hours of the reaction time, a significant improvement compared with 67% of the previous one (test 04) with 20 bar of hydrogen, which demonstrates the positive effect of the solubilized hydrogen in oil on the hydrogenation reaction step precedes the deoxygenation one. Figure 5.8 illustrates the relative percentage of light hydrocarbons, diesel range, oxygenates, and others, 3%, 78%, 18%, and 0.8%, respectively.

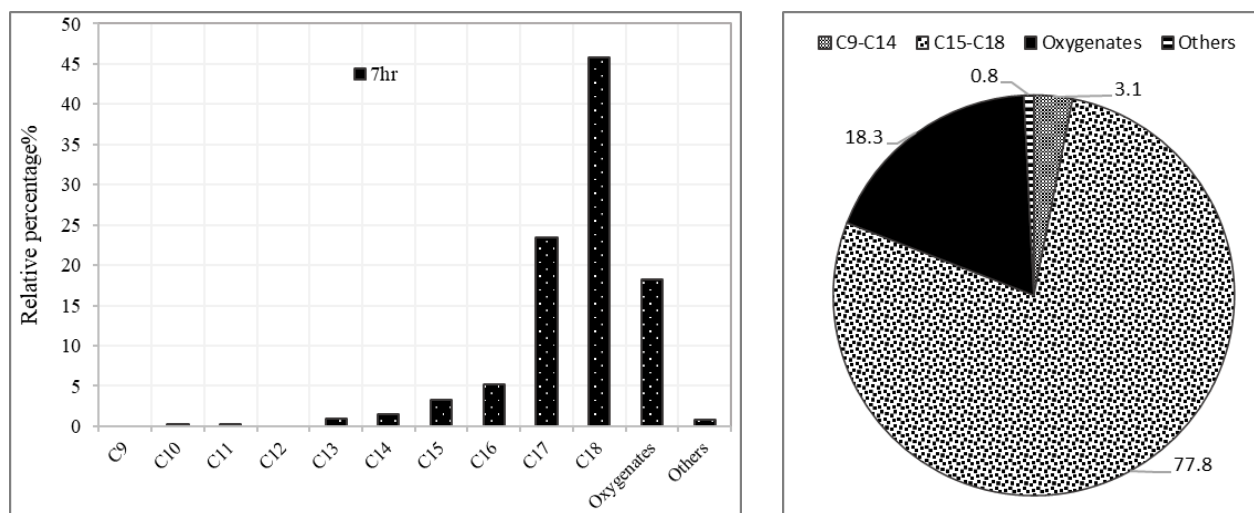


Figure 5.8 Test 05 (320 °C, 40 bar H₂ and 10% cat.) deoxygenation with sunflower oil and Pd/FAC results, distribution of the light and diesel range hydrocarbons at the best conditions (right) relative percentage of product compounds vs. time (left)

From Table 5.5 and the previous graphs Figure 5.6, Figure 5.7, and, Figure 5.8 we can conclude that the selectivity of the Pd/FAC catalyst is more towards C₁₇ and C₁₅ in the case of stearic acid (test 03), which means that the catalyst is more selective towards DCO₂/DCO, where $SI_{15/16}$ and $SI_{15/16} > 1$, this is confirmed with kinds of literature that the deoxygenation reactions are more favored towards the DCO_x using fatty acids as feedstocks [220][221]. On the other hand, catalyst selectivity using sunflower oil (tests 05 and 06) is more towards C₁₆ and C₁₈, that is more towards the hydrodeoxygenation reaction pathway HDO, where $SI_{15/16}$ and $SI_{15/16} < 1$.

Table 5.5 Pd/FAC catalytic hydrothermal deoxygenation test results, total conversion, GD conversion, and HDO selectivity.

Entry	X _{TG} (%)	X _n (s%)	Y _{GD} (%)	SI _{15/16}	SI _{17/18}
Test 03	82.7	21.3	4.0	5.9	9.8
Test 04	69.7	66.7	25.6	0.9	1.2
Test 05	90.5	40.01	30.5	0.63	0.51

These values are calculated for the product after the transesterification reaction.

Figure 5.9 shows the yields % of the final product after the transesterification analysis for the test 04 and 05, in order to compare the pressure effect on deoxygenation test activity using Pd/FAC catalyst under 20 bar and 40 bar: the green diesel yield hydrocarbons are about 26% and 31% respectively, and the yield of the oxygenates compositions are about 33% and 60%, respectively, and this, because there were heavier, oxygenates that we couldn't see it by the GC before the transesterification analysis, which mean that increasing the H₂ pressure has increased the conversion of TG 69.7 % and 90.5 % respectively for 20 and 40 bar not only towards the green diesel hydrocarbons range, but the oxygenates too.

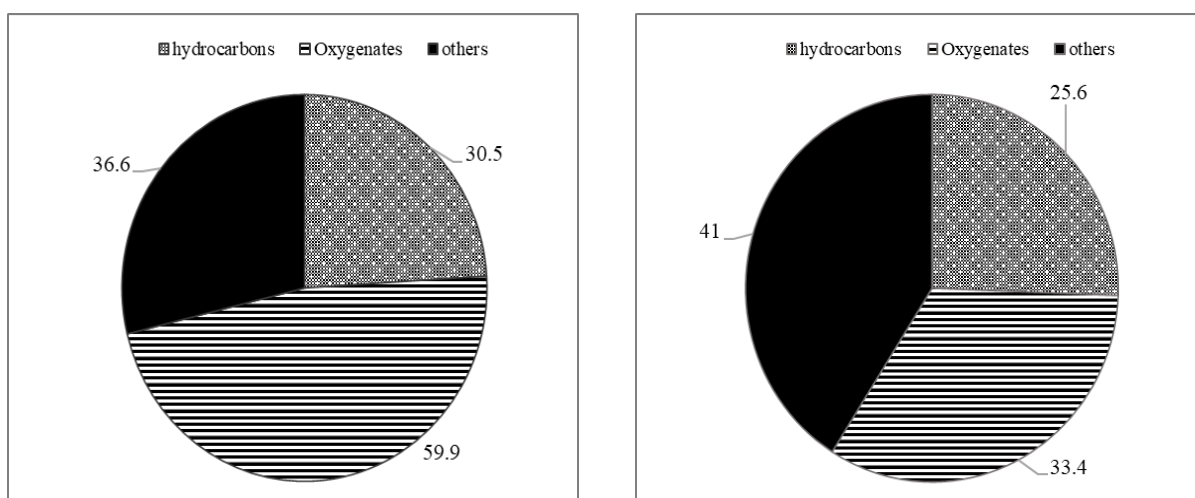


Figure 5.9 Test 04 and 05 (320 °C, 10 wt% cat.) deoxygenation with sunflower oil and Pd/FAC: percentage results green diesel hydrocarbons, oxygenates, and others. 20 bar H₂ (right) and 40 bar H₂ (left).

In order to study the sustainability and the possible deactivation phenomenon of the catalyst under the best reaction conditions have been obtained (320 °C, 40 bar H₂, hexane solvent, and 10 wt% cat), it was recovered and characterized with SEM (Scanning Electron Microscopy) combined with EDS (Energy Dispersive X-ray Spectrometry) for studying the post-test morphological, textural, and chemical surface analysis.

5.2.1 POST-TEST 05 Pd/FAC

Error! Reference source not found. illustrates the comparison of the as-synthesized Pd/FAC before and after the catalytic hydrothermal deoxygenation reaction processes (320 °C, 40 bar H₂, and 10 wt% cat) through SEM-EDS analysis, where the catalyst structure about doesn't change.

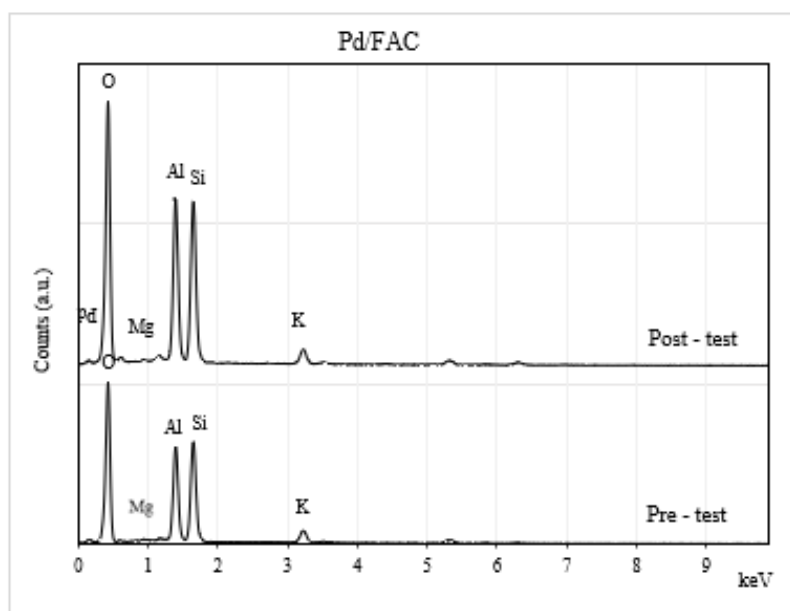
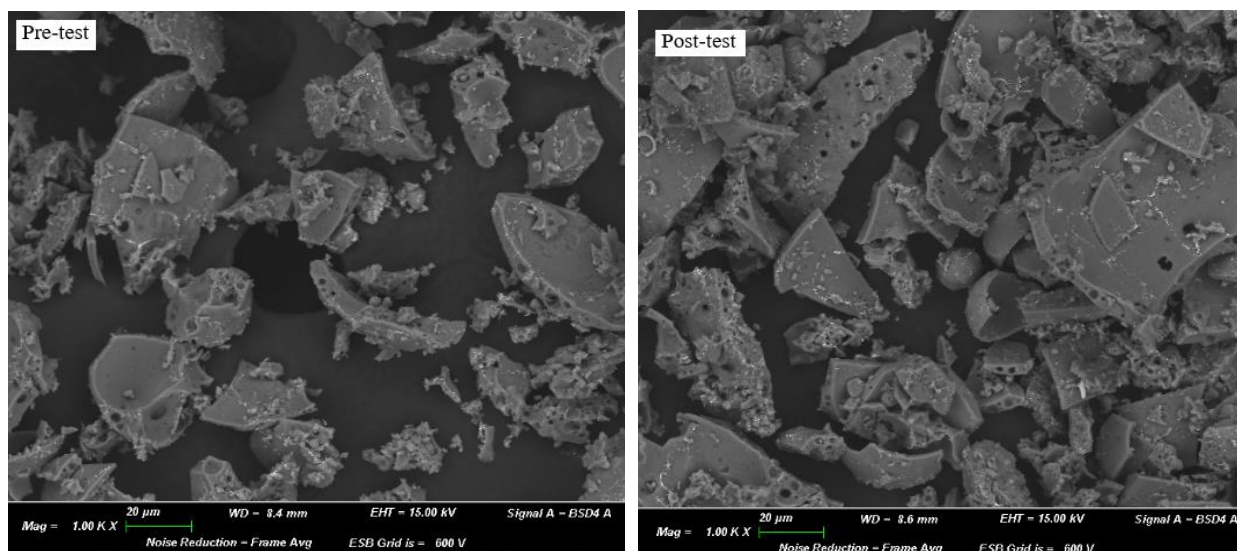


Figure 5.10 Pd/FAC pre and post-test analysis, SEM image (on top), and relative EDS analysis (on bottom).

5.3 CoMo/FAC CATALYST DEOXYGENATION

REACTIVITY TESTS

It was worth studying the effect of the bimetallic supported catalysts on the deoxygenation of the vegetable oils in order to produce the green diesel hydrocarbons range because almost all the works of the literature confirmed that the bimetallic catalysts are more active in the deoxygenation reactions than the monometallic one [102][105]. Test 06 was carried out with a bimetallic CoMo supported over the FAC and using sunflower oil as a feedstock under 320 °C, 40 bar H₂, and 10 wt% cat. The catalytic deoxygenation results meaningful performed with test 06 are reported in Table 5.6 and Table 5.7.

Table 5.6 CoMo/FAC catalytic hydrothermal deoxygenation test results with sunflower oil.

Entry	Cat/TG (wt%)	T (C)	P (bar)	C ₉	C ₁₀	C ₁₁	C ₁₂	C ₁₃	C ₁₄	C ₁₅	C ₁₆	C ₁₇	C ₁₈	Oxygenates	Others
Test 06	10	320	40 H ₂	5	3.39	2.36	1.99	1.94	3.06	23.8	4.04	18.5	2.1	33.9	0
<p>These results correspond to the maximum relative percentage of the range of alkanes C₁₅-C₁₈ obtained during the tests.</p> <p>Oxygenates are methyl stearate, methyl myristate, methyl palmitate, and nonadecane</p> <p>Others are the non-identified GC peaks.</p>															

After 8 hours of the reaction time, about 43% of the diesel range (C₁₅-C₁₈) and 46% of the oxygenates is obtained, but also after 6 hours, the results were good, about 39% of the diesel range as illustrates in Figure 5.11.

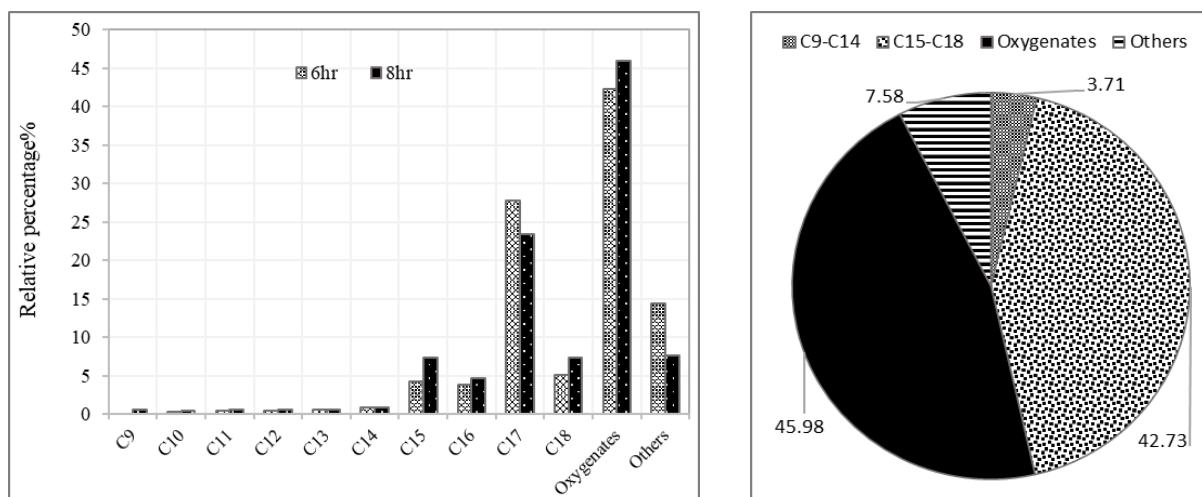


Figure 5.11 Test 06 (320 °C, 40 bar H_2 and 10 wt% cat.) deoxygenation with sunflower oil and CoMo/FAC results, distribution of the light and diesel range hydrocarbons at the best conditions (right) relative percentage of product compounds vs. time (left)

Table 5.7 and Figure 5.12 shows that the conversion and the yield of green diesel after the final transesterification reaction is about 67% and 17%, respectively, and this result is definitely lower than the literature [222], where Krár et. al. has obtained nearly 100% of the conversion and 75% of the diesel range using CoMo/ Al_2O_3 , which could be explained by the partial reduction of Co in our CoMo/FAC and this was confirmed by the XRD and TPR analysis (T reduction of Co 678 °C and the reduction has been made at 600 °C), the lower specific surface area of our catalyst CoMo/FAC (6.94 m^2/g vs. 11.6 m^2/g) and also their higher reaction temperature 380°C.

Regarding the selectivity, it could be resumed from Table 5.7 where the selectivity of CoMo/FAC catalyst is a little more towards C₁₅ and C₁₇, which means that the deoxygenation reaction is more selective towards the DCO₂/DCO pathway, where $SI_{15/16}$ and $SI_{17/18} > 1$.

Table 5.7 CoMo/FAC catalytic hydrothermal deoxygenation test results, total conversion, Green diesel conversion, and HDO selectivity.

Entry	X _{TG} (%)	X _n (s%)	Y _{GD} (%)	SI _{15/16}	SI _{17/18}
Test 06	67.6	19.8	16.9	1.6	3.2
These values are calculated for the product after the transesterification reaction.					

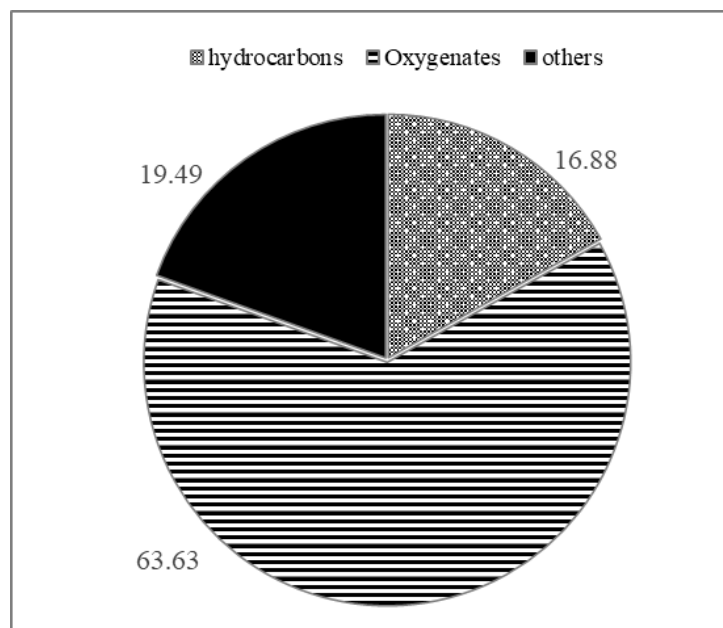


Figure 5.12 Test 06 (320 °C, 40 bar H₂ and 10 wt% cat.) deoxygenation with sunflower oil and CoMo/FAC results of green diesel hydrocarbons, oxygenates, and others.

5.3.1 POST-TEST 06 CoMo/FAC

Regarding the as-synthesized CoMo/FAC catalyst which has been used for the test 06 under (320 °C, 40 bar H₂, and 10 wt% cat), as seen in **Error! Reference source not found.**, there is no change of the structure but, it possible to suppose that about some sintering is happened.

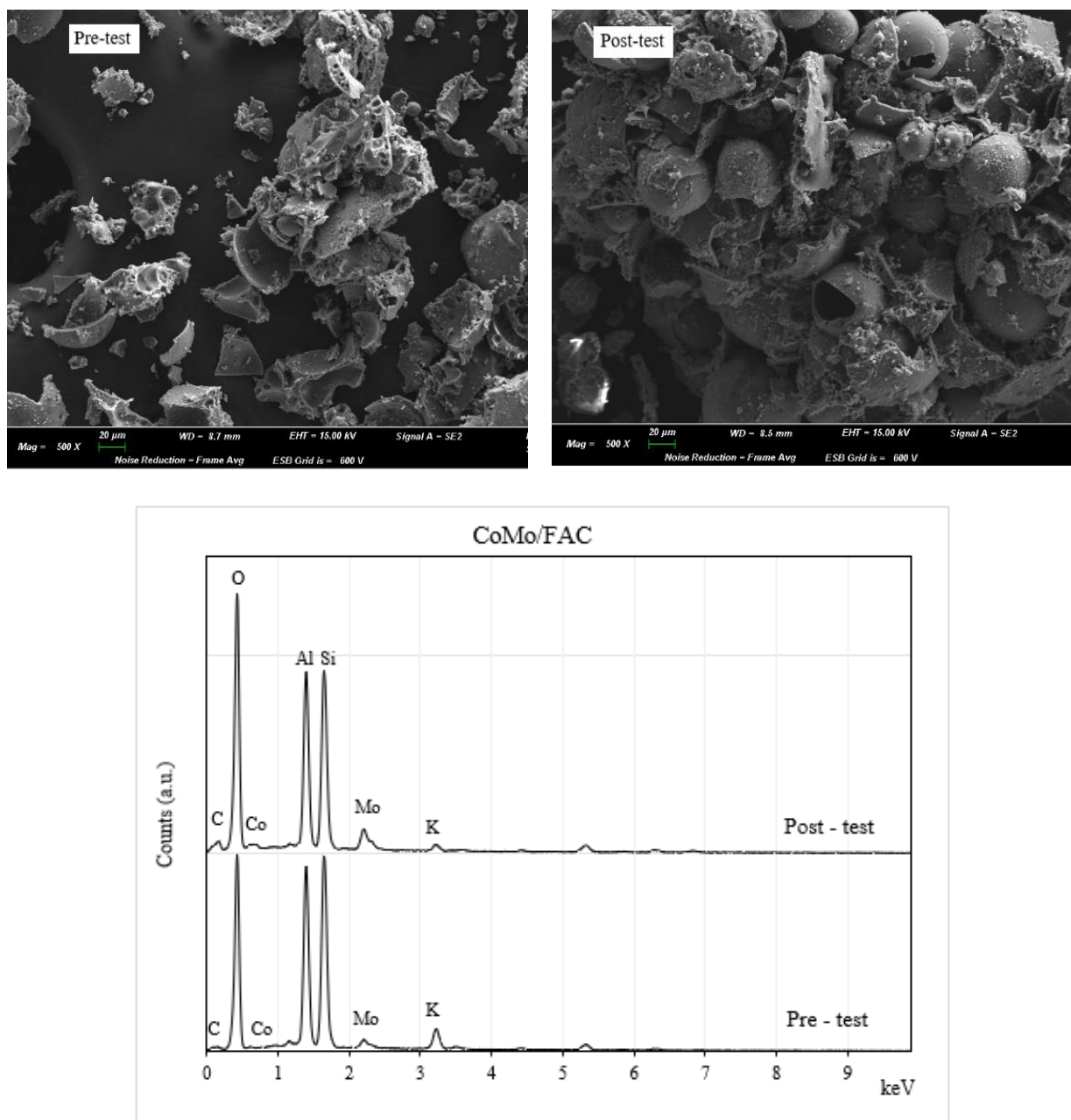


Figure 5.13 CoMo/FAC pre and post-test analysis, SEM image (on top), and relative EDS analysis (on bottom).

5.4 NiMo/FAC CATALYST DEOXYGENATION

REACTIVITY TESTS

The most part of the literature is focused on nickel and molybdenum catalyst and has shown the power of using these supported elements on various nanomaterials (active carbon), oxides, and zeolites in the catalytic hydrothermal processes of the vegetable oils (edible, not edible,

and used) to produce green diesel range (C₁₅-C₁₈) [223][224][225][226]. In order to examine the effect of our based materials, cenospheres FAC, with these two active metals, the catalytic deoxygenation activities using NiMo/FAC is carried out firstly without using a solvent (only sunflower oil) test 07, (320 °C, 40 bar H₂, and 2.5 wt% cat.); then with adding 20g of solvent test 08 (320 °C, 40 bar H₂, hexane solvent, and 10 wt% cat.) (Table 2.7). Results performed with these tests are illustrated in this section in term of light hydrocarbons (C₉, C₁₀, C₁₁, C₁₂, C₁₃, C₁₄), Diesel range hydrocarbons (C₁₅, C₁₆, C₁₇, C₁₈), selectivity, conversions, and yield of the product compositions after transesterification; the most meaningful tests' results are reported in Table 5.8 and Table 5.9.

Table 5.8 NiMo/FAC catalytic hydrothermal deoxygenation test results with sunflower oil.

Entry	Cat/TG (wt%)	T (C)	P (bar)	C ₉	C ₁₀	C ₁₁	C ₁₂	C ₁₃	C ₁₄	C ₁₅	C ₁₆	C ₁₇	C ₁₈	Oxygenates	Others
Test 07	2.5	320	40 H ₂	0.79	0.89	0.65	0.40	0.35	0.33	1.67	1.72	9.99	9.83	55.99	17.2
Test 08	10	320	40 H ₂	0	0	0	0	0	0	3.2	2.8	26	27	39	2

These results correspond to the maximum relative percentage of the range of alkanes C₁₅-C₁₈ obtained during the tests.

Oxygenates are methyl palmitate, methyl stearate, octadecanol, and stearic acid

Others are the non-identified GC peaks.

Using only oil without solvent test 07 does not give very good result as it is clear from Table 5.8, where the diesel range (C₁₅-C₁₆) is about 23% after 6 hours of the reaction time, and it was about impossible recover the final product in order to do the transesterification process, whereas it is about 60% and 20% for the oxygenates and the others, respectively Figure 5.14 which might be explained by the complex composition of the oil to be used without solvent,

probably if we want to work without solvent, we must increase the temperature, pressure, and the catalyst concentration. So, it is better always to carry out the activity with the solvent.

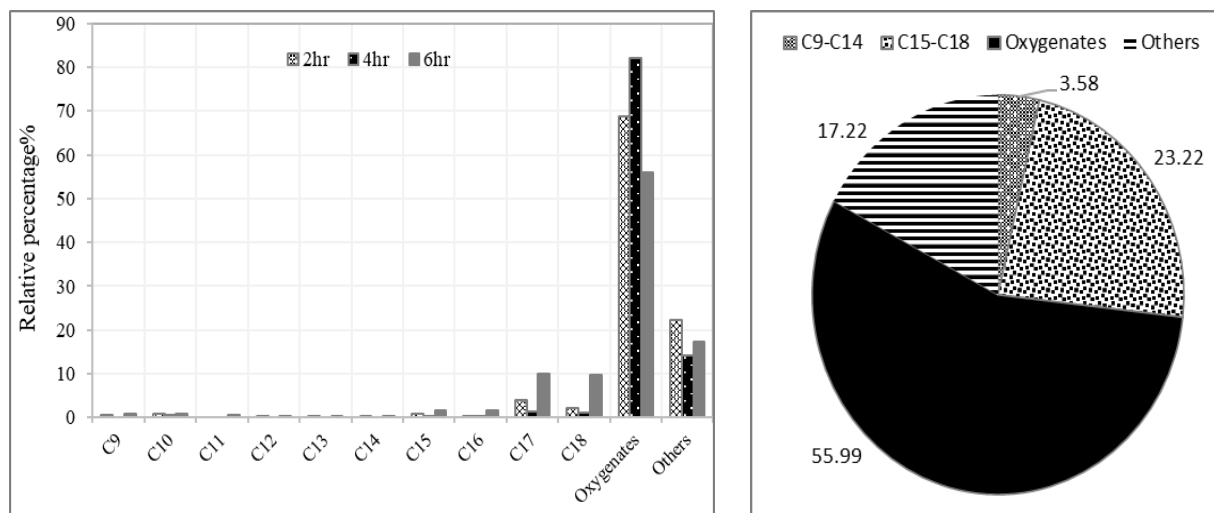


Figure 5.14 Test 07 (320 °C, 40 bar H₂ and 2.5% cat.) deoxygenation with commercial sunflower oil and NiMo/FAC results, distribution of the light and diesel range hydrocarbons at the best conditions (right) relative percentage of product compounds vs. time (left)

The deoxygenation reactivity test on the commercial sunflower oil as triglycerides TG in the presence of the solvent using NiMo/FAC catalyst demonstrates very interesting results, a good diesel range (C₁₅-C₁₈) production after 4 hours 53% and about 47% of the oxygenates (methyl palmitate, methyl stearate, octadecanol, and stearic acid), whereas the best result is obtained after 6 hours of the reaction time with about 60% of the diesel range (C₁₅-C₁₈) and 40% of the oxygenates as illustrates in the Figure 5.15 and this is in accordance with literature et. al. Kiatkittipong [227] where they obtained 70% of diesel range using NiMo/Al₂O₃ under (400 °C, 40 bar H₂), although our materials FAC are wastes.

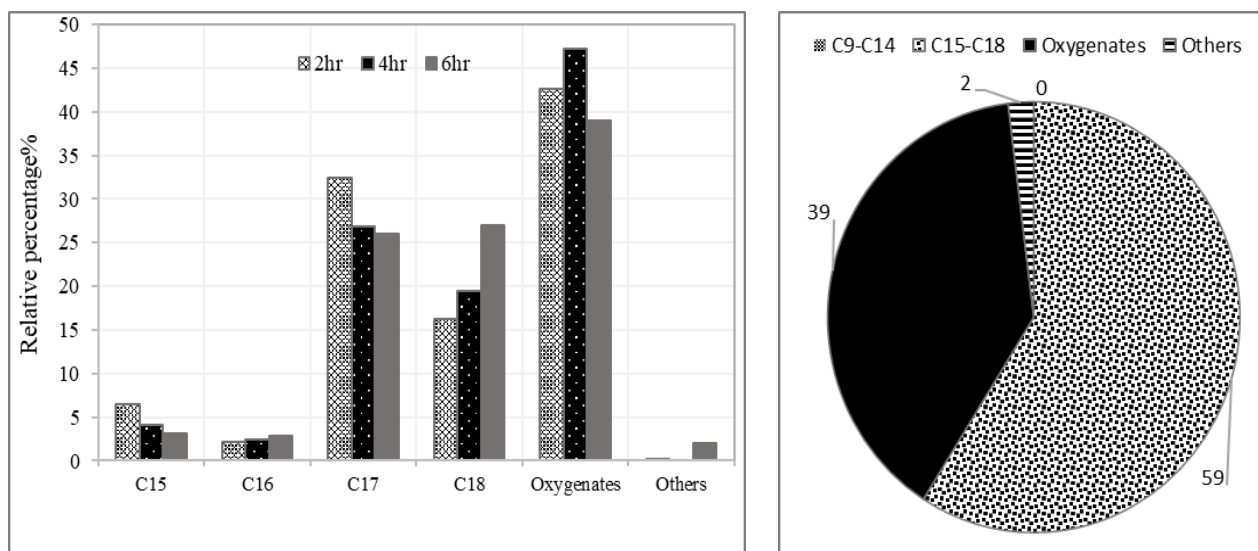


Figure 5.15 Test 08 (320 °C, 40 bar H_2 and 10 wt% cat.) deoxygenation with sunflower oil and NiMo/FAC results, distribution of the light and diesel range hydrocarbons at the best conditions (right) relative percentage of product compounds vs. time (left)

Table 5.9 illustrates the total conversion of the raw material X_{TG} (sunflower oil), the green diesel yield Y_{GD} , conversion in hydrocarbons X_n , and the selectivity towards HDO and/or DCO_2/DCO , $SI_{15/16}/SI_{17/18}$, the selectivity of NiMo/FAC catalyst is towards both pathways HDO and DCO_2/CO , where the $SI_{15/16} > 1$ and $SI_{17/18} < 1$.

Table 5.9 NiMo/FAC catalytic hydrothermal deoxygenation test results, total conversion, Green diesel conversion, and HDO selectivity.

Entry	X_{TG} (%)	X_n (s%)	Y_{GD} (%)	$SI_{15/16}$	$SI_{17/18}$
Test 07	-		-	0.79	1.02
Test 08	61.8	62.8	24.6	1.14	0.96

These values are calculated for the product after the transesterification reaction.

Figure 5.16 shows the yield of the final product after the transesterification analysis for test 08: the yield of the green diesel hydrocarbons is about 25%, and the yield of the oxygenated compositions is about 37%, with conversion in hydrocarbons about 63%, which could be estimated as a very good results, although the low specific area of the FAC (0.58 m^2/g) support and its non-acidity properties, which usually plays as an important key in deoxygenation

reactions. Practically it is possible to estimate that using NiMo/FAC catalyst in the deoxygenation process of 1-liter sunflower oil under 40 bar of hydrogen produce 246 g green diesel range (C15-C18) and 628 g of hydrocarbons range (C9-C18).

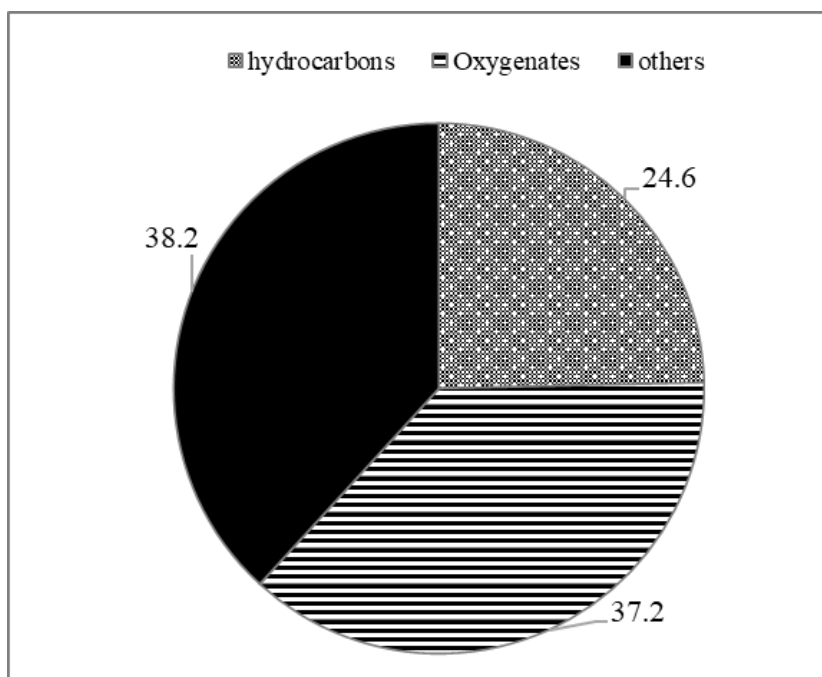


Figure 5.16 Test 08 (320 °C, 40 bar H₂ and 10 wt% cat.) deoxygenation with commercial sunflower oil and NiMo/FAC percentage results of green diesel hydrocarbons, oxygenates, and others.

5.4.1 POST-TEST 08 NiMo/FAC

Also, in the case of the as-synthesized NiMo/FAC catalyst with (320 °C, 40 bar H₂, and 10 wt% cat), **Error! Reference source not found.** EDS analysis shows no change with structure and no coke formation, although the SEM illustrates kind of sintering of the impregnated elements on the support.

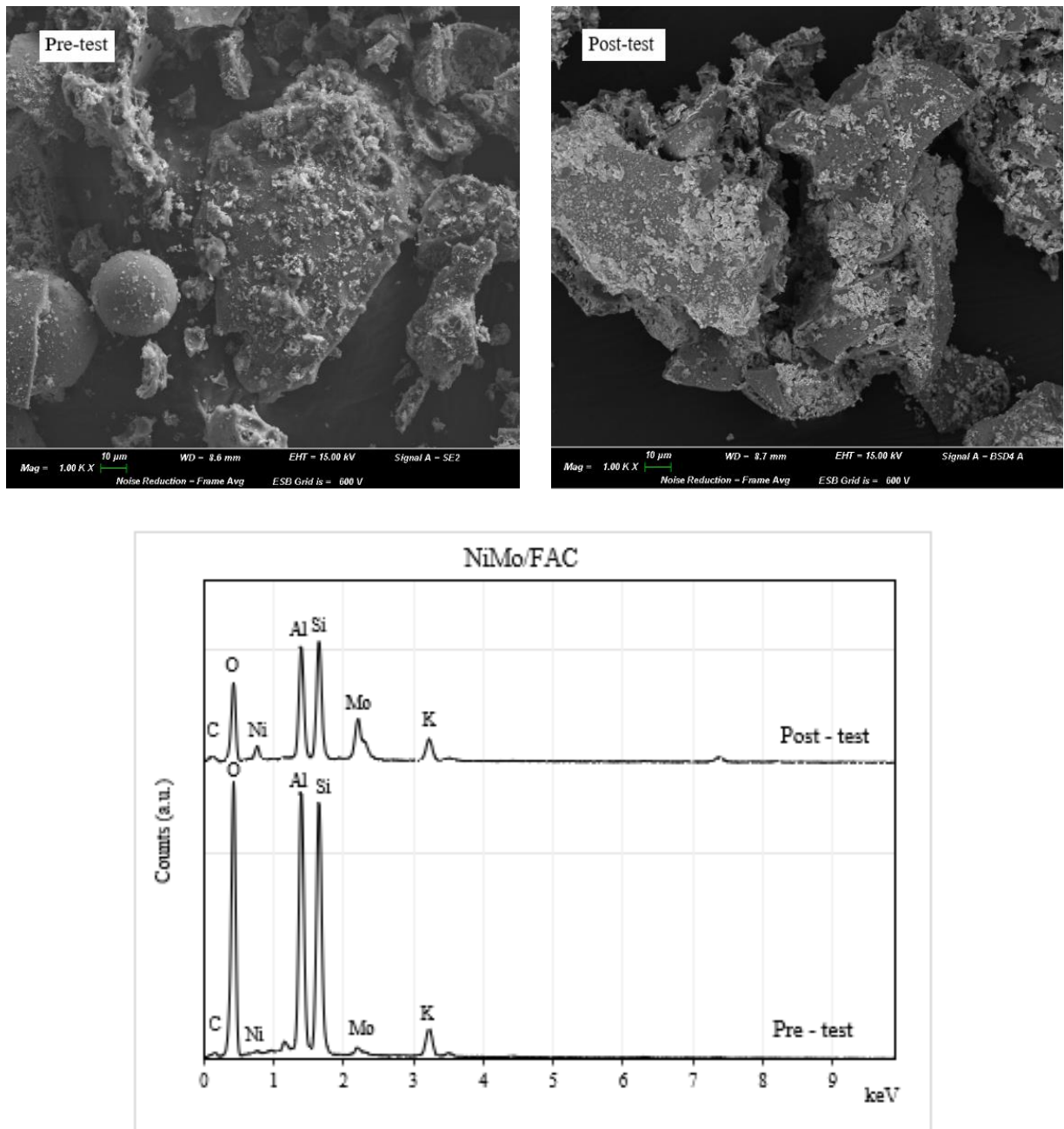


Figure 5.17 NiMo/FAC pre and post-test analysis, SEM image (on top), and relative EDS analysis (on bottom).

5.5 NiMo/ZEOLITE X CATALYST DEOXYGENATION

REACTIVITY TESTS

As the zeolites have very interesting properties from the point of view of the specific surface area, pores size, and acidic sites, a lot of researchers have been concentrated on the development of these widely used materials in their researches and at the industrial scale as molecular sieves and supports of many types of metals, Pd, Ni, Mo,.... [203][228][229]. These materials have shown very good and important results with the deoxygenation processes of the triglycerides from the point of the green diesel production as it is reported in the literature, for instance, Pt/SAPO-31 [227], NiMo/zeolite beta [223], Pd/Al-SBA-15[223].

For this reason, we have decided to extend our research on the cenospheres material and use it in order to synthesis the zeolite material. Using this new zeolite X as a support of the NiMo metals was an important point to stay in line with the literature, which uses the zeolite as a very excellent support material and uses the Ni and Mo metals as a very effective precursor [223][225][230]. We have carried out the catalytic deoxygenation activity tests using 3% NiO and 12% MoO₃ supported on zeolite X with commercial sunflower oil. Three tests were carried out in order to choose the best conditions: test 09 (280 °C, 40 bar H₂, hexane solvent, and 10 wt% cat.), test 10 (320 °C, 40 bar H₂, hexane solvent, and 2.5% cat.), and then test 11, (320 °C, 40 bar H₂, hexane solvent, and 10% cat.) (indicated in Table 2.7). Green diesel range, light hydrocarbons range, pathway selectivity, and yield results are reported in Table 5.10 and Table 5.11.

Table 5.10 NiMo/zeolite X catalytic hydrothermal deoxygenation test results with commercial sunflower oil.

Entry	Cat/TG (wt%)	T (°C)	P (bar)	C ₉	C ₁₀	C ₁₁	C ₁₂	C ₁₃	C ₁₄	C ₁₅	C ₁₆	C ₁₇	C ₁₈	Oxygenates	Others
Test 10	2.5	320	40 H ₂	0.1	0.04	0.05	0.03	0.04	0.07	0.85	1.18	2.7	3.62	82.69	8.63
Test 11	10	320	40 H ₂	0.52	0.54	0.68	0.53	0.73	0.51	2.80	2.84	23.4	18.9	43.8	2.8

These results correspond to the maximum relative percentage of the range of alkanes C₁₅-C₁₈ obtained during the tests.

Oxygenates are methyl palmitate, methyl stearate, octadecanol, and stearic acid

Others are the non-identified GC peaks.

Table 5.10 shows that, for test 09 with 280 °C, the relative percentage of hydrocarbons after 6 hours of the reaction time is about 0.39% then increasing the temperature and decreasing the catalyst percentage with test 10 also was not a good choice because we have got about 10% of green diesel hydrocarbons yield as illustrates in Figure 5.18 and this means that low temperature and low catalyst concentration are not suitable for this type of reaction with zeolite materials, and this was confirmed with the most part of literature with up to 320 °C as the standard reaction temperature [202][223][175]

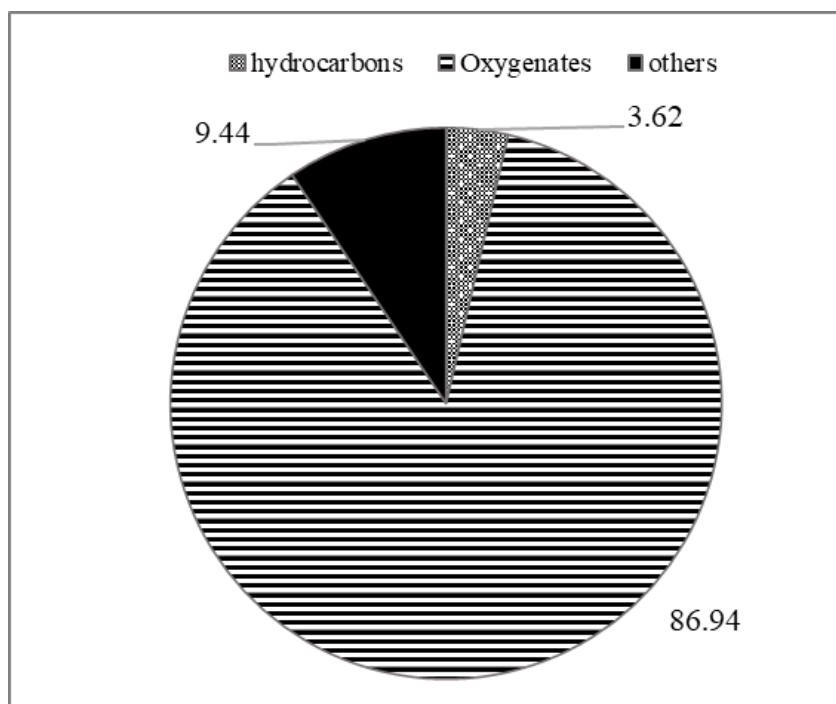


Figure 5.18 Test 10 (320 °C, 40 bar H₂ and 2.5 wt% cat.) deoxygenation with commercial sunflower oil and NiMo/zeolite X results% in green diesel hydrocarbons, oxygenates, and others.

Increasing the catalyst concentration of 10 wt% with the same high temperature 320 °C, and 40 bar H₂, test 11 demonstrates an impressive green diesel range (C₁₅-C₁₈) of about 43% after 3 hours and 50% after 6 hours of the reaction time, whereas, the oxygenate compounds (methyl palmitate, methyl stearate, octadecanol, and stearic acid), are about 50% and 40% after 3 hours and 6 hours, respectively. Definitely, the best conditions are under test 11, after 6 hours of the reaction time, as illustrates in Figure 5.19.

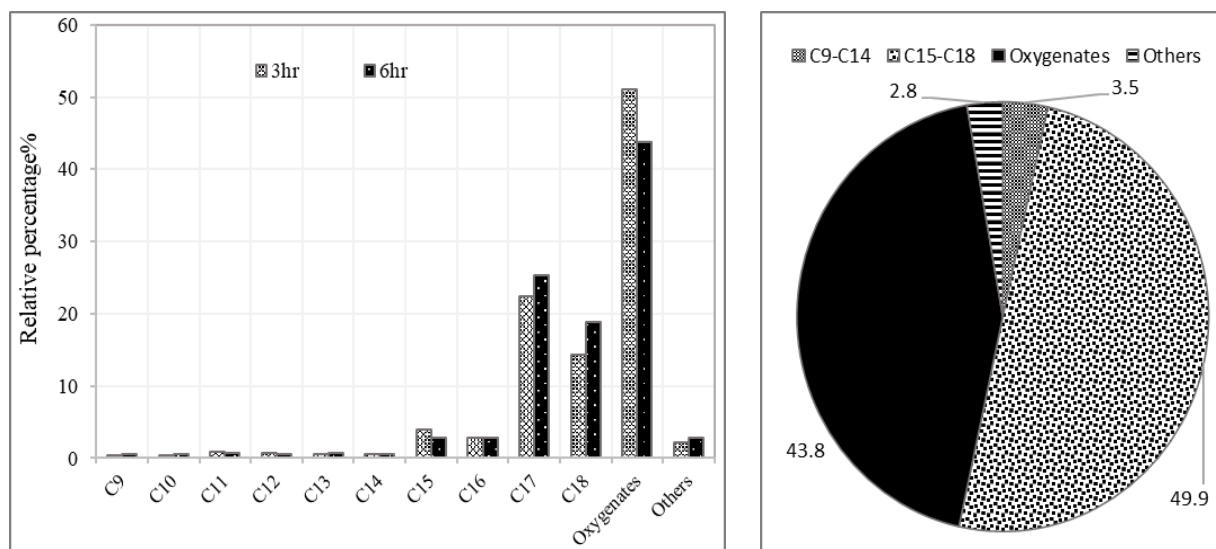


Figure 5.19 Test 11 (320 °C, 40 bar H_2 and 10 wt% cat.) deoxygenation with commercial sunflower oil and NiMo/zeoliteX results, distribution of the light and diesel range hydrocarbons at the best conditions (right) relative percentage of product compounds vs. time (left)

In order to examine the selectivity of the NiMo/zeolite X catalyst towards the HDO or/and DCO₂/DCO pathway, Table 5.11 and Figure 5.19 show that the NiMo/zeolite X catalyst selectivity is towards the both HDO and DCO₂/DCO pathways, where $SI_{15/16} < 1$ and $SI_{17/18} > 1$.

Table 5.11 NiMo/zeolite X hydrothermal catalytic deoxygenation test results, total conversion, Green diesel conversion, and HDO selectivity.

Entry	X_{TG} (%)	X_n (s%)	Y_{GD} (%)	$SI_{15/16}$	$SI_{17/18}$
Test 11	57.9	77.9	34.8	0.9	1.3
These values are calculated for the product after the transesterification reaction.					

Table 5.11 shows that the conversion in hydrocarbons about 78%, which could be explained by the zeolite x acidity (weak and medium types), and this plays a significant role in increasing the deoxygenation reaction activity towards the hydrocarbons content [203]; from Figure 5.20, we can observe that the yield of the final product after the transesterification analysis is about 35% for the green diesel hydrocarbons and about 22% for the oxygenates, which is about in line with the literature [231] where Zarchin et. al. obtained about 50 of diesel yield with Ni2P/HY and soybean oil although it is always less because the best temperature for the

deoxygenation reaction of the sunflower vegetable oil if more than 350 °C and in our bench scale plant we cannot reach this condition due to technical limitation. In fact, it is evaluated that NiMo/zeolite X produces about 350 g green diesel range (C15-C18) and 780 g of hydrocarbons (C9-C18) from 1 liter sunflower oil.

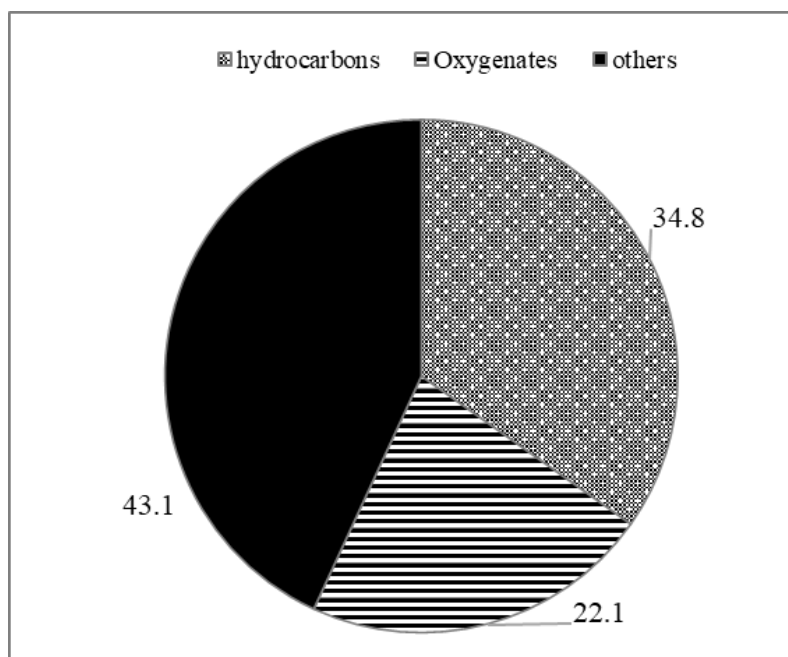


Figure 5.20 Test 11 (320 °C, 40 bar H₂t, and 10 wt% cat.) deoxygenation with commercial sunflower oil and NiMo/zeolite X: percentage results of green diesel hydrocarbons, oxygenates, and others.

5.5.1 POST-TEST 11 NiMo/ZEOLITE X

Figure 5.21 illustrates the comparison of the NiMo/zeolite X before and after the catalytic hydrothermal deoxygenation reaction processes (320 °C, 40 bar H₂, and 10 wt% cat), where the catalyst structure became less crystallized, there is a kind of agglomeration with SEM post-test, the EDS analysis clarifies an increasing of the carbon intensity which could lead to suppose the formation of some coke during the test and may lead to the deactivation phenomenon of the catalyst [232][233].

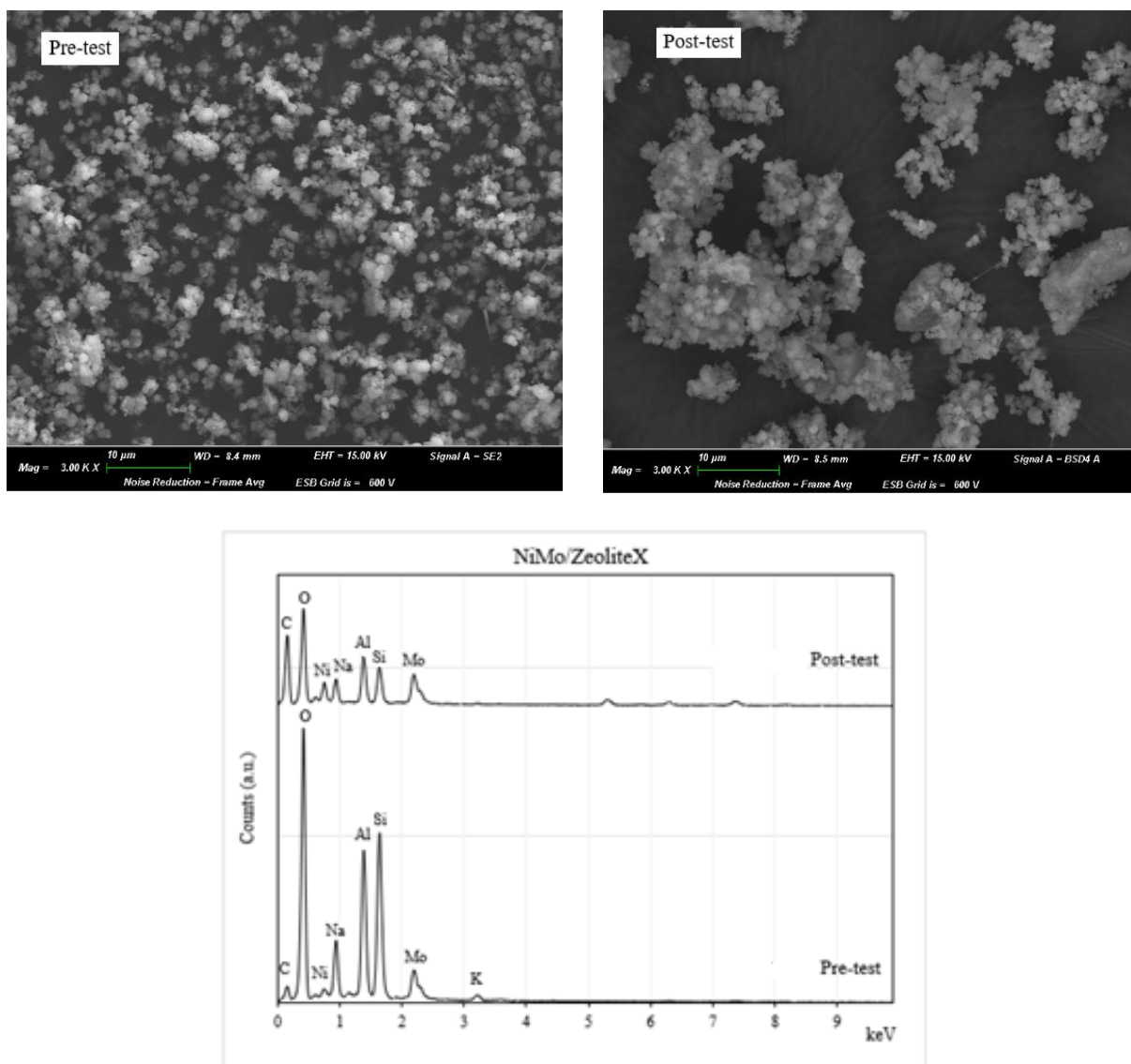


Figure 5.21 NiMo/zeolite X pre and post-test analysis, SEM image (on top), and relative EDS analysis (on bottom).

5.6 CONCLUSIONS

Mono-metallic (Lindlar, 2% wt Pd/FAC) and bimetallic catalysts (CoMo/FAC, NiMo/FAC, and NiMo/zeolite X) in the catalytic hydrothermal deoxygenation of triglycerides, stearic acid, and vegetable oil (sunflower oil) was proved in this doctoral thesis.

Table 5.12 comparison of deoxygenation results obtained with various mono and bimetallic catalysts.

Cat.	T (°C)	P (bar)	% wt/wt	X _{TG} (%)	X _n (%)	Y _{GD} (%)	SI _{15/16}	SI _{17/18}
Pd-Lindlar	300	20 N ₂	10	85.8	22.1	4.0	4.3	20.5
	300	40 H ₂	10	69.4	56.4	22.9	1.6	3.2
Pd-FAC	300	20 N ₂	10	82.7	21.3	4.0	5.9	9.8
	320	20 H ₂	10	69.7	66.7	25.6	0.9	1.2
	320	40 H ₂	10	90.5	40.01	30.5	0.63	0.51
CoMo/FAC	320	40 H ₂	10	67.6	19.8	16.9	1.6	3.2
NiMo/FAC	320	40 H ₂	2.5	-	-	-	0.79	1.02
	320	40 H ₂	10	61.8	62.8	24.6	1.14	0.96
NiMo/FAC	320	40 H ₂	2.5	-	-	-	-	-
	320	40 H ₂	10	57.9	77.9	34.8	0.9	1.3

The main highlights obtained from the deoxygenation reactions over these catalysts are:

I Using Lindlar catalyst as a reference point, based on the previous hydrogenation research, was a good idea because there is no literature on the deoxygenation reactions with Lindlar. After 8 hours of the reaction with sunflower oil, the diesel range formation was about 45% and 23% of diesel yield.

II For the synthesized Pd/FAC, the best reaction conditions were (320 °C, 40 bar H₂, hexane solvent, and 10% cat) with 78% of diesel range after 6 hours of the reaction and about 31% diesel yield after the transesterification reaction. The selectivity of Pd/FAC was towards DCO/DCO₂ and the formation of hydrocarbons with one less carbon atom than the starting fatty acid (i.e., C₁₅ and C₁₇).

III Bimetallic CoMo/FAC catalyst has shown less diesel range 43%, and less diesel yield 17% compared with the previous monometallic Pd/FAC, and this could be interpreted by, Co partial

reduction at 600 °C, low interaction between the metallic phase and the support, and its non-acidity

IV Using the nickel-metal with molybdenum as promoter and FAC as support NiMo/FAC in order to deepen research on the bimetallic metals supported on the cenospheres materials.

NiMo/FAC catalyst has produced more diesel percentage of about 60% and diesel yield 25% after 6 hours of the reaction comparing with the CoMo/FAC, which ensures that the nickel is more active than the cobalt.

V Despite the low specific surface area of the cenospheres materials and its non-acidity, which are very important parameters in catalytic deoxygenation reactions as reported in almost all the literature [224][234][221], and also the temperature limit operative value, it has exhibited a very good activity with the conversion of vegetable oils in hydrocarbons diesel range C₁₅-C₁₈.

V1 In order to improve the cenosphere's performance, a synthesized zeolite X based on the cenospheres was performed.

VII Carrying out the deoxygenation reaction with the synthesized NiMo/zeolite X under (320 °C, 40 bar H₂, and 10% cat) has shown 78 % conversion in hydrocarbons and diesel yield, about 40% after the transesterification reaction.

VIII Comparison between the cenosphere-based catalyst and the zeolite X-based one, we can say that both catalysts seem to prefer both pathways HDO and DCO / DCO₂.

IX The operative limit of temperature value was one of the most significant obstacles that affected this work: it is 350 °C, which we couldn't arrive due to the plant security reasons. whereas, the best temperature for the deoxygenation of the sunflower oil, as reported in the literature, is above 350 °C [235][223].

X Regarding the pathway selectivity, it is still necessary carrying out the analysis of the gas phase (as mentioned in chapter 1), which would allow obtaining information about the selectivity of the HDO and DCO / DCO₂ pathway reaction (besides the SI17/18 and SI15/16 values) and would also allow us to know if in our reactor we are in the presence of gas-phase reactions like methanation.

6 GENERAL CONCLUSIONS

Nowadays, it is not acceptable anymore to close our eyes in front of global problems such as pollution and the exhaustion of non-renewable materials. The development of biodegradable biofuels would solve both problems and would ensure the development of a sustainable product, which also dramatically reduces environmental pollution, and which is able to replace the hydrocarbons deriving from fossil fuels completely.

In this Ph.D. thesis, a study on the catalytic hydrothermal processing on vegetable oils (partial hydrogenation and deoxygenation) was carried out; the objective of the work was to develop innovative catalysts for the production of green diesel as a clean automotive fuel and high oleic vegetable oils to be used for many different industrial applications, such as the production of lubricants and cosmetics.

Different catalysts, commercial, and synthesized in the laboratory, were characterized and tested in different operating conditions; a summary of the main results for each catalyst is reported here:

Commercial Pd **Lindlar catalyst** has shown a small surface area related to the low pore volume of the support calcium. Calcium carbonate by XRD is the only phase, and Pd has a good dispersion percentage of 95% by H₂-Chemisorption;

Pd Lindlar with the hydrogenation process is active at 180 °C with the high formation of C18:1 (more than 85%) and low formation of stearic acid (less than 10% at the maximum C18:1 relative percentage); at a lower temperature (120 °C), it is less active and more trans C18:1 was formed; its recyclability was tested in cyclic tests, and although it decreased by every cycle, with a catalyst make-up it is probably reusable over multiple cycles;

Pd Lindlar with the deoxygenation process in order to produce green diesel has demonstrated a good activity under (320 °C, 40 bar H₂, and 10 wt%) with 57% conversion in hydrocarbons (C₉-C₁₄ and C₁₅-C₁₈).

II Laboratory palladium supported on hydrotalcite (**Pd/HT**) has clarified:

Pd/HT catalyst method proves to be reliable in the synthesis of palladium supported hydrotalcites with the wanted content of Pd (ICP-AES); the catalyst has 50.7 m²/g BET surface area, and the Pd has a good dispersion percentage 80%, hydrotalcite is the only phase observed by XRD;

Pd/HT has lower activity than Lindlar catalyst with the hydrogenation activities; longer reaction times are required to obtain the same degree of hydrogenation (IV or conversion of C18:2) at the same high temperature 180 °C, cyclical tests are also investigated and, unlike Lindlar, during the first repeated tests, the catalyst undergoes an activation mechanism probably related to a change in the structure of the hydrotalcites, induced by the combined effect of temperature and pressure;

III The main challenge and the point of power in this research was discovering the utility of the waste **cenospheres (FAC)** materials as supports for different metals and test it in the catalytic hydrogenation/deoxygenation reactions;

IV **Pd/FAC** as a synthesized catalyst has illustrated:

An accordance with the ICP-AES analysis with a nominal one, a good dispersion percentage of Pd 88%, the support structure is totally destroyed after the impregnation process;

Pd/FAC has a good activity with the hydrogenation process but with a higher temperature (240 °C) than Pd Lindlar and P/HT.

Using Pd/FAC in the deoxygenation reaction with (320 °C, 40 bar H₂, and 10 wt%) in order to obtain the green diesel has shown that it is very active with high temperature, 91% of the oil total conversion.

V **CoMo/FAC** bimetallic as-synthesized catalyst was characterized and tested with the deoxygenation reactions:

The CoMo/FAC catalyst has observed that the ICP-AES analysis is in line with the nominal one, Co partially reduced with (600 °C) from the XRD and TPR analysis;

Its partially reduction has may affect its activity with the deoxygenation reaction, whereas only 20 % conversion in hydrocarbons obtained with (320 °C, 40 bar H₂, and 10 wt%);

VI **NiMo/FAC** bimetallic catalyst has been synthesized, characterized, and tested;

NiMo/FAC ICP-AES results were less than the nominal one, which may occur due to the preparation procedure of the sample for the ICP-AES, where, after the attack with the H₂SO₄ it has been filtered, TPR has illustrates that Ni and Mo are strongly bonded with the FAC support, whereas the TPR results higher than the metals alone without the support;

A good conversion in hydrocarbons 62% in the deoxygenation process with NiMo/FAC catalysts was obtained under (320 °C, 40 bar H₂, and 10 wt%);

VII **NiMo/zeolite X** bimetallic was synthesized using zeolite X material as a support, which was synthesized from FAC materials; NiMo/zeolite X then was characterized and tested in the deoxygenation process:

NiMo/zeolite X has illustrated an increase in the BET surface area of the zeolite X comparing with its original FAC materials, and two types of acidic sites (weak and medium) obtained with NH₃-TPD;

Deoxygenation reaction with NiMo/zeolite X catalysts has demonstrated about the best green diesel yield 35% and conversion percentage in hydrocarbons 78% obtained after the transesterification process, which could be explained by its high surface area and its acidity.

Obviously, these activities will not stop here because many points and aspects still need to be clarified, studied, and in-depth in order to optimize the work. In fact, carrying out the deoxygenation reactions was just a starting step in order to go forward in the green diesel production from vegetable oil (edible, non-edible, and spent).

Regarding the deoxygenation activities, in reality the future work is already in progress, where as a group of new catalysts supported on FAC and zeolite with different loading percentage of metals (5% NiO 15% MoO/FAC, 5% NiO 15% MoO/zeolite, 5% NiO 15% MoO 5% CeO/FAC, 5% NiO 15% MoO 5% CeO /zeolite, 5% NiO 15% MoO 20% CaO /FAC, and 5% NiO 15% MoO 20% CaO /zeolite) was synthesized and characterized (Addendum C);

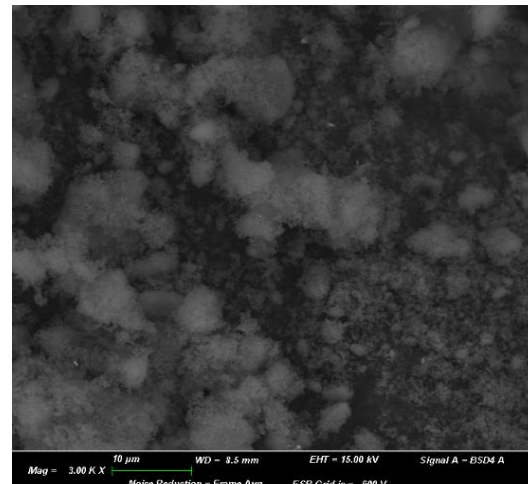
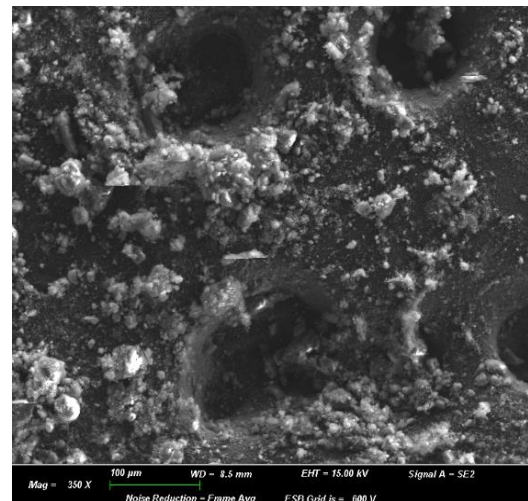
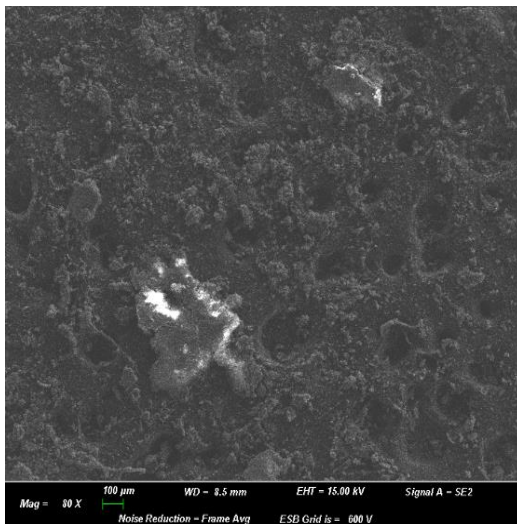
In fact, keeping in mind the twelve principles of Green chemistry [6], the ideal would be to work in the absence of solvent and therefore only in oil, but we have seen that this leads to a technical-operational problem such as difficulties during sampling and low yield of hydrocarbons; however, the study of reactions carried out in the absence of solvent is not excluded, trying to find the suitable conditions for this to be possible.

Analyzing the gas phase is very important not only for knowing the selectivity of the reaction's pathway HDO and/or DCO₂/DCO, but also to examine the cracking reactions happening, which produce light hydrocarbons with carbon number less than 9.

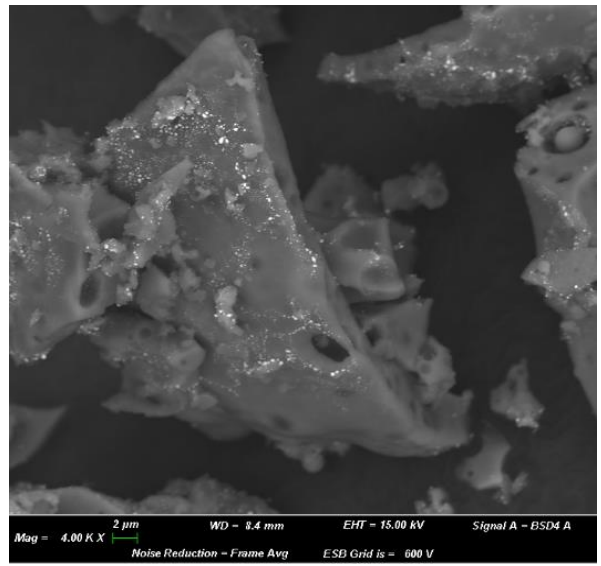
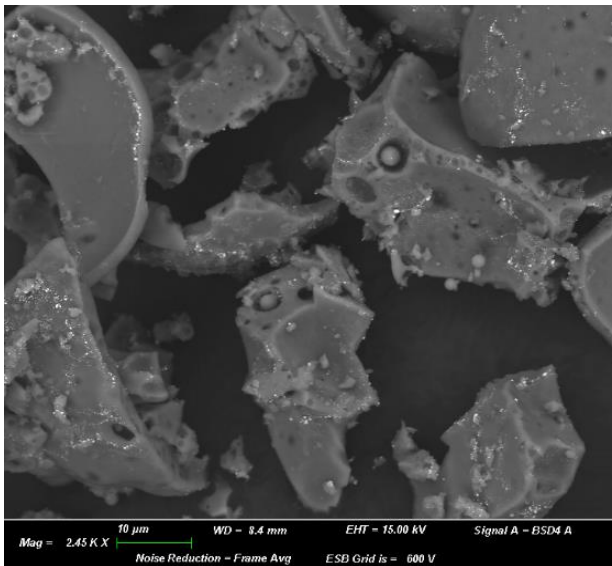
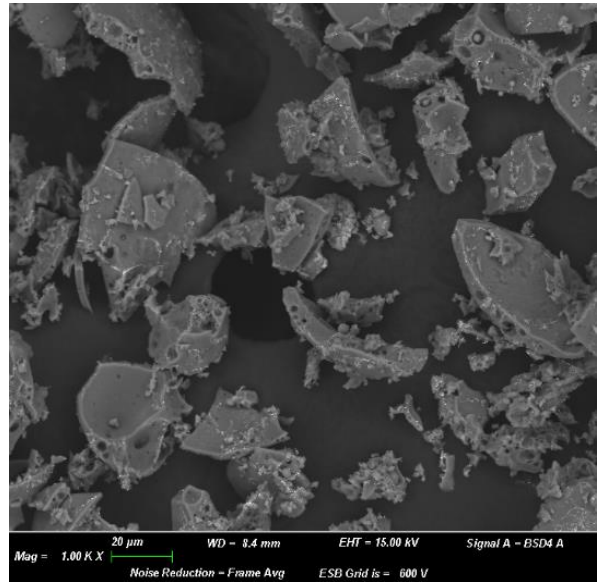
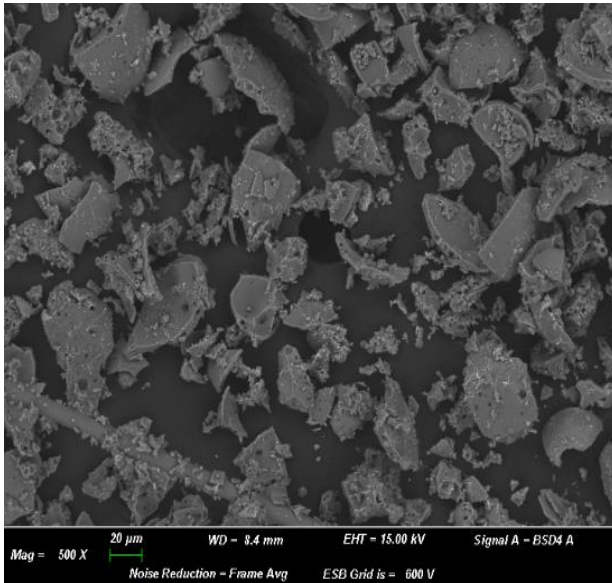
Future studies should also be focused on the modelling of both the kinetic and the mass transfer evaluation of both the hydrogenation and the deoxygenation reactors.

7 ADDENDUM A: SEM RESULTS

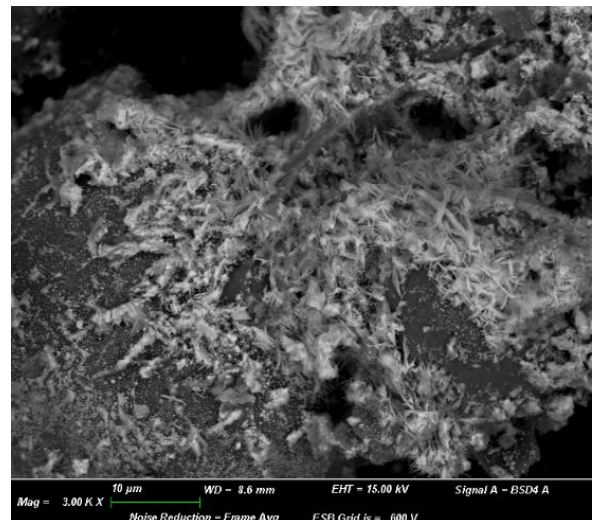
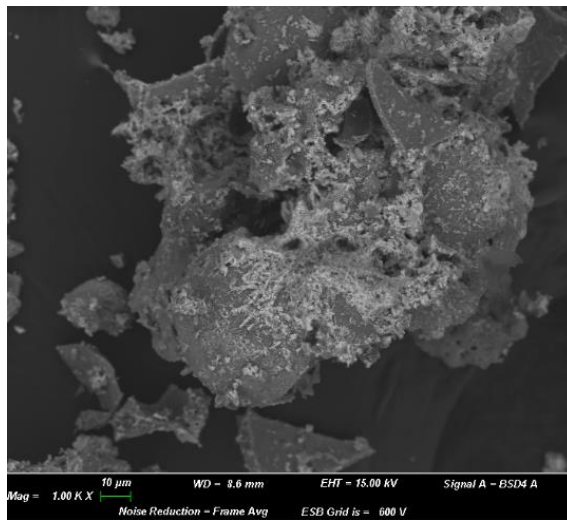
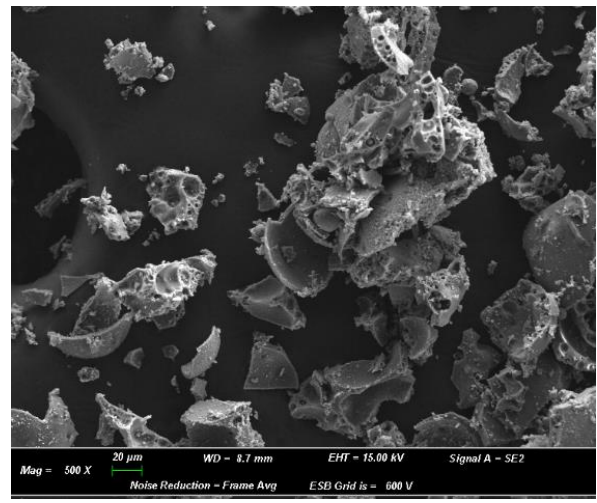
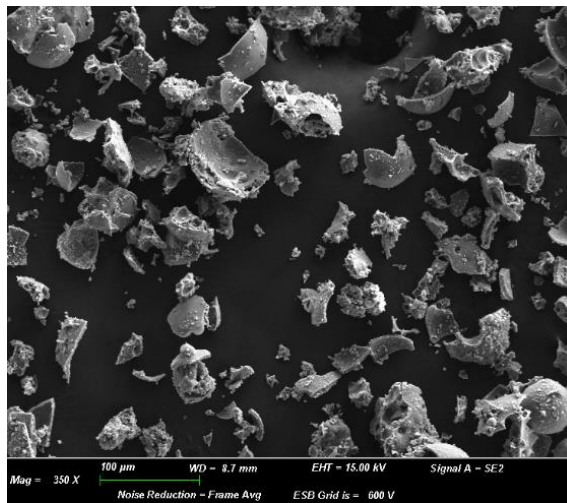
7.1 A.1 Pd/HT



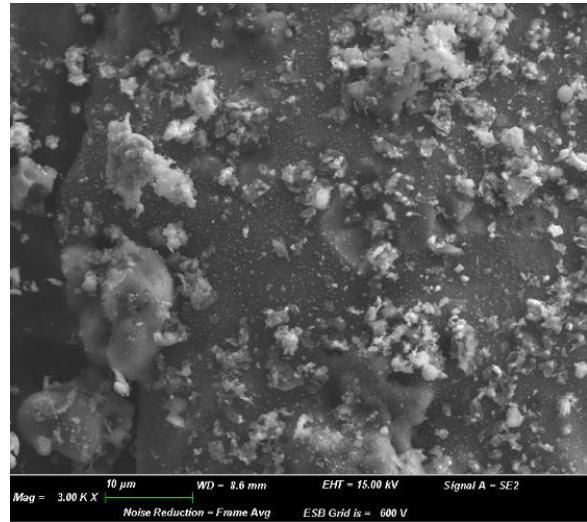
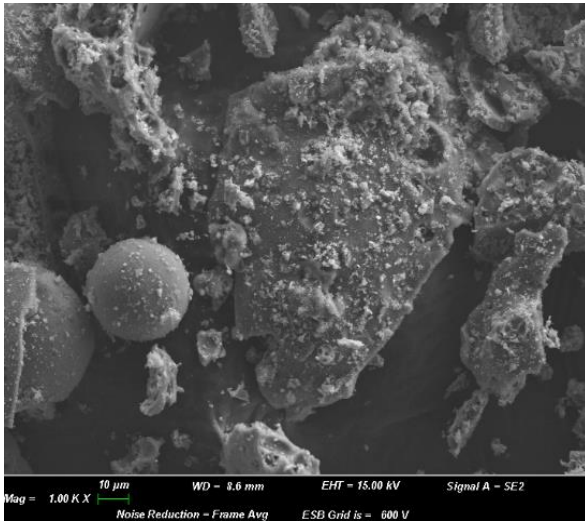
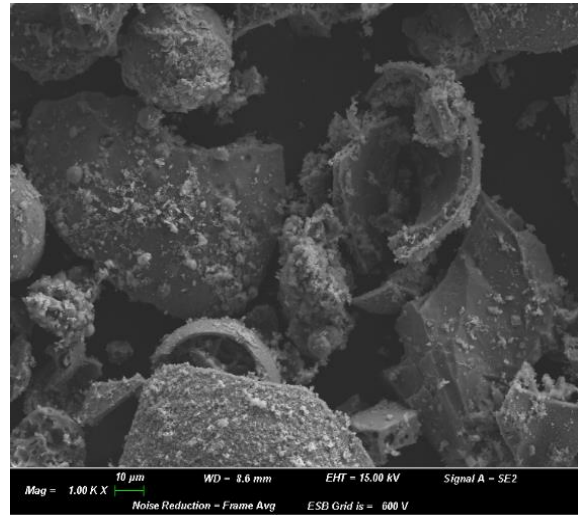
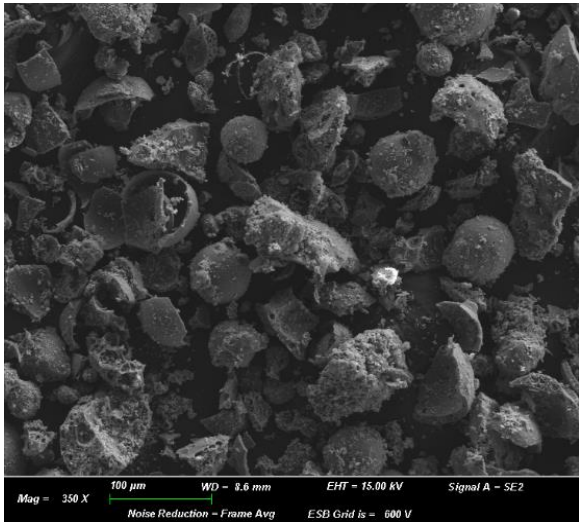
7.2 A.2 Pd/FAC



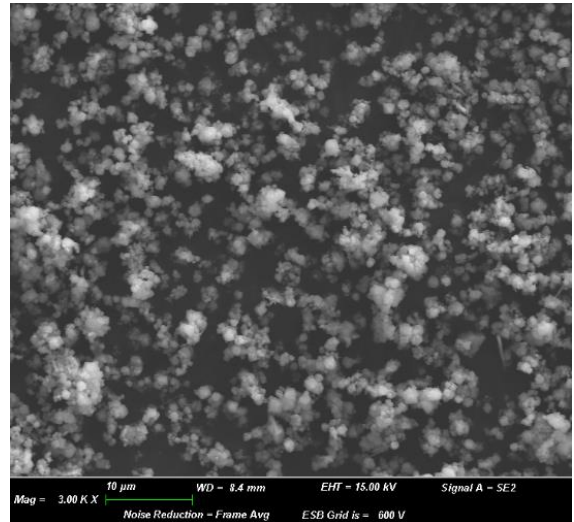
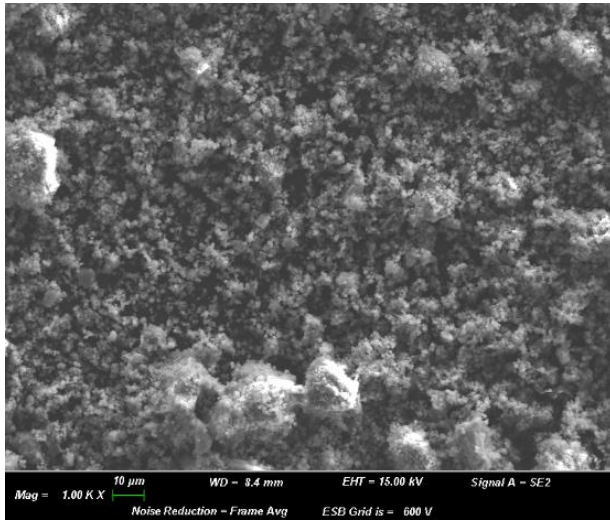
7.3 A.3 CoMo/FAC



7.4 A.4 NiMo/FAC



7.5 A.5 NiMo/ZEOLITE X



8 ADDENDUM B: HYDROGENATION

TESTS RESULTS

```

> restart
> with(ExcelTools) :
> Ln0 := Import("Hydrogenation.xlsx", "Test01", "B1", emptycell
    = 0.0) :

> Ln := Import("Hydrogenation.xlsx", "Test01", "B2", emptycell = 0.0)
> Le := Import("Hydrogenation.xlsx", "Test01", "C1", emptycell = 0.0) :

> Le0 := Import("Hydrogenation.xlsx", "Test01", "C2", emptycell
    = 0.0) :

> Ol := Import("Hydrogenation.xlsx", "Test01", "D1", emptycell = 0.0) :

> Ol0 := Import("Hydrogenation.xlsx", "Test01", "D2", emptycell
    = 0.0) :

> t := 30 :
>
> eq1 := Ln - Ln0·exp(-k3·t) = 0
> eq2 := Le - Ln0· $\left(\frac{k3}{k2 - k3}\right) \cdot (\exp(-k3 \cdot t) - \exp(-k2 \cdot t)) - Le0$ 
    ·exp(-k2·t) = 0
>
> eq3 := Ol - Ln0· $\left(\frac{k3}{k2 - k3}\right) \cdot \left(\frac{k2}{k1 - k3}\right) \cdot (\exp(-k3 \cdot t) - \exp(-k1$ 
    ·t)) + Ln0· $\left(\frac{k3}{k2 - k3}\right) \cdot \left(\frac{k2}{k1 - k2}\right) \cdot (\exp(-k2 \cdot t) - \exp(-k1$ 
    ·t)) - Le0· $\left(\frac{k3}{k2 - k3}\right) \cdot (\exp(-k2 \cdot t) - \exp(-k1 \cdot t)) - Ol0 \cdot (-k1$ 
    ·t) = 0
>
> solve({eq1, eq2, eq3}, {k1, k2, k3})

```

8.1 B.1 TEST 01- TEST 02

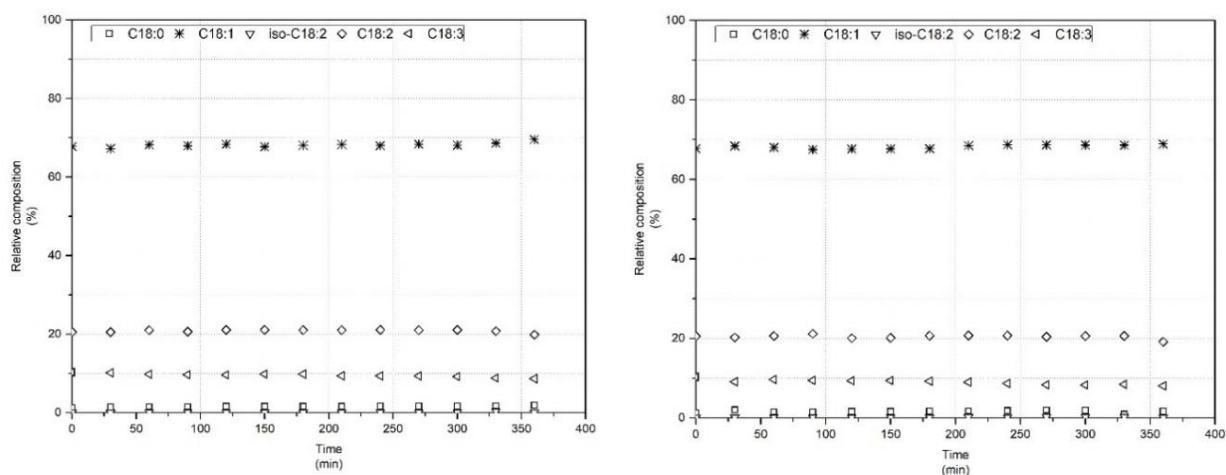


Figure 8.1 Test 01 (60 °C, 4 bar, 4 mg_{catalyst}/mL_{oil}) on the left, Test 02 (60 °C, 4 bar, 4 mg_{catalyst}/mL_{oil}) on the right.

8.2 B.2 MODEL FITTING WITH PD LINDLAR

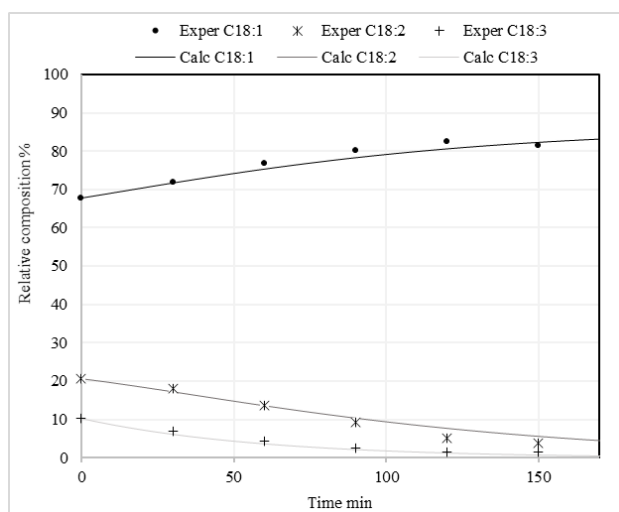


Figure 8.2 Test 03 (120 °C, 8 bar, 4 mg_{catalyst}/mL_{oil})
 $K1=0.0001$, $K2=0.0121$, $K3=0.0171$.

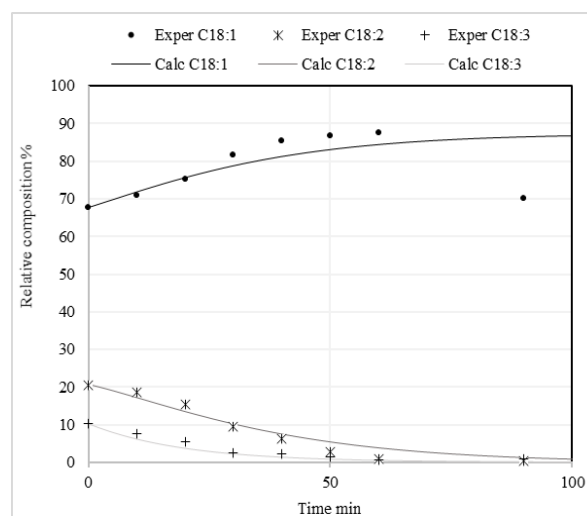


Figure 8.3 Test 05 (180 °C, 12 bar, 4 mg_{catalyst}/mL_{oil})
 $K1=0.0001$, $K2=0.040211$,
 $K3=0.051134$.

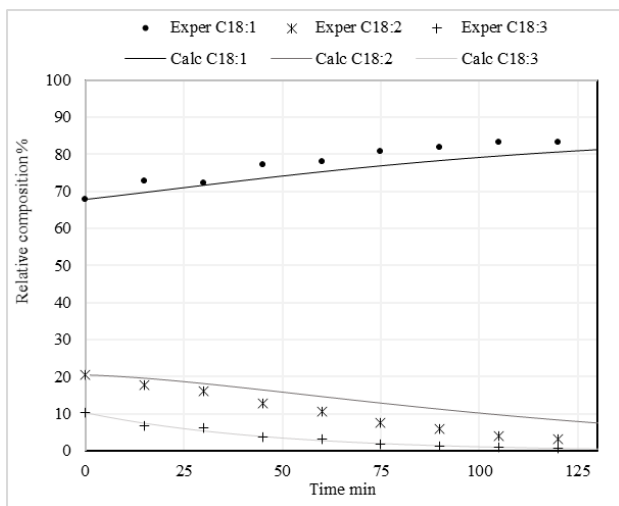


Figure 8.4 Test 06 (180 °C, 4 bar, 1 mg_{catalyst}/mL_{oil})
($K1=0.0001, K2=0.0122, K3=0.021207$)

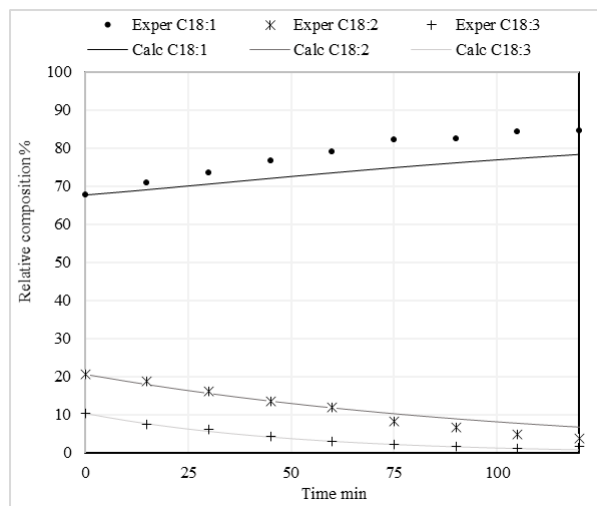


Figure 8.5 Test 07 (180 °C, 4 bar, 0.5 mg_{catalyst}/mL_{oil})
($K1=0.0001, K2=0.009097, K3=0.019804$)

8.3 B.3 MODEL FITTING WITH PD/HT

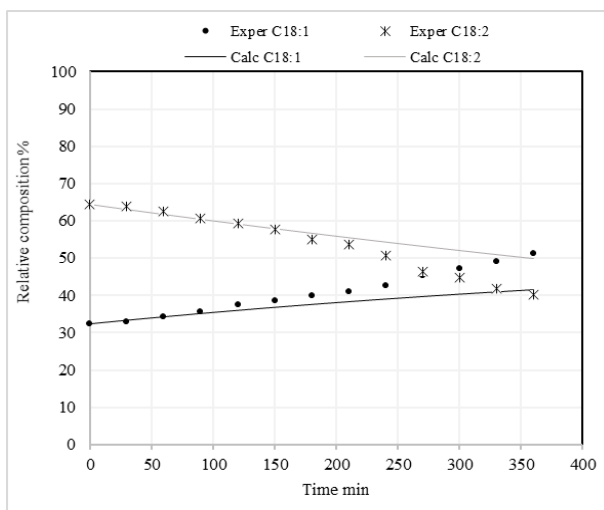


Figure 8.6 Test 22 (120 °C, 4 bar, 1 mg_{catalyst}/mL_{oil})
($K1=0.0001, K2=0.00095$)

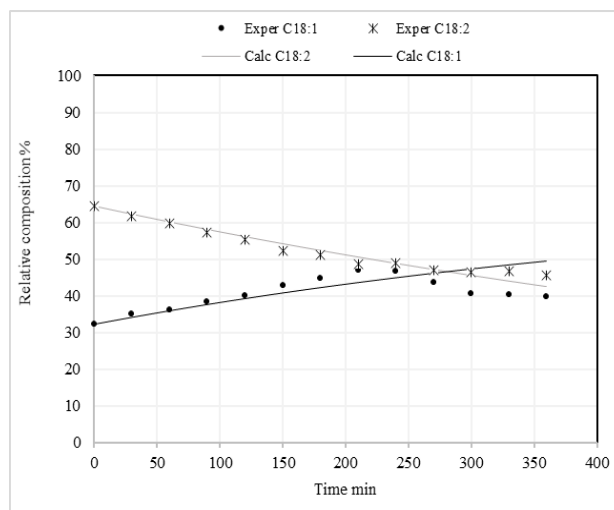


Figure 8.7 Test 16 (120 °C, 4 bar, 0.5 mg_{catalyst}/mL_{oil})
($K1=0.0003, K2=0.001143$)

8.4 B.4 MODEL FITTING WITH PD/FAC

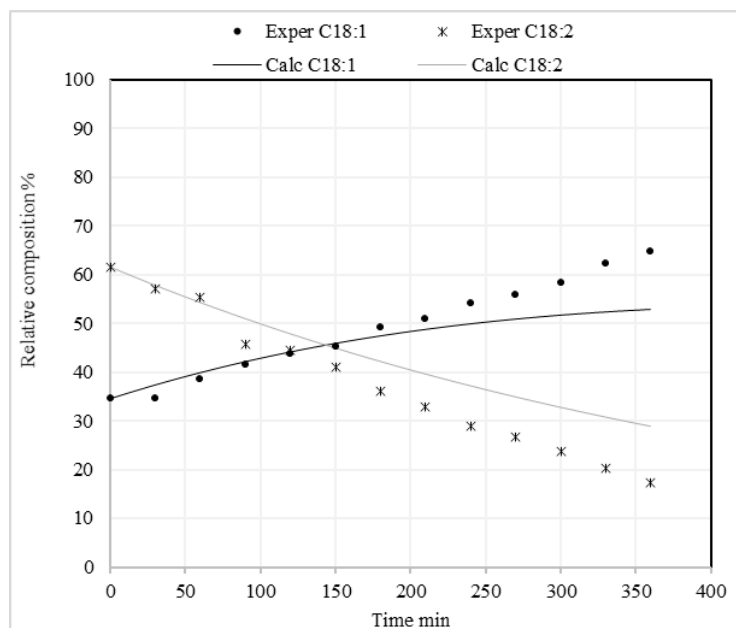


Figure 8.8 Test 22 (180 °C, 4 bar, 2 mg_{catalys}/mL_{oil}), ($K1=0.0009$,
 $K2=0.0021$).

9 ADDENDUM C: CHARACTERIZATION RESULTS FOR FUTURE ACTIVITIES

9.1 C.1 ICP-AES ELEMENTAL ANALYSIS

Table 9.1 ICP-AES analysis results

Sample	Ni (%)	Mo (%)	Ce (%)	Ca (%)	Al (%)	Si (%)
NiMo/zeolite	4.1 ± 0.2	10.8 ± 0.5	0	0	12.2 ± 0.5	6.3 ± 0.1
NiMo/FAC	4.4 ± 0.1	11.7 ± 0.3	0	0	13.0 ± 0.3	20 ± 1
NiMoCe/zeolite	4 ± 0.1	10.2 ± 0.2	3.55 ± 0.07	0	11.1 ± 0.2	9.1 ± 0.4
NiMoCe/FAC	4.2 ± 0.1	11.7 ± 0.4	4.4 ± 0.1	0	12.7 ± 0.7	13.2 ± 0.5
NiMoCa/zeoilte	4.3 ± 0.1	11.2 ± 0.3	0	4.5 ± 0.1	1.45 ± 0.4	8.4 ± 0.4
NiMoCa/FAC	4.2 ± 0.2	10.8 ± 0.2	0	6.5 ± 0.2	2.70 ± 0.4	16 ± 0.2

9.2 C.2 H₂-CHEMISORPTION ANALYSIS

Table 9.2 Metallic surface area, dispersion, and particle size

Sample	surface (m ² /g)	dispersion (%)	particle size (nm)
NiMo/zeolite	1	4	25.3
NiMo/FAC	1	4	23.9
NiMoCe/zeolite	3	10	9.78
NiMoCe/FAC	1	3	37.6
NiMoCa/zeoilte	1	2	45.2
NiMoCa/FAC	1	3	36.8

9.3 C.3 TPR TEMPERATURE PROGRAMMED

Table 9.3 Metals reduction temperatures

Sample	Ni T _{red} (C)	Mo T _{red} (C)	Ce T _{red} (C)	Ca T _{red} (C)
NiMo/zeolite	549.47	742.1	0	0
NiMo/FAC	570.54	781.56	0	0
NiMoCe/zeolite	610.9	783.26	898.96	0
NiMoCe/FAC	466.68	635.07	807.96	0
NiMoCa/zeoilte	600.93	705.27	0	892.68
NiMoCa/FAC	388.58	555.29	0	904.12

9.4 C.4 NH₃-TPD – ACIDITY ANALYSIS

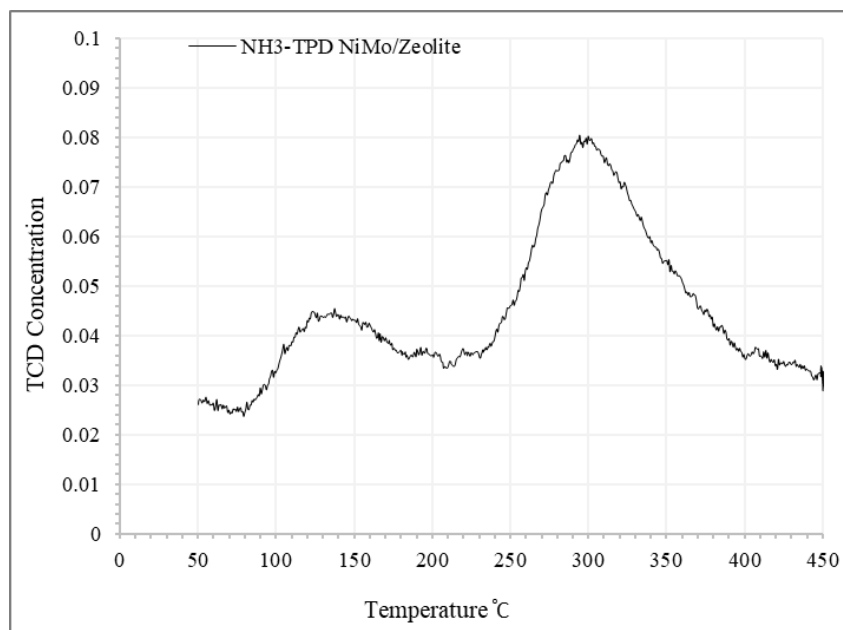


Figure 9.1 NH₃-TPD acidity analysis NiMo/Zeolite

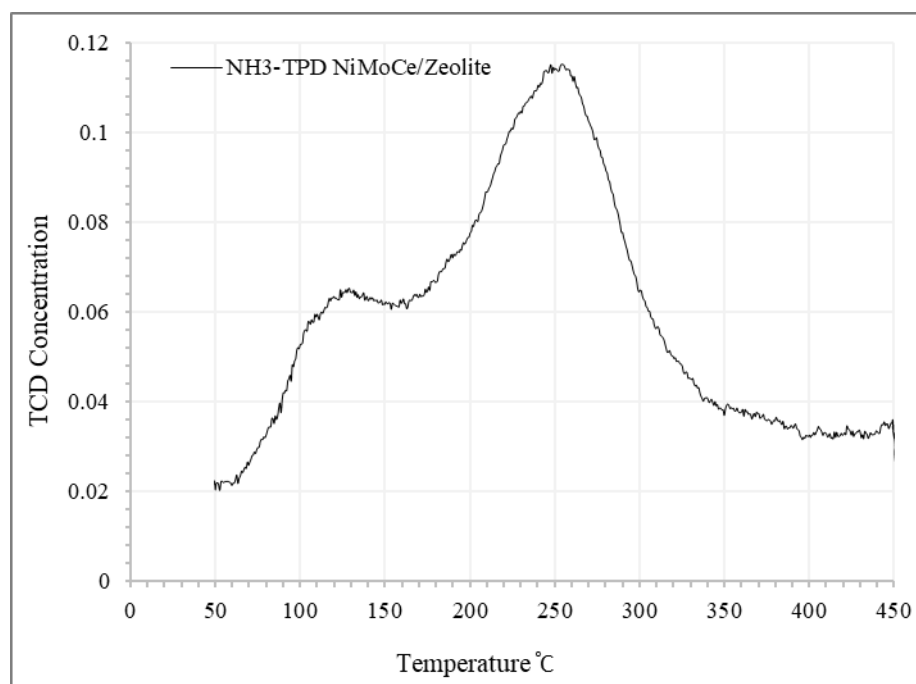


Figure 9.2 NH₃-TPD acidity analysis NiMoCe/Zeolite

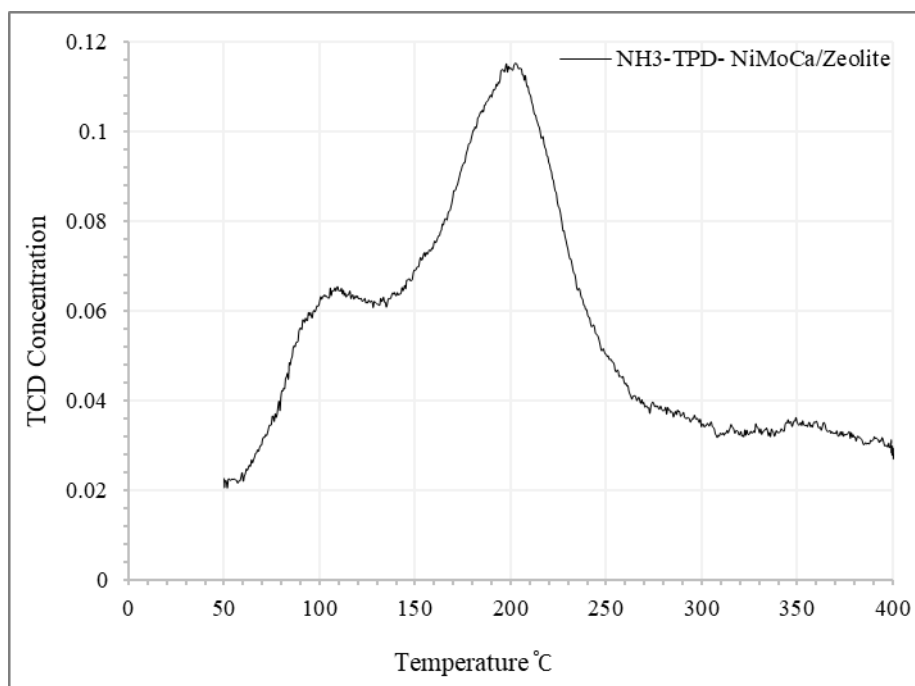


Figure 9.3 NH₃-TPD acidity analysis NiMoCa/Zelite

10 ADDENDUM D: DESALINATION TECHNOLOGIES

This part was carried out under the supervision and the collaboration of: Prof. Pier Ugo Foscolo, Prof. Antonio Germanà, and Dr. Marilana Taddei.

ABSTRACT

The demand for freshwater supply is exceedingly increasing due to the rapid growth of the global population and economic development. With limited freshwater sources, desalination of sea and brackish water offers the potential to meet the increasing water demands. But, the suitability of these desalination technologies depends on several criteria, including the level of feed water quality (Q_f), source of energy, removal efficiency or recovery (RR), energy requirement, etc. In this review, we have presented different desalination methods, Multistage flash (MSF), multi-effect distillation (MED), reverse osmosis (RO), etc. The comparison between these desalination technologies to be able to see which one is the best from the economic, environmental wastes, and efficiency points of view. Thermal desalination plants normally have higher energy requirements and unit capital cost than membrane plants and produce huge waste heat. Also, corrosion scaling and fouling problems are more serious in

thermal processes compared with the membrane processes. On the other hand, membrane processes required feed water pre-treatment to remove particulates so that the membranes last longer. Scientists' studies are still working in order to reduce the total energy consumption production, waste heat, and costs arriving at the ideal desalination technologies. Almost, reverse osmosis and multistage flash processes are becoming the choice for desalination in most parts of the world.

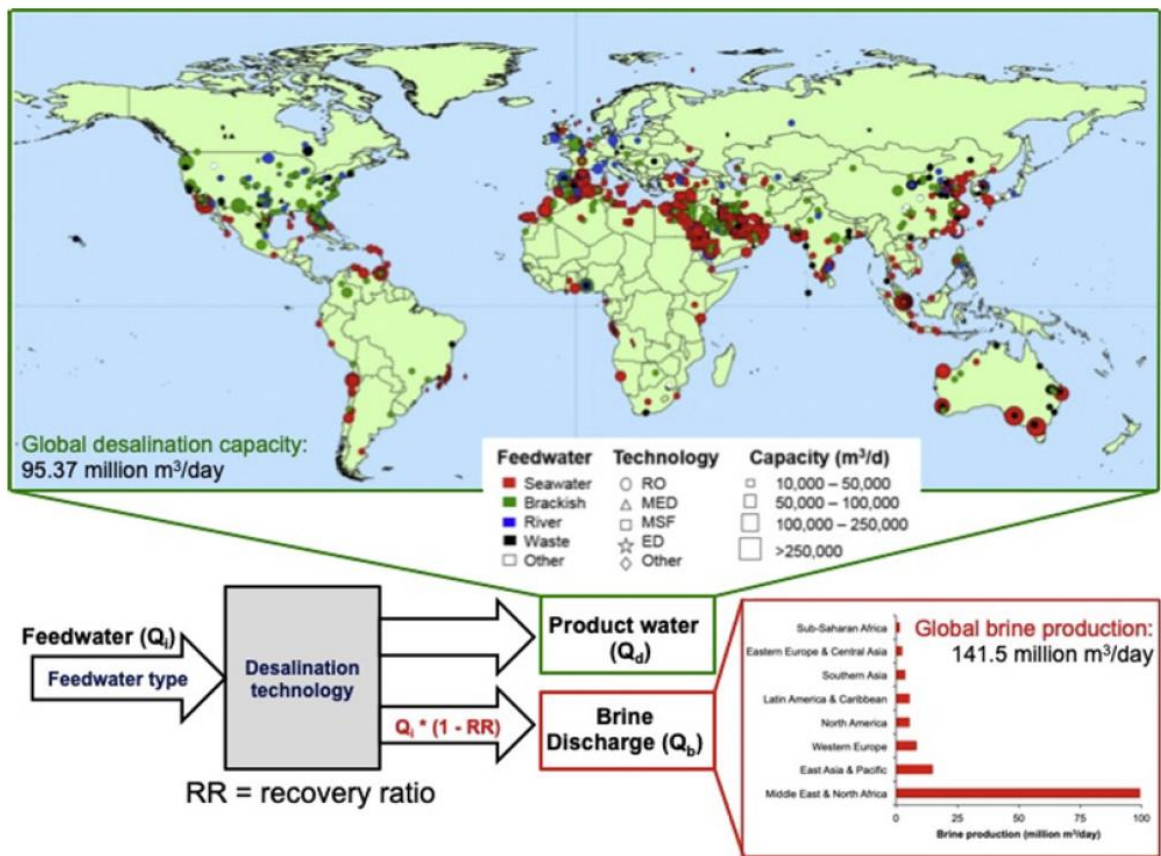


Figure 10.1 Graphical abstract of global, conventional water resources, desalinated water production, and brine production [236].

Keywords : Desalination technologies ; thermal desalination; membrane desalination; Energy; salinity.

10.1 INTRODUCTION

Water is a vital resource for the existence of living beings on the earth's surface and is necessary for economic and social development [237]. Only about 0.5% of the overall global water is available as freshwater, while seawater accounts for about 97% of them[237]. In many parts of the world, a huge amount of fresh water is required for agricultural, industrial, and domestic uses. Desalination is the term broadly used to describe the production of potable water from various sources of raw water. The sources may include brackish water, rivers water, wastewater, pure water, and seawater. In this sense, desalination is the process of reducing the concentration of dissolved solids TDS in the raw water. Freshwater is defined as containing less than 1000mg/l of salts or total dissolved solids [238].

In recent years, increased attention has been drawn to the promise and prospects of desalination technology for alleviating the growing water scarcity. Factors that have the largest effect on the cost of desalination are feed water quality (salinity levels), product water quality, energy costs, as well as economies of scale [237][239].

The desalination process is divided into two main categories, thermal processes, and membrane processes. Membrane desalination plants produce potable water by molecular separation, while thermal desalination plants work by breaking bonds between water molecules. Both approaches require an energy input for seawater under standard atmospheric temperature and pressure conditions. The energy input for membrane processes reflects the pressure energy required to pump water molecules through a size/charge selective membrane and is expressed as kWh/m³ of product water, while the energy input for thermal processes reflects a combination of the heat required to break the bonds between the water molecules (expressed as kJ/m³) and the energy required to pump the seawater through the process (expressed as kWh/m³) [240].

Thermally activated systems include multi-stage flash distillation (MSF), multiple-effect distillation (MED), vapor compression distillation (VCD), humidification - dehumidification desalination (HDH), solar distillation (SD), and freezing (Frz). In these systems, heat transfer is used either to boil or freeze the seawater or brackish water to convert it to vapor or ice, so the salts are separated from the water [240]. Pressure activated systems use permeable membranes to create two zones where water can pass through and leave salt behind, and these technologies consist of reverse osmosis (RO), forward osmosis (FO), electro-dialysis (ED), and nanofiltration (NF) [237]. Figure. 2 shows the flow chart of the most applied desalination technologies:

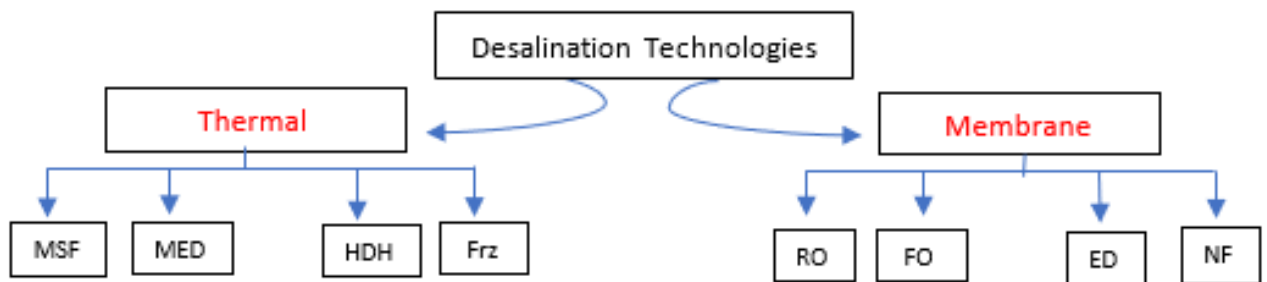


Figure 10.2 Classification of the most applied desalination technologies.

The most applied desalination technologies are Multi-stage flash (MSF), Reverse osmosis (RO), and Multi-Effect Desalination (MED). It was found during 2013, among the worldwide installed desalination capacity, 65% was based on RO, while MSF accounts for 22% and MED for only 8% [241], while the current production of desalinated water from RO now stands at 65.5 million m³/day, in which about 69% of the volume of the global desalinated water produced [242].

This study is to present an overview of current desalination technologies for seawater and brackish water to produce freshwater, also to show and discuss the advantages and

disadvantages of these technologies, evaluating the best one considering the cost, removal efficiency, and TDS.

10.2 HISTORY OF DESALINATION

Early research on desalination was conducted during World War II to satisfy freshwater needs in remote locations, and the United States and other countries continued that work after the war [238]. The desalination technologies are commercially available since 1960, and most of them based on thermal processes. Later, multi-stage flash distillation had become popular, and the Arabian Gulf was the main area of many commercial plants set up [243]. In the late 1960s, membranes had entered the desalination market and were initially used for brackish water treatment. Desalination became a commercial enterprise development in both thermal and membrane technology by the 1980s, which led to an exponential growth in world desalination capacity. The worldwide distribution of desalination capacity until 2010 is shown in Table1[236]:

Table 10.1 Top 10 countries employing desalination technologies

Sl. No.	Country total	Capacity (million m ³ /d)	Market share (%)
1	Saudi Arabia	9.9	16.5
2	USA	8.4	14.0
3	UAE	7.5	12.5
4	Spain	5.3	8.9
5	Kuwait	2.5	4.2
6	China	2.4	4.0
7	Japan	1.6	2.6
8	Qatar	1.4	2.4
9	Algeria	1.4	2.3
10	Australia	1.2	2.0

By the time, a large growing desalination capacity the world has seen, in which so clear in the analysis study by Eduard Jones, arriving about 96 million m³/day desalination capacity in 2020 as shown in Figure 10.3[236].

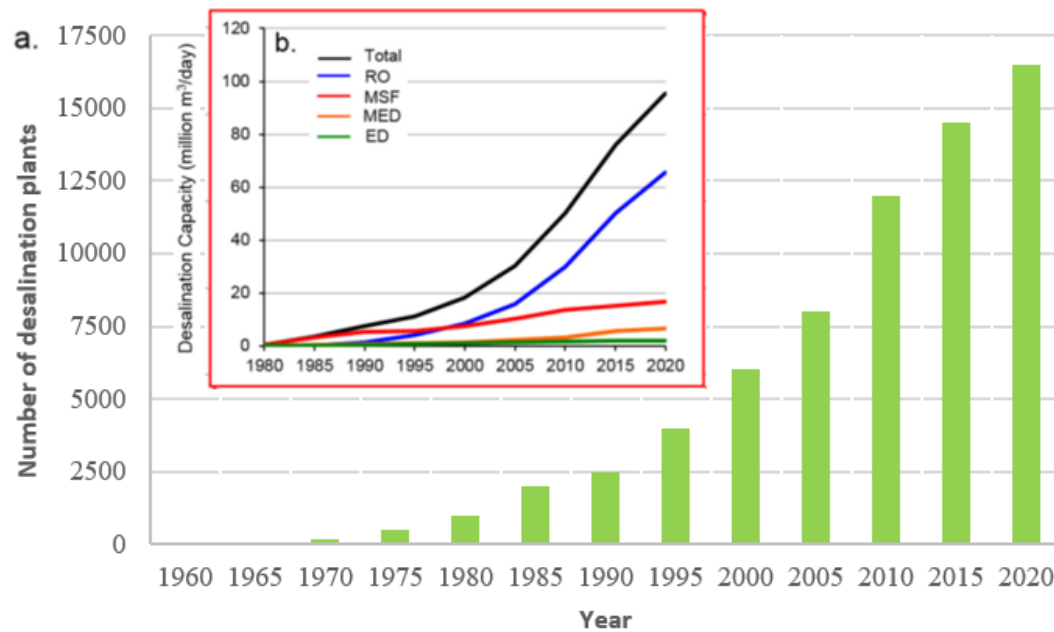


Figure 10.3 Global desalination by number and capacity (a) of total and operational desalination facilities and (b) of desalination technology

10.3 OVERVIEW OF DESALINATION TECHNOLOGIES

The notable increase in the use of desalination technologies over the past years is to a great extent the result of a long history of research and development efforts. The total global desalination capacity is expected to reach about 100 million m³/d by 2015 [244], and it continues to increase because of successfully studying to reduce desalination costs, which it has already investigated by Eduard Jones et. al. [236], but these costs are different depending on the desalination technology which is used and the type of source water. For example, the inland brackish groundwater desalination facilities will use wells and pumps to bring the source water to the facility, and these systems may need little or no pretreatment, While the

seawater desalination with RO may require extensive pretreatment and a specific design intake structure.

The five key components of a desalination system are [245]:

1. Intake: are the structures used to extract raw water and pump it to supply the desalination process.
2. Pretreatment: is the removal of suspended solids by sedimentation and filtration systems and adding some chemicals to prepare the raw water for further processing.
3. The main process for removing dissolved solids (the main desalination process)
4. Post-treatment is the addition of chemicals to the product water to adjust the pH value.
5. The concentrate disposal or reuse method at the outlet from the desalination system.

Several parameters affect the selection of desalination systems, including the quality of salty water to be desalinated, the salinity level of produced potable water, input energy, environmental impact, and cost.

According to the salinity of water as the most important parameter for the desalination process, it could be categorized into brackish or seawater. Brackish water contains total dissolved solids (TDS) higher than potable water and lower than seawater. Potable water should have TDS lower than 1000 ppm (or mg/l) and brackish water in the range of 1,000 to 25,000 ppm, while seawater has an average of 35,000 ppm TDS concentration [240]. Figure .4 shows the variation of feed water and produced water salinity for the listed technologies. It is clear from this figure that MSF desalination technology can handle feed water with the highest salinity and produce water with the lowest salinity.

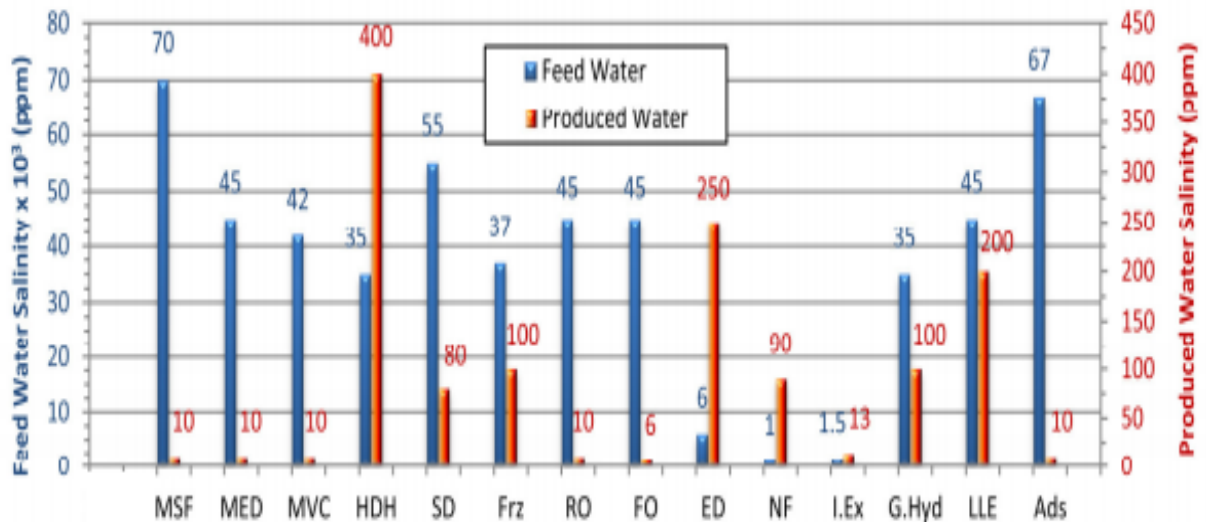


Figure 10.4 Different Desalination Systems Capabilities Regarding Salinity of Feed and Produced Water measured in ppm

10.3.1 THERMAL DESALINATION PROCESSES

This process is worked to heat salty water (brackish or sea) water producing a vapor that in a run to condensed and form freshwater. So, the important factors in this process to be considered are the temperature for source water, energy, and scale formation.

10.3.1.1 MULTISTAGE FLASH PROCESS (MSF)

Multistage flash (MSF) accounts for the major portion of desalinated municipal drinking water produced in the world and is used primarily for desalinating seawater [240]. MSF units are widely used in the Middle East (particularly in Saudi Arabia, United Arab Emirates, and Kuwait), and they account for over 22% of the world's desalination capacity [237].

Figure 10.5 shows a schematic diagram of the MSF system [244]; the system involves six main streams: intake seawater, rejected cooling seawater, distillate product, rejected brine, brine recycle, and heating steam. The system contains flashing stages and a brine heater. The flashing stages are divided into two sections: heat recovery and heat rejection. The number of flashing

stages in the heat rejection section is commonly limited to three. On the other hand, the number of flashing stages in the heat recovery section varies between 21 and 40. The intake seawater is introduced into the inside of the preheater/condenser tubes of the last flashing stage in the heat rejection section. Similarly, the brine recycles stream is introduced into the inside of the preheater/condenser tubes of the last flashing stage in the heat recovery section.

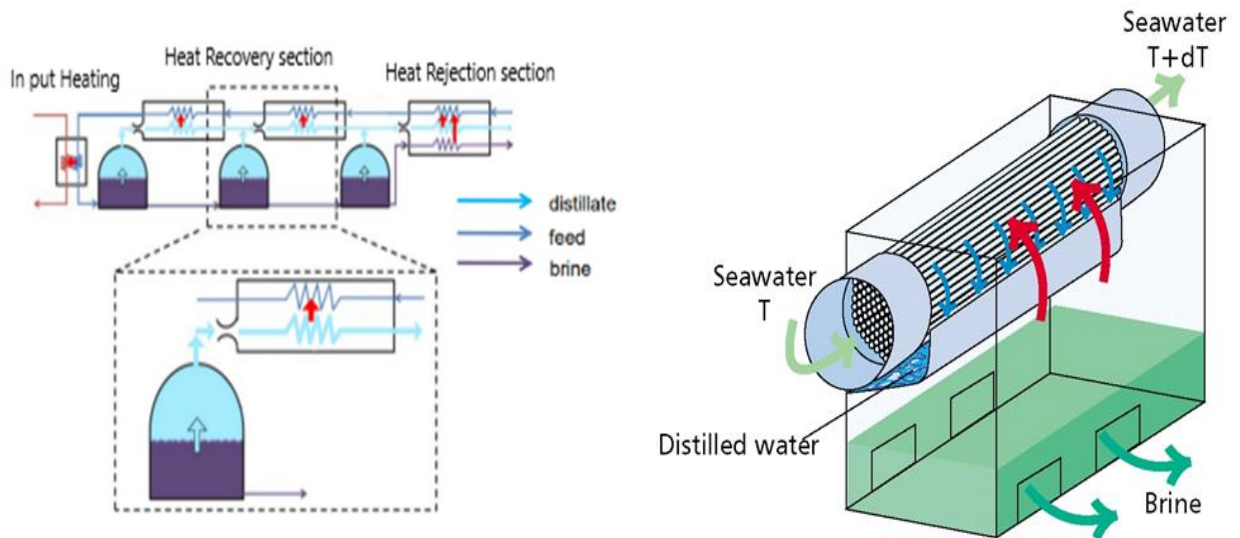


Figure 10.5 MSF desalination process with some adding [244]

10.3.1.2 MULTI-EFFECT DISTILLATION (MED)

The MED process takes place in a series of evaporators called effects and uses the principle of reducing the ambient pressure in the various effects. This process permits the seawater feed to undergo multiple boiling without supplying additional heat after the first effect. The seawater enters the first effect and is raised to the boiling point after being preheated in tubes. The seawater is sprayed onto the surface of evaporator tubes to promote rapid evaporation. The tubes are heated by externally supplied steam from a normally dual-purpose power plant. The steam is condensed on the opposite side of the tubes, and the steam condensate is recycled to the power plant for its boiler feed water. The MED plant's steam economy is proportional to the number of effects. The total number of effects is limited by the total temperature range

available and the minimum allowable temperature difference between one effect and the next effect [246].

Only a portion of the seawater applied to the tubes in the first effect is evaporated. The remaining feed water is fed to the second effect, where it is again applied to a tube bundle. These tubes are, in turn, heated by the vapors created in the first effect. This vapor is condensed to the freshwater product while giving up heat to evaporate a portion of the remaining seawater feed in the next effect. The process of evaporation and condensation is repeated from effect to effect, each at a successively lower pressure and temperature. This continues for several effects, with 4 to 21 effects and performance ratio from 10 to 18 being found in a typical large plant [Figure 10.6 shows a description of the multi-effect desalination process [245].

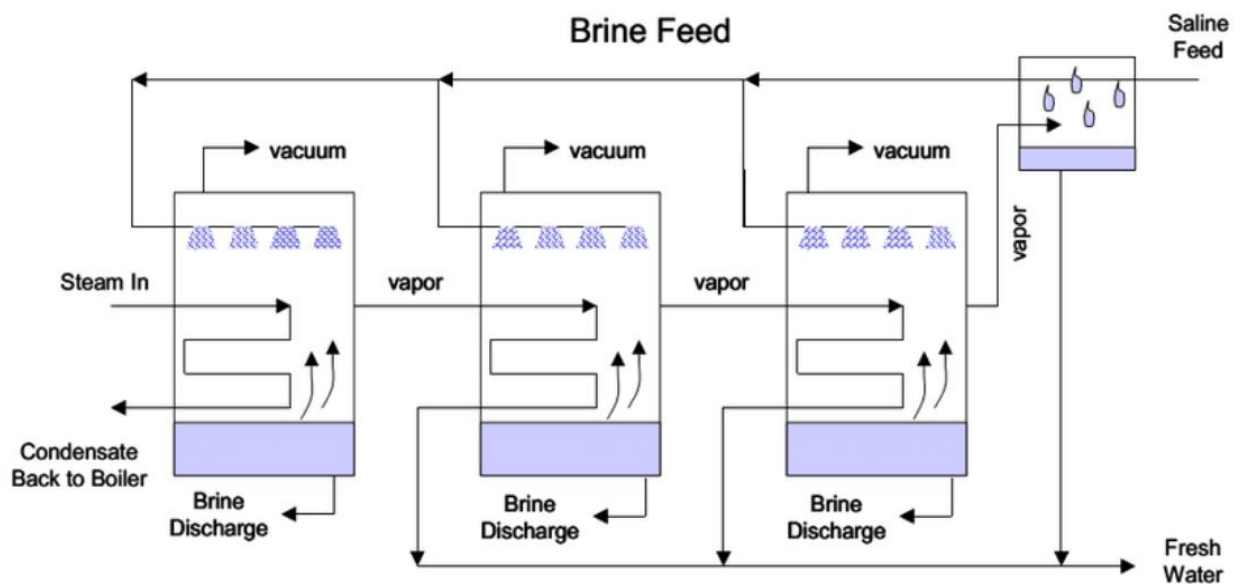


Figure 10.6 Multi-Effect desalination process scheme

10.3.1.3 VAPOR COMPRESSION DISTILLATION VCD

In the VCD process, the heat for evaporating the seawater comes from the compression of vapor. Two methods are used to condense water vapor to produce enough heat to evaporate

incoming seawater a mechanical compressor and a steam jet. The mechanical compressor is usually electrically driven, while the steam jet is thermal driven. VCD units have been built in a variety of configurations to promote the exchange of heat to evaporate the seawater. The compressor creates a vacuum in the evaporator and then compresses the vapor taken from the evaporator and condenses it inside of a tube bundle. Seawater is sprayed on the outside of the heated tube bundle where it boils and partially evaporates, producing more vapor Figure 10.7 [246].

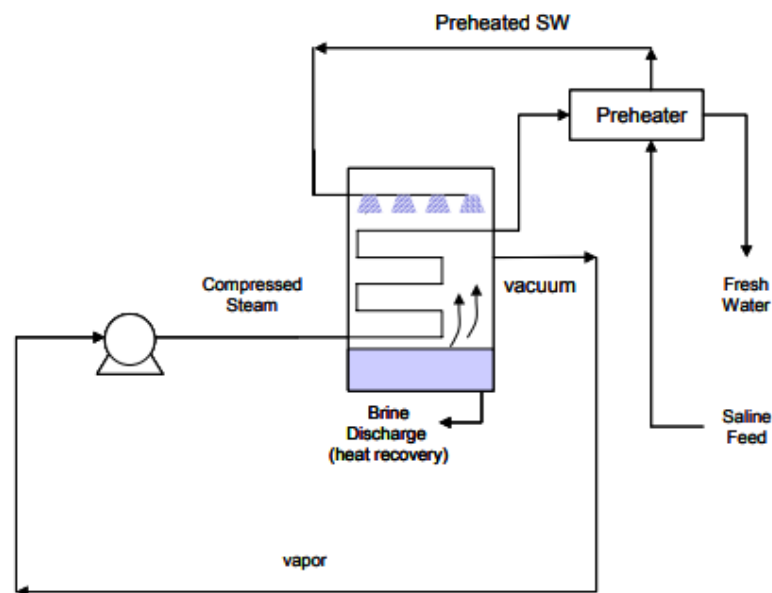


Figure 10.7 Schematic diagram of a single mechanical vapor compression distillation process.

10.3.2 MEMBRANE PROCESS

The fundamental principle of the membrane processes is that the membrane separates two phases allow transporting of one or more components readily than that of other components. The driving force for transport can be a pressure gradient, a temperature gradient, a concentration gradient, or an electrical potential gradient. There are mainly three types of membrane processes usually used for desalination: reverse osmosis (RO) and electro dialysis (ED), and forward osmosis (FO).

10.3.2.1 REVERSE OSMOSIS DESALINATION RO

The reverse osmosis (RO) process is a membrane separation process Figure.6, where the osmotic pressure is overcome by applying external pressure higher than the osmotic pressure on the seawater. Thus, water flows in the reverse direction to the natural flow across the membrane, leaving the dissolved salts behind with an increase in salt concentration. The major energy required for desalting is for pressurizing the seawater feed.

A typical large seawater RO plant consists of four major components: feedwater pre-treatment, high-pressure pumping, membrane separation, and permeate post-treatment.

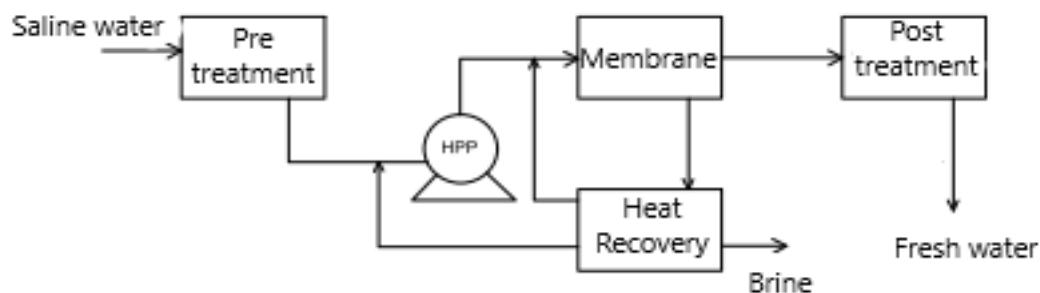


Figure 10.8 Block diagram of reverse osmosis operations.

Reverse osmosis can remove from brines dissolved not only solids but also organic material, colloidal material, and some microorganisms [237].

RO is usually used for brackish water where the total dissolved solids TDS ranging from 100 to 10000 mg/l, low-pressure membranes have decreased the pressure requirements for some reverse osmosis operations by up to 50%, the efficiency of reverse osmosis operation will undoubtedly increase and cost decrease as membranes are also improved the use of chemicals for cleaning is low [237]. On the other hand, raw seawater flows into the intake structure through trash racks and traveling screens to remove debris in the seawater. The seawater is

cleaned further in a multimedia gravity filter that removes suspended solids; typical media are anthracite, silica, and granite or only sand and anthracite. From the media filter, the saltwater flows to the micron cartridge filter that removes particles larger than 10 microns, where the filtered seawater protects the high-pressure pumps and then to the RO section of the plant.

So, the pre-treatment technologies, as seen in Figure 10.9 include sedimentation, chemical treatments, filtration.

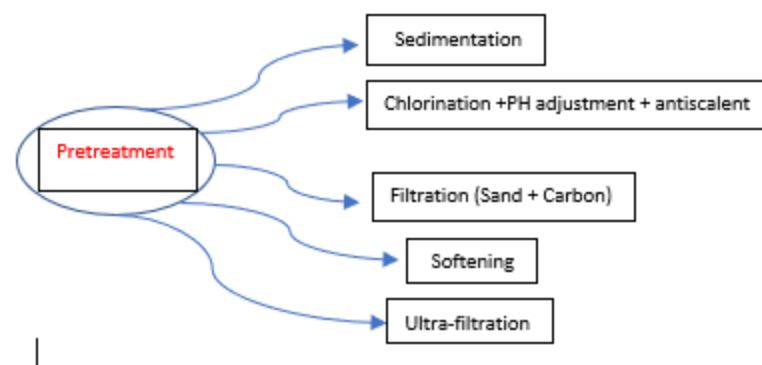


Figure 10.9 Pretreatment processes in the RO desalination technology.

The high-pressure pump HPP raises the pressure of the pretreated feedwater to the pressure appropriate for the membrane. The semipermeable membrane restricts the passage of dissolved salts while permitting water to pass through. The concentrated brine is discharged into the sea. Pretreatment is needed to eliminate the undesirable constituents in the seawater, which would otherwise cause membrane fouling. The most commercially successful membrane configurations are spiral wound and fine hollow fiber (HFF).

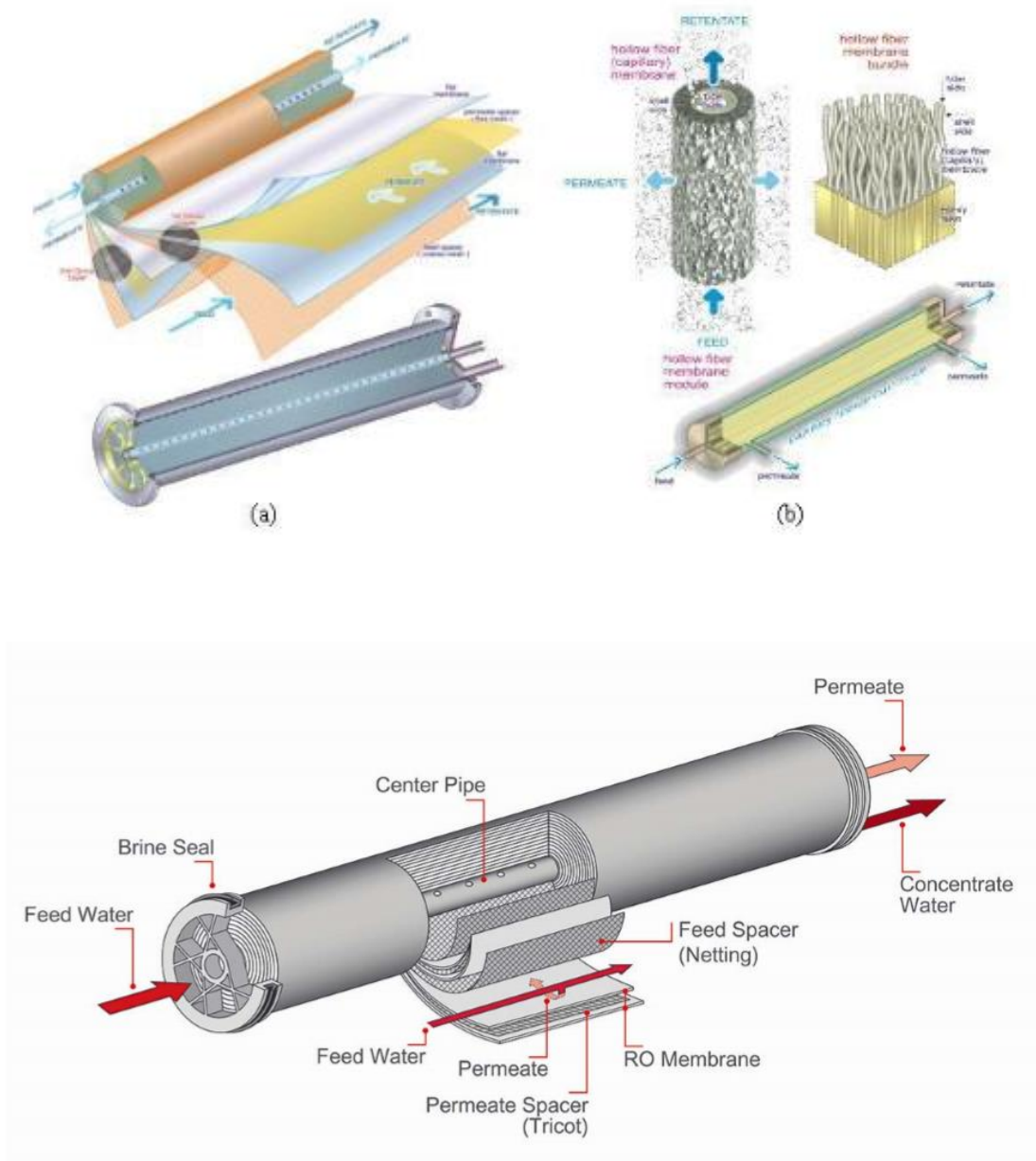


Figure 10.10 Major Types of RO membrane (a)Spiral wound, (b)Hollow fiber [242].

Two developments have helped to reduce the operating costs of RO plants during the past decade: the development of membranes that can operate efficiently with longer duration and the use of energy recovery devices. The recovery devices are connected to the concentrated stream as it leaves the pressure vessel. The concentrated brine loses only about 1–4 bar relative to the applied pressure from the high-pressure pump. The recovery devices are mechanical and generally consist of turbines or pumps of some types that can convert a pressure drop to

rotating energy. Figure 10.11 shows a block diagram of the RO plant is combined with the power plant and the energy recovery turbine [237].

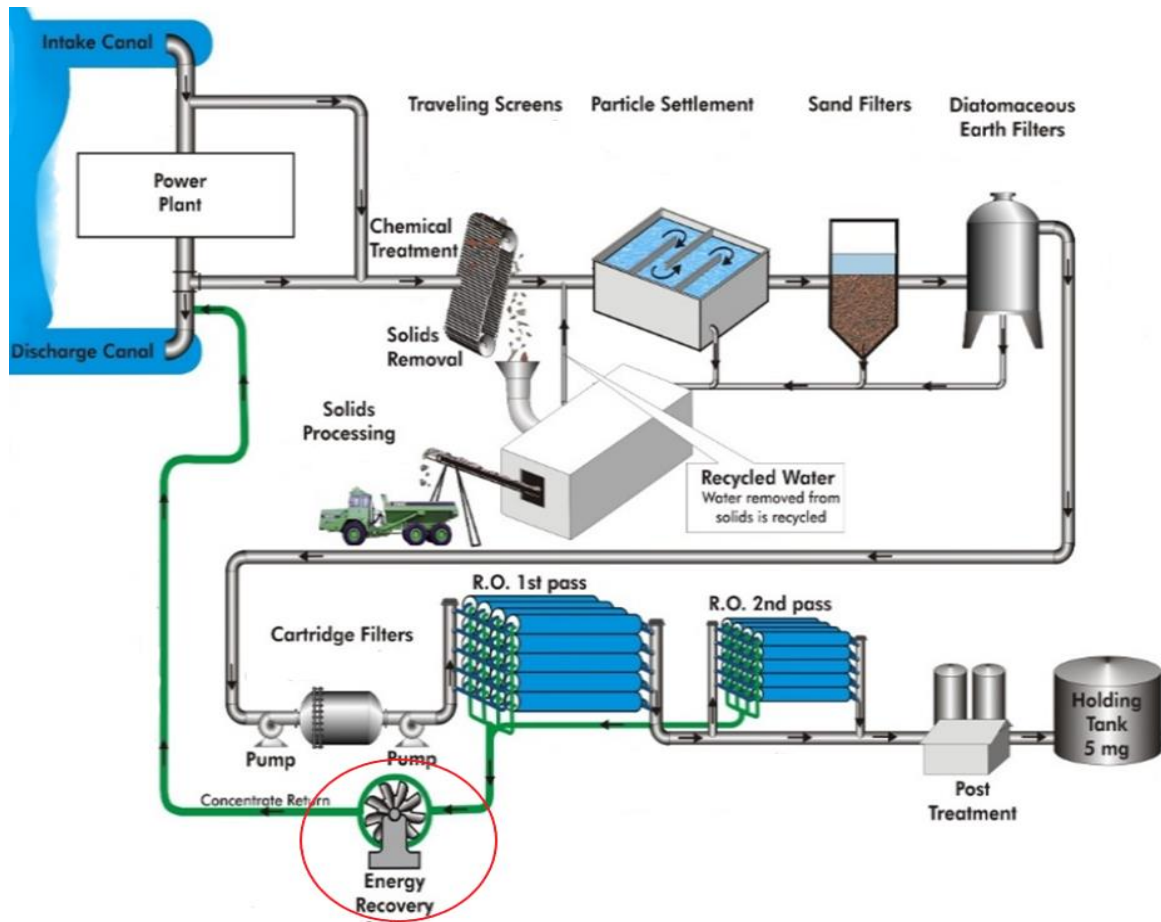


Figure 10.11 Reverse Osmosis Desalination process diagram

10.3.2.2 FORWARD OSMOSIS (FO)

In the FO process, the osmotic pressure gradient generated by a highly concentrated solution (known as “draw” solution) to allow water to diffuse through a semi-permeable membrane from saline feed water, which has a relatively lower concentration as seen in Figure .9. Consequently, a less concentrated draw solution is being produced, which may be further treated to extract freshwater. With the use of a suitable draw solution, very high osmotic pressure driving forces can be generated to achieve high recoveries that, in principle, can lead to salt precipitation. The saline feed water is fed to the FO unit, which can incorporate spiral

wound or hollow fiber membrane modules. The feed water and draw solution flow tangent to the membrane in a crossflow mode. Through osmosis, water transports from the seawater across the salt rejecting membrane and into the draw solution. To yield potable water, the diluted draw solution is sent to a separation unit comprising a distillation column or a membrane gas separation unit. The separated draw solution is recycled back to the FO unit. The FO process is characterized by relatively low fouling potential, low energy consumption, simplicity, and reliability [247].

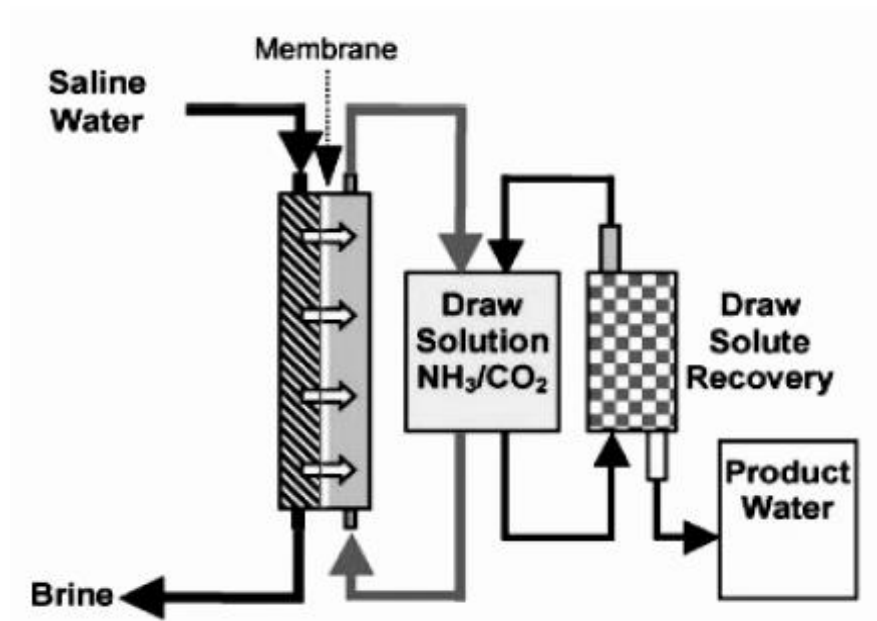


Figure 10.12 Forward osmosis process schematic

10.3.3 OTHERS DESALINATION TECHNOLOGIES

Besides the commercially available desalination technologies, numbers of other processes have been developed as an innovative in the desalination of seawater; although these processes couldn't reach the level of commercial success like MSF, MED, RO, they may become valuable in some special conditions. These new technologies include Solar evaporation distillation and membrane distillation:

10.3.3.1 SOLAR EVAPORATION DISTILLATION SD

The use of direct solar energy for desalinating seawater has been investigated quite extensively and used for some time. The process generally is similar to a part of the natural hydrologic cycle in which the seawater is heated by the sun's rays to produce water vapor. The water vapor is then condensed on a cool surface, and the condensate is collected as product water. An example of this type of process is the solar greenhouse still, in which the saline water is heated in a basin on the floor, and the water vapor condenses on the sloping glass roof that covers the basin [240].

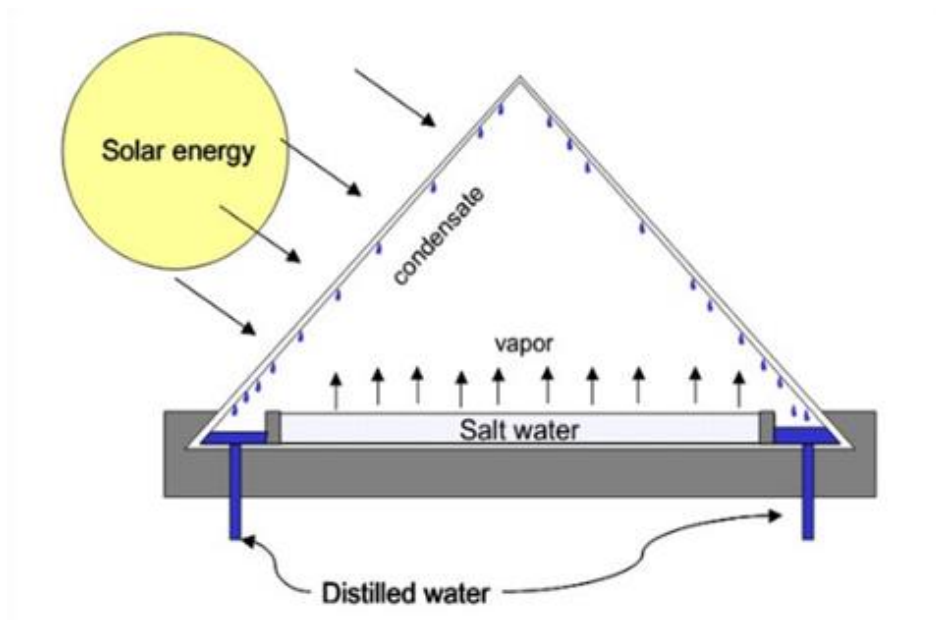


Figure 10.13 The basic design of a solar distillation desalination unit.

Variations of this type of solar still have been made in an effort to increase efficiency, but they share difficulties in the requirement of a large solar collection area (e.g., 25 hectares land/1000 m³ of product water/day) [242], high capital cost vulnerability to weather-related damage. Although thermal energy may be free, additional energy is needed to pump the water to and from the facility.

10.3.3.2 MEMBRANE DISTILLATION MD

MD is a thermally driven membrane process in which a hydrophobic microporous membrane separates saline water into a hot brine and a cold distillate. A hydrophobic membrane can prevent the passage of liquid by surface tension force, but not the passage of vapor. Therefore, the water vapor will be able to pass from the hot solution side of higher vapor pressure to the cold distillate side of lower vapor pressure. The large vapor chamber (because of phase change) used by conventional distillation is replaced by small holes in the microporous membrane. Small vapor space translates to a lower equipment cost and land use [236]. These membranes are made of hydrophobic synthetic material (e.g., PTFE, PVDF, or PP) and offer pores with a standard diameter between (0.1-0.5) μm [236]. The schematic of the membrane distillation is given in Figure 10.14 [240].

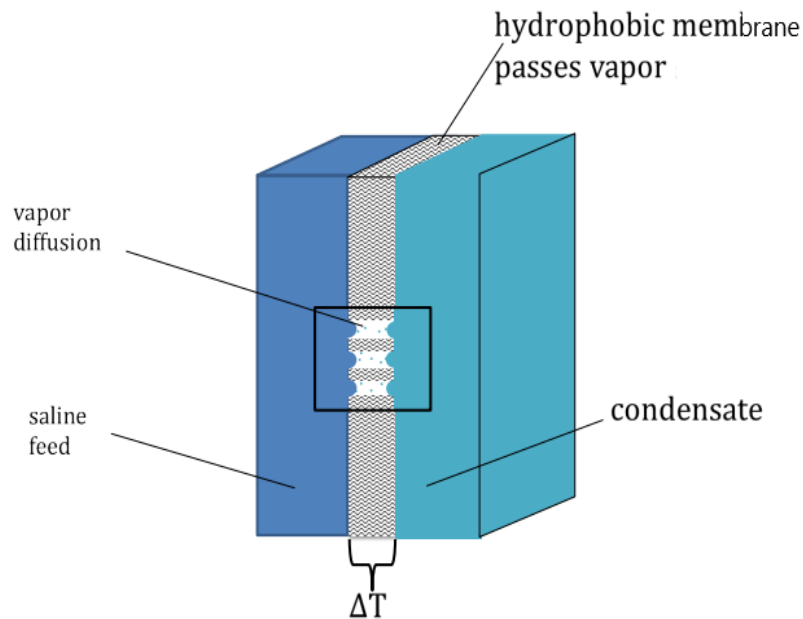


Figure 10.14 Membrane Distillation Process

Therefore, MD combines the advantages of conventional distillation and membrane methods, which are:

compactness in the facility, less energy cost, high degree of purity in water product, lower operating temperatures than conventional distillation, reduced chemical interaction between membrane and process solution, less demanding in membrane's mechanical strength with many advantages from a commercial standpoint; however, MD has not yet gained any acceptance in seawater desalination [238]. On the other hand, because MD is a thermally-driven process and the brine evaporates on one side of the membrane at the entrances of many tiny pores, fouling is very likely to occur. Fouling problem is very important to the effectiveness and the cycle-life of the membrane: both are crucial factors for MD to compete successfully with other desalination methods.

10.3.3.3 ADSORPTION DESALINATION SYSTEM ADS

AD has its origins in adsorption chillers, which use freshwater as the refrigerant that circulates between an evaporator, adsorption /desorption beds, and condenser. In ADS, however, saline water replaces the freshwater and switches the system from the closed cycle (in an adsorption chiller) to an open cycle in ADS. In this method, instead of using recycled pure water (from the condenser), saline or brackish water is supplied to the evaporator from an external source. The vapor created in the evaporated using low-large heat (from the sun or waste process) travels into the bed of silica gel where it is adsorbed until the silica is saturated. Once saturated, the bed of silica is heated using once again, low-grade heat to drive off the desalinated water before being re-condensed in a receiving vessel [247]. Figure 10.15 shows a schematic of two-bed adsorption-based desalinators.

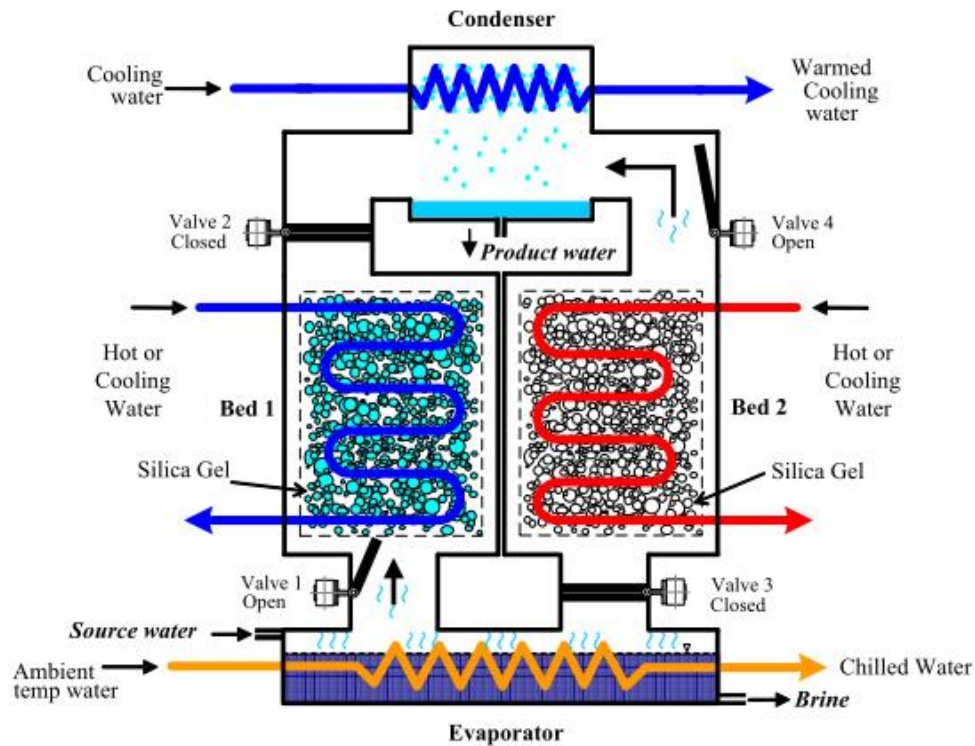


Figure 10.15 Schematic of the two-bed adsorption desalination system.

10.4 PARAMETRIC COMPARISON OF DESALINATION TECHNOLOGIES

Many technical parameters can be evaluated to make the comparison, like energy requirement, efficiency and performance ratio, scale and fouling, corrosion, thermal discharge and operating temperature, quality of feed water. We will see some of these parameters:

10.4.1 REMOVAL EFFICIENCY AND PERFORMANCE RATIO

Removal efficiency in the membrane technologies (RO, NF) is the best among all of the process, while its lower in the MSF and MED. Also, for performance ratio, it's the best in the membrane technologies. Figure 10.16 represents the performance ratio PR of different desalination technologies.

Where, $PR = (\text{Net Distillate mass flow rate}) / (\text{Energy level} / 2326 \text{ KJ})$ in Figure 10.16 [248].

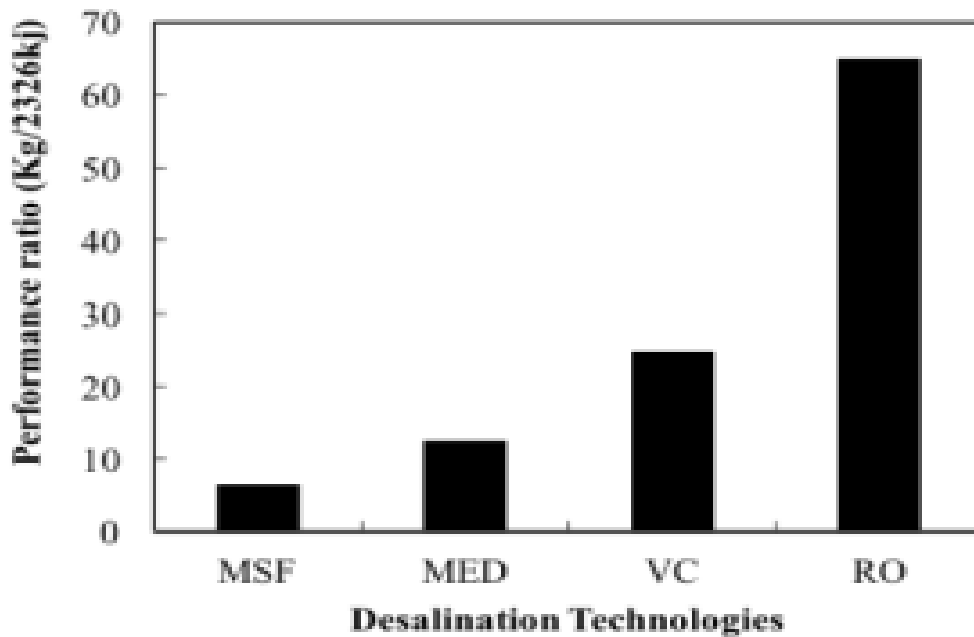


Figure 10.16 Performance ratio of different desalination technologies.

From this figure, it is clear that the membrane process RO has a higher performance ratio comparing to the thermal process MSF, MED, VC. We can see that RO has the highest performance ratio (30-100 kg/2326kJ) while MSF has the lowest performance ratio (6.4kg/2326kJ).

10.4.2 SPECIFIC ENERGY CONSUMPTION SEC

The energy requirement is in of the most important parameter for choosing proper desalination technologies, and the main barrier to extend desalination is higher water costs, which are seriously influenced by energy consumption (represents > 50–60% of total costs) [249]. The energy requirements for the thermal technologies: multi-stage flash, multi-effect distillation, and VC are independent of salt concentration, while the energy requirements for the membrane process are highly dependent on salt concentration [240]. Subsequently, as thermal technologies use much energy, RO is currently the most prevalent technology, with

approximately 65% of the installed capacity and with the majority of new facilities. A summarization of the energy consumption by different desalination technologies are shown in the following Table 10.2[243]:

Table 10.2 The Energy consumption by different seawater Desalination technologies

Desalination method	Total equivalent electrical energy (kWh/m ³)	Production capacity m ³ /d
MSF	13.5-25.5	50,000-70,000
MED	6.5-11	5,000-15,000
RO	3-3.5	24,000
"Electrical equivalent" refers to the amount of electrical energy that could be generated using a given quantity of thermal energy and an appropriate turbine generator.		

From Table 10.2, we can see that the energy consumption of the thermal processes MSF is much higher than the energy consumption in the membrane processes RO; furthermore, the production capacity with MSF is higher than RO.

10.4.3 QUALITY OF FEED WATER

This parameter is determining the degree of pretreatment necessary for the process and determine the costs need for this step. In the reverse osmosis process RO, the quality of feed water must be very good, and it needs the pretreatment step, while in MSF, MED, VC (thermal process) it is not necessary to pretreat the feed water. So, from this point of view, the thermal technologies are better because it is less cost in this step.

10.4.4 CORROSION, SCALING, AND FOULING

These parameters are more serious in the thermal process comparing to the membrane process. The fouling problem, e.g., by suspended solids, is the most disadvantages in the thermal

desalination plants, it is a big problem in the membrane technologies too., corrosion causes by oxidized components such as chlorine and scaling (CaCO_3 , CaSO_4 , and BaSO_4) are also another possible problem for both thermal and membrane processes; consequently, the pretreatment process is usually needed to ensure stable performance.

Finally, the comparison of all salient feature of different thermal and membrane desalination technologies are shown in Table 10.3[237].

Table 10.3 Comparison of all salient features of different desalination technologies

Salient features								
		Energy requirement	Efficiency and PR	Scale and Fouling	Corrosion	Thermal discharge	Quality of feed water	Production capacity
Technologies	MSF	4	2	3	4	4	3	4
	MED	4	2	4	4	4	3	3
	RO	2	4	3	3	0	4	2
	ED	-	3	2	1	0	2	1
Index value 0: none, 1: low, 2: medium, 3: high, and 4: extreme								

In fact, as a choice among the commercially available desalination technologies largely depends on how the process applies in some specific conditions, together with both technical and economic considerations [250], all the individual technologies have their relative pros and cons consequently, the selection is made according to the available data.

10.5 OPERATIONAL DESALINATION MSF&RO

PLANTS TECHNOLOGIES

The following sections discuss elements of thermal desalination MSF and membrane desalination RO processes, which include brief process description, modeling, system design, and costing.

10.5.1 METHODOLOGY AND DESIGN OF MULTI-STAGE FLASH

DISTILLATION

MSF process is a method that uses the vapors of the water instead of hot liquid directly, where the freshwater is produced in the evaporator of each stage by flashing some of the hot feed saline water due to low pressure. The produced water vapor passes through a demister to remove the entrainment of brine droplets and condenses on the external surface of the heat exchanger [16]. The heat released from condensation is transferred to the flowing feed seawater through successive stages resulting in increasing its temperature. After the feed seawater brine passes the first stage, its temperature is increased to the required temperature (90-110 °C) in a brine heater. The brine heater receives the low-grade steam from a fossil fuel boiler, industrial waste, or it is extracted from the low-pressure turbine of a power plant. MSF process produces high-quality water (~10 ppm), needs minimal pre-treatment, and could be constructed to produce a large capacity of water [243]. The focus of this section is to introduce an efficient MSF desalination plant supplied by a 14.2 MW power plant that provides feedwater salinity 40000 ppm. Thus, practical correlations are defined to design the system, and thus operating parameters are determined.

The following is a summary of the model equations [245] [241].

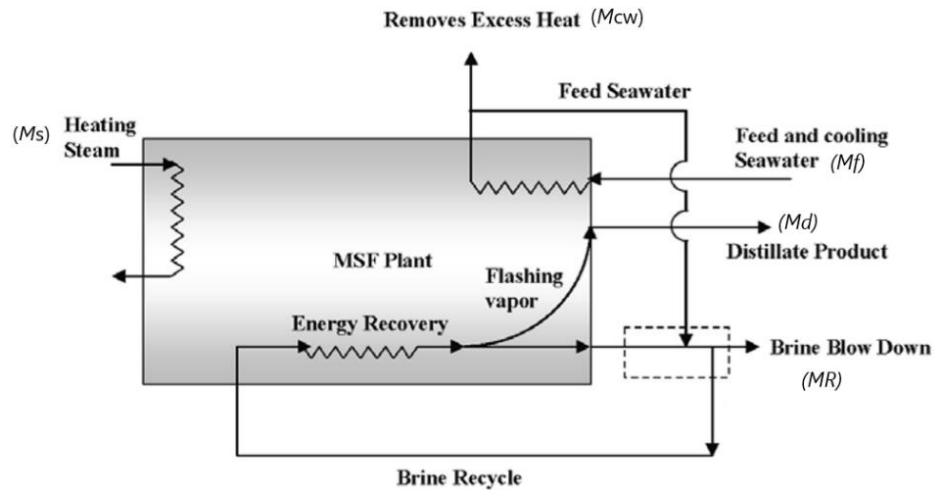


Figure 10.17 Heat and mass transfer in MSF brine circulation plant.

The brine recycle flow rate is obtained from the brine heater energy balance, where;

$$M_s \lambda_s = M_R C_p (T_{bo} - T_f) \quad \text{Equation 10.1}$$

Division of Equation 10.1 by the production capacity (M_d) gives

$$(M_R/M_d) = ((M_s/M_d) \lambda_s) / C_p (T_{bo} - T_f) \quad \text{Equation 10.2}$$

(M_d/M_s) gives the system performance ratio (PR). Therefore, Equation 10.2 is reduced to:

$$(M_R/M_d) = (\lambda_s / PR) / C_p (T_{bo} - T_f) \quad \text{Equation 10.3}$$

By performing the overall energy balance on the system shown in Figure 10.17, the cooling water flow rate could be obtained

$$M_{cw} = (M_s \lambda_s - M_f C_p (T_{bn} - T_{cw})) / (C_p (T_{bn} - T_{cw})) \quad \text{Equation 10.4}$$

Division of Equation 10.4 by the (M_d) gives

$$(M_{cw}/M_d) = \left(\frac{M_s}{M_d} \lambda_s - (M_f/M_d) C_p (T_{bn} - T_{cw}) \right) / (C_p (T_{bn} - T_{cw})) \quad \text{Equation 10.5}$$

(M_d/M_s) gives the system **performance ratio** (PR), and (M_d/M_f) gives the **conversion ratio** (CR). Therefore, Equation 10.5 is reduced to:

$$(M_{cw}/M_d) = \left(\lambda \frac{S}{PR} \right) - (1/CR) C_p (T_{bn} - T_{cw}) / (C_p (T_{bn} - T_{cw})) \quad \text{Equation 10.6}$$

The conversion ratio (CR) is obtained through a simple material balance:

$$CR = (X_{bn} - X_f)/X_{bn} \quad \text{Equation 10.7}$$

Demister length is obtained from the definition of the vapor velocity across the flashing stage:

$$L_p = (D V_v)/(v v_{wst}) \quad \text{Equation 10.8}$$

The stage length is obtained from:

$$L_{st} = L_p + L_{tb} \quad \text{Equation 10.9}$$

The tube bundle length is obtained as a function of the number of tubes, tube diameter, and the tube spacing.

$$L_{tb} = n t^{1/2} d_t S_t \quad \text{Equation 10.10}$$

The number of tubes is obtained as a function of the stream flow rate and velocity.

$$n_{tr} = 4 M R / (\rho V R d_r^2 \pi) \quad \text{Equation 10.11}$$

$$n_{tj} = 4 (M_{cw} + M_f) / (\rho V_{cw} d_j^2 \pi) \quad \text{Equation 10.12}$$

The stage height is obtained from:

$$H_{st} = H_b + H_{pb} + L_{tb} \quad \text{Equation 10.13}$$

The design model mentioned above is a simple model that could be used to obtain the performance characteristics of MSF desalination plants. In Table 10.4, Table 10.5, and

Table 10.6 are reported all the symbols of the assumed, designing, and costing parameters and their meanings.

Table 10.4 Assumed parameters for designing MSF desalination plant

Assumed parameters	Symbol	Value	Assumed parameters	Symbol	Value
Number of stages	n	24	Specific heat	C _p	4.2 kJ/kgk
Plante capacity	M _d	655kg/s	Vapor velocity in the	V _{v1}	2 m/s

			first stage		
Heat steam T	T_s	120 C	Vapor velocity in the first stage	V_{v2}	12 m/s
Top brine T	T_{bo}	110 C	Stage width	W_{st}	20 m
T of brine recycle	T_f	102 C	Liquid density	ρ	1000 kg/m ³
T of brine blow	T_{bn}	37 C	Velocity of brine	V_R	2 m/s
Intake seawater T	T_{sw}	30 C	Velocity of cool water	V_{cw}	2 m/s
Salinity of seawater	X_f	40000ppm	High of a brine pool	H_b	0.2 m
Salinity of brine water	X_{bn}	70000ppm	Performance ratio	PR	9.5
Diameter of condenser tube	d_r, d_j	0.0312m	Latent heat at 120C	λ_s	92202.6 kJ/kg

Table 10.5 Design parameters for MSF desalination plant

Design parameters	Symbol	Value	Design parameters	Symbol	Value
Brine recycle flow rate	M_R	4519.7 kg/s	Number of tubes in heat rejection section	n_{ij}	3378
Cooling flow rate	M_{cw}	3637 kg/s	Length of tube bundle in heat recovery section	L_{tbr}	2.54 m
Conversion ratio	C_R	0.429	Length of tube bundle in heat rejection section	L_{tbj}	2.72 m
Specific heat	S_A	253.4	Length of heat recovery	L_{str}	5.13 m

transfer area		m ² /(kg/s)	stage		
Demister length in first stage	L _{p1}	0.826 m	Length of rejection stage	L _{stj}	5.31 m
Vapor specific volume in first stage	V _{vn}	1.21 m ³ /kg	Height of heat recovery stage	H _{str}	4.74 m
Demister length in last stage	L _{pn}	2.56 m	Height of heat rejection stage	H _{stj}	4.92 m
Vapor specific volume in last stage	V _{vn}	22.7 m ³ /kg	Number of tubes in heat recovery section	n _{tr}	2956

Table 10.6 Costing parameters for MSF plant designing

Costing parameters	Value
Capacity m ³ /h	2847
Specific power kWh/m ³	5
Annual production m ³ /year	22447390
Electric power consumption kW	14235

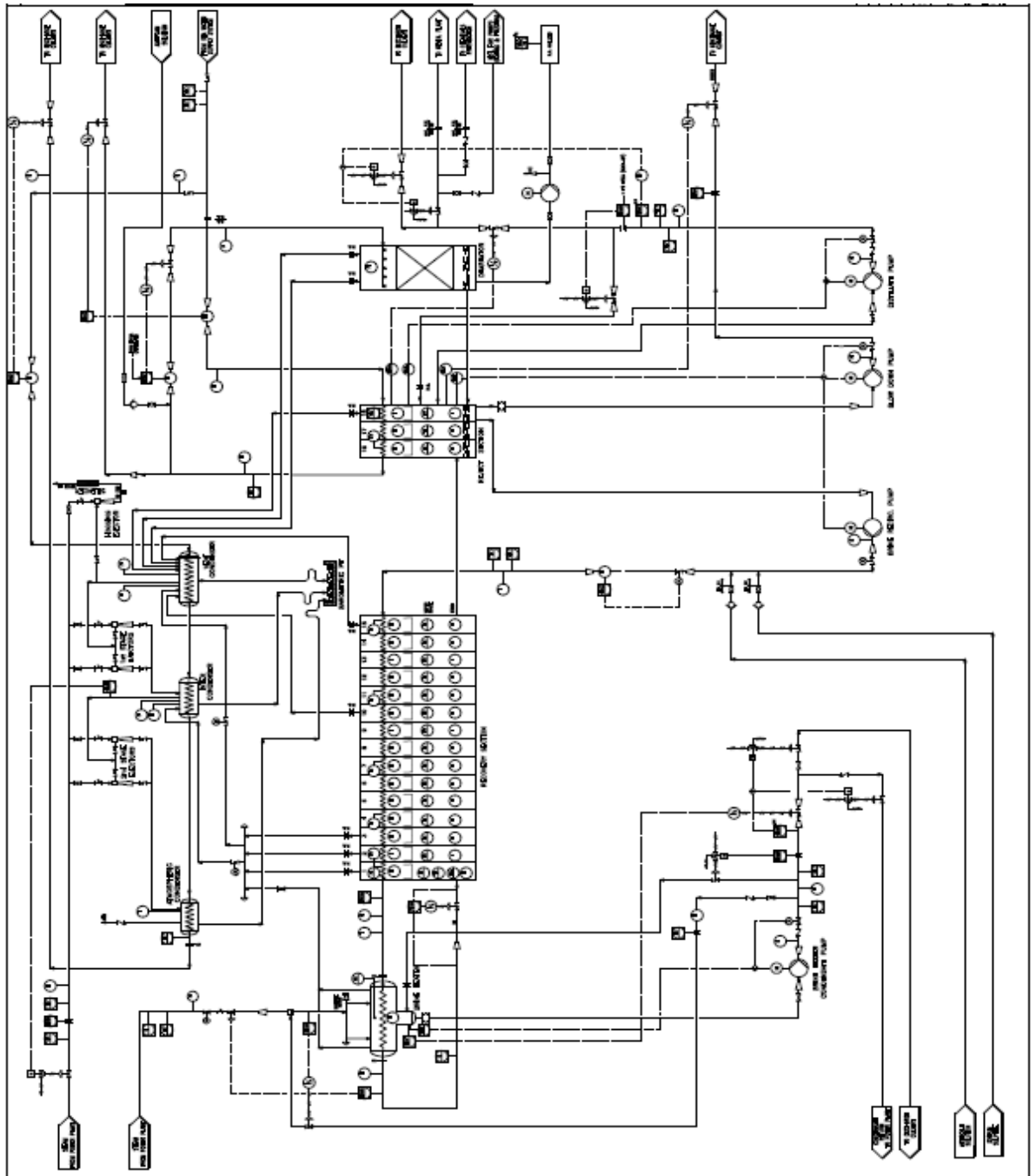


Figure 10.18 MSF Industrial plant design.

10.5.2 MYTHOLOGY AND DESIGN OF RO REVERSE OSMOSIS

DESALINATION

RO process is a pressure-driven process in which pressure is applied to a membrane to separate salt, and other minerals from water, whereas quantity of freshwater that penetrates the

membrane depends on the difference between the applied pressure and the osmotic pressure of the feed saltwater, the osmotic pressure related directly to the salt concentration in the saline water, and the discharge brine from the RO unit ranges from 20% to 70% of the flow feed water, depend on the salinity of the feed water, applied pressure, and type of membrane. The usual quality of the freshwater produced from a single-stage seawater RO unit is less than 500ppm [245].

RO plant is cheap to build, needs less capital investment, is simple to operate, and can be built with a system capacity that ranges from a few liters to hundreds of thousands of m³ per day. It also has a high production /space ratio, low energy consumption, and there is no need to shut down the whole plant when there is a problem or for routine maintenance due to the modular design of the plant [239].

The main disadvantages of RO system are high maintenance cost resulting from replacing the membrane (usually every two years or more); bacterial growth on the membrane which can bring odors and bad tests of the product water; and expectation of some mechanical failure in system equipment due to the system's high pressure. Many developments have occurred in the desalination processes as the membrane life multiplied, and the TDS in the product are now as low as 100mg/l. Besides, the recoveries of 40-50% have been achieved [239]. By recycling energy, RO desalination plants have significantly lowered their total energy consumption with the help of energy recovery devices (ERDs), So it is now possible to decrease power consumption and increase the efficiency of the seawater reverse osmosis desalination plant. The main function of an energy recovery device would be to improve energy efficiency by harnessing spent energy from the reject and delivering it back to the feed. Several methods have been explored in this domain of energy recovery devices (ERDs), which are classified as follows:

- hydraulic to mechanical-assisted pumping.
- hydraulically driven pumping in series.
- hydraulically driven pumping in parallel.

The major types of ERDs are the turbocharger, pressure exchanger, Pelton wheel, and Francis turbine [238]. Specific energy consumption is largely dominated by two factors the amount of trans-membrane pressure difference required to achieve the necessary permeate flow rate at various mass-transfer conditions, as well as the design and efficiency of the feedwater pump in combination with the respective energy-recovery system installed to recover the available hydraulic energy in the discharge brine.

As an example of modeling for cost evaluation, a case study was made for the realization of seawater desalination plant by RO with a maximum production capacity of potable water 9500 m³/day and feed water salinity 72000 ppm in the aqueduct system of a Mediterranean Island in Italy. Thus, practical correlations are defined to design the system, and thus operating parameters are determined [239][250].

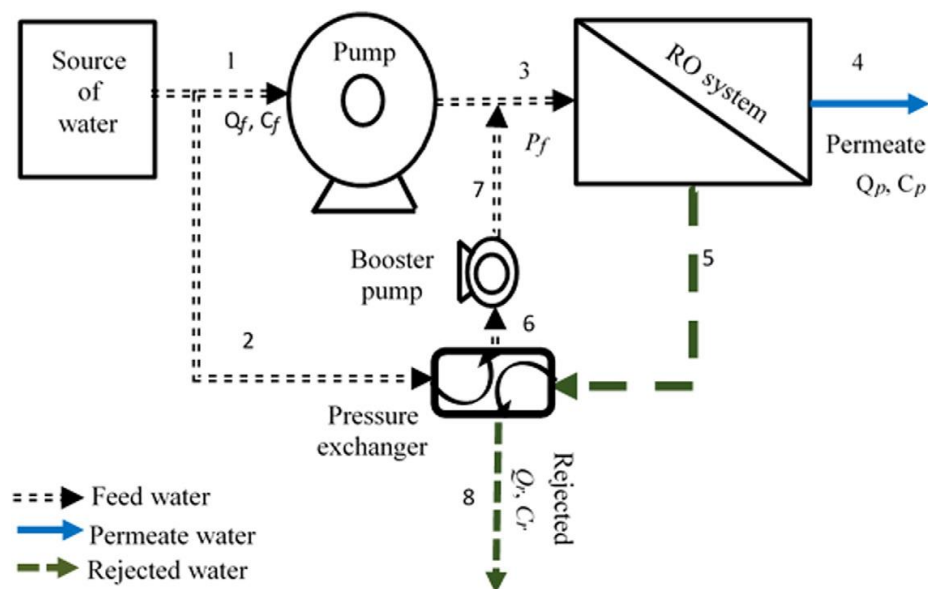


Figure 10.19 Heat and mass transfer in RO plant.

The simple design model which was used to estimate the RO design unit is:

Permeate flux (m/s):

$$JW = A_w(\Delta P - \Delta\pi) \quad \text{Equation 10.14}$$

A_w Permeability coefficient (m/s-Pa), ΔP Transmembrane pressure difference (Pa), $\Delta\pi$ Osmotic pressure difference (Pa).

Solvent permeability coefficient:

$$A_w = D_w C_w V_w / \delta m RT \quad \text{Equation 10.15}$$

C_w Water concentration in the membrane (mol/m³), D_w Water diffusivity (m²/s), V_w Water molar volume (m³), T Temperature (K), R Gas constant (J/mol-k), δm Membrane thickness (m)

Solute transport(m/s):

$$J_s = B_s(C_m - C_p) \quad \text{Equation 10.16}$$

C_p Solute concentration at permeate (mol/m³), C_m Solute concentration in the membrane (mol/m³), B_s Solute transport parameter (m/s)

Solute permeability coefficient:

$$B_s = D_s K_s / \delta m \quad \text{Equation 10.17}$$

D_s Diffusivity of solute (m/s), K_s Solubility of solute (m²/s)

Salt rejection %:

$$R_s = [1 + (B_s/A_w(\Delta\rho - \Delta\pi))] - 1 \quad \text{Equation 10.18}$$

Osmotic Pressure:

$$\Delta\pi = RT\Sigma(n/v) \quad \text{Equation 10.19}$$

Specific energy kWh/m³:

$$E = [P_f Q_f (E_{\text{pump}}) - 1 - P_r Q_r E_{\text{ERD}}] / Q_p \quad \text{Equation 10.20}$$

P_f Feed water pressure (Pa), Q_f Feed flow rate (m³/day), E_{pump} Pump energy consumption (kWh), P_r Rejected pressure (Pa), Q_r Rejected flow rate (m³/day), Q_p Mass flow rate of permeate in one element (kg/s), E_{ERD} Turbine energy (kWh)

Recovery ratio %:

$$R = Q_p / Q_f \quad \text{Equation 10.21}$$

Total mass balance:

$$Q_f C_f = Q_p C_p + Q_r C_r \quad \text{Equation 10.22}$$

C_f Concentration of feed water (mol/m³), C_r Concentration in the concentrate (mol/m³).

Delta pressure:

$$\Delta P = [(P_f + P_r) / 2] - P_p \quad \text{Equation 10.23}$$

P_f Feed water pressure (Pa), P_r Rejected pressure (Pa), P_p Permeate pressure (Pa)

The design model mentioned is a simple model that could be used to obtain the performance characteristics of the RO desalination plant. In order to obtain a project with a maximum capacity of 9500 m³/day, a system with three parallel units of RO was provided, and the characteristics of every unit of the RO plant, the chemical dosing, and the final cost are illustrated in Table 10.7, Table 10.8, and Table 10.9.

Table 10.7 Design parameters of RO plant

Design parameters	Value	Design parameters	Value
Product water flow rate	135m ³ /h	Number of streams line	3 / parallel
Salinity of product water	300ppm	Maximum vessel pressure	80bar
Seawater feed temperature	25 °C	Membrane type	Polyamide hollow fiber
High pressure pump capacity	137m ³ /h	Membrane dimension	8 X 40 inches
PX efficiency	98%	Vessels number	36
Membrane recovery factor	45%	Separation efficiency	98.7%
Membrane salt rejection	99.7%	Maximum membrane pressure	69 bar
Unit flow rate permeated	>15 litre/m ² /h	Booster pump capacity	163 m ³ /h

Total membrane number	252	Number of membrane/vessels	7
-----------------------	-----	----------------------------	---

Table 10.8 Chemical doses treatment for RO plant desalination design

Chemicals doses	Concentration %	Flow rate kg/h
Ferric chloride FeCl ₃	41	11
Sodium bisulfite NaHSO ₃	10	45
Sulfuric acid H ₂ SO ₄	98	4.6
Antiscalant	10	45
Calcium hydroxide Ca (OH) ₂ (Post-treatment)	5	112
Hypochlorite sodium NaOCl	0.15	5.5
Hypochlorite sodium NaOCl (post treatment)	0.15	1.2

Table 10.9 Final costing and consumption parameters of RO plant designing

Costing parameters	Value
Capacity m ³ /h	405
Specific power kWh/m ³	3.94
Annual production m ³ /year	3547800
Electric power consumption kW	1596.2

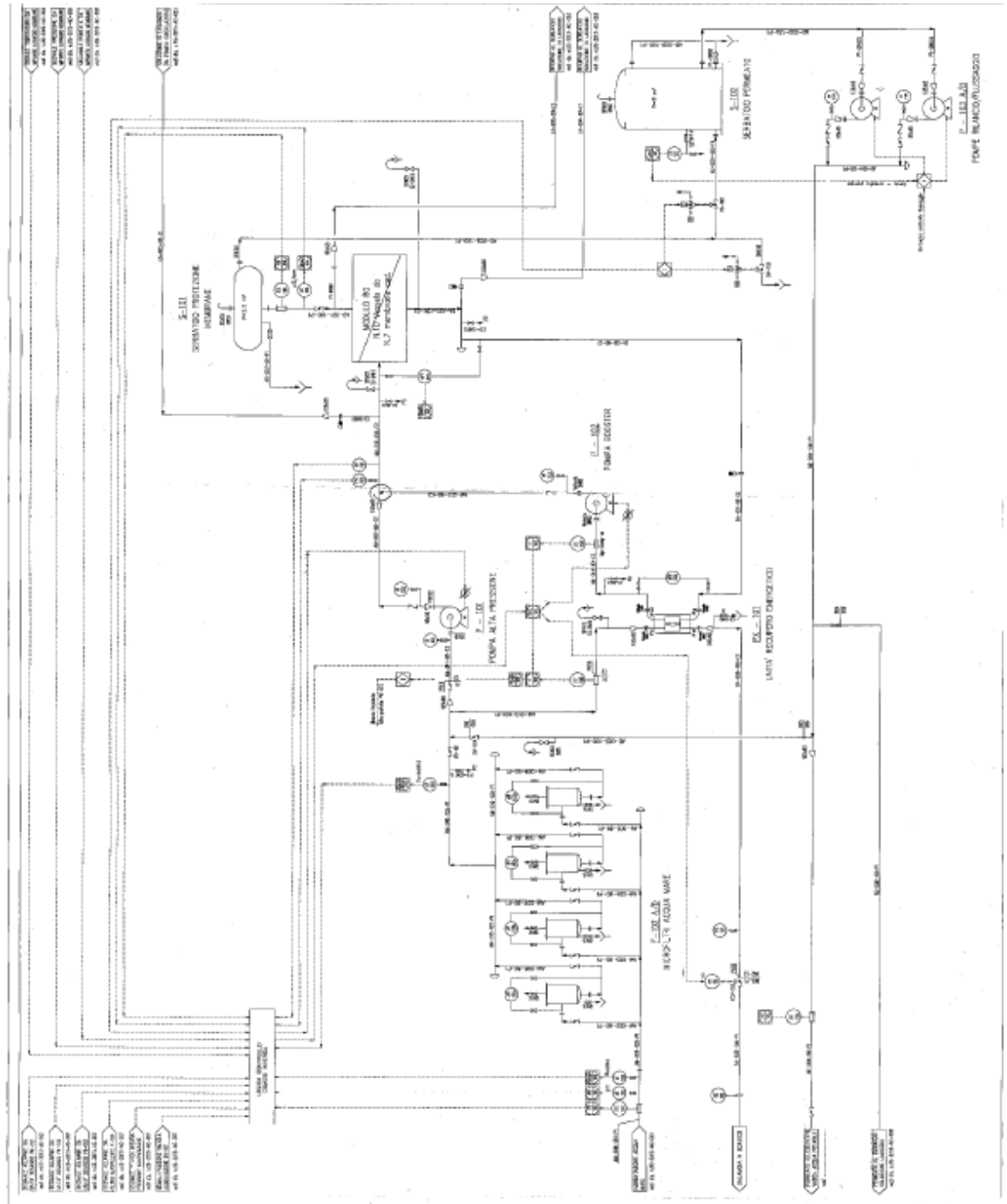


Figure 10.20 RO industrial plant design.

10.6 CONCLUSIONS

It is quite difficult to choose which method is the best for the desalination process because all the desalination technologies have their advantages and disadvantages. Thermal desalination plants normally have higher energy requirements and unit capital cost than membrane plants.

Also, corrosion, scaling, and fouling problems are more serious in the thermal process comparing with the membrane processes. A huge amount of waste heat is produced in the thermal desalination processes.

On the other hand, membrane processes do not destroy biological substances, and the pretreatment process of the feed water is required in order to remove particulate so that the membranes last longer. However, in the MSF, MED, and VC, it is not necessary to pre-treat the feed water. The unit capital cost in desalinating brackish water is lower comparing with desalinating seawater in the membrane technologies. Therefore, we can say that the choices it depends on the sources of energy; as in the developing countries, the main problem is with energy sources, so it is better to use RO, EDR, or FO to desalinate the saline water to get fresh water, whereas in other countries like Saudi Arabia they can use thermal technologies.

11 BIBLIOGRAPHY

- [1] Cop24 Special Report Cop24 Special Report Health and Climate n.d.
- [2] UNITED NATIONS UN Climate Change Summit 2019 n.d. <https://www.un.org/en/climatechange/cop24.shtml> (accessed June 9, 2020).
- [3] Slangen ABA, Church JA, Agosta C, Fettweis X, Marzeion B, Richter K. Anthropogenic forcing dominates global mean sea-level rise since 1970. *Nat Clim Chang* 2016;6:701–5. <https://doi.org/10.1038/nclimate2991>.
- [4] Leading Health Organizations Rally Around Call to Action to Protect People’s Health from Climate Change - Public Health Institute n.d. <https://www.phi.org/press/leading-health-organizations-rally-around-call-to-action-to-protect-peoples-health-from-climate-change/> (accessed June 9, 2020).
- [5] Kaza S, Yao L, Bhada-Tata P, Van Woerden F. What a Waste 2.0: A Global Snapshot of Solid Waste Management to 2050. The World Bank; 2018. <https://doi.org/10.1596/978-1-4648-1329-0>.
- [6] Anastas P, Eghbali N. Green Chemistry: Principles and Practice. *Chem Soc Rev*

- 2010;39:301–12. <https://doi.org/10.1039/b918763b>.
- [7] Mulvaney D, Gibbs BJ. *Green Metrics. Green Technol. An A-to-Z Guid.*, SAGE Publications, Inc.; 2012. <https://doi.org/10.4135/9781412975704.n61>.
- [8] pasqual laverdura U. *Study of selective catalytic hydrogenation of triglycerides and their derivatives* 2019.
- [9] Toba M, Abe Y, Kuramochi H, Osako M, Mochizuki T, Yoshimura Y. Hydrodeoxygenation of waste vegetable oil over sulfide catalysts. *Catal. Today*, vol. 164, Elsevier; 2011, p. 533–7. <https://doi.org/10.1016/j.cattod.2010.11.049>.
- [10] Cao Y, Zhou H, Li J. Preparation of a supported acidic ionic liquid on silica-gel and its application to the synthesis of biodiesel from waste cooking oil. *Renew Sustain Energy Rev* 2016;58:871–5. <https://doi.org/10.1016/j.rser.2015.12.237>.
- [11] Chung YS, Lee JW, Chung CH. Molecular challenges in microalgae towards cost-effective production of quality biodiesel. *Renew Sustain Energy Rev* 2017;74:139–44. <https://doi.org/10.1016/j.rser.2017.02.048>.
- [12] Abomohra AEF, Jin W, Tu R, Han SF, Eid M, Eladel H. Microalgal biomass production as a sustainable feedstock for biodiesel: Current status and perspectives. *Renew Sustain Energy Rev* 2016;64:596–606. <https://doi.org/10.1016/j.rser.2016.06.056>.
- [13] ExxonMobil's energy outlook projects energy demand increase and decline in carbon intensity |ExxonMobil n.d. https://corporate.exxonmobil.com/news/newsroom/news-releases/2016/0125_exxonmobils-energy-outlook-projects-energy-demand-increase-and-decline-in-carbon-intensity (accessed September 28, 2020).
- [14] Fabbisogno energetico mondiale situazione attuale e prospettive future n.d.

- <https://www.greenplanner.it/2014/01/30/fabbisogno-energetico-mondiale-situazione-attuale-e-prospettive-future/> (accessed September 28, 2020).
- [15] Hermida L, Abdullah AZ, Mohamed AR. Deoxygenation of fatty acid to produce diesel-like hydrocarbons: A review of process conditions, reaction kinetics and mechanism. *Renew Sustain Energy Rev* 2015;42:1223–33. <https://doi.org/10.1016/j.rser.2014.10.099>.
- [16] Li X, Luo X, Jin Y, Li J, Zhang H, Zhang A, et al. Heterogeneous sulfur-free hydrodeoxygenation catalysts for selectively upgrading the renewable bio-oils to second generation biofuels. *Renew Sustain Energy Rev* 2018;82:3762–97. <https://doi.org/10.1016/j.rser.2017.10.091>.
- [17] ENVIRONMENTAL EVALUATION OF BIOFUELS | Periodica Polytechnica Social and Management Sciences n.d. <https://pp.bme.hu/so/article/view/1701> (accessed June 10, 2020).
- [18] Knothe G, Dunn RO, Bagby MO. Biodiesel: The Use of Vegetable Oils and Their Derivatives as Alternative Diesel Fuels. n.d.
- [19] Demirbaş A. Bioenergy, Global Warming, and Environmental Impacts. *Energy Sources* 2004;26:225–36. <https://doi.org/10.1080/00908310490256581>.
- [20] Ameen M, Azizan MT, Yusup S, Ramli A, Yasir M. Catalytic hydrodeoxygenation of triglycerides: An approach to clean diesel fuel production. *Renew Sustain Energy Rev* 2017;80:1072–88. <https://doi.org/10.1016/j.rser.2017.05.268>.
- [21] Da Costa Evangelista JP, Gondim AD, Souza L Di, Araujo AS. Alumina-supported potassium compounds as heterogeneous catalysts for biodiesel production: A review. *Renew Sustain Energy Rev* 2016;59:887–94. <https://doi.org/10.1016/j.rser.2016.01.061>.

- [22] Banković-Ilić IB, Miladinović MR, Stamenković OS, Veljković VB. Application of nano CaO-based catalysts in biodiesel synthesis. *Renew Sustain Energy Rev* 2017;72:746–60. <https://doi.org/10.1016/j.rser.2017.01.076>.
- [23] Huber GW, O'Connor P, Corma A. Processing biomass in conventional oil refineries: Production of high quality diesel by hydrotreating vegetable oils in heavy vacuum oil mixtures. *Appl Catal A Gen* 2007;329:120–9. <https://doi.org/10.1016/j.apcata.2007.07.002>.
- [24] Naik SN, Goud V V., Rout PK, Dalai AK. Production of first and second generation biofuels: A comprehensive review. *Renew Sustain Energy Rev* 2010;14:578–97. <https://doi.org/10.1016/j.rser.2009.10.003>.
- [25] Hermida L, Abdullah AZ, Mohamed AR. Deoxygenation of fatty acid to produce diesel-like hydrocarbons: A review of process conditions, reaction kinetics and mechanism. *Renew Sustain Energy Rev* 2015;42:1223–33. <https://doi.org/10.1016/j.rser.2014.10.099>.
- [26] Li X, Chen G, Liu C, Ma W, Yan B, Zhang J. Hydrodeoxygenation of lignin-derived bio-oil using molecular sieves supported metal catalysts: A critical review. *Renew Sustain Energy Rev* 2017;71:296–308. <https://doi.org/10.1016/j.rser.2016.12.057>.
- [27] Bhuiya MMK, Rasul MG, Khan MMK, Ashwath N, Azad AK, Hazrat MA. Prospects of 2nd generation biodiesel as a sustainable fuel - Part 2: Properties, performance and emission characteristics. *Renew Sustain Energy Rev* 2016;55:1129–46. <https://doi.org/10.1016/j.rser.2015.09.086>.
- [28] Kubičková I, Kubička D. Utilization of triglycerides and related feedstocks for production of clean hydrocarbon fuels and petrochemicals: A review. *Waste and*

- Biomass Valorization 2010;1:293–308. <https://doi.org/10.1007/s12649-010-9032-8>.
- [29] Diya'Uddeen BH, Abdul Aziz AR, Daud WMAW, Chakrabarti MH. Performance evaluation of biodiesel from used domestic waste oils: A review. *Process Saf Environ Prot* 2012;90:164–79. <https://doi.org/10.1016/j.psep.2012.02.005>.
- [30] Damartzis T, Zabaniotou A. Thermochemical conversion of biomass to second generation biofuels through integrated process design-A review. *Renew Sustain Energy Rev* 2011;15:366–78. <https://doi.org/10.1016/j.rser.2010.08.003>.
- [31] Brennan L, Owende P. Biofuels from microalgae-A review of technologies for production, processing, and extractions of biofuels and co-products. *Renew Sustain Energy Rev* 2010;14:557–77. <https://doi.org/10.1016/j.rser.2009.10.009>.
- [32] Lee RA, Lavoie J-M. From first- to third-generation biofuels: Challenges of producing a commodity from a biomass of increasing complexity. *Anim Front* 2013;3:6–11. <https://doi.org/10.2527/af.2013-0010>.
- [33] Abdullah B, Syed Muhammad SAF ad, Shokravi Z, Ismail S, Kassim KA, Mahmood AN, et al. Fourth generation biofuel: A review on risks and mitigation strategies. *Renew Sustain Energy Rev* 2019;107:37–50. <https://doi.org/10.1016/j.rser.2019.02.018>.
- [34] Demirbas A. Competitive liquid biofuels from biomass. *Appl Energy* 2011;88:17–28. <https://doi.org/10.1016/j.apenergy.2010.07.016>.
- [35] Philippaerts A, Jacobs P, Sels B. CHAPTER 10. Catalytic Hydrogenation of Vegetable Oils, 2014, p. 223–41. <https://doi.org/10.1039/9781782620099-00223>.
- [36] Montero De Espinosa L, Meier MAR. Plant oils: The perfect renewable resource for polymer science?! *Eur Polym J* 2011;47:837–52.

- <https://doi.org/10.1016/j.eurpolymj.2010.11.020>.
- [37] Selective catalytic hydrogenation of vegetable oils on Lindlar catalyst fin 280120(1) n.d.
- [38] 768 B2 1 METHODS OF PREPARING CASTING RESINS AND COATING COMPOSITIONS USING POLYOLS DERIVED FROM HIGH OLEIC ACID CONTENT FATTY ACID MIXTURES FIELD OF THE INVENTION. 1997.
- [39] Gosselink RW, Hollak SAW, Chang SW, Van Haveren J, De Jong KP, Bitter JH, et al. Reaction pathways for the deoxygenation of vegetable oils and related model compounds. *ChemSusChem* 2013;6:1576–94. <https://doi.org/10.1002/cssc.201300370>.
- [40] Gui MM, Lee KT, Bhatia S. Feasibility of edible oil vs. non-edible oil vs. waste edible oil as biodiesel feedstock. *Energy* 2008;33:1646–53. <https://doi.org/10.1016/j.energy.2008.06.002>.
- [41] Ashraful AM, Masjuki HH, Kalam MA, Fattah IMR, Imtenan S, Shahir SA, et al. Production and comparison of fuel properties, engine performance, and emission characteristics of biodiesel from various non-edible vegetable oils: A review 2014. <https://doi.org/10.1016/j.enconman.2014.01.037>.
- [42] Biswas S, Katiyar R, Gurjar BR, Pruthi V. Biofuels and Their Production Through Different Catalytic Routes. *Chem Biochem Eng Q* 2017;31:47–62. <https://doi.org/10.15255/CABEQ.2016.897>.
- [43] EN. 2007.
- [44] Fact sheet: Renewable energy progress report n.d. https://ec.europa.eu/commission/presscorner/detail/en/MEMO_15_5181 (accessed June 12, 2020).

- [45] Douvartzides SL, Charisiou ND, Papageridis KN, Goula MA. Green diesel: Biomass feedstocks, production technologies, catalytic research, fuel properties and performance in compression ignition internal combustion engines. *Energies* 2019;12. <https://doi.org/10.3390/en12050809>.
- [46] Ameen M, Azizan MT, Yusup S, Ramli A, Yasir M. Catalytic hydrodeoxygenation of triglycerides: An approach to clean diesel fuel production. *Renew Sustain Energy Rev* 2017;80:1072–88. <https://doi.org/10.1016/j.rser.2017.05.268>.
- [47] Zaccheria F, Psaro R, Ravasio N. Selective hydrogenation of alternative oils: A useful tool for the production of biofuels. *Green Chem* 2009;11:462–46. <https://doi.org/10.1039/b817625f>.
- [48] Bouriazos A, Mouratidis K, Psaroudakis N, Papadogianakis G. Catalytic conversions in aqueous media. Part 2. A novel and highly efficient biphasic hydrogenation of renewable methyl esters of linseed and sunflower oils to high quality biodiesel employing Rh/TPPTS complexes. *Catal Letters* 2008;121:158–64. <https://doi.org/10.1007/s10562-007-9314-3>.
- [49] Dijkstra AJ. Kinetics and mechanism of the hydrogenation process - the state of the art. *Eur J Lipid Sci Technol* 2012;114:985–98. <https://doi.org/10.1002/ejlt.201100405>.
- [50] Šimon P, Čelkova A, Šchmidt S. A simplified Horiuti-Polanyi scheme for the hydrogenation of triacylglycerols. *J Am Oil Chem Soc* 1991;68:74–8. <https://doi.org/10.1007/BF02662320>.
- [51] Dijkstra AJ. On the mechanism of the copper-catalysed hydro-genation; a reinterpretation of published data. *Eur J Lipid Sci Technol* 2002;104:29–35. [https://doi.org/10.1002/1438-9312\(200201\)104:1<29::AID-EJLT29>3.0.CO;2-O](https://doi.org/10.1002/1438-9312(200201)104:1<29::AID-EJLT29>3.0.CO;2-O).

- [52] Alsobaai AM, Shaibani AM Al, Moustafa T, Derhem A. Effect of hydrogenation temperature on the palm mid-fraction fatty acids composition and conversion. *J King Saud Univ - Eng Sci* 2012;24:45–51. <https://doi.org/10.1016/j.jksues.2011.02.004>.
- [53] Andrade GMS, da Rocha Filho GN, Taqueda MES. Statistical evaluation of the effects of process variables during catalytic hydrogenation of passion fruit (*passiflora edulis*) seed oil. *Brazilian J Chem Eng* 1998;15:51–8. <https://doi.org/10.1590/S0104-66321998000100005>.
- [54] Zajcew M. The hydrogenation of fatty oils with palladium catalyst. III. Hydrogenation of fatty oils for shortening stock. *J Am Oil Chem Soc* 1960;37:11–4. <https://doi.org/10.1007/BF02630813>.
- [55] Dijkstra AJ. Revisiting the formation of trans isomers during partial hydrogenation of triacylglycerol oils. *Eur J Lipid Sci Technol* 2006;108:249–64. <https://doi.org/10.1002/ejlt.200500335>.
- [56] Šimon P, Čelkova A, Šchmidt S. A simplified Horiuti-Polanyi scheme for the hydrogenation of triacylglycerols. *J Am Oil Chem Soc* 1991;68:74–8. <https://doi.org/10.1007/BF02662320>.
- [57] Dijkstra AJ. Selectivities in partial hydrogenation. *JAOCs, J Am Oil Chem Soc* 2010;87:115–7. <https://doi.org/10.1007/s11746-009-1507-z>.
- [58] Chen X, Zhang M, Yang K, Williams CT, Liang C. Raney Ni-Si catalysts for selective hydrogenation of highly concentrated 2-butyne-1,4-diol to 2-butene-1,4-diol. *Catal Letters* 2014;144:1118–26. <https://doi.org/10.1007/s10562-014-1259-8>.
- [59] Catalysts NV. *Hydrogenation of Edible Oils and Fats*. vol. 44. 1995.

- [60] Mohr C, Claus P. Hydrogenation properties of supported nanosized gold particles. *Sci Prog* 2001;84:311–34. <https://doi.org/10.3184/003685001783238925>.
- [61] Nohair B, Especel C, Marécot P, Montassier C, Hoang LC, Barbier J. Selective hydrogenation of sunflower oil over supported precious metals. *Comptes Rendus Chim* 2004;7:113–8. <https://doi.org/10.1016/j.crci.2003.10.012>.
- [62] Alshaibani A, Yaakob Z, Alsobaai A, Sahri M. Effect of chemically reduced palladium supported catalyst on sunflower oil hydrogenation conversion and selectivity. *Arab J Chem* 2017;10:S1188–92. <https://doi.org/10.1016/j.arabjc.2013.02.014>.
- [63] Kubička D, Horáček J, Setnička M, Bulánek R, Zukal A, Kubičková I. Effect of support-active phase interactions on the catalyst activity and selectivity in deoxygenation of triglycerides. *Appl Catal B Environ* 2014;145:101–7. <https://doi.org/10.1016/j.apcatb.2013.01.012>.
- [64] Vásquez MC, Silva EE, Castillo EF. Hydrotreatment of vegetable oils: A review of the technologies and its developments for jet biofuel production. *Biomass and Bioenergy* 2017;105:197–206. <https://doi.org/10.1016/j.biombioe.2017.07.008>.
- [65] Sonthalia A, Kumar N. Hydroprocessed vegetable oil as a fuel for transportation sector: A review. *J Energy Inst* 2019;92:1–17. <https://doi.org/10.1016/j.joei.2017.10.008>.
- [66] Kubička D, Šimáček P, Žilková N. Transformation of vegetable oils into hydrocarbons over mesoporous-alumina-supported CoMo catalysts. *Top Catal* 2009;52:161–8. <https://doi.org/10.1007/s11244-008-9145-5>.
- [67] Veriansyah B, Han JY, Kim SK, Hong SA, Kim YJ, Lim JS, et al. Production of renewable diesel by hydroprocessing of soybean oil: Effect of catalysts. *Fuel* 2012;94:578–85. <https://doi.org/10.1016/j.fuel.2011.10.057>.

- [68] Guo JH, Xu GY, Shen F, Fu Y, Zhang Y, Guo QX. Catalytic conversion of Jatropha oil to alkanes under mild conditions with a Ru/La(OH)₃ catalyst. *Green Chem* 2015;17:2888–95. <https://doi.org/10.1039/c4gc02406k>.
- [69] Vonghia E, Boocock DGB, Konar SK, Leung A. Pathways for the Deoxygenation of Triglycerides to Aliphatic Hydrocarbons over Activated Alumina. *Energy and Fuels* 1995;9:1090–6. <https://doi.org/10.1021/ef00054a024>.
- [70] Šimáček P, Kubička D, Šebor G, Pospíšil M. Fuel properties of hydroprocessed rapeseed oil. *Fuel* 2010;89:611–5. <https://doi.org/10.1016/j.fuel.2009.09.017>.
- [71] Zheng A, Huang Z, Wei G, Zhao K, Jiang L, Zhao Z, et al. Controlling Deoxygenation Pathways in Catalytic Fast Pyrolysis of Biomass and Its Components by Using Metal-Oxide Nanocomposites. *IScience* 2020;23. <https://doi.org/10.1016/j.isci.2019.100814>.
- [72] Kubička D, Kaluža L. Deoxygenation of vegetable oils over sulfided Ni, Mo and NiMo catalysts. *Appl Catal A Gen* 2010;372:199–208. <https://doi.org/10.1016/j.apcata.2009.10.034>.
- [73] Rogers KA, Zheng Y. Selective Deoxygenation of Biomass-Derived Bio-oils within Hydrogen-Modest Environments: A Review and New Insights. *ChemSusChem* 2016;9:1750–72. <https://doi.org/10.1002/cssc.201600144>.
- [74] Pattanaik BP, Misra RD. Effect of reaction pathway and operating parameters on the deoxygenation of vegetable oils to produce diesel range hydrocarbon fuels: A review. *Renew Sustain Energy Rev* 2017;73:545–57. <https://doi.org/10.1016/j.rser.2017.01.018>.
- [75] Lestari S, Mäki-Arvela P, Beltramini J, Lu GQM, Murzin DY. Transforming triglycerides and fatty acids into biofuels. *ChemSusChem* 2009;2:1109–19. <https://doi.org/10.1002/cssc.200900107>.

- [76] Donnis B, Egeberg RG, Blom P, Knudsen KG. Hydroprocessing of bio-oils and oxygenates to hydrocarbons. Understanding the reaction routes. *Top Catal* 2009;52:229–40. <https://doi.org/10.1007/s11244-008-9159-z>.
- [77] Peng B, Yuan X, Zhao C, Lercher JA. Stabilizing catalytic pathways via redundancy: Selective reduction of microalgae oil to alkanes. *J Am Chem Soc* 2012;134:9400–5. <https://doi.org/10.1021/ja302436q>.
- [78] Veriansyah B, Han JY, Kim SK, Hong SA, Kim YJ, Lim JS, et al. Production of renewable diesel by hydroprocessing of soybean oil: Effect of catalysts. *Fuel* 2012;94:578–85. <https://doi.org/10.1016/j.fuel.2011.10.057>.
- [79] Busacca CA, Fandrick DR, Song JJ, Senanayake CH. The growing impact of catalysis in the pharmaceutical industry. *Adv Synth Catal* 2011;353:1825–64. <https://doi.org/10.1002/adsc.201100488>.
- [80] Santen RA van (Rutger A. *Catalysis : an integrated approach*. Elsevier; 2000.
- [81] THE ORGANOMETALLIC CHEMISTRY OF THE TRANSITION METALS. n.d. <https://doi.org/10.1002/0471718769.fmatter>.
- [82] Abdeaghani I. “ Optimization of late transition metal based catalytic applications towards high added value processes under mild and selective conditions ” PhD thesis 2017.
- [83] Heterogeneous hydrogenation of vegetable oils: A literature review (1997) | www.narcis.nl n.d. <https://www.narcis.nl/publication/RecordID/oai%3Apure.rug.nl%3Apublications%2F4f83fccb-e991-48f9-a622-698ed2e644c9> (accessed October 1, 2020).

- [84] Rothenberg G. Catalysis: Concepts and Green Applications n.d. https://www.researchgate.net/publication/285398199_Catalysis_Concepts_and_Green_Applications (accessed June 13, 2020).
- [85] Behr A, Westfechtel A, Pérez Gomes J. Catalytic processes for the technical use of natural fats and oils. *Chem Eng Technol* 2008;31:700–14. <https://doi.org/10.1002/ceat.200800035>.
- [86] Gosselink RW, Hollak SAW, Chang SW, Van Haveren J, De Jong KP, Bitter JH, et al. Reaction pathways for the deoxygenation of vegetable oils and related model compounds. *ChemSusChem* 2013;6:1576–94. <https://doi.org/10.1002/cssc.201300370>.
- [87] List GR, King JW. Hydrogenation of Fats and Oils: Theory and Practice: Second Edition. Elsevier Inc.; 2010. <https://doi.org/10.1016/C2015-0-02451-0>.
- [88] Appl M. Ammonia, Ullmann's Encyclopedia of Industrial Chemistry. Ullmann's Encycl. Ind. Chem., Weinheim, Germany: Wiley-VCH Verlag GmbH & Co. KGaA; 2006. https://doi.org/10.1002/14356007.a02_143.pub2.
- [89] Van Der Laan GP, Beenackers AACM. Kinetics and Selectivity of the Fischer-Tropsch Synthesis: A Literature Review. *Catal Rev - Sci Eng* 1999;41:255–318. <https://doi.org/10.1081/CR-100101170>.
- [90] Krstić J, Gabrovska M, Lončarević D, Nikolova D, Radonjić V, Vukelić N, et al. Influence of Ni/SiO₂ activity on the reaction pathway in sunflower oil hydrogenation. *Chem Eng Res Des* 2015;100:72–80. <https://doi.org/10.1016/j.cherd.2015.05.001>.
- [91] Cabrera MI, Grau RJ. Advanced concepts for the kinetic modeling of fatty acid methyl esters hydrogenation. *Int J Chem React Eng* 2008;6. <https://doi.org/10.2202/1542-6580.1718>.

- [92] Veldsink J., Bouma M., Schoon NH, Beenackers A. CM. Heterogeneous hydrogenation of vegetable oils: A literature review. *Catal Rev Eng* 1997;39:253–318.
- [93] Deliy I V., Simakova IL, Ravasio N, Psaro R. Catalytic behaviour of carbon supported platinum group metals in the hydrogenation and isomerization of methyl oleate. *Appl Catal A Gen* 2009;357:170–7. <https://doi.org/10.1016/j.apcata.2009.01.026>.
- [94] Numwong N, Luengnaruemitchai A, Chollacoop N, Yoshimura Y. Effect of metal type on partial hydrogenation of rapeseed oil-derived FAME. *JAOCS, J Am Oil Chem Soc* 2013;90:1431–8. <https://doi.org/10.1007/s11746-013-2276-2>.
- [95] McArdle S, Leahy JJ, Curtin T, Tanner D. Hydrogenation of sunflower oil over Pt-Ni bimetallic supported catalysts: Preparation, characterization and catalytic activity. *Appl Catal A Gen* 2014;474:78–86. <https://doi.org/10.1016/j.apcata.2013.08.033>.
- [96] Belkacemi K, Kemache N, Hamoudi S, Arul J. Hydrogenation of sunflower oil over bimetallic supported catalysts on mesostructured silica material. *Int J Chem React Eng* 2007;5. <https://doi.org/10.2202/1542-6580.1528>.
- [97] Wright AJ, Wong A, Diosady LL. Ni catalyst promotion of a Cis-selective Pd catalyst for canola oil hydrogenation. *Food Res Int* 2003;36:1069–72. <https://doi.org/10.1016/j.foodres.2003.08.005>.
- [98] Numwong N, Luengnaruemitchai A, Chollacoop N, Yoshimura Y. Effect of SiO₂ pore size on partial hydrogenation of rapeseed oil-derived FAMEs. *Appl Catal A Gen* 2012;441–442:72–8. <https://doi.org/10.1016/j.apcata.2012.07.020>.
- [99] Ferrari M, Bosmans S, Maggi R, Delmon B, Grange P. CoMo/carbon hydrodeoxygenation catalysts: Influence of the hydrogen sulfide partial pressure and of the sulfidation temperature. *Catal Today* 2001;65:257–64.

[https://doi.org/10.1016/S0920-5861\(00\)00559-9](https://doi.org/10.1016/S0920-5861(00)00559-9).

- [100] Speight J. A review of: “ Hydrotreating Catalysis Science and Technology ” Topsoe, H., Clausen, B.S., and Massoth, F.E., Springer-Verlag New York, 1996. ISBN No. 3-540-60380-8 Price not available at time of review . *Fuel Sci Technol Int* 1996;14:1465–1465. <https://doi.org/10.1080/08843759608947653>.
- [101] Şenol OI, Viljava TR, Krause AOI. Hydrodeoxygenation of methyl esters on sulphided NiMo/ γ -Al₂O₃ and CoMo/ γ -Al₂O₃ catalysts. *Catal. Today*, vol. 100, Elsevier; 2005, p. 331–5. <https://doi.org/10.1016/j.cattod.2004.10.021>.
- [102] Harnos S, Onyestyák G, Kalló D. Hydrocarbons from sunflower oil over partly reduced catalysts. *React Kinet Mech Catal* 2012;106:99–111. <https://doi.org/10.1007/s11144-012-0424-6>.
- [103] Snåre M, Kubičková I, Mäki-Arvela P, Chichova D, Eränen K, Murzin DY. Catalytic deoxygenation of unsaturated renewable feedstocks for production of diesel fuel hydrocarbons. *Fuel* 2008;87:933–45. <https://doi.org/10.1016/j.fuel.2007.06.006>.
- [104] Morgan T, Grubb D, Santillan-Jimenez E, Crocker M. Conversion of triglycerides to hydrocarbons over supported metal catalysts. *Top Catal* 2010;53:820–9. <https://doi.org/10.1007/s11244-010-9456-1>.
- [105] Kubička D, Kaluža L. Deoxygenation of vegetable oils over sulfided Ni, Mo and NiMo catalysts. *Appl Catal A Gen* 2010;372:199–208. <https://doi.org/10.1016/j.apcata.2009.10.034>.
- [106] Veriansyah B, Han JY, Kim SK, Hong SA, Kim YJ, Lim JS, et al. Production of renewable diesel by hydroprocessing of soybean oil: Effect of catalysts. *Fuel* 2012;94:578–85. <https://doi.org/10.1016/j.fuel.2011.10.057>.

- [107] Vonortas A, Papayannakos N. Hydrodesulphurization and hydrodeoxygenation of gasoil-vegetable oil mixtures over a Pt/ γ -Al₂O₃ catalyst. *Fuel Process Technol* 2016;150:126–31. <https://doi.org/10.1016/j.fuproc.2016.05.013>.
- [108] Snåre M, Kubičková I, Mäki-Arvela P, Eränen K, Murzin DY. Heterogeneous catalytic deoxygenation of stearic acid for production of biodiesel. *Ind Eng Chem Res* 2006;45:5708–15. <https://doi.org/10.1021/ie060334i>.
- [109] Peng B, Yao Y, Zhao C, Lercher JA. Towards quantitative conversion of microalgae oil to diesel-range alkanes with bifunctional catalysts. *Angew Chemie - Int Ed* 2012;51:2072–5. <https://doi.org/10.1002/anie.201106243>.
- [110] Ishihara A, Kawaraya D, Sonthisawate T, Kimura K, Hashimoto T, Nasu H. Catalytic cracking of soybean oil by hierarchical zeolite containing mesoporous silica-aluminas using a Curie point pyrolyzer. *J Mol Catal A Chem* 2015;396:310–8. <https://doi.org/10.1016/j.molcata.2014.10.010>.
- [111] Twaiq FA, Zabidi NAM, Bhatia S. Catalytic conversion of palm oil to hydrocarbons: Performance of various zeolite catalysts. *Ind Eng Chem Res* 1999;38:3230–7. <https://doi.org/10.1021/ie980758f>.
- [112] HYDROTALCITES IN CATALYSIS UNIQUE PRODUCTS THROUGH UNIQUE TECHNOLOGIES. n.d.
- [113] Lu Z, Qian L, Xu W, Tian Y, Jiang M, Li Y, et al. Dehydrated layered double hydroxides: Alcohothermal synthesis and oxygen evolution activity. *Nano Res* 2016;9:3152–61. <https://doi.org/10.1007/s12274-016-1197-4>.
- [114] Sikander U, Sufian S, Salam MA. A review of hydrotalcite based catalysts for hydrogen production systems. *Int J Hydrogen Energy* 2017;42:19851–68.

- <https://doi.org/10.1016/j.ijhydene.2017.06.089>.
- [115] Yap MH, Fow KL, Chen GZ. Synthesis and applications of MOF-derived porous nanostructures. *Green Energy Environ* 2017;2:218–45. <https://doi.org/10.1016/j.gee.2017.05.003>.
- [116] Cassano D, Pocoví-Martínez S, Voliani V. Ultrasmall-in-Nano Approach: Enabling the Translation of Metal Nanomaterials to Clinics. *Bioconjug Chem* 2018;29:4–16. <https://doi.org/10.1021/acs.bioconjchem.7b00664>.
- [117] Choy JH, Choi SJ, Oh JM, Park T. Clay minerals and layered double hydroxides for novel biological applications. *Appl Clay Sci* 2007;36:122–32. <https://doi.org/10.1016/j.clay.2006.07.007>.
- [118] Vassilev S V., Vassileva CG. A new approach for the classification of coal fly ashes based on their origin, composition, properties, and behaviour. *Fuel* 2007;86:1490–512. <https://doi.org/10.1016/j.fuel.2006.11.020>.
- [119] Patel SK, Satpathy HP, Nayak AN, Mohanty CR. Utilization of Fly Ash Cenosphere for Production of Sustainable Lightweight Concrete. *J Inst Eng Ser A* 2020;101:179–94. <https://doi.org/10.1007/s40030-019-00415-6>.
- [120] Fomenko E V, Anshits NN, Pankova M V, Solovyov LA, Anshits AG. Fly Ash Cenospheres: Composition, Morphology, Structure, and Helium Permeability. n.d.
- [121] Ranjbar N, Kuenzel C. Cenospheres: A review. *Fuel* 2017;207:1–12. <https://doi.org/10.1016/j.fuel.2017.06.059>.
- [122] Islam MM, Kim HS. Manufacture of syntactic foams using starch as binder: Post-mold processing. *Mater Manuf Process* 2008;23:884–92.

<https://doi.org/10.1080/10426910802413661>.

- [123] Fomenko E V., Anshits NN, Solovyov LA, Mikhaylova OA, Anshits AG. Composition and morphology of fly ash cenospheres produced from the combustion of Kuznetsk coal. *Energy and Fuels* 2013;27:5440–8. <https://doi.org/10.1021/ef400754c>.
- [124] Wasekar PA, Kadam PG, Mhaske ST. Effect of Cenosphere Concentration on the Mechanical, Thermal, Rheological and Morphological Properties of Nylon 6. *J Miner Mater Charact Eng* 2012;11:807–12. <https://doi.org/10.4236/jmmce.2012.118070>.
- [125] Fomenko E V, Anshits NN, Pankova M V, Solovyov LA, Anshits AG. Fly Ash Cenospheres: Composition, Morphology, Structure, and Helium Permeability. n.d.
- [126] Gehrcke H. Fluid Catalytic Cracking with Zeolite Catalysts: Von P. B. Venuto und E. T. Habib, Jr. Marcel Dekker, Inc., New York, Basel 1979. VI, 156 S., zahlr. Zeichn. und Tab., geb., SFr. 44,-. *Nachrichten Aus Chemie, Tech Und Lab* 1980;28:228–228. <https://doi.org/10.1002/nadc.19800280410>.
- [127] Anbia M, Aghaei M. Study of the effect of organic binders on 13X zeolite agglomeration and their CO₂ adsorption properties. *Sci Iran* 2019;26:1497–504. <https://doi.org/10.24200/sci.2018.21198>.
- [128] Prasanth KP, Pillai RS, Bajaj HC, Jasra R V., Chung HD, Kim TH, et al. Adsorption of hydrogen in nickel and rhodium exchanged zeolite X. *Int J Hydrogen Energy* 2008;33:735–45. <https://doi.org/10.1016/j.ijhydene.2007.10.047>.
- [129] Ameh AE, Fatoba OO, Musyoka NM, Louis B, Petrik LF. Transformation of fly ash based nanosilica extract to BEA zeolite and its durability in hot liquid. *Microporous Mesoporous Mater* 2020;305:110332. <https://doi.org/10.1016/j.micromeso.2020.110332>.

- [130] Navrotsky A, Trofyrnluk O, Levchenko AA. Thermochemistry of microporous and mesoporous materials. *Chem Rev* 2009;109:3885–902. <https://doi.org/10.1021/cr800495t>.
- [131] Fu Q, Qin Y, Zhang D. Investigation of host-guest bonding site in the zeolite NaX/CHF₃ and CHClF₂ system. *Microporous Mesoporous Mater* 2020;306:110395. <https://doi.org/10.1016/j.micromeso.2020.110395>.
- [132] Turnes Palomino G, Otero Areán C, Llop Carayol MR. Hydrogen adsorption on the faujasite-type zeolite Mg-X: An IR spectroscopic and thermodynamic study. *Appl Surf Sci* 2010;256:5281–4. <https://doi.org/10.1016/j.apsusc.2009.12.118>.
- [133] Di Nicola A, Arcadi A, Gallucci K, Mucciante V, Rossi L. Hydrotalcite-supported palladium nanoparticles as catalysts for the hydroarylation of carbon-carbon multiple bonds. *New J Chem* 2018;42:1952–7. <https://doi.org/10.1039/c7nj04046f>.
- [134] Zhang S-Y, Yu K, Guo Y-S, Mou R-Q, Lu X-F, Guo D-S. Preparation and Reactivation of Heterogeneous Palladium Catalysts and Applications in Sonogashira, Suzuki, and Heck Reactions in Aqueous Media. *ChemistryOpen* 2018;7:803–13. <https://doi.org/10.1002/open.201800139>.
- [135] Catalyst Preparation: Science and Engineering | John Regalbuto | download n.d. <https://b-ok.cc/book/563804/e00991> (accessed September 16, 2020).
- [136] Jentoft R. Thermal analysis methods *Modern Methods in Heterogeneous Catalysis Research*. n.d.
- [137] He J, Wei M, Li B, Kang Y, Evans DG, Duan X. Preparation of layered double hydroxides. *Struct Bond* 2005;119:89–119. https://doi.org/10.1007/430_006.

- [138] Laverdura UP, Rossi L, Gallucci K, Aloisi I, Ferrante F, Foscolo PU. Sorbenti solidi a base di CaO nella tecnologia CaL per la separazione della CO₂ ad alta temperatura. *MINISTERO DELLO SVILUPPO ECONOMICO*. n.d.
- [139] Park JE, Youn HK, Yang ST, Ahn WS. CO₂ capture and MWCNTs synthesis using mesoporous silica and zeolite 13X collectively prepared from bottom ash. *Catal Today* 2012;190:15–22. <https://doi.org/10.1016/j.cattod.2011.09.032>.
- [140] Kumar P, Mal N, Oumi Y, Yamana K, Sano T. Mesoporous materials prepared using coal fly ash as the silicon and aluminium source. *J Mater Chem* 2001;11:3285–90. <https://doi.org/10.1039/b104810b>.
- [141] Lindlar H, Dubuis R. Palladium Catalyst for Partial Reduction of Acetylenes. *Org. Synth.*, Hoboken, NJ, USA: John Wiley & Sons, Inc.; 2003, p. 89–89. <https://doi.org/10.1002/0471264180.os046.27>.
- [142] Tripathi B, Paniwnyk L, Cherkasov N, Ibadon AO, Lana-Villarreal T, Gómez R. Ultrasound-assisted selective hydrogenation of C-5 acetylene alcohols with Lindlar catalysts under the Creative Commons Attribution-NonCommercial-NoDerivatives 4.0 International <http://creativecommons.org/licenses/by-nc-nd/4.0/> Ultrasound-Assisted Selective Hydrogenation of C-5 Acetylene Alcohols with Lindlar Catalysts. *Ultrason Sonochem* 2015;26:445–51. <https://doi.org/10.1016/j.ultsonch.2015.03.006>.
- [143] Mallát T, Szabó S, Petró J. The role of lead in the selectivity of palladium-lead (lindlar type) catalysts. *Appl Catal* 1987;29:117–23. [https://doi.org/10.1016/S0166-9834\(00\)82611-1](https://doi.org/10.1016/S0166-9834(00)82611-1).
- [144] Rajaram J, Narula APS, Chawla HPS, Dev S. Semihydrogenation of acetylenes. Modified lindlar catalyst. *Tetrahedron* 1983;39:2315–22. <https://doi.org/10.1016/S0040->

4020(01)91960-X.

- [145] Arcadi A, Cacchi S, Marinelli F. Palladium-catalysed reductive addition of aryl iodides to aryl and alkylethynylsilanes: A stereo and regioselective route to functionalized 2,2-disubstituted vinylsilanes. *Tetrahedron Lett* 1986;27:6397–400. [https://doi.org/10.1016/S0040-4039\(00\)87818-1](https://doi.org/10.1016/S0040-4039(00)87818-1).
- [146] Lukić I, Krstić J, Glišić S, Jovanović D, Skala D. Biodiesel synthesis using K₂CO₃/Al-O-Si aerogel catalysts. *J Serb Chem Soc* 2010;75:789–801. <https://doi.org/10.2298/JSC090707047L>.
- [147] Hang S-Y, Ai Yu K, Shuang Guo Y, Qi Mou R, Lu X-F, Guo D-S. Preparation and Reactivation of Heterogeneous Palladium Catalysts and Applications in Sonogashira, Suzuki, and Heck Reactions in Aqueous Media n.d. <https://doi.org/10.1002/open.201800139>.
- [148] Laverdura UP, Rossi L, Gallucci K, Aloisi I, Ferrante F, Foscolo PU, et al. Sorbenti solidi a base di CaO nella tecnologia CaL per la separazione della CO₂ ad alta temperatura n.d.
- [149] Rogers KA, Zheng Y. Selective Deoxygenation of Biomass-Derived Bio-oils within Hydrogen-Modest Environments: A Review and New Insights. *ChemSusChem* 2016;9:1750–72. <https://doi.org/10.1002/cssc.201600144>.
- [150] Brunauer, Emmet and Teller, Adsorption of gases in multimolecular layers, 1938.pdf | Adsorption | Gases n.d. <https://www.scribd.com/document/335114308/Brunauer-Emmet-and-Teller-Adsorption-of-gases-in-multimolecular-layers-1938-pdf> (accessed September 16, 2020).
- [151] Barrett EP, Joyner LG, Halenda PP. The Determination of Pore Volume and Area

- Distributions in Porous Substances. I. Computations from Nitrogen Isotherms. *J Am Chem Soc* 1951;73:373–80. <https://doi.org/10.1021/ja01145a126>.
- [152] Agilent Technologies Application eHandbook ICP-OES. INDUCTIVELY COUPLED PLASMA OPTICAL EMISSION SPECTROSCOPY (ICP-OES) Application eHandbook ICP-OES Application eHandbook 2017:1–103.
- [153] Agilent 700 Series ICP Optical Emission Spectrometers Site Preparation Guide. n.d.
- [154] Sintesi, caratterizzazione di un materiale bifunzionale, sorbente e catalizzatore a base di CaO/Fly Ash/ Fe₂O₃. | Request PDF n.d. https://www.researchgate.net/publication/331530184_Sintesi_caratterizzazione_di_un_materiale_bifunzionale_sorbente_e_catalizzatore_a_base_di_CaOFly_Ash_Fe2O3 (accessed September 16, 2020).
- [155] Kniseley R. George L. Clark (Editor): the encyclopedia of spectroscopy. *Spectrochim Acta* 1961;17:904–5. [https://doi.org/10.1016/0371-1951\(61\)80161-6](https://doi.org/10.1016/0371-1951(61)80161-6).
- [156] Döbelin N. Lesson 2: Diffractometers and Phase Identification. n.d.
- [157] Thommes M, Kaneko K, Neimark A V, Olivier JP, Rodriguez-Reinoso F, Rouquerol J, et al. IUPAC Technical Report Physisorption of gases, with special reference to the evaluation of surface area and pore size distribution (IUPAC Technical Report). *Pure Appl Chem* 2015:aop. <https://doi.org/10.1515/pac-2014-1117>.
- [158] Landers J, Gor GY, Neimark A V. Density functional theory methods for characterization of porous materials. *Colloids Surfaces A Physicochem Eng Asp* 2013;437:3–32. <https://doi.org/10.1016/j.colsurfa.2013.01.007>.
- [159] Handbook of Heterogeneous Catalysis 1-8 | Ertl G., Knoezinger H., Schueth F.,

- Weitkamp J. | download n.d. <https://b-ok.cc/book/1235339/b84338> (accessed September 24, 2020).
- [160] Catalyst T. *AutoChem II* 2920. 2000.
- [161] Lin HY, Chen YW. The mechanism of reduction of cobalt by hydrogen. *Mater Chem Phys* 2004;85:171–5. <https://doi.org/10.1016/j.matchemphys.2003.12.028>.
- [162] full-text n.d.
- [163] Girard B. Retention index calculation using Kováts constant model for linear temperature-programmed gas chromatography. *J Chromatogr A* 1996;721:279–88. [https://doi.org/10.1016/0021-9673\(95\)00790-3](https://doi.org/10.1016/0021-9673(95)00790-3).
- [164] 41.1.29 AOAC Official Method 963.22 Methyl Esters of Fatty Acids in Oils and Fats Gas Chromatographic Method First Action 1963 Final Action 1984 AOAC-IUPAC Method Codex-Adopted-AOAC Method*. 2000.
- [165] Nohair B, Especel C, Lafaye G, Marécot P, Hoang LC, Barbier J. Palladium supported catalysts for the selective hydrogenation of sunflower oil. *J Mol Catal A Chem* 2005;229:117–26. <https://doi.org/10.1016/j.molcata.2004.11.017>.
- [166] Lligadas G, Ronda JC, Galià M, Cádiz V. Renewable polymeric materials from vegetable oils: A perspective. *Mater Today* 2013;16:337–43. <https://doi.org/10.1016/j.mattod.2013.08.016>.
- [167] Albright LF, Wisniak J. Selectivity and isomerization during partial hydrogenation of cottonseed oil and methyl oleate: Effect of operating variables. *J Am Oil Chem Soc* 1962;39:14–9. <https://doi.org/10.1007/BF02633340>.
- [168] Laverdura UP, Rossi L, Ferella F, Courson C, Zarli A, Alhajjoussef R, et al. Selective

- Catalytic Hydrogenation of Vegetable Oils on Lindlar Catalyst. *ACS Omega* 2020;5:22901–13. <https://doi.org/10.1021/acsomega.0c02280>.
- [169] Pasqual Laverdura U, Courson C, Gallucci K, Zarli A, Rossi L. Selective catalytic hydrogenation of sunflower oil in “mild” conditions. *n.d.*:67100.
- [170] Albright LF. Quantitative measure of selectivity of hydrogenation of triglycerides. *J Am Oil Chem Soc* 1965;42:250–3. <https://doi.org/10.1007/BF02541141>.
- [171] Bailey AE. Some additional notes on the kinetics and theory of fatty oil hydrogenation. *J Am Oil Chem Soc* 1949;26:644–8. <https://doi.org/10.1007/BF02651503>.
- [172] Philippaerts A, Jacobs P, Sels B. CHAPTER 10. Catalytic Hydrogenation of Vegetable Oils, 2014, p. 223–41. <https://doi.org/10.1039/9781782620099-00223>.
- [173] Demirbas A. Importance of biodiesel as transportation fuel. *Energy Policy* 2007;35:4661–70. <https://doi.org/10.1016/j.enpol.2007.04.003>.
- [174] Biomass for Biofuels - 1st Edition - Katarzyna Bulkowska - Zygmunt Ma n.d. <https://www.routledge.com/Biomass-for-Biofuels/Bulkowska-Gusiatin-Klimiuk-Pawlowski-Pokoj/p/book/9781138026315> (accessed September 25, 2020).
- [175] Li Z, Huang Z, Ding S, Li F, Wang Z, Lin H, et al. Catalytic conversion of waste cooking oil to fuel oil: Catalyst design and effect of solvent. *Energy* 2018;157:270–7. <https://doi.org/10.1016/j.energy.2018.05.156>.
- [176] Huang Z, Ding S, Li Z, Lin H, Li F, Li L, et al. Catalytic conversion of stearic acid to fuel oil in a hydrogen donor. *Int J Hydrogen Energy* 2016;41:16402–14. <https://doi.org/10.1016/j.ijhydene.2016.05.265>.
- [177] Ameen M, Azizan MT, Yusup S, Ramli A, Shahbaz M, Aqsha A. Process optimization

- of green diesel selectivity and understanding of reaction intermediates. *Renew Energy* 2020;149:1092–106. <https://doi.org/10.1016/j.renene.2019.10.108>.
- [178] Shin EW, Cho S Il, Kang JH, Kim WJ, Park JD, Moon SH. Palladium-Hydrogen Interaction on Supported Palladium Catalysts of Different Metal Dispersions. *Korean J Chem Eng* 2000;17:468–72. <https://doi.org/10.1007/BF02706862>.
- [179] Zhao W, Fierro V, Zlotea C, Izquierdo MT, Chevalier-César C, Latroche M, et al. Activated carbons doped with Pd nanoparticles for hydrogen storage. *Int J Hydrogen Energy* 2012;37:5072–80. <https://doi.org/10.1016/j.ijhydene.2011.12.058>.
- [180] Vilé G, Almora-Barrios N, Mitchell S, López N, Pérez-Ramírez J. From the Lindlar Catalyst to Supported Ligand-Modified Palladium Nanoparticles: Selectivity Patterns and Accessibility Constraints in the Continuous-Flow Three-Phase Hydrogenation of Acetylenic Compounds. *Chem - A Eur J* 2014;20:5849–5849. <https://doi.org/10.1002/chem.201400431>.
- [181] Thommes M, Kaneko K, Neimark A V., Olivier JP, Rodriguez-Reinoso F, Rouquerol J, et al. Physisorption of gases, with special reference to the evaluation of surface area and pore size distribution (IUPAC Technical Report). *Pure Appl Chem* 2015;87:1051–69. <https://doi.org/10.1515/pac-2014-1117>.
- [182] Hibino T, Tsunashima A. Characterization of repeatedly reconstructed Mg-Al hydrotalcite-like compounds: Gradual segregation of aluminum from the structure. *Chem Mater* 1998;10:4055–61. <https://doi.org/10.1021/cm980478q>.
- [183] Molano-Mendoza M, Donneys-Victoria D, Marriaga-Cabrales N, Mueses MA, Li Puma G, Machuca-Martínez F. Synthesis of Mg-Al layered double hydroxides by electrocoagulation. *MethodsX* 2018;5:915–23.

<https://doi.org/10.1016/j.mex.2018.07.019>.

- [184] Kordouli E, Pawelec B, Bourikas K, Kordulis C, Fierro JLG, Lycourghiotis A. Mo promoted Ni-Al₂O₃ co-precipitated catalysts for green diesel production. *Appl Catal B Environ* 2018;229:139–54. <https://doi.org/10.1016/j.apcatb.2018.02.015>.
- [185] Laverdura UP, Rossi L, Gallucci K, Aloisi I, Ferrante F, Foscolo PU, et al. Sorbenti solidi a base di CaO nella tecnologia CaL per la separazione della CO₂ ad alta temperatura n.d.
- [186] Vanga G, Stendardo S. Sintesi , caratterizzazione di un materiale bifunzionale , sorbente e catalizzatore a base di CaO / Fly Ash / Fe₂O₃ n.d.
- [187] Chou CW, Chu SJ, Chiang HJ, Huang CY, Lee CJ, Sheen SR, et al. Temperature-programmed reduction study on calcination of nano-palladium. *J Phys Chem B* 2001;105:9113–7. <https://doi.org/10.1021/jp011170g>.
- [188] James OO, Maity S. *Journal of Petroleum Technology and Alternative Fuels* Temperature programme reduction (TPR) studies of cobalt phases in γ -alumina supported cobalt catalysts 2016;7:1–12. <https://doi.org/10.5897/JPTAF2015.0122>.
- [189] Phan DP, Vo TK, Le VN, Kim J, Lee EY. Spray pyrolysis synthesis of bimetallic NiMo/Al₂O₃–TiO₂ catalyst for hydrodeoxygenation of guaiacol: Effects of bimetallic composition and reduction temperature. *J Ind Eng Chem* 2020;83:351–8. <https://doi.org/10.1016/j.jiec.2019.12.008>.
- [190] Olusola OJ, Sudip M. Temperature programme reduction (TPR) studies of cobalt phases in γ -alumina supported cobalt catalysts. *J Pet Technol Altern Fuels* 2016;7:1–12. <https://doi.org/10.5897/jptaf2015.0122>.

- [191] Garces LJ, Hincapie B, Zerger R, Suib SL. The effect of temperature and support on the reduction of cobalt oxide: An in situ x-ray diffraction study. *J Phys Chem C* 2015;119:5484–90. <https://doi.org/10.1021/jp5124184>.
- [192] Said AEAA, Abd El-Wahab MMM, Abd El-Aal M. Catalytic dehydration of methanol to dimethyl ether over nanosized WO₃/Al₂O₃ system under inert and oxidative atmosphere. *Monatshefte Fur Chemie* 2016;147:1507–16. <https://doi.org/10.1007/s00706-015-1649-7>.
- [193] Ou Y, Tian W, Liu L, Zhang Y, Xiao P. Bimetallic Co₂Mo₃O₈ suboxides coupled with conductive cobalt nanowires for efficient and durable hydrogen evolution in alkaline electrolyte. *J Mater Chem A* 2018;6:5217–28. <https://doi.org/10.1039/c7ta11401j>.
- [194] Ranjbar N, Kuenzel C. Cenospheres: A review. *Fuel* 2017;207:1–12. <https://doi.org/10.1016/j.fuel.2017.06.059>.
- [195] Aghamohammadi S, Haghghi M, Maleki M, Rahemi N. Sequential impregnation vs. sol-gel synthesized Ni/Al₂O₃-CeO₂ nanocatalyst for dry reforming of methane: Effect of synthesis method and support promotion. *Mol Catal* 2017;431:39–48. <https://doi.org/10.1016/j.mcat.2017.01.012>.
- [196] Jeangros Q, Hansen TW, Wagner JB, Damsgaard CD, Dunin-Borkowski RE, Hébert C, et al. Reduction of nickel oxide particles by hydrogen studied in an environmental TEM. *J Mater Sci* 2013;48:2893–907. <https://doi.org/10.1007/s10853-012-7001-2>.
- [197] Steiger P, Alxneit I, Ferri D. Nickel incorporation in perovskite-type metal oxides – Implications on reducibility. *Acta Mater* 2019;164:568–76. <https://doi.org/10.1016/j.actamat.2018.11.004>.
- [198] Méndez FJ, Bravo-Ascención G, González-Mota M, Puente-Lee I, Bokhimi X, Klimova

- TE. NiMo catalysts supported on Al, Nb, Ti or Zr-containing MCM-41 for dibenzothiophene hydrodesulfurization. *Catal Today* 2020;349:217–27. <https://doi.org/10.1016/j.cattod.2018.03.039>.
- [199] Kumar P, Maity SK, Shee D. Role of NiMo Alloy and Ni Species in the Performance of NiMo/ Alumina Catalysts for Hydrodeoxygenation of Stearic Acid: A Kinetic Study 2019. <https://doi.org/10.1021/acsomega.8b03592>.
- [200] Lin TJ, Meng X, Shi L. Ni-exchanged Y-zeolite: An efficient heterogeneous catalyst for acetylene hydrocarboxylation. *Appl Catal A Gen* 2014;485:163–71. <https://doi.org/10.1016/j.apcata.2014.07.036>.
- [201] Babajide O, Musyoka N, Petrik L, Ameer F. Novel zeolite Na-X synthesized from fly ash as a heterogeneous catalyst in biodiesel production. *Catal Today* 2012;190:54–60. <https://doi.org/10.1016/j.cattod.2012.04.044>.
- [202] Ameen M, Tazli M, Yusup S, Ramli A. ScienceDirect H-Y zeolite as hydrodeoxygenation catalyst for diesel range hydrocarbon production from rubber seed oil. *Mater Today Proc* 2019;16:1742–9. <https://doi.org/10.1016/j.matpr.2019.06.044>.
- [203] Busca G. Acidity and basicity of zeolites: A fundamental approach. *Microporous Mesoporous Mater* 2017;254:3–16. <https://doi.org/10.1016/j.micromeso.2017.04.007>.
- [204] Bardone E, Marzocchella A, Keshavarz T, Laverdura UP, Ferella F, Creati M, et al. Selective Catalytic Hydrogenation of Triglycerides: Activity and Selectivity Towards C18:1. *Chem. Eng. Trans.*, vol. 64, 2018. <https://doi.org/10.3303/CET1864020>.
- [205] List GR, King JW. *Hydrogenation of Fats and Oils: Theory and Practice: Second Edition*. Elsevier Inc.; 2010. <https://doi.org/10.1016/C2015-0-02451-0>.

- [206] El-Shattory Y, deMan L, deMan JM. Hydrogenation of Canola Oil: Influence of Catalyst Concentration. *Can Inst Food Sci Technol J* 1981;14:53–8. [https://doi.org/10.1016/s0315-5463\(81\)72677-4](https://doi.org/10.1016/s0315-5463(81)72677-4).
- [207] Edvardsson J, Rautanen P, Littorin A, Larsson M. Deactivation and coke formation on palladium and platinum catalysts in vegetable oil hydrogenation. *JAOCS, J Am Oil Chem Soc* 2001;78:319–27. <https://doi.org/10.1007/s11746-001-0263-6>.
- [208] Pandarus V, Gingras G, Béland F, Ciriminna R, Pagliaro M. Selective hydrogenation of vegetable oils over Silia Cat Pd(0). *Org Process Res Dev* 2012;16:1307–11. <https://doi.org/10.1021/op300115r>.
- [209] Edvardsson J, Irandoust S. Reactors for hydrogenation of edible oils. *J Am Oil Chem Soc* 1994;71:235–42. <https://doi.org/10.1007/BF02638048>.
- [210] Stanković M, Čupić Ž, Gabrovska M, Banković P, Nikolova D, Jovanović D. Characteristics and catalytic behavior of supported NiMgAg/D catalysts in the partial hydrogenation of soybean oil. *React Kinet Mech Catal* 2015;115. <https://doi.org/10.1007/s11144-014-0829-5>.
- [211] Ameen M, Azizan MT, Yusup S, Ramli A, Yasir M. Catalytic hydrodeoxygenation of triglycerides: An approach to clean diesel fuel production. *Renew Sustain Energy Rev* 2017;80:1072–88. <https://doi.org/10.1016/j.rser.2017.05.268>.
- [212] Fu H, Xiao F, Wang S, Yang L, Lo YM. Production of low-trans fatty acids edible oil by electrochemical hydrogenation in a diaphragm reactor under controlled conditions. *JAOCS, J Am Oil Chem Soc* 2011;88:133–41. <https://doi.org/10.1007/s11746-010-1649-z>.
- [213] Fernández MB, Tonetto GM, Crapiste GH, Ferreira ML, Damiani DE. Hydrogenation of

- edible oil over Pd catalysts: A combined theoretical and experimental study. *J Mol Catal A Chem* 2005;237:67–79. <https://doi.org/10.1016/j.molcata.2005.04.047>.
- [214] McArdle S, Girish S, Leahy JJ, Curtin T. Selective hydrogenation of sunflower oil over noble metal catalysts. *J Mol Catal A Chem* 2011;351:179–87. <https://doi.org/10.1016/j.molcata.2011.10.004>.
- [215] Burkhard. under the supervision of Prof. 2009.
- [216] Vásquez MC, Silva EE, Castillo EF. Hydrotreatment of vegetable oils: A review of the technologies and its developments for jet biofuel production. *Biomass and Bioenergy* 2017;105:197–206. <https://doi.org/10.1016/j.biombioe.2017.07.008>.
- [217] Ao I, Sk K. The Reduction of Alkynes Over Pd-Based Catalyst Materials - A Pathway to Chemical Synthesis 2018. <https://doi.org/10.4172/2157-7048.1000376>.
- [218] Edeh I, Overton T, Bowra S. Catalytic hydrothermal deoxygenation of fatty acids over palladium on activated carbon catalyst (Pd/C) for renewable diesel production. *Biofuels* 2019. <https://doi.org/10.1080/17597269.2019.1580971>.
- [219] Veriansyah B, Han JY, Kim SK, Hong SA, Kim YJ, Lim JS, et al. Production of renewable diesel by hydroprocessing of soybean oil: Effect of catalysts. *Fuel* 2012;94:578–85. <https://doi.org/10.1016/j.fuel.2011.10.057>.
- [220] Lestari S, Beltramini J, Lu GQM. Catalytic deoxygenation of stearic acid over palladium supported on acid modified mesoporous silica. *Stud Surf Sci Catal* 2008;174:1339–42. [https://doi.org/10.1016/S0167-2991\(08\)80137-1](https://doi.org/10.1016/S0167-2991(08)80137-1).
- [221] De Sousa FP, Cardoso CC, Pasa VMD. Producing hydrocarbons for green diesel and jet fuel formulation from palm kernel fat over Pd/C. *Fuel Process Technol* 2016;143:35–42.

- <https://doi.org/10.1016/j.fuproc.2015.10.024>.
- [222] Krár M, Kasza T, Kovács S, Kalló D, Hancsók J. Bio gas oils with improved low temperature properties. *Fuel Process Technol* 2011;92:886–92. <https://doi.org/10.1016/j.fuproc.2010.12.007>.
- [223] Sankaranarayanan TM, Banu M, Pandurangan A, Sivasanker S. Hydroprocessing of sunflower oil-gas oil blends over sulfided Ni-Mo-Al-zeolite beta composites. *Bioresour Technol* 2011;102:10717–23. <https://doi.org/10.1016/j.biortech.2011.08.127>.
- [224] Kubička D, Kaluža L. Deoxygenation of vegetable oils over sulfided Ni, Mo and NiMo catalysts. *Appl Catal A Gen* 2010;372:199–208. <https://doi.org/10.1016/j.apcata.2009.10.034>.
- [225] Liu Y, Sotelo-Boyás R, Murata K, Minowa T, Sakanishi K. Hydrotreatment of vegetable oils to produce bio-hydrogenated diesel and liquefied petroleum gas fuel over catalysts containing sulfided Ni-Mo and solid acids. *Energy and Fuels* 2011;25:4675–85. <https://doi.org/10.1021/ef200889e>.
- [226] Srifa A, Faungnawakij K, Itthibenchapong V, Viriya-empikul N, Charinpanitkul T, Assabumrungrat S. Production of bio-hydrogenated diesel by catalytic hydrotreating of palm oil over NiMoS₂/γ-Al₂O₃ catalyst. *Bioresour Technol* 2014;158:81–90. <https://doi.org/10.1016/j.biortech.2014.01.100>.
- [227] Kiatkittipong W, Phimsen S, Kiatkittipong K, Wongsakulphasatch S, Laosiripojana N, Assabumrungrat S. Diesel-like hydrocarbon production from hydroprocessing of relevant refining palm oil. *Fuel Process Technol* 2013;116:16–26. <https://doi.org/10.1016/j.fuproc.2013.04.018>.
- [228] Ferella F, Puca A, Taglieri G, Rossi L, Gallucci K. Separation of carbon dioxide for

- biogas upgrading to biomethane. *J Clean Prod* 2017;164:1205–18. <https://doi.org/10.1016/j.jclepro.2017.07.037>.
- [229] Nagy G, Hancsók J, Varga Z, Pölczmán G, Kalló D. Investigation of hydrodearomatization of prehydrogenated gas oil fractions on Pt–Pd/H-USY catalysts. *Top Catal* 2007;45:195–201. <https://doi.org/10.1007/s11244-007-0265-0>.
- [230] Liu Q, Zuo H, Zhang Q, Wang T, Ma L. Hydrodeoxygenation of palm oil to hydrocarbon fuels over Ni/SAPO-11 catalysts. *Cuihua Xuebao/Chinese J Catal* 2014;35:748–56. [https://doi.org/10.1016/s1872-2067\(12\)60710-4](https://doi.org/10.1016/s1872-2067(12)60710-4).
- [231] Zarchin R, Rabaev M, Vidruk-Nehemya R, Landau M V., Herskowitz M. Hydroprocessing of soybean oil on nickel-phosphide supported catalysts. *Fuel* 2015;139:684–91. <https://doi.org/10.1016/j.fuel.2014.09.053>.
- [232] Ochoa A, Bilbao J, Gayubo AG, Castaño P. Coke formation and deactivation during catalytic reforming of biomass and waste pyrolysis products: A review. *Renew Sustain Energy Rev* 2020;119:109600. <https://doi.org/10.1016/j.rser.2019.109600>.
- [233] Argyle MD, Bartholomew CH. Heterogeneous catalyst deactivation and regeneration: A review. *Catalysts* 2015;5:145–269. <https://doi.org/10.3390/catal5010145>.
- [234] Méndez FJ, Bravo-Ascención G, González-Mota M, Puente-Lee I, Bokhimi X, Klimova TE. NiMo catalysts supported on Al, Nb, Ti or Zr-containing MCM-41 for dibenzothiophene hydrodesulfurization. *Catal Today* 2020;349:217–27. <https://doi.org/10.1016/j.cattod.2018.03.039>.
- [235] Duan J, Han J, Sun H, Chen P, Lou H, Zheng X. Diesel-like hydrocarbons obtained by direct hydrodeoxygenation of sunflower oil over Pd/Al-SBA-15 catalysts. *Catal Commun* 2012;17:76–80. <https://doi.org/10.1016/j.catcom.2011.10.009>.

- [236] Jones E, Qadir M, van Vliet MTH, Smakhtin V, Kang S mu. The state of desalination and brine production: A global outlook. *Sci Total Environ* 2019;657:1343–56. <https://doi.org/10.1016/j.scitotenv.2018.12.076>.
- [237] Fahmida P, Sultana A. *Desalination Technologies for Developing Countries : A Review* 2018.
- [238] Acknowledgment Professor El-Dessouky dedicates this book to the memory of his parents . Also , he dedicates the book to his family , Fatma , Sarah , Sameh , and Sanyia . Professor Ettouney dedicates this book to his parents , Mohamed and Fatma , his broth n.d.
- [239] Cost P. *RO Economics* 7.1 2019:163–87. <https://doi.org/10.1016/B978-0-12-811468-1.00007-4>.
- [240] Miller JE. *Review of Water Resources and Desalination Technologies* 2014. <https://doi.org/10.2172/809106>.
- [241] Karan H, Antar MA, An JHL V, Mistry KH, Antar MA, V JHL. Version An improved model for multiple effect distillation 2013:0–25.
- [242] Greenlee LF, Lawler DF, Freeman BD, Marrot B, Moulin P, Ce P. Reverse osmosis desalination : Water sources , technology , and today ’ s challenges. *Water Res* 2009;43:2317–48. <https://doi.org/10.1016/j.watres.2009.03.010>.
- [243] Alkaisi A, Mossad R, Sharifian-barforoush A. A review of the water desalination systems integrated with renewable energy. *Energy Procedia* 2017;110:268–74. <https://doi.org/10.1016/j.egypro.2017.03.138>.
- [244] Huddar D, Holikar A, Mandhare A, Jaiswal S, Bhopale NN. Design of Multi-stage flash

process as desalination and power generation plant 2017;1:12–21.

- [245] Al-Sahali M, Ettouney H. Developments in thermal desalination processes: Design, energy, and costing aspects. *Desalination* 2007. <https://doi.org/10.1016/j.desal.2006.08.020>.
- [246] Martinez H, Programme E. DEPARTMENT OF TECHNOLOGY AND BUILT ENVIRONMENT Aspects to Consider Examiner : Claes Åkerman Supervisor : Claes Åkerman 2010.
- [247] Purification W, Program D. Handbook 2003.
- [248] Atab MS, Smallbone AJ, Roskilly AP. An operational and economic study of a reverse osmosis desalination system for potable water and land irrigation. *DES* 2016;397:174–84. <https://doi.org/10.1016/j.desal.2016.06.020>.
- [249] Zarzo D, Prats D. Desalination and energy consumption . What can we expect in the near future ? *Desalination* 2018;427:1–9. <https://doi.org/10.1016/j.desal.2017.10.046>.
- [250] Fulajj A. Dynamic Modeling of Multi Stage Flash (MSF) Desalination Plant Supervisors : Professor David Bogle 2011.

12 ACKNOWLEDGMENTS

Arriving at the end of this path, it does not seem real to me to write the last lines of three years of Ph.D. research, a period really full of difficulties, memories, and emotions.....

I deeply thank my thesis director, Prof. Katia Gallucci, for letting me work and learn in her research team. She kindly led and supported me, becoming a fundamental point of reference. I am grateful for her encouragement and enduring strength of spirit.

I would like to express my special thanks and appreciation to Prof. Leucio Rossi (department of physical and chemical sciences) to become a fundamental help for the experimental hydrogenation/deoxygenation research activities and the important experience I learned with GC instruments in his laboratory.

It is also my pleasure to express heartfelt thanks to Prof. Pier Ugo Foscolo, Prof. Antonio Germanà, and Dr. Marilena Taddei for their fundamental support with the desalination research part.

I thank Fabiola Ferrante, Maria Giammatteo, Giampaolo Antonelli for their availability in L'Aquila laboratories.

I am grateful to Prof. Claire Courson and her team for their technical support in some catalyst's analysis in Strasbourg laboratories.

Moreover, I thank my friends Umberto Pasqual Laverdura, Ludovico Macera, and Giuseppe di Vito Nolfi for their availability on many occasions.

I would like to pass an exceptional heartfelt thanks to Ing. Mimmo Srour for his reinforcement, encouragement, and support during these years.

Together with already mentioned people, I thank those who shared with me part of my time and gave me a warm welcome, making me feel like a member of Italian families. So, thanks to my best friend and her family Annalisa Nicoli.

Drawing to an end, I would like to thank my family for their patience, faith, and supporting me throughout all my life.

